7-11-2015

De-icing in Photovoltaic Devices by Ultrasonic Waves and Surface Engineering

Ryan Matthew Fillion
University of Windsor

Recommended Citation

Fillion, Ryan Matthew, "De-icing in Photovoltaic Devices by Ultrasonic Waves and Surface Engineering" (2015). *Electronic Theses and Dissertations.* Paper 5332.

De-icing in Photovoltaic Devices by Ultrasonic Waves and Surface Engineering

by

Ryan Matthew Fillion

A Thesis
Submitted to the Faculty of Graduate Studies
through Materials Engineering
in Partial Fulfillment of the Requirements for
the Degree of Master of Applied Science at the
University of Windsor

Windsor, Ontario, Canada

De-icing in Photovoltaic Devices by Ultrasonic Waves and Surface Engineering

by

Ryan Matthew Fillion

APPROVED BY:

S. Cheng
Department of Civil and Environmental Engineering

A. T. Alpas
Department of Mechanical, Automotive, and Materials Engineering

R. Riahi, Advisor
Department of Mechanical, Automotive, and Materials Engineering

A. Edrisy, Advisor
Department of Mechanical, Automotive, and Materials Engineering

05/27/2015

Author's Declaration of Originality

I hereby certify that I am the sole author of this thesis and that no part of this thesis has been published or submitted for publication.

I certify that, to the best of my knowledge, my thesis does not infringe upon anyone's copyright nor violate any proprietary rights and that any ideas, techniques, quotations, or any other material from the work of other people included in my thesis, published or otherwise, are fully acknowledged in accordance with the standard referencing practices. Furthermore, to the extent that I have included copyrighted material that surpasses the bounds of fair dealing within the meaning of the Canada Copyright Act, I certify that I have obtained a written permission from the copyright owner(s) to include such material(s) in my thesis and have included copies of such copyright clearances to my appendix.

I declare that this is a true copy of my thesis, including any final revisions, as approved by my thesis committee and the Graduate Studies office, and that this thesis has not been submitted for a higher degree to any other University or Institution.

Abstract

A review of the literature shows there is much potential for the decrease and prevention of ice accumulation and adhesion on many materials including renewable energy devices with the use of well-designed hydrophobic coatings. It has also been shown that the addition of ultrasonic vibration can dramatically decrease or break the adhesion of ice altogether. A combination of hydrophobic coatings and ultrasonic vibration could result in a system capable of delaminating accumulated ice efficiently and remotely, which could replace outdated and expensive de-icing alternatives. Currently, however, there is not a standard method for measuring the ice adhesion of various materials of various surface conditions and an apparatus for this purpose cannot be purchased for research in the ice adhesion field. It is the objective of this project to design and fabricate a method of measuring the ice adhesion of various materials with differing surface conditions with the option of adding ultrasonic vibrational input. The objective of this investigation has been completed in that a method of measuring the ice adhesion of various materials with differing surface conditions with the option of adding ultrasonic vibrational input has been designed, fabricated and successfully tested on various materials and coating of differing surface conditions, the addition of ultrasonic vibrational input using the apparatus has also been successfully tested. Additionally, a custom-designed apparatus was built to investigate the surface wettability of samples of varying materials with differing surface conditions, called a goniometer, which has been used to measure the water contact angle and corresponding hysteresis of all samples.

Dedication

To my wife, Simina, and my parents, Rene and Irene,

for the love and support you've given me throughout

my education.

Acknowledgements

I would like to offer my sincere thanks to my advisors Dr. Edrisy and Dr. Riahi for their guidance and supervision throughout the course of my research. It is their knowledge and skill that enables their students to succeed.

I would also like to thank the members of my committee, Dr. A. Alpas and Dr. Cheng for their time and commitment attending my presentations and reviewing my thesis. Their input and feedback was invaluable for the completion of my work.

Funding from the Natural Science and Engineering Council of Canada (NSERC) is gratefully acknowledged.

Additional thanks to the senior technologist at the Centre for Engineering Innovation, Andy Jenner, for his help and dedication to the success of my research.

Finally, I would like to thank my wife and family for their love and support throughout my education, I would not be here without your help.

Table of Contents

List of Tables

List of Figures

List of Appendices

Nomenclature

List of Symbols

E	Energy required to form a unit of the solid-liquid interface
f	Contact area fraction
g	Gravitational acceleration
K_R	Interfacial adhesion parameter
m	Mass of water droplet
q	Charge on ice surface
q'	Image charge
r	Roughness factor
S_1	Liquid surface tension
S_{12}	Energy content of a measured unit area after wetting
W	Width of water droplet
Greek Symbols	
α	Sliding angle
α'	Sliding angle for a rough surface
γ_{LV}	Interface free energy per unit area of the liquid-gas interface

γ_{SL}	Interfacial free energy per unit area of the solid-liquid interface
γ_{SV}	Interfacial free energy per unit area of the solid-gas interface
ε	Dielectric constant
θ	Water contact angle
θ'	Water contact angle as measured on a rough surface
θ_A	Advancing contact angle
θ_R	Receding contact angle
ρ	Density of liquid
σ_1	Total area of the solid-liquid interface
σ_2	Total area of the liquid-air interface

1. Introduction

With advances in technology and the recent shift in mindsets toward sustainability, the renewable energy industry has become a more viable source to meet the energy needs of the world and is being widely researched in all areas (1) (2) (3) (4) (5). In 2010, The U.S. Energy Information Administration's International Energy Outlook reported that renewable energy will be the fastest growing world energy source over the period 2007-2035 (6). The increase in this demand may be attributed to several factors: the decline in fossil fuels, climate change, and the abundance of renewable energy potential. The migration away from fossil fuel usage is an appropriate response to the knowledge that fossil fuel resources are finite and cannot sustain society indefinitely (5) (7). As of 2010, oil production has been nearly static for the past 5 years and marginal productivity is showing signs of stress worldwide (7). Renewable energy has dawned as a possible solution that may alleviate the growing concerns over greenhouse gas emissions, increasing energy prices, and the dependency on foreign energy sources, and this includes the geopolitical climate that is associated with the production of fossil fuels in some regions of the world (8). In addition, renewable energy offers the benefits of being clean, abundant, inexhaustible, and for a variety of applications it can even be the most cost-effective source of energy, meeting between 15 and 20% of the total world energy demand as of 2007 (9).

Usable Global Renewable Energy Resources (exajoules per year)

Resource	Current Use	Technical Potential	Theoretical Potential
Hydropower	10.0	50	150
Biomass Energy	50.0	>250	2,900

Solar Energy	0.2	>1,600	3,900,000
Wind Energy	0.2	600	6,000
Geothermal Energy	2.0	5,000	140,000,000
Ocean Energy	--	--	7,400
Total	62.4	>7,500	>143,000,000

Table 1.The potential resources of global renewable energy (10). Source: U.S. Energy Information Administration (July 2010).

There are now many methods of extracting energy from renewable sources such as wind turbines for harvesting energy from wind (11), geothermal processes that use the heat from the Earth (12) and solar voltaic cells that convert sunlight into electricity (13). In many places where renewable energy systems are used, climactic conditions are severe and icing is prevalent. This is a problem because the efficiency of wind turbines and solar panels is greatly reduced due to icing and snow accumulation; it may even stop the production of energy all together (1) (14) (15) (16). Due to the crippling effect ice accretion has on the ability of solar cells to produce electricity, many researchers have been turning their attention to designing systems of ice removal. The removal of ice can be classified into two categories: active solutions and passive solutions.

Active solutions are methods of removing ice after it has been deposited; these include mechanical scraping, thermal treatments, and the use of de-icing fluids. Passive solutions would include treatments that can be applied to a surface prior to its use that would prevent the ice from adhering or cause it to delaminate under its own weight. Active methods are currently widely used, but passive methods have found few industrial uses despite being environmentally friendly, compared to de-icing fluids. Passive methods also represent a cheaper option than active methods which are energy hungry and can be expensive to produce and operate (17). One such possible passive solution may lie in hydrophobic coatings. Currently, there is no known material that can completely prevent ice or snow from accumulating on its surface, however, some coatings are believed to provide reduced adhesion (18) and for smooth surfaces, there is a clear trend that the ice adhesion strength decreases as the surface becomes more hydrophobic (19).Furthermore, it was also shown that despite the rough surface of a superhydrophobic coating, it will reduce the adhesion of ice more than a smooth hydrophobic surface of the same chemical composition, and superhydrophobic coatings exhibiting a contact angle hysteresis lower than 5° lead to very high icephobic properties (18) (20) (21). However, the durability and mechanical robustness of the coating are particularly important to consider because the fragile hierarchical roughness can be irreversibly destroyed, which will inevitably lead to an increase in the contact angle hysteresis and a rapid decrease in the static contact angle (22).

Another physical factor that may affect the adhesion of ice to a superhydrophobic coating is particle size. Cao et al. (23) developed superhydrophobic coatings on aluminum substrates and determined that the critical particle sizes that determine the superhydrophobicity of the coating and the ice resistant property respectively are in two different length scales. The hierarchical coatings were made with particles up to 10 micrometers in diameter for the micro-roughness regime which rendered them all superhydrophobic. The anti-icing properties of these coatings, however, are distinctly different. No ice formed on the samples when particles of 20 and 50 nanometers were used for the nano-scale roughness regime, but the probability of icing increases remarkably when the particle diameter is larger than 50 nm. Indeed it has been shown that the size of the microcracks at the interface is the critical parameter that will govern the adhesion of ice to a superhydrophobic surface even though high receding angles are well correlated with reduced ice adhesion. This can help to explain why some superhydrophobic surfaces can result in strong ice adhesion if they do not provide sufficiently large voids at the interface.The stability of a superhydrophobic coating in the Cassie-Baxter wetting state is also an important factor that needs to be considered. In a humid atmosphere, when water condenses in the rough structure of the coating, the contact angle of water will decrease as the droplet switches from a Cassie-Baxter state to a Wenzel state. If a droplet freezes in this condition, it may lead to very large values of ice adhesion called the anchor effect (24).This shows that it is uncertain whether a superhydrophobic surface can be ice resistant without having a detailed knowledge of the surface morphology and caution should be taken when the ice resistant properties are correlated to the superhydrophobicity.

In contrast, recent studies have been undertaken to test the proficiency of using ultrasonic waves generated by a piezoelectric transducer targeted at the ice/substrate interface with the aims of breaking the adhesive bonds between the two. Early studies, though few, have shown positive results. In experiments performed by Palacios et al. (25), at -20º C, ice was allowed to accrete to 2.5 mm thick on the surface of a steel plate for 5 hours. This steel plate was raised and placed in the vertical direction so that the ice, when delaminated, would fall to the ground due to gravity. When the transducer was excited at radial resonance of 28.5 kHz and voltages in excess of 43V, the accreted ice layer was instantaneously removed. Thus validating the ultrasonic shear deicing method. To eliminate any concern about the thermal propagation from the ultrasonic transducer being a major contributor on the delamination of the ice layer, thermocouples were placed both on the transducer and the steel plate showed temperatures of -18 º C at the moment of ice delamination. This experimental set-up takes advantage of the low shear adhesion strength of ice and shows that ultrasonic piezoelectric transducers can demonstrate the capability of delaminating thin layers of ice, less than 3mm, instantly. Also, because the ice interface transverse shear stresses will vary with the ice thickness, as the thickness of the ice increases, the ultrasonic vibration will create even larger stresses at the ice/substrate interface as the inertia of the layer of ice also increases, allowing the thicker layers of ice to also be delaminated.

Therefore, these test results demonstrate that a radial resonance disk transducer (28 – 32 KHz) can create ultrasonic transverse shear stresses that are capable of instantaneously delaminating thin ice layers. At environment temperatures of -20º C, the system delaminates 2.5 mm thick ice layers with power input densities as low as 0.07 W/cm 2 (0.5 W/in 2) (25).

In conclusion, a review of the literature shows there is much potential for the decrease and prevention of ice accumulation and adhesion with the use of well-designed hydrophobic coatings and that in the proper installation the addition of ultrasonic vibration can dramatically decrease or break the adhesion of ice altogether. A combination of these could result in a system capable of delaminating accumulated ice remotely. Currently, however, there is not a standard method for measuring the ice adhesion of various materials of various surface conditions and an apparatus for this purpose cannot be purchased for research in ice adhesion. It is the objective of this investigation to design and fabricate a method of measuring the ice adhesion of various materials with differing surface conditions with the option of adding ultrasonic vibrational input.

Organization of thesis

Ch1. – Introduction to the basic background of the research along with the overall organization of the thesis.

Ch2. – Literature survey introducing the wettability of surfaces, active and passive methods of ice removal, hydrophobic coatings, properties of hydrophobic coatings such as ice adhesion, transparency, antireflective capabilities, durability and methods of fabrication. The survey also discusses scientific studies of ice nucleation and the use of ultrasonic vibration waves to break the adhesion of ice.

Ch3. – An outline of the materials and experimental procedures used to characterize the wettability, surface, and icing, and coating properties of the materials tested. The design parameters of the goniometer and ice adhesion testing machines and their features are explained in detail. The chapter elaborates on different tests and characterization techniques used in this study.

Ch.4 – Outlines in detail the results obtained by the ice adhesion testing, ultrasonic ice adhesion testing and characterization testing of the various sample materials. The chapter also includes observations obtained as a result of the characterization testing done with environmental scanning electron microscopy and Wyko.

Ch.5 – Discussion of the ice adhesion to various substrate materials, the effect of surface condition on ice adhesion, the effect of ultrasonic vibration waves on ice adhesion, the effect of hydrophobic coatings (sprayed and dipped) on wettability of glass, the effect of dipped hydrophobic coatings on ice adhesion to glass.

Ch.6 – Summarizes in point form the conclusions obtained in this study as well as recommendations for future study.

2. Literature Survey

Hydrophobic Surfaces

Hydrophilicity refers to the physical property of a material that can transiently bond with water through hydrogen bonding. A water droplet will spread itself on a hydrophilic surface; it may also enter the pores of the material and completely saturate it. Most natural materials are hydrophilic. A water droplet on a hydrophilic surface will occupy as large a surface as possible, thus making the water contact angle significantly low. Hydrophobicity refers to the physical property of a material that repels a mass of water. A water droplet being repelled by the material will not touch a large area of the surface and will take a spherical shape, thus making the water contact angle very large. The evaluation of hydrophilicity and hydrophobicity are made through measuring the angle at which water contacts a surface.

A surface with a water contact angle greater than 90° is usually referred to as hydrophobic, and one with a water contact angle higher than 140° is qualified as ultra-hydrophobic. The surfaces with very high water contact angles, particularly greater than 150°, are usually called superhydrophobic surfaces. The contact angle of water has been commonly used as a criterion to evaluate the static hydrophobicity of a surface, as depicted in figure 1. Alone, however, that factor is not adequate for the evaluation of dynamic hydrophobicity, which is the sliding of water droplets. Dynamic hydrophobicity is describing a surface's ability to shed water. Furthermore, to completely describe a superhydrophobic state, the contact angle hysteresis should also be measured. For an optimal superhydrophobic state, the static contact angle should be maximized, and the contact angle hysteresis minimized (26).

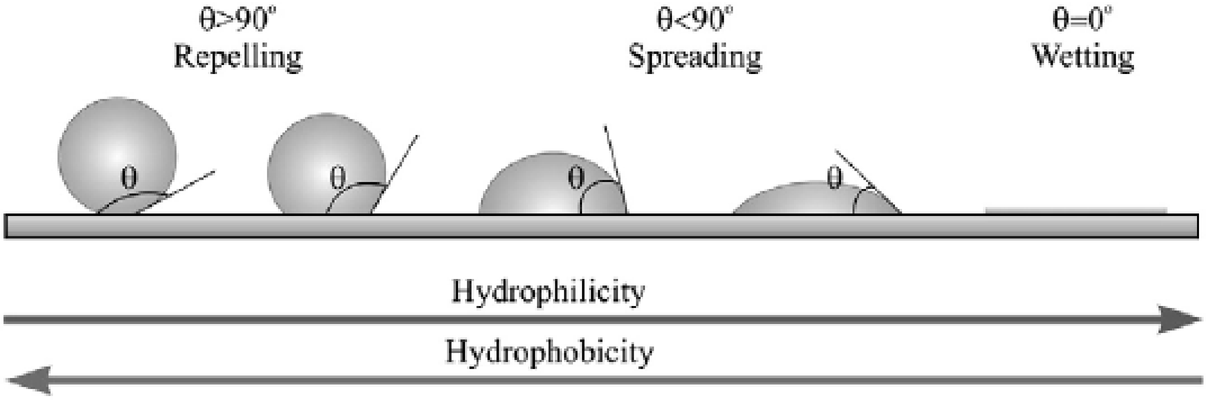

Figure 1. The wettability of a surface can be determined by the water contact angle measured.

Contact Angle Hysteresis

The contact angle hysteresis is the difference between the advancing and receding contact angles. The sliding angle and/or the contact angle hysteresis are commonly utilized as criteria for dynamic hydrophobicity on a solid hydrophobic surface (26). Hysteresis is a phenomenon that can arise from the molecular interactions between the solid and liquid or from irregularities in the surface, such as roughness or heterogeneities. In the case of a sessile drop: when further liquid is added, the contact line advances forward. When the motion of the drop stops it exhibits an advancing contact angle, θ_A. However, if liquid is removed from the sessile drop, the contact angle decreases before the contact line retreats back to a receding value, θ_R. The contact angle hysteresis is referred to as the difference between θ_A and θ_R . Furthermore, in the case of a droplet moving along the solid surface, the contact angle that appears at the front of the droplet, θ_A, will be greater than that at the back of the droplet, θ_R. This is due to roughness and surface heterogeneity, resulting in the contact angle hysteresis (27) (28). Furmidge (29) derived an equation describing the relationship between the sliding angle and contact angle hysteresis for a drop of water on a solid surface.

$$\left(\frac{mg}{w}\right)\sin\alpha = \gamma_{LV}(\cos\theta_R - \cos\theta_A) \qquad (1)$$

Where m is the mass of the water droplet, w is the width of the droplet, g is the gravitational acceleration, α is the sliding angle, γ_{LV} is the free energy of the liquid at the liquid-gas interface, and θ_A and θ_R are the advancing and receding angles, respectively.

Origin of Hydrophobic Surfaces

The phenomenon of hydrophobicity and self-cleaning surfaces was observed for the first time in nature. The term "Lotus effect" is accredited to the botanist Wilhelm Barthlott (30) (31) and refers to a special ability of the Lotus. The Lotus flower can stay clean and unaffected by dirt and pollution, even when growing in muddy waters. The Lotus leaf's "self-cleaning" surface, which reaches water contact angle values greater than 150°, is hydrophobic and rough. Its surface is comprised of two layers, a lower layer of micro-sized roughness covered by a second waxy layer of hydrophobic crystalloids of nano-sized roughness. The self-cleaning mechanism is characterized by three characteristics: superhydrophobicity, low sliding angle, and removal of dirt particles by the sliding droplet (32). The amazing functions and capabilities of the Lotus, like other biological species, have developed over millions of years through evolution. The ambition to recreate biological systems found in nature has sparked interest in a wide range of research and has led to the development of advanced functional materials or devices that can be found in literature: A dye-sensitized solar cell mimics the photosynthesis process (33) (34), a specialized adhesive surface mimics a gecko's foot or a mussel's ability to adhere to wet surfaces (35) (36) (37) (38) (39), a photonic crystal mimics the wings of a butterfly (40) (41) (42) (43) (44), an anti-reflective coating mimics the eyes of a moth (45) (46) (47), and a superhydrophobic and self-cleaning surface mimics the surface of a Lotus leaf, water strider's leg and a cicada orni's wing (48) (49) (50) (51) (52) (53) (54) (55) (56) (57) (58) (59).

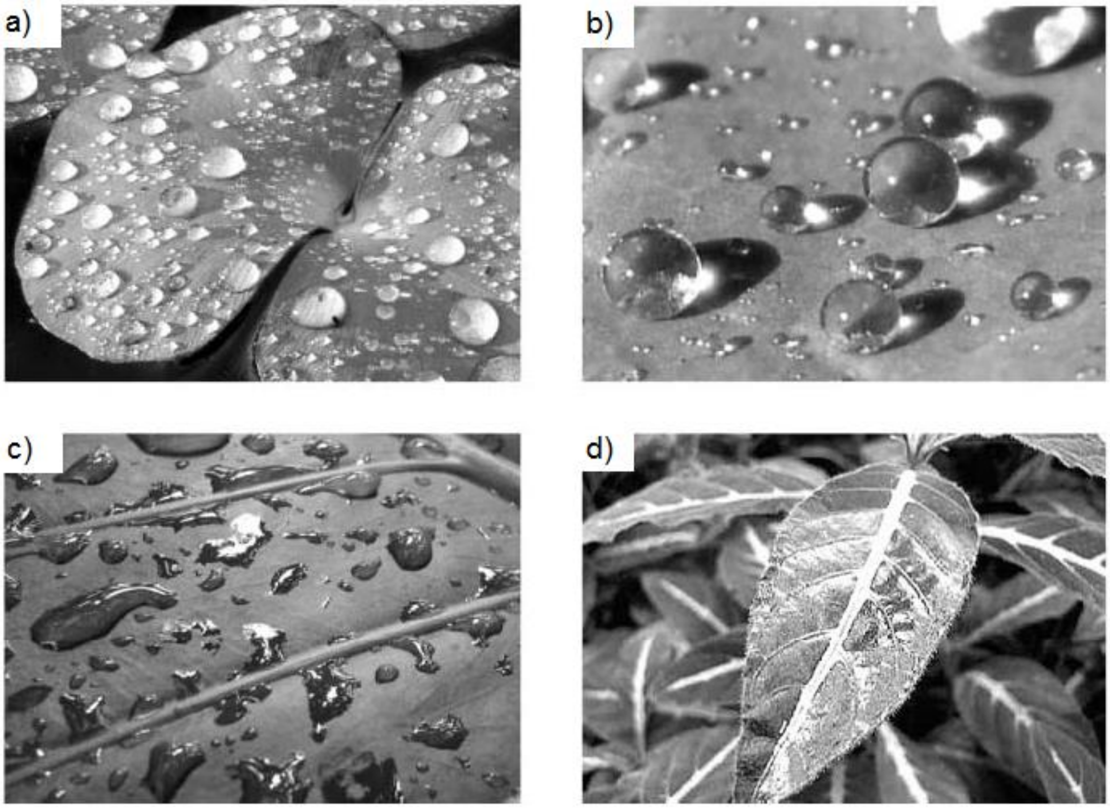

Figure 2. Examples of surface wettability in nature, a) the hydrophobic leaves of the *Regnellidiumdiphyllum*, b) *Brassica oleracea* leaves show superhydrophobicity, c) the *Alocasiaodora* has hydrophilic leaves, and d) the superhydrophilic leaves of the *Ruelliadevosiana*.

Progressive Theories on Surface Wettability

The thermodynamics between a liquid and a solid was described by Young in 1805 (60). His paper explained the wetting phenomenon for smooth surfaces and the forces causing liquids and solids to behave in a predictable manner. Though not appearing in his publication, this equation is attributed to him.

$$\cos\theta = (\gamma_{SV} - \gamma_{SL})/\gamma_{LV} \tag{2}$$

Where γ_{SL}, γ_{SV}, and γ_{LV} are the interfacial free energies per unit area of the solid-liquid, solid-gas, and liquid-gas interfaces respectively.

Wenzel (61) (62) proposed a modification to Young's equation after he observed the effect of surface roughness on the contact angle of water. His modification included a roughness factor, r , which is defined as the ratio between the actual rough surface area and the geometric projected area. Wenzel's equation can predict that a solid hydrophilic substrate will experience increased wetting, or a lower contact angle, due to roughness on its surface. However, a solid hydrophobic substrate will experience less wetting, or a higher contact angle, due to surface roughness.

$$rA = r(S_1 - S_{12}) = S_2\cos\theta \tag{3}$$

Where r is a roughness factor, A is the adhesion tension, S_2 is the surface tension of the liquid, and S_1 and S_{12} are the energy contents of a measured unit area before and after wetting respectively.

The theories of Young and Wenzel could be applied to a chemically homogeneous surface, but not to a non-homogeneous surface. It was Cassie and Baxter (63) (64) who extended the work of Wenzel to include non-homogeneous and porous surfaces. The Cassie-Baxter equation represents a contact angle at a surface that is composed of both solid and air because the liquid is prevented from fully penetrating into the pores of the surface due to its inherit repellence towards it which leaves air trapped in the roughness morphology.

$$\cos\theta = -\frac{E}{\gamma_{LV}} = \sigma_1 \cos\theta_1 - \sigma_2 \tag{4}$$

Where E is the energy gained by forming a unit area of the solid-liquid interface, γ_{LV} is the liquid-gas interfacial energy, and $\sigma_1$and σ_2 are the total areas of the solid-liquid interface and the liquid-gas interface respectively.

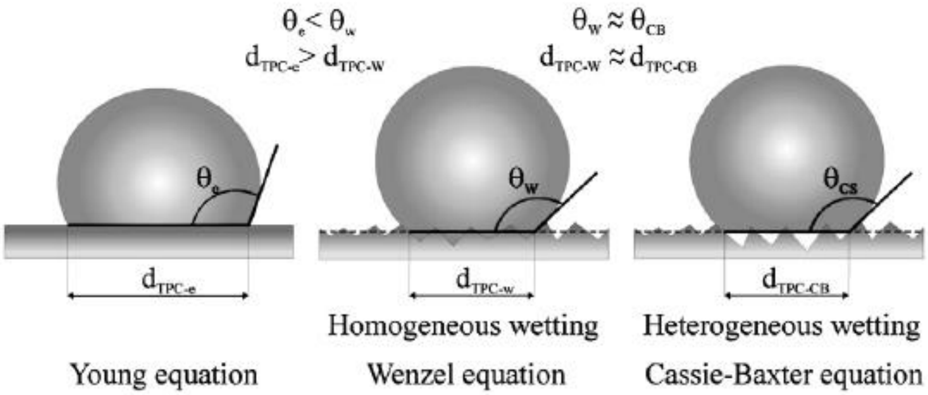

Figure 3. Schematic of progressive theories on surface wettability: Young's theory, Wenzel's theory and Cassie-Baxter's theory.

Influence of Roughness

Superhydrophobic surfaces require both low surface energy and the appropriate surface roughness (58) (65). Hare et al. (66) showed that fluorinated surfaces create the lowest polymer surface energies, resulting in highest contact angles. Nishino et al. (67) furthered this work by demonstrating that regularly aligned and close-packed CF_3 groups attains the lowest surface free energy of any flat solid. This surface exhibited a contact angle of 120° and contact angle higher than this can only be obtained by roughening the surface (68). Roughness can enhance hydrophobicity and decrease resistance to the flow with the correct factors considered (28). The roughness of the coating should be hierarchical as that of the lotus leaf, with micro-scale roughness and nano-scale roughness to achieve best results (28) (69) (70) (71). For most superhydrophobic surfaces, it is important that a composite solid-liquid-air interface is formed. A composite interface drastically decreases the adhesion of a droplet to the solid surface and contact angle hysteresis by decreasing the area of contact between the liquid and solid (70).

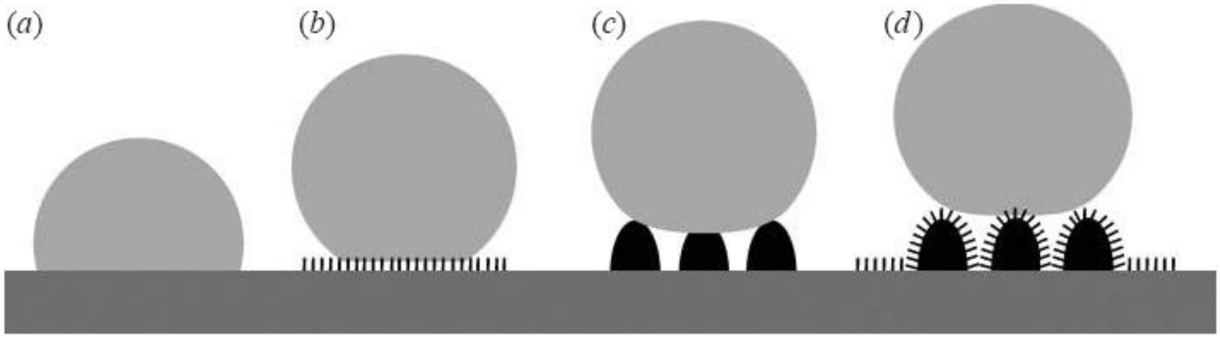

Figure 4. Schematic displaying the different roughness regimes, a) smooth surface, b) nano-roughness, c) micro-roughness, and d) a combination of micro- and nano-roughness (hierarchical roughness).

A composite state is essential for superhydrophobicity. Therefore, in the design of a superhydrophobic surface, the stability of the composite state should be addressed. With better knowledge of the parameters affecting the hydrophobicity of a surface, new models are being formed. Rios et al. (72) (73) proposed an equation to create a more comprehensive definition of a hydrophobic surface that includes the effects of both the contact and sliding angles.

$$\sin\alpha' = \frac{K_R \pi f}{g}\left[\frac{3}{\rho\pi(2 - 3\cos\theta' + \cos^3\theta')}\right]^{\frac{2}{3}} \sin^2\theta' \, m^{\frac{1}{3}} \tag{5}$$

Where α’ is the sliding angle for a rough surface, θ’ is the contact angle, and f is the contact area fraction. K_R represents the interfacial adhesion parameter, g is the gravitational acceleration, ρ is the density of the liquid, and *m* the mass of the droplet. Since *Sinα'* is proportional to *f*, this equation demonstrates that the rougher the hydrophobic surface is, the smaller *f* will become and thus the lower the sliding angle will be. It also indicates that as the roughness scale is decreased into the nano-scale, the sliding angle will be at its lowest.

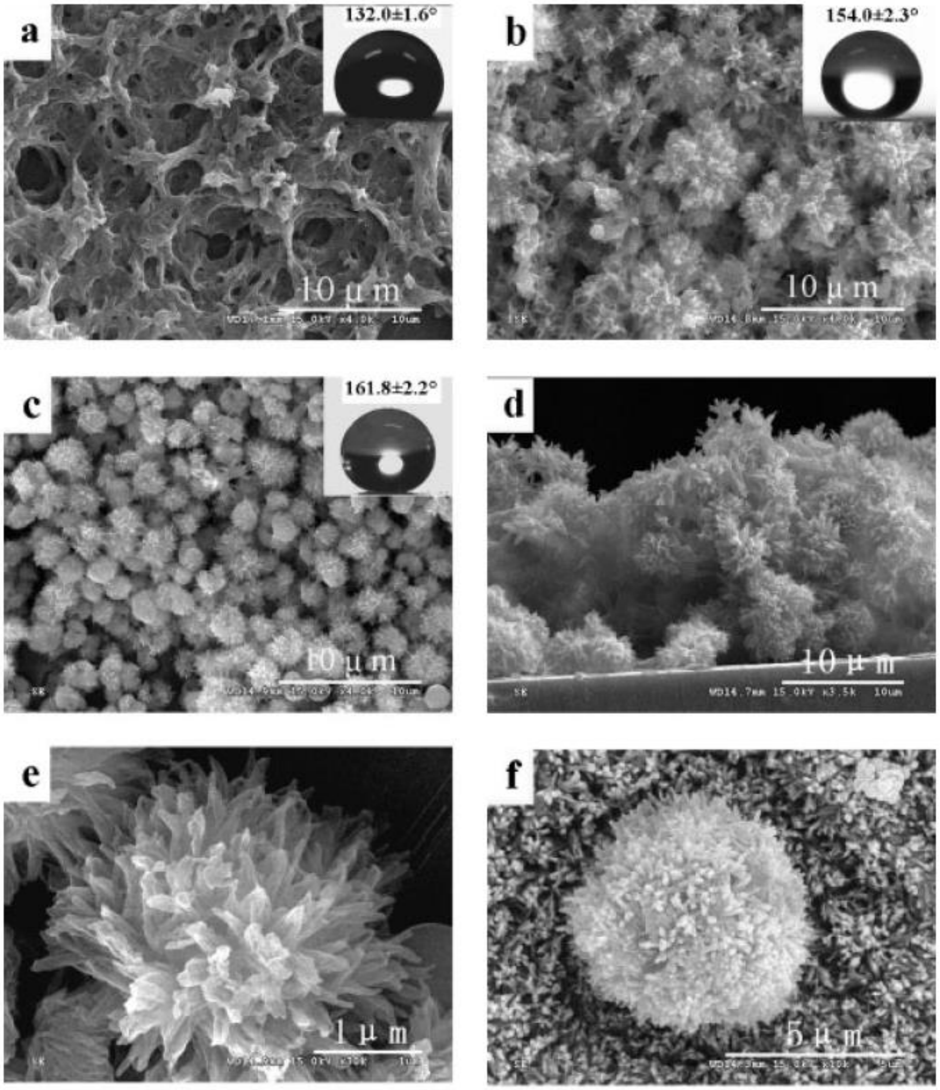

Figure 5. Scanning electron microscope (SEM) images of biomimetic hydrophobic coatings, a-c) increased hierarchical roughness displays higher water contact angles, d-e) close up images of fabricated coating, and f) a single papilla on a natural lotus leaf.

Deposition of Coating

To date, many methods have been explored for the deposition of thin coatings with special wettability including chemical vapour deposition (74) (75) (76) (77), sol-gel technique (78) (79) (80) (81) (82) (83) (84) (85), plasma etching (86) (87) (88) (89), the utilization of templates (50) (58) (59) (90) (91), spray pyrolysis technique (92) (93) (94), layer-by-layer deposition (95) (96) (97), and lithography (98) (99) (100) (101). When choosing a process for the deposition of hydrophobic coatings for industrial use, one should consider the monetary cost, the simplicity, and the ability of a process to be expanded for large-scale manufacturing. Some simple and inexpensive methods would include the sol-gel technique, spray pyrolysis, and layer-by-layer deposition. Patil (94) has demonstrated that spray pyrolysis technique has several advantages over other methods. These include simplicity, safety, low cost of apparatus and raw materials, as well as large-scale deposition. Additionally, the layer-by-layer technique is capable of depositing the desired coating compositions on many different surfaces, including flat and rough surfaces of large areas, and has been shown to be simple, inexpensive, and versatile (95).

Coating Design

Icephobicity

The design of an effective ice resistant coating for use in the solar industry would require the optimization of multiple factors as well as its ice resistance properties. The overall factors that need to be considered are the ice resistant properties, transparency, self-cleaning capabilities, antireflective effects, and the durability of the coating. A fully optimized superhydrophobic coating would show great promise for maintaining the efficiency of solar cells by preventing the accumulation of ice, snow, dirt, and dust.

Ice Nucleation

In order to properly discuss the ice resistant properties of hydrophobic coatings, it is necessary to understand the nucleation of ice on a solid surface and its adhesion to that surface. A small amount of liquid that has been cooled below its equilibrium temperature will not freeze immediately, but will be in a metastable supercooled state for some amount of time. Because it is energetically favourable for a supercooled liquid to crystallize, only a limited degree of supercooling can be achieved before spontaneous crystallization of the liquid into ice will occur. During the freezing process, a very small volume of liquid must crystallize and grow until all the liquid is frozen because freezing is a continuous process (102). However, due to the crystal embryo's very large surface-to-volume ratio, it is in an energetically unfavourable state. There is a free energy barrier to be overcome by the crystal embryo before freezing can occur due to the positive free energy associated with its interface and the liquid. This barrier must be overcome by a nucleation process. If a small crystal embryo grows on an insoluble foreign surface or particle to increase its stability, the nucleation process is termed heterogeneous. Homogeneous nucleation would take place within the pure liquid itself if there are no foreign surfaces or particles for the crystal embryo to grow upon. In heterogeneous nucleation, the growth of an ice-like cluster that is bounded on one side by a foreign surface will be promoted because it will have a lower free energy than a cluster that is independent. When the crystal embryo has crystallized, the growth of the crystal can occur (102). It is the same process of supercooled water droplets within the atmosphere making contact with a surface and nucleating as ice crystals that accounts for atmospheric icing events (103). Ice deposited on a surface can exist in different variations; when there is no liquid layer and no run-off when the ice is being deposited, the icing process is called 'dry growth' and the resulting ice is referred27 to as 'rime'. However, it is called 'wet growth' if there is a liquid layer on the surface of the accumulated ice and freezing is taking place beneath this layer, resulting in ice referred to as 'glaze' (104).

Ice Adhesion

Preventing ice from forming on surfaces at sub-zero temperatures may be accomplished by producing coating materials that are icephobic in nature. Therefore, understanding of the ice-solid interface should be considered an important aspect in achieving icephobic surfaces. The mechanisms involved in ice adhesion are often complex and involve the nature of the substrate, the ice, and the mode of fracture. The adhesion of ice will differ from one type of substrate to another, such as a polymeric material to a metal. If water has been frozen to a metallic surface, the interface created is stronger than the shear strength within the ice which will result in fractures occurring within the ice itself. However, when water is frozen onto a polymeric surface, the interface created is weaker than the shear strength within the ice and failure can now occur at the interface (105). A superhydrophobic coating can both decrease and prevent ice accumulation, and reduce the adhesion of any ice that forms on its surface. Superhydrophobic coatings can prevent and decrease ice accumulation by delaying freezing time (106) (107) (108) (109) and by shedding the water on its surface before it can freeze (108) (109) (110). There are two explanations for the ability of a superhydrophobic coating to delay the onset of freezing. Tourkine et al. (108) proposed that it was due to the layer of air in the voids of the rough superhydrophobic coating that creates a thermal barrier which insulates the liquid from the surface, thus delaying freezing. Additionally, Alizadeh et al. (107) suggested that the delayed freezing, or reduction of macroscopic nucleation rate, is caused by both a reduction of the water-substrate interfacial area and an increase in nucleation activation energy which are characteristic of high contact angles. However, this relationship does not hold true at lower supercooling temperatures. Wang et al. (111) demonstrated that a superhydrophobic coating can not only be effective in delaying the start of icing, but also in increasing the whole icing process time compared with the plain surface under the same experimental conditions. In addition, the morphology and composition of the iced solid surface plays an important role. For a superhydrophobic coating, as the contact area of water is negligible, such a surface would reduce the contact area of ice on the surface and should significantly reduce the adhesion of ice (78).

In ice adhesion research, a common theme has been to compare the contact angle, or wettability, of a surface with the adhesion of ice to that surface. This is often plotted as ice adhesion strength as a function of the water contact angle, however, researchers have seen that data presented in this way does not always follow expected trends. In some cases, researchers have reported that the ice adhesion decreases with an increasing water contact angle, and others have found insufficient relation between the two parameters (112). It was later shown that the ice adhesion strength on a rough hydrophobic surface is not correlated with the water contact angle but is correlated with the contact angle hysteresis, or dynamic hydrophobicity. It was also shown that despite the rough surface of a superhydrophobic coating, it will reduce the adhesion of ice more than a smooth hydrophobic surface of the same chemical composition, and superhydrophobic coatings exhibiting a contact angle hysteresis lower than 5° lead to very high icephobic properties (113) (20) (21). The continuing research in the ice resistance of superhydrophobic coatings further revealed that only the receding contact angle was important in matters of ice adhesion (114). Meuler et al. (112), after testing 22 surfaces of varying wettability, concluded that ice adhesion is related to the receding contact angle of the surface and by minimizing the receding contact angle the ice adhesion would also be reduced. Nosonovsky and Hejazi (114) further showed that a composite, or Cassie-Baxter, wetting state introduces voids between the solid surface and the ice which serve as stress concentrators, or microcracks, thereby decreasing the adhesion of ice. They showed that is was the size of the microcracks at the interface that is the critical parameter that will govern the adhesion of ice to a superhydrophobic surface even though high receding angles are well correlated with reduced ice adhesion. This can help to explain why some superhydrophobic surfaces can result in strong ice adhesion if they do not provide sufficiently large voids at the interface. The stability of a superhydrophobic coating in the Cassie-Baxter wetting state is also an important factor that needs to be considered. In a humid atmosphere, when water condenses in the rough structure of the coating, the contact angle of water will decrease as the droplet switches from a Cassie-Baxter state to a Wenzel state. If a droplet freezes in this condition, it may lead to very large values of ice adhesion called the anchor effect (24). Ice exhibits a very strong adhesion to materials which is largely due to the polar ice molecules strongly interacting with the solid surface. There are three physical mechanisms involved in the adhesion of ice to a surface, specifically, hydrogen bonding, van der Waals forces, and direct electrostatic interactions. Of these three, the direct electrostatic interactions have been found to be the dominant factor (115) (116). Charges on ice induce equal and opposite charges on metals, whereas on dielectrics, the induced charge is smaller and is related to the dielectric constant by the following equation:

$$q' = q\frac{\varepsilon - 1}{\varepsilon + 1} \tag{6}$$

Where q' is the image charge induced by a charge q on the ice surface and ε is the dielectric constant of the insulating material on which ice is deposited (115). Therefore, the interacting force between ice and a metal is greater than that between ice and a dielectric material. Based on the previous equation, materials with a very low dielectric constant would significantly reduce the adhesion of ice by reducing the electrostatic interaction (117) (78) (116).

Another physical factor that may affect the adhesion of ice to a superhydrophobic coating is particle size. Cao et al. (23) developed superhydrophobic coatings on aluminum substrates (figure 6) and determined that the critical particle sizes that determine the superhydrophobicity of the coating and the ice resistant property respectively are in two different length scales. The hierarchical coatings were made with particles up to 10 micrometers in diameter for the micro-roughness regime which rendered them all superhydrophobic. The anti-icing properties of these coatings, however, are distinctly different. No ice formed on the samples when particles of 20 and 50 nanometers were used for the nano-scale roughness regime, but the probability of icing increases remarkably when the particle diameter is larger than 50 nm. They show that it is uncertain whether a superhydrophobic surface can be ice resistant without having a detailed knowledge of the surface morphology and caution should be taken when the ice resistant properties are correlated to the superhydrophobicity.

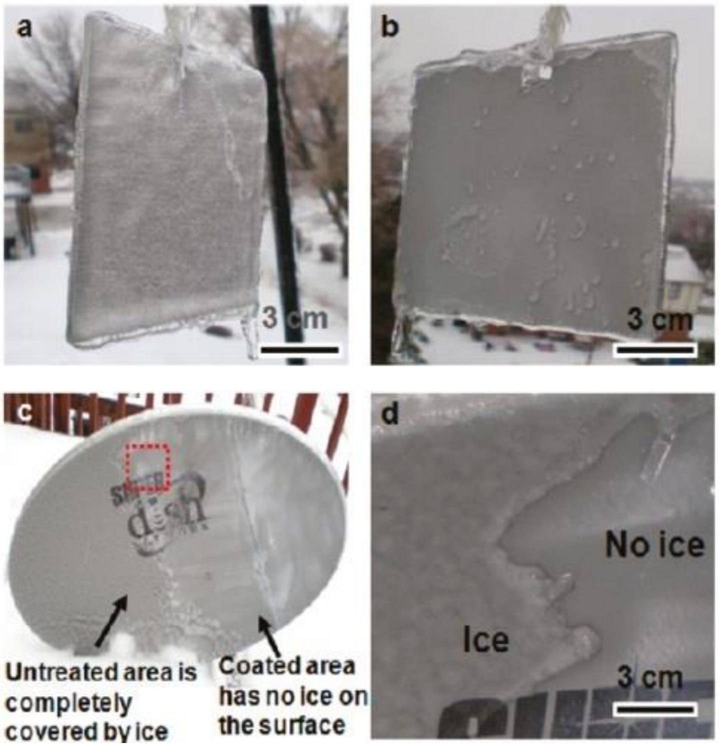

Figure 6. Test of anti-icing properties in naturally occurring "freezing rain". (a) Untreated side of an aluminum plate after the natural occurrence of "freezing rain". (b) Treated side of the aluminum plate coated with a superhydrophobic composite after the "freezing rain". (c) Satellite dish antenna after the freezing rain. The left side is untreated and is completely covered by ice, while the right side is coated with the superhydrophobic composite and has no ice. (d) Close-up view of the area labeled by a red square in (c), showing the boundary between the coated (no ice) and uncoated area (ice) on the satellite dish antenna.

Moisture Condensation

Dew condensation is commonly observed in nature. When the air temperature drops below the dew point, water vapor in the air becomes liquid and condensation occurs. At the dew point, there is a change of the interfacial free energy of the solid-gas interface by water adsorption and the contact angle decreases which suggests an unstable composite state, or mode transition from Cassie-Baxter to Wenzel (118). As the temperature of some superhydrophobic surfaces is lowered past the dew point, they display sudden and undesirable decreases in the receding water contact angles. The observed decrease in water contact angle indicates a transition from the Cassie-Baxter state to the Wenzel state, likely due to the capillary condensation of liquid water in the crevices of the textured surface. For a surface to be effectively icephobic it must be able to resist transitions to the fully wetted state which may be caused by the condensation of moisture from the ambient atmosphere or by the kinetic energy of falling rain droplets (119). In contrast, however, Wang et al. (120) developed a superhydrophobic coating that maintains contact angles above 150° in temperature ranges from -10 to 17.5°C.

It is not always the case that water vapor forms a liquid condensate once undergoing a phase transition on a supercooled surface. Frosting, which is the process of water desublimation onto a surface and forming small ice crystals, may also happen. Varanasi et al. (121) demonstrated that frost formation could significantly compromise the icephobic properties of superhydrophobic surfaces. They used an environmental scanning electron microscope to take snapshot images of the nucleation and growth of frost on the superhydrophobic surfaces. It was shown that indiscriminate frost formation cannot be avoided on surfaces comprised of spatially uniform intrinsic surface energy (figure 7) once the necessary supersaturation conditions are achieved. The formation of frost can result in the loss of the superhydrophobic state and complete saturation of the surface morphology by frost which will lead to an increased ice-substrate contact area, and thus to increased ice adhesion and the loss of icephobicity. It was concluded that superhydrophobic textures will increase the adhesion of ice whenever frost can form indiscriminately on the surface. These findings are important to the consideration of superhydrophobic protective coatings for solar applications in climates that experience freezing temperatures at night which result in frosting. Controlling the condensate nucleation spatially offers one possible route for overcoming the frost-driven transition into the Wenzel state. It may be possible to form weakly-adhered composite ice if the nucleation of ice is constrained to the upper regions of the surface texture and prevent forming the strongly-adhered Wenzel ice (119). Although frost formation will occur when the temperature of a surface is below the freezing point of water and exposed to humid air, just like the freezing of water, frost formation on a superhydrophobic coating can be delayed. Liu et al. (122) demonstrated that a superhydrophobic coating with a CA of 162° was able to delay frost deposition for 55 minutes, compared with the uncoated sample. Additionally, Cai et al. (123) tested frost growth on a normal copper surface as well as one with a hydrophobic coating and found frost appeared on the hydrophobic coating surface later with lower frost height, sparse distribution, and less aggradations of ice crystals than that on the normal copper surfaces.

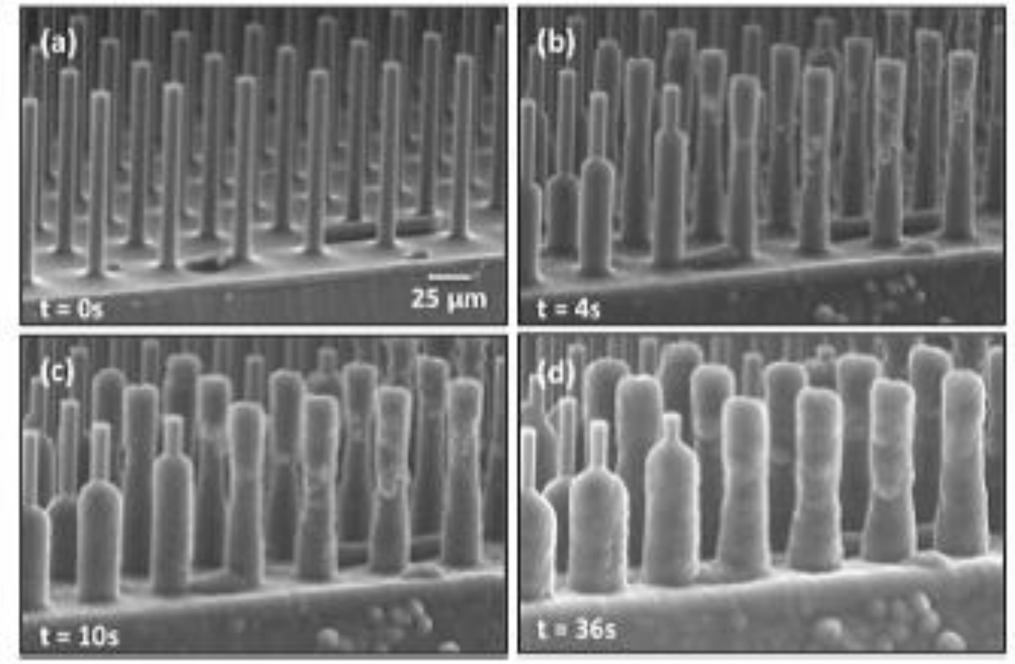

Figure 7. SEM images of frost formation on a superhydrophobic surface.

Snow Adhesion

Another important factor in the design of a superhydrophobic coating for use in freezing climates is the adhesion of snow to its surface. Snow is generally a mixture of ice and water and its adhesion to surfaces is affected by many factors such as the surface's roughness and composition, as well as the atmospheric temperature and wind velocity. The temperature of the ground also alters the adhesion behaviour of snow as the ground temperature affects the water content of snow, below -1 or -2°C the snow is dry but above that, a thin layer of water covers the ice, creating wet ice with properties between that of ice and water. Due to the difference in water content, dry snow exhibits different sliding or adhesion behaviors than wet snow (26). Various investigations have examined the adhesion behaviour of snow on a solid surface. Nakajima demonstrated that a superhydrophobic coating showed an excellent anti-snow adhesion property against both dry and wet snow along with acceleration of sliding of dry snow (26). Other studies have found poor sliding behaviour of wet snow on superhydrophobic surfaces (124).

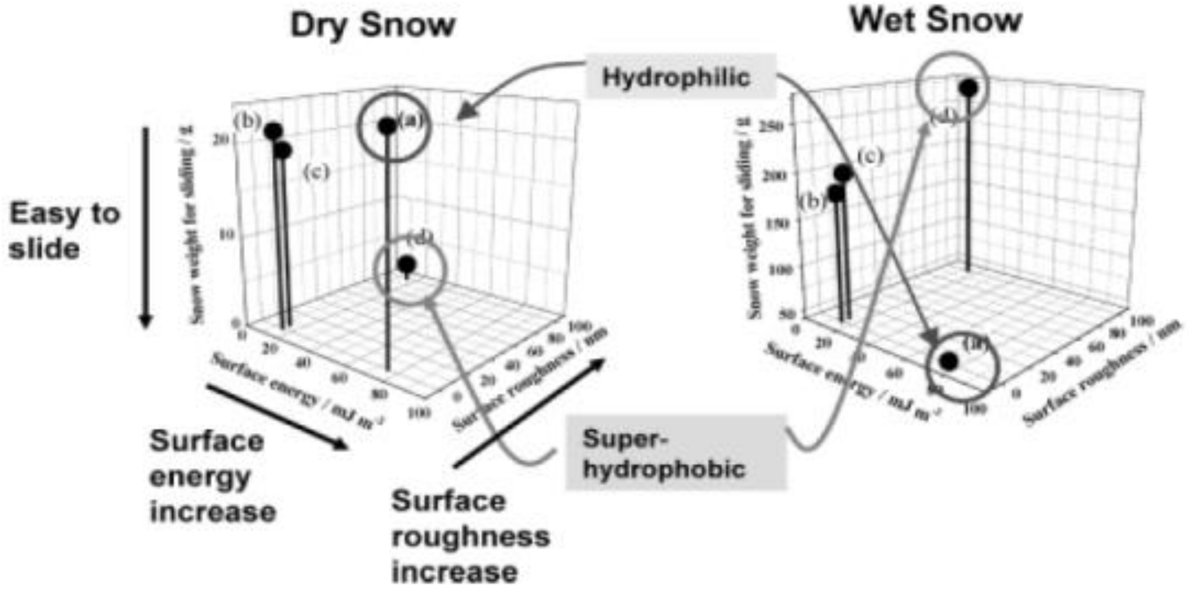

Figure 8. Relationship between hydrophobicity and maximum snow weight for sliding on various hydrophobic surfaces: (a) normal glass surface; (b) glass surface coated with fluoroalkylsilane; (c) glass surface coated with both colloidal silica and fluoroalklsilane; (d) superhydrophobic film surface.

Evidence of Icephobic Characteristics

Although much research is being performed in this field, not everyone agrees. Chen et al. (125) disagree that a superhydrophobic (rough) surface can decrease ice adhesion. In their experiment, the superhydrophobic surfaces displayed ice adhesion values near superhydrophilic surfaces; this was determined to be caused by mechanical interlocking from water penetrating the roughness of the microstructure. The cause of the water penetration was related to the cold temperature. When water rests on a superhydrophobic surface at room temperature, it is in a composite state and the liquid water is in thermodynamic equilibrium with the air trapped in the roughness of the surface beneath the liquid. If the temperature of the surface is lowered, it becomes more hydrophilic as the water molecules adsorb at the walls of the surface textures. Simultaneously, water condensation occurring on the inside the surface texture drives a transition from a composite state to the Wenzel state. When water freezes in the Wenzel state, the ice and the surface texture are mechanically interlocked, resulting in large increases in ice adhesion strength. Despite some disagreements on the icephobicity of a superhydrophobic coating, there have been many studies of superhydrophobic coatings exhibiting drastically reduced ice adhesion (17) (113) (110) (111) (112) (20) (21) (114) (116) (126) (117) (127) (128). Dodiuk et al. (129) developed a superhydrophobic coating that reduced the ice adhesion by 18 times when compared to bare aluminum and Sarkar et al. (78) developed a superhydrophobic coating and froze small cylinders of water to the surface using a mould and tested the adhesion of ice. The untreated aluminum surface showed an ice adhesion strength of 369±89 kPa, whereas the ice debonded spontaneously on its own from the superhydrophobic surface.

Transparency

It has been shown that with proper consideration and understanding of the mechanisms of ice adhesion and the prerequisite surface properties, it is possible to minimize ice-substrate interactions and facilitate the successful development of an ice resistant coating. Equally important consideration should be given to the transparency of the superhydrophobic coating if it is to be utilized for solar applications. The notion of coupling superhydrophobicity and transparency is counterintuitive since the optimization of superhydrophobicity involves maximizing surface roughness, and the increased feature size, either from particles or through induced roughness, results in increased light scattering (130). In general, transmittance of light through the coating decreases with increasing roughness, especially if the roughness exceeds the wavelength of light (47). However, despite the challenges associated with developing a transparent superhydrophobic coating, many have been reported in literature (26) (65) (68) (74) (80) (81) (82) (83) (84) (85) (92) (93) (95) (97) (131) (132) (133) (134) (135) (136) (137) (138) (139). In order to sustain optical transparency in the visible light range (wavelength of 380-760nm), the roughness of the coating surface should either be much lower than this range, or much higher (less than 80nm or more than a few microns) (26). Reports of superhydrophobic coatings with visible light transmittance of over 90% are not unheard of (80) (136) (137) and some have reached transmittances of over 98% for wavelengths longer than 590 nm (97) (138). Thus, it is apparent that with an optimized superhydrophobic coating a solar cell's performance can remain unaffected due to the effects of light scattering (131).

Figure 9. Photograph of water droplets on F-SiO_2 NP-coated glass substrate.

Self-Cleaning

Another beneficial property of a superhydrophobic coating is their self-cleaning capability. A coating that has self-cleaning properties is important in order to prevent efficiency degradation of the solar cells by the accumulation of dirt and dust on the coating surface (140) (141). Both hydrophobic and hydrophilic surfaces exhibit self-cleaning properties through the nature of the interaction of water on the surface The former does this by creating sheets of water that carry dust and dirt as it flows; the latter by rolling droplets (and entrapped dust and dirt) off the surface (140) (141) (142). Not every superhydrophobic surface exhibits self-cleaning properties; there are some important factors that need to be taken into consideration to ensure the desired self-cleaning characteristics. When considering self-cleaning surfaces, the factor of water drop adhesion to the surface is paramount. A common method used to characterize the adhesion of a water droplet to a surface is to use the critical tilting angle, or sliding angle. When a droplet of known weight is placed on a surface and tilted; the point at which the weight of the droplet overcomes the adhesion to the surface and slides off is referred to as the critical tilting angle (68). In the case when a superhydrophobic surface is prepared by coating hydrophobic materials directly onto hydrophilic ones, the coating homogeneity is very important. Any remaining hydrophilic material exposed on the surface will become an anchor site for the water droplets due to their affinity for water. If this is the case, even if the apparent contact angle is sufficiently large, the sliding angle will be increased dramatically. Generally, the effects of coating heterogeneity are less conspicuous on the static contact angle of water than on the sliding behaviour (26).

Antireflection

Many nanostructured surfaces have intrinsic antireflective properties and this has promoted the convergence of antireflective structures with self-cleaning structures which could be used in solar cells and other outdoor optical applications (84) (95) (131) (132) (133) (137) (138) (143) (144) (145) (146) (147) (148) (149) (150). Due to the high refractive index of the material surfaces in conventional solar cells and panels, up to 30% of incident light can be reflected back and dust and moisture accumulation can scatter an additional 10% (151). Some superhydrophobic coatings have antireflective capabilities because the light being reflected from the coating-substrate and coating-air interfaces is subject to descructive interference, resulting in high optical transmission and low reflectivity (132).

Antireflective surfaces can not only improve the transparency of optical devices through improving the light transmittance ratio (84) (135) (137) (138) (152) (figure 10), but can also improve the photovoltaic conversion efficiency of solar cells (153) (154). Two of the most crucial physical parameters in designing an antireflective coating are the thickness of the coating, and its refractive index (153). Suppressing reflection over a broad spectral range can be accomplished by forming a gradual transition of the refractive index by subwavelength antireflective structures and gradual transition in the refractive index is generally regarded as the preffered way to achieve the perfect antireflective effect (47) (155). Furthermore, the hierarchical roughness of a superhydrophobic coating is advantageous over a smooth hydrophobic coating due to the decreased angle dependence of its antireflective property (155). From literature, more sources can be found that show an antireflective coating can increase the efficiency of a solar cell (138) (156) (157). Minemoto et al. (153) were able to increase the average conversion effiency of Si solar cells by 25% (relative) by applying ZnO antireflective coatings and Prevo et al. (158) increased the efficiency by 10% (relative) with the use of their antireflective coating.

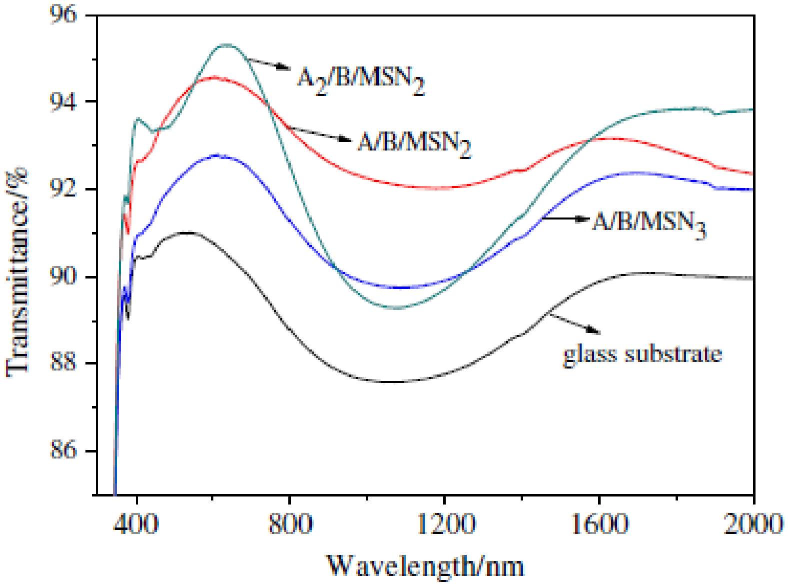

Figure 10. Transmission spectra of glass substrate and glass substrates coated with broadband antireflective superhydrophobic A/B/MSN$_2$, A/B/MSN$_3$ and A$_2$/B/MSN$_2$ coatings in the wavelength range of 400-2000 nm.

Durability

Lastly, the durability of the superhydrophobic coating should be taken into consideration. The durability and mechanical robustness of the coating are particularly important to consider because the fragile hierarchical roughness can be irreversibly destroyed, which will inevitably lead to an increase in the contact angle hysteresis and a rapid decrease in the static contact angle (159).

The outdoor testing of coatings with special properties (superhydrophobicity, self-cleaning, and antireflection) is necessary to evaluate their degradation when they are exposed to the natural environment because long periods of exposure to dirt, light, abrasion, and other factors that are typically experienced outdoors. These natural factors contribute to the degradation in the following ways: the decomposition of the hierarchal roughness structure, the accumulation of strains adhering to the surface, and the gradual removal of the water-repellent agents from the surface (26). Although a rough superhydrophobic coating is sensitive to degradation, many improvements have been made to increase its durability (160) (161) (162) (163) and new self-healing superhydrophobic surfaces are being created (162). Sasaki et al. (164) reported that the formation of an indium-tin oxide (ITO) layer on the surface of the base-film will decrease the surface electric resistance and improve the durability of superhydrophobicity during exposure outdoors. Additionally, Nakajima et al. (165) reported that the addition of only a small fraction of TiO_2 photocatalyst provides an effective self-cleaning property to superhydrophobic coatings and maintains high contact angles during long periods of outdoor exposure. Subsequently, superhydrophobic coatings with desirable mechanical properties have been reported in literature. Menini et al. (117) developed a superhydrophobic coating that was able to reduce the adhesion of ice to aluminum by 4 times and after 14 ice-shedding events using an aggressive centrifugal technique, the icephobicity was unaffected. Deng et al. (131) reported a transparent superhydrophobic coating that was able to undergo adhesion tape peeling tests and sand abrasion, but still retain its superhydrophobic properties. Boinovich et al. (166) developed a durable icephobic coating for stainless steel that after 100 icing/deicing cycles, which were accompanied by mechanical stresses, long-term contact with water and saturated vapour, was still demonstrating multimodal roughness, low surface energy, and stability of the superhydrophobic state. In addition to mechanical properties, there have been other properties reported that are sought after in the design of a superhydrophobic coating for outdoor applications. Wang et al. (167) demonstrated a transparent superhydrophobic nanostructured coating that was able to withstand extended exposure to UV illumination without a significant loss of hydrophobic properties, which favors outdoor self-cleaning applications. Kavale et al. (65) reported a transparent superhydrophobic coating that had undergone a humidity test in which the coating was subjected to a relative humidity of 90% at 30°C for a period of 45 days. After completing the test, the coating exhibited a decrease of only 2° in its water contact angle, from 171±1° to 169°. This slight drop in water contact angle was determined to be caused by a slight adsorption of moisture from the atmosphere; when the samples where dried in an oven, their contact angles returned to their original values. Finally, Hou et al. (48) developed a stable polytetrafluoroethylene superhydrophobic surface which could be immersed in water for long periods of time without affecting the water contact angle, demonstrating the coating's hydrophobic stability.

Coating selection for study

The first factor that needs to be considered is the substrate to be coated, for the considered coatings, each has been successfully used in conjunction with glass which is the primary material under consideration and therefore all conform to the needs of this study. Secondly there is the reported contact angle and sliding angle which are indicators of the coatings ice adhesion reducing potential, the larger the contact angle and the smaller the sliding angle the more likely the coating is to maintain a composite wetting state (Cassie-Baxter) and not allow the penetration of moisture into the roughness and will therefore significantly reduce the adhesion. The third factor is the method that the coating can be applied. For industry use it is imperative that the method be simple, affordable, and scalable to large production capacity. Fourth, and lastly, the coating must be transparent in order to allow the light waves to penetrate which is necessary for the photovoltaic device to produce electricity. Table 2 includes a list of the current potential hydrophobic coatings reported in literature that may be considered for use in this study. The final candidates chosen are presented in the next chapter.

Authors	**Year**	**Composition of Coating**	**WCA**
Alizadeh et al. (107)	2012	2[methoxy(polyethyleneoxy) propyl]trimethoxysilane	44°
Alizadeh et al. (107)	2012	tridecafluoro-1,1,2,2-tetrahydrooctyl trichlorosilane	109°
Alizadeh et al. (107)	2012	tridecafluoro-1,1,2,2-tetrahydrooctyl trichlorosilane	145°
Alizadeh et al. (107)	2012	tridecafluoro-1,1,2,2-tetrahydrooctyl trichlorosilane	149°
Antonini et al. (110)	2011	Poly(methyl methacrylate)	74°
Antonini et al. (110)	2011	10:1 v/v solution of FC-75 and Teflon AF (DuPont)	161°
Bhushan et al. (49)	2008	n-hexatriacontane	169°
Bhushan et al. (49)	2008	n-hexatriacontane	154°
Bhushan et al. (168)	2008	n-hexatriacontane	91°
Bhushan et al. (168)	2008	n-hexatriacontane	158°

Bravo et al. (132)	2007	trichloro(1H,1H,2H,2H-perfluorooctyl)silane	161°
Camargo et al. (169)	2012	PTFE-like	169°
Camargo et al. (169)	2012	Nano-sized silica particles treated with silane	161°
Cao et al. (148)	2006	Fluorooctylmethyldimethoxysilane	161°
Cao et al. (23)	2009	Nanoparticle-polymer composite	158°
Chang et al. (170)	2008	Hexamethyldisilazane	156°
Chen et al. (171)	1999	2,2,3,3,4,4,4-heptafluorobutyl acrylate	174°
Chen et al. (171)	1999	Poly(tetrafluoroethylene)	172°
Chen et al. (171)	1999	Compressed pellets of Poly(tetrafluoroethylene)	177°
Chen et al. (171)	1999	Methylene iodide	140°
Chen et al. (171)	1999	Hexadecane	140°
Dodiuk et al. (68)	2007	fluoro (13) disilanol isobutyl polyhedral oligomeric silsesquioxane compounds	165°
Fang et al. (79)	2009	Tridecafluorooctyltriethoxysilane	168°
Farhadi et al. (127)	2011	Perfluoroalkyl methacrylic copolymer	152°
Farhadi et al. (127)	2011	1H,1H,2H,2H-perfluoro-octyltriethoxysilane	153°
Farhadi et al. (127)	2011	TiO2 doped RTV SR (room temperature vulcanized silicone rubber)	155°

Furuta et al. (118)	2010	1H,1H,2H,2H-perfluorodecyltrimethoxysilane	160°
Furuta et al. (118)	2010	trifluoroproplytrimethoxysilane	146°
Ganbavle et al. (83)	2011	Methyltrimethyloxysilane/tetraethoxysilane/ Methanol/Ammonium Fluoride	105°
Gao et al. (69)	2011	Poly(dimethylsiloxane)	147°
Gaswami et al. (172)	2011	1,1,1,3,3,3-hexamethyl disilazane (HDMS)	168°
Hou et al. (48)	2009	Polytetrafluoroethylene (PTFE)	162°
Hwang et al. (92)	2011	3-[tris[(trimethylsilyl)oxy]-silyl]propyl methacrylate	178°
Jin et al. (173)	2005	Polydimethylsiloxane (PDMS)	162°
Kavale et al. (65)	2011	Methyltrimethyloxysilane	171°
Latthe et al. (82)	2010	Methyltriethoxysilane (MTES)	160°
Latthe et al. (81)	2009	Trimethylethoxysilane (TMES)	151°
Manca et al. (84)	2009	Trimethylsiloxane (TMS) and Methyltriethoxysilane (MTEOS)	168°
Rao et al. (162)	2011	Methyltriethoxysilane (MTES)	155°

Table 2. List of hydrophobic coatings reviewed in literature

Ice delamination with ultrasonic vibration

In contrast, recent studies have been undertaken to test the proficiency of using ultrasonic waves generated by a piezoelectric transducer targeted at the ice/substrate interface with the aims of breaking the adhesive bonds between the two. Early studies, though few, have shown positive results. In experiments performed by Palacios et al. (25), at -20º C, ice was allowed to accrete to 2.5 mm thick on the surface of a steel plate for 5 hours. This steel plate was raised and placed in the vertical direction so that the ice, when delaminated, would fall to the ground due to gravity. When the transducer was excited at radial resonance of 28.5 kHz and voltages in excess of 43V, the accreted ice layer was instantaneously removed.

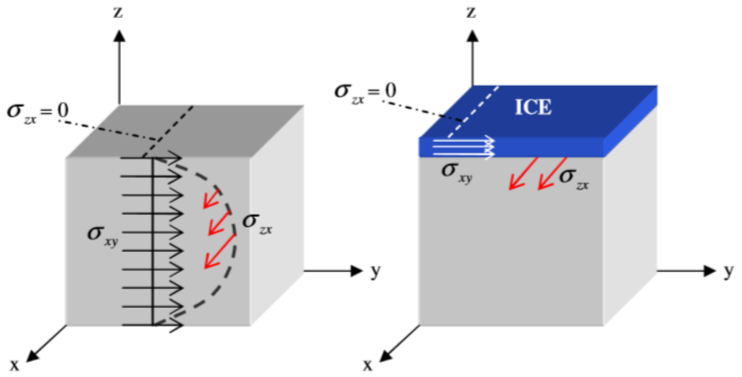

Figure 11. Stresses σ_{zx} is zero at the elements free traction surface, but promotes delamination between a host structure and accreted ice layer. The ice layer will also undergo σ_{xy} stresses through its thickness (stress responsible for ice cracking) (25)

Figure 12. Experimental ice de-bonding and fracture patterns under ultrasonic ZX and XY shear stresses (28.5 kHz, 50V, -20° C) (25)

Thus validating the ultrasonic shear deicing method. To eliminate any concern about the thermal propagation from the ultrasonic transducer being a major contributor on the delamination of the ice layer, thermocouples were placed both on the transducer and the steel plate showed temperatures of -18 º C at the moment of ice delamination. This experimental set-up takes advantage of the low shear adhesion strength of ice and shows that ultrasonic piezoelectric transducers can demonstrate the capability of delaminating thin layers of ice, less than 3mm, instantly. Also, because the ice interface transverse shear stresses will vary with the ice thickness, as the thickness of the ice increases, the ultrasonic vibration will create even larger stresses at the ice/substrate interface as the inertia of the layer of ice also increases, allowing the thicker layers of ice to also be delaminated.

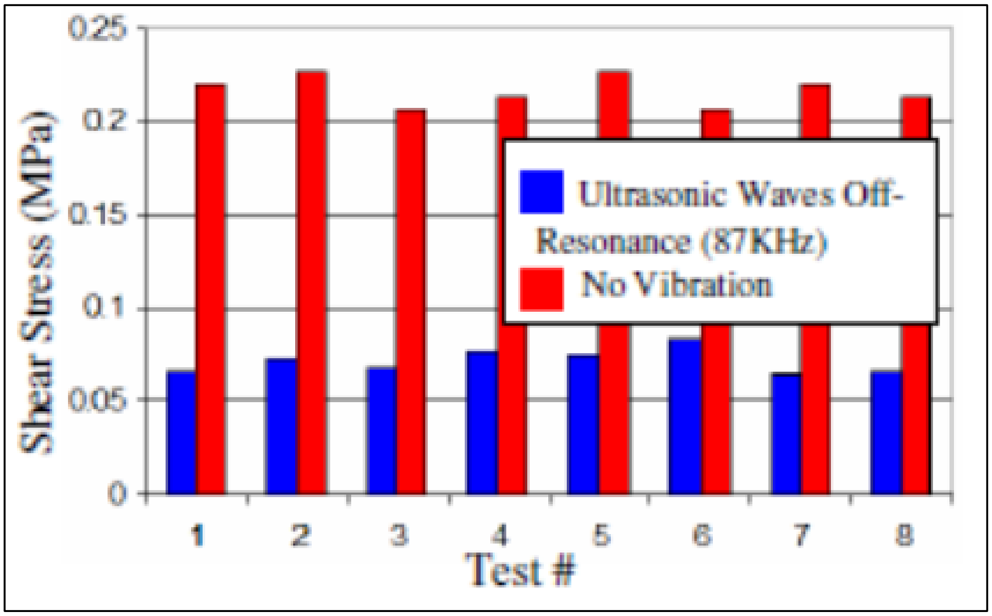

Figure 13. Ice adhesion bonding strength results (174)

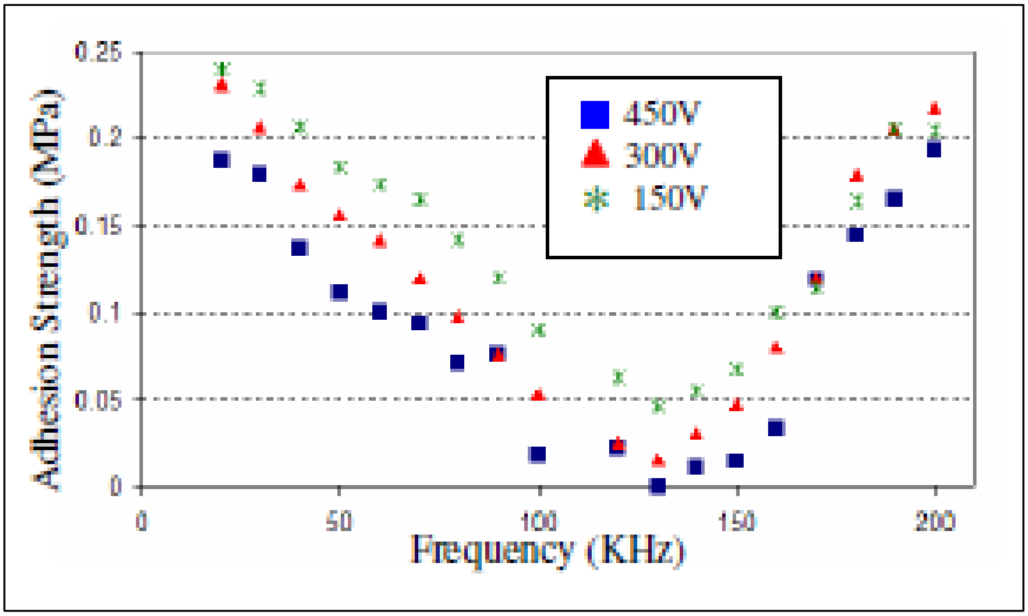

Figure 14. The change in ice adhesion strength with variation in transducer voltage and frequency (174)

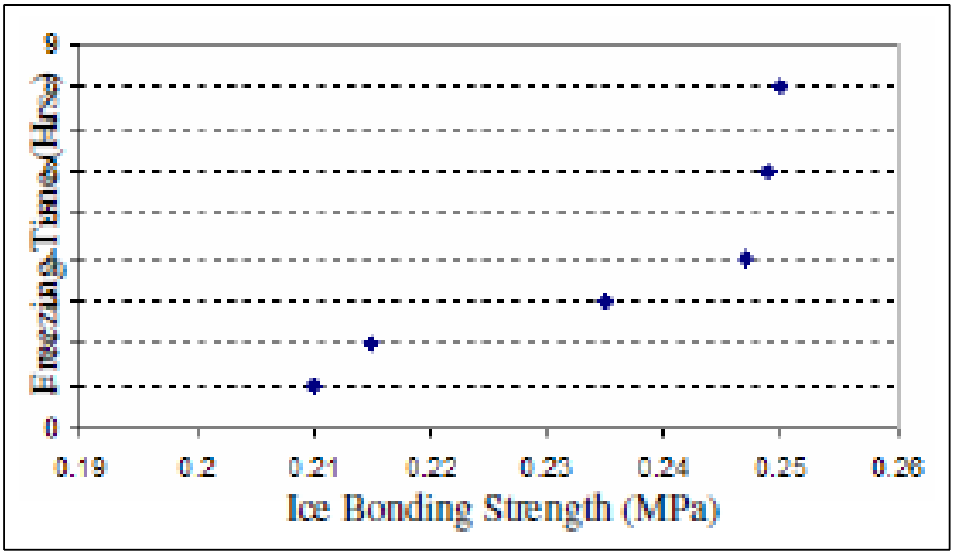

Figure 15. Influence of freezing time on ice adhesion strength (Environment Temp. -20° C) (174)

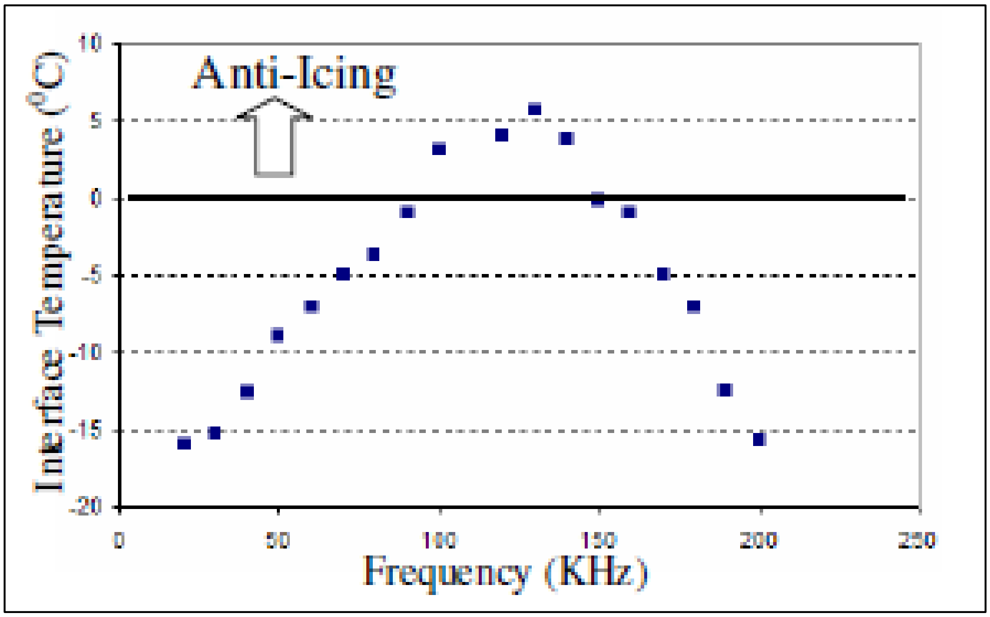

Figure 16. Anti-icing is produced on a 1.5mm aluminum plate by continuous driving of ultrasonic shear waves (300V) at various frequencies (174)

Therefore, these test results demonstrate that a radial resonance disk transducer (28 – 32 KHz) can create ultrasonic transverse shear stresses that are capable of instantaneously delaminating thin ice layers. At environment temperatures of -20º C, the system delaminates 2.5 mm thick ice layers with power input densities as low as 0.07 W/cm 2 (0.5 W/in 2) (25).

Furthermore, Palacios et al. (174) demonstrated that when ultrasonic waves were applied to the plate by the piezoelectric actuators (87 kHz, 450 V amplitude), the bonding strength of ice was reduced by 70%. Additionally, well accreted ice to the aluminum surface was obtained by the researchers and ultrasonic shear waves were propagated on the plate. Shear forces were applied to the thin layer of ice 90 seconds later. They tested the effects of the shear ultrasonic waves on ice adhesion for varying amplitudes and frequencies of vibration (Figure 14). It was found that as the ultrasonic shear vibration approaches the resonance frequency of the shear patches-aluminum system, the adhesion strength of the accreted ice decreases. The ice adhesion bonding strength showed to be dependent on the time allowed for the water to freeze (Figure 15). The effects of the ultrasonic waves were also captured by a microscope (Figures 17 & 18). As the ultrasonic waves were being applied to the aluminum-ice structure (130 kHz, 450V), instantaneous cracks and melting around the cracks was observed at temperatures under negative 15°C. The researchers measured no significant thermal activity in the actuators region using thermal imaging. In conclusion, a well optimized hydrophobic coating that could dramatically reduce the adhesion of ice to most substrates could be combined with an efficiently delivered shock of ultrasonic vibration to create a system capable of remotely removing accreted ice layers repeatedly at very low energy inputs.

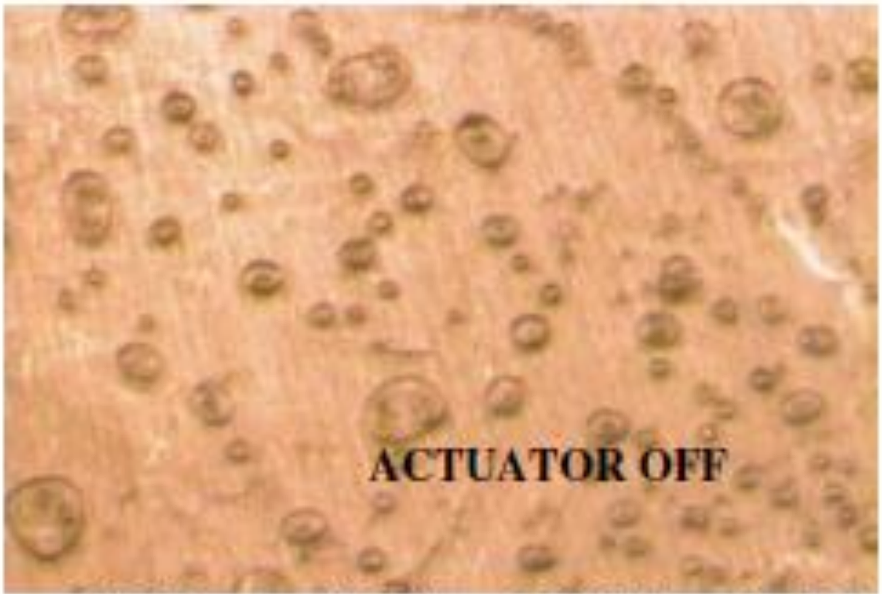

Figure 17. Microscopic view of well attached frozen ice on an aluminum plate (174)

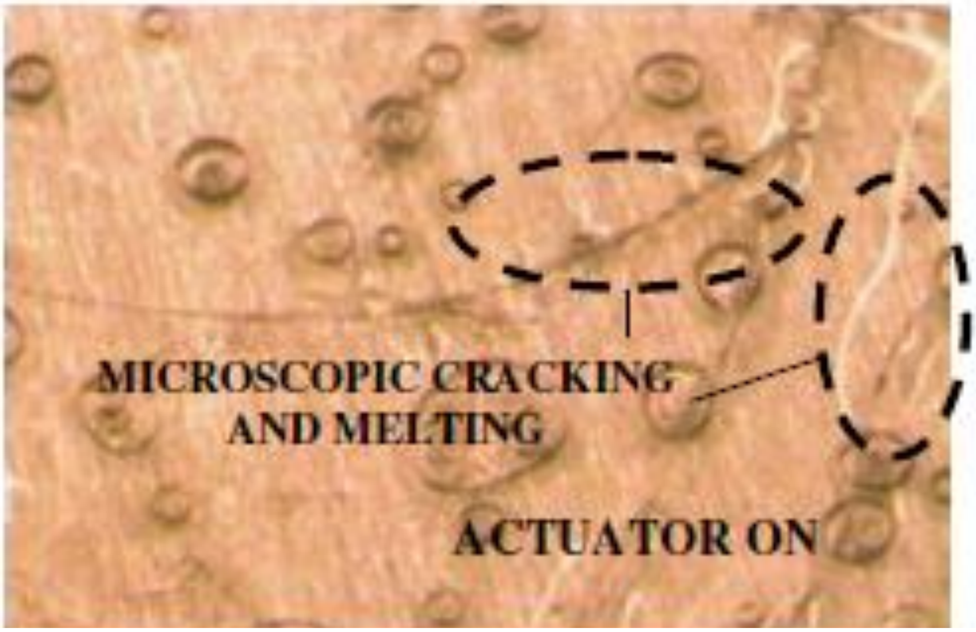

Figure 18. Instantaneous microscopic view of cracking and melting ice on an aluminum plate under ultrasonic shear waves (130 kHz, 450V) (174)

3. Materials and Experimental Procedure

Chapter 3 gives an outline of the materials and experimental procedures used to characterize the wettability, surface, and icing, and coating properties of the materials tested. The design parameters of the goniometer and ice adhesion testing machines and their features are explained in detail. The chapter elaborates on different tests and characterization techniques used in this study.

Materials Used

Glass Sample

A major component of all solar panel arrays are the protective glass panels used to shield the sensitive solar voltaic cells from the outside conditions. Due to the wide use of glass in solar panel arrays and the prevalence of icing conditions in temperate climates, it is important to understand the interaction occurring between ice and glass. To investigate the adhesion properties of ice to glass, small glass pre-cleaned microscope slides (J. Melvin Feed Brand) were purchased and used. The slides dimensions were 25mm x 75mm x 1mm. The glass slides were made of glass with a composition containing, in weight percent, 42% oxygen, 40% silicon, 10% sodium, 5% calcium, and 3% magnesium with trace amounts of aluminum, as shown in figure 19.

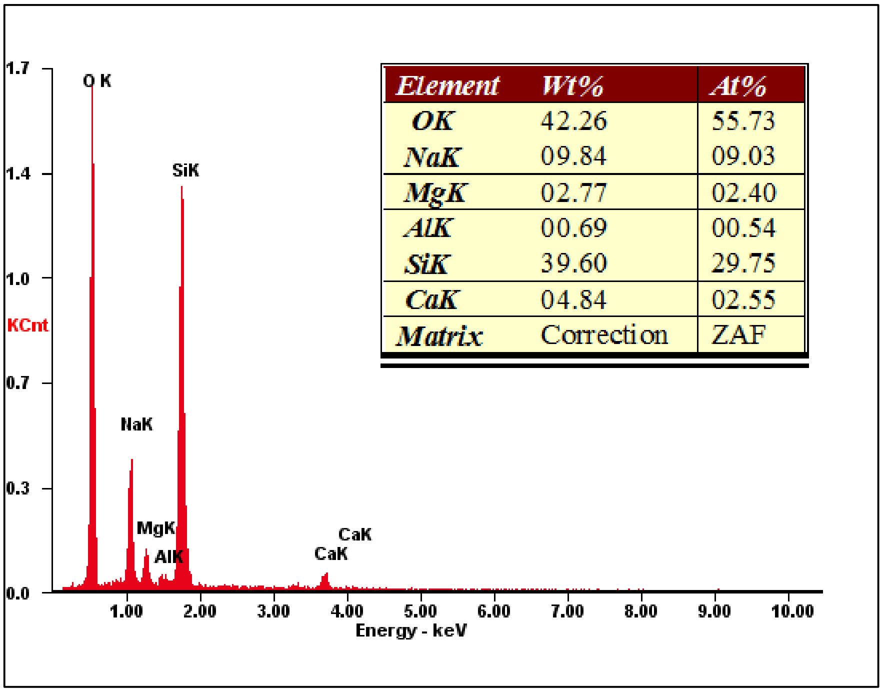

Element	Wt%	At%
OK	42.26	55.73
NaK	09.84	09.03
MgK	02.77	02.40
AlK	00.69	00.54
SiK	39.60	29.75
CaK	04.84	02.55
Matrix	Correction	ZAF

Figure 19. Energy dispersive X-ray spectroscopy (EDS) graph and reading of quartz glass slides

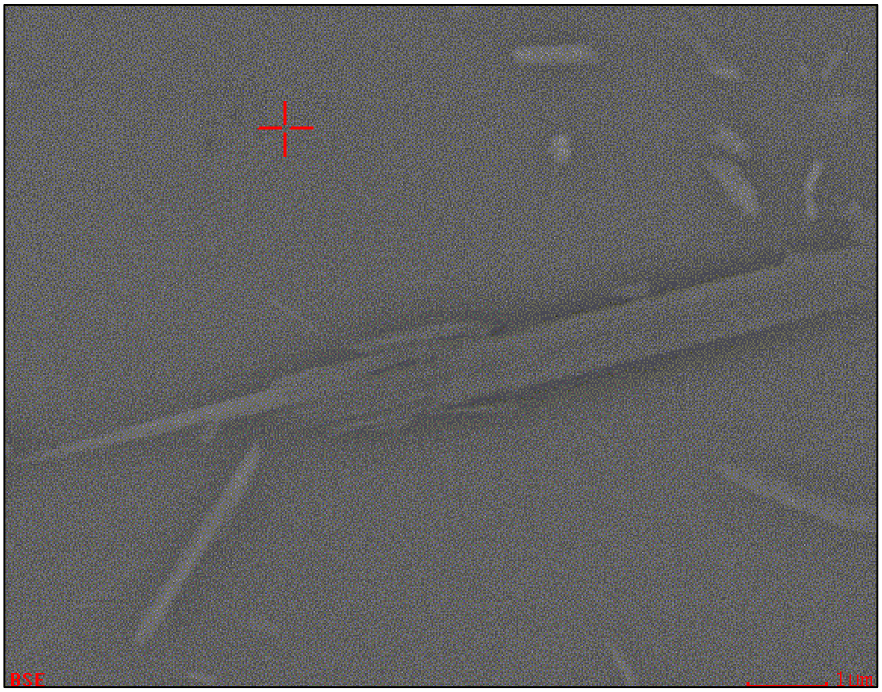

Figure 20. Environmental scanning electron microscopy (ESEM) image of location of EDS scan

Soda-lime glass is the most predominantly used type of glass currently, due to it being relatively inexpensive, chemically stable, reasonably hard, and extremely workable, it is used for windowpanes, glass containers and some commodity items. Because of this, soda-lime glass accounts for 90% of manufactured glass. Soda-lime glass is also ideal for glass recycling, because it is capable of being re-softened and melted multiple times.

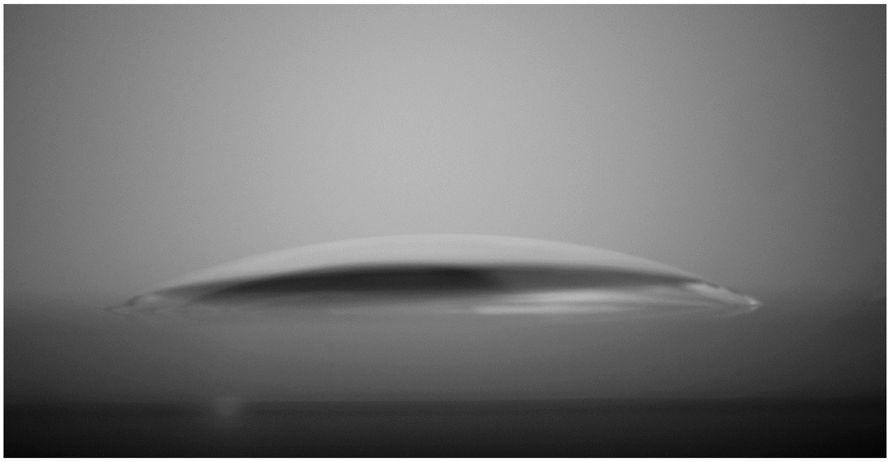

Figure 21. Profile of water droplet on glass for measuring the water contact angle

Trial	WCA (degrees °) (Glass)
1	21
2	22.5
3	23
Average	**22.17**
Std. Dev.	**1.04**

Table 3. Summary of water contact angle measurements on glass

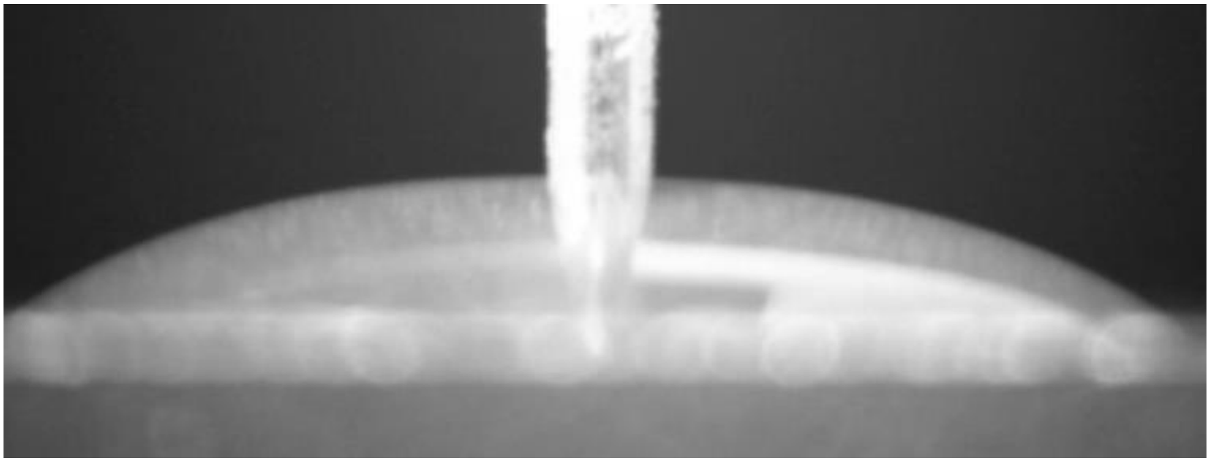

Figure 22. Profile of advancing water droplet on glass for measuring the water contact angle hysteresis

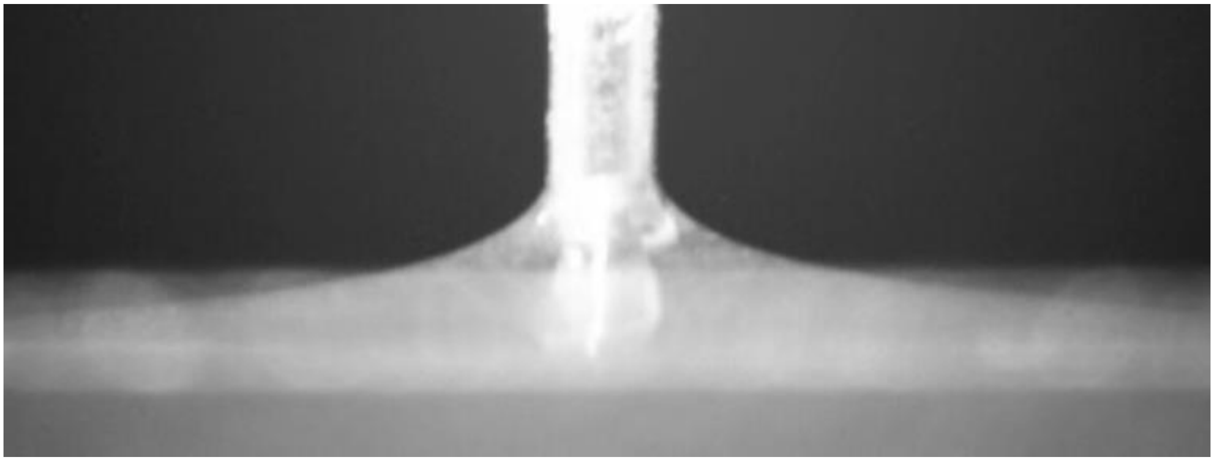

Figure 23. Profile of receding water droplet on glass for measuring the water contact angle hysteresis

Hysteresis (degrees °) (Glass)			
Trial	**Advancing Angle**	**Receding Angle**	**Hysteresis Angle**
1	24	12	12

2	24.5	7	17.5
3	25.5	8.5	17
Average			**15.5**
Std. Dev.			**2.48**

Table 4. Summary of water contact angle hysteresis measurements on glass

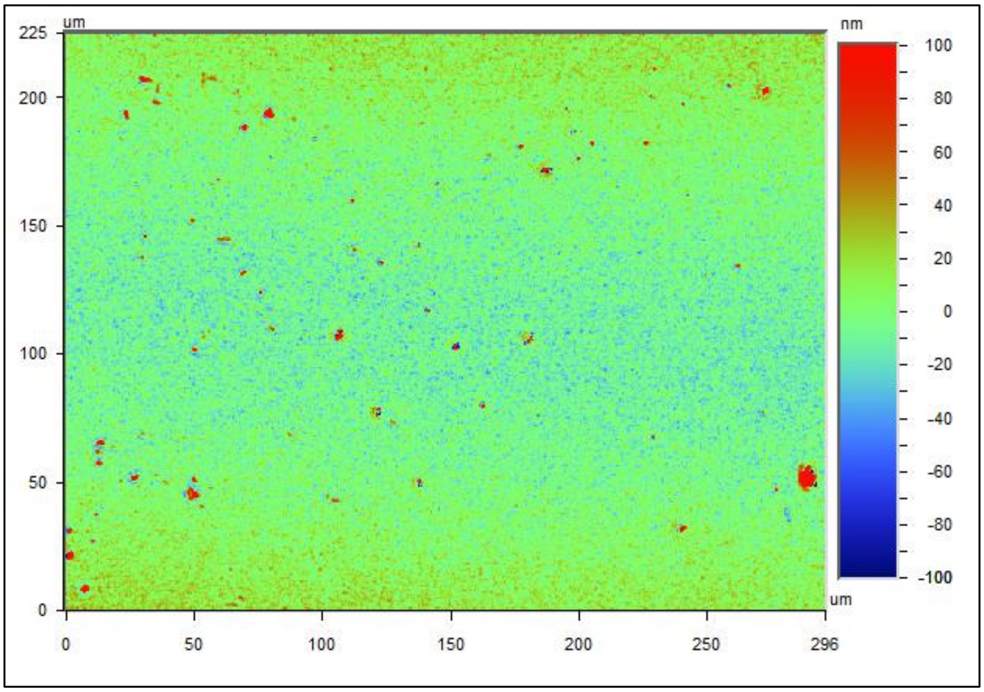

Figure 24. A two-dimensional surface profilometry scan of the surface of the glass sample, shown at 20X magnification

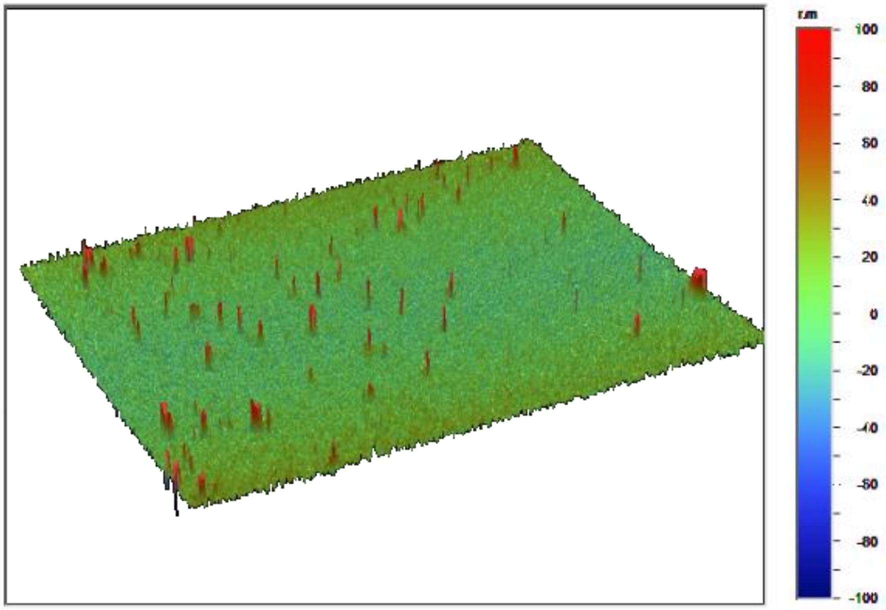

Figure 25. A three-dimensional surface profilometry scan of the surface of the glass sample, shown at 20X magnification

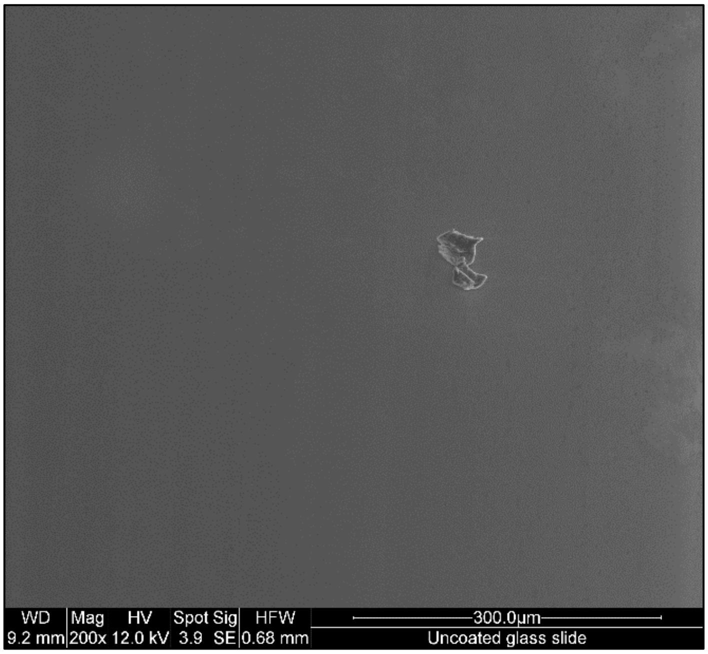

Figure 26. An ESEM image of the surface of the glass sample, a small piece of dust is visible at 200X magnification

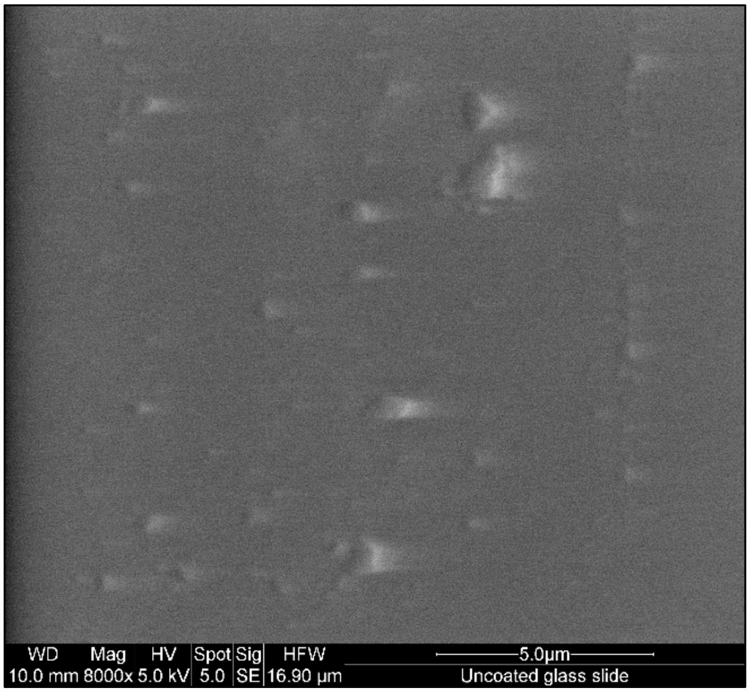

Figure 27. An ESEM image of the surface of the glass sample, at 8000X magnification small cups formations (<1 µm) are only visible features

The soda-lime glass microscope slides used had an average surface roughness of 11.27 nm, a root-mean-square value of 24.51 nm, and the peak-to-valley difference calculated over the entire measured array was 1.90 µm.

Aluminum Samples

Due to the nature of solar panel arrays needing to capture sunlight in order to convert that into electrical energy, they need to be in locations that are sunny. Often times they are raised up and fastened to the roofs of residential houses, commercial buildings, or a specially designed raised support. The installation locations of many solar panel arrays make weight reduction an important factor in the design of any good product, and as such, aluminum is often used in the manufacturing of the protective casing for the photovoltaic cells. Due to the wide use of aluminum in solar panel arrays and the prevalence of icing conditions in temperate climates, it is important to understand the interaction occurring between ice and aluminum. To investigate the adhesion properties of ice to aluminum, small aluminum sample slides were manufactured and used. The slides dimensions were 25mm x 75mm x 1mm and were made of aluminum 6061. Three surface conditions were prepared to simulate and test the effects that surface morphology will have on the adhesion of ice to the aluminum. Of the three samples, one sample is mirror polished using a 1µm diamond suspension, the second is moderately textured using a medium grit with sandblasting, and the third is roughly textured using heavy grit with sandblasting.

Polished Aluminum

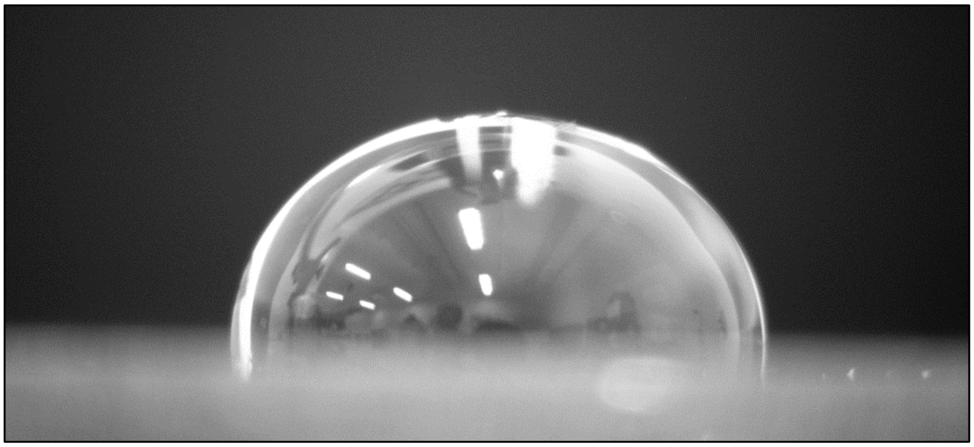

Figure 28. Profile of water droplet on polished aluminum for measuring the water contact angle

Trial	**WCA (degrees °) (Aluminum - Polished)**
1	104
2	104.5
3	102
Average	**103.5**
Std. Dev.	**1.32**

Table 5. Summary of water contact angle measurements on polished aluminum

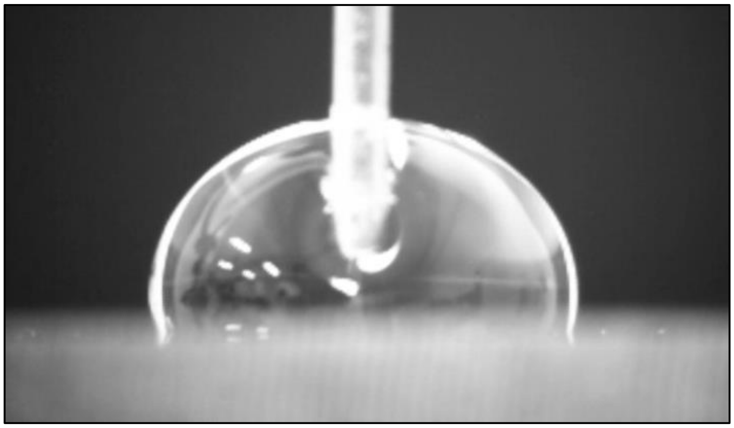

Figure 29. Profile of advancing water droplet on polished aluminum for measuring the water contact angle hysteresis

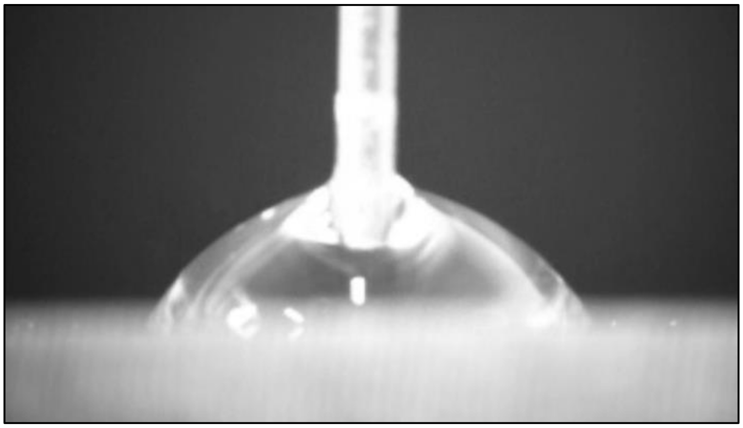

Figure 30. Profile of receding water droplet on polished aluminum for measuring the water contact angle hysteresis

Hysteresis (degrees °) (Aluminum - Polished)			
Trial	**Advancing Angle**	**Receding Angle**	**Hysteresis Angle**
1	107.5	64	43.5
2	111.5	63	48.5
3	105.5	66	39.5
Average			**43.83**
Std. Dev.			**3.68**

Table 6. Summary of water contact angle hysteresis measurements on polished aluminum

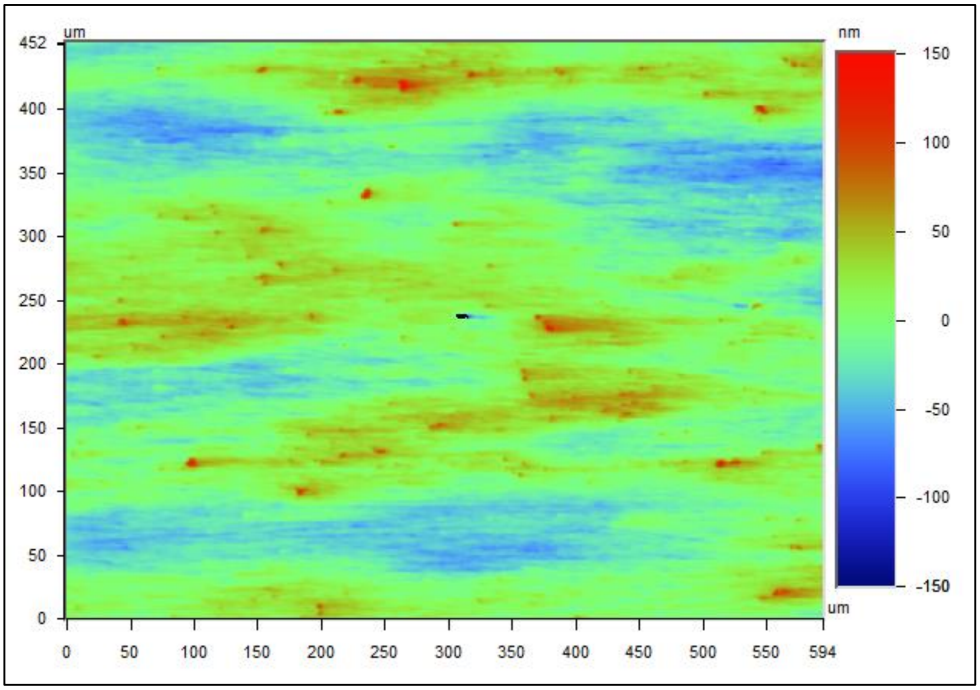

Figure 31. A two-dimensional surface profilometry scan of the surface of the polished aluminum sample, shown at 10X magnification

The polished aluminum samples used had an average surface roughness 22.2 of nm, a root-mean-square value of 27.9 nm, and the peak-to-valley difference calculated over the entire measured array was 243.3 nm.

Moderate Aluminum

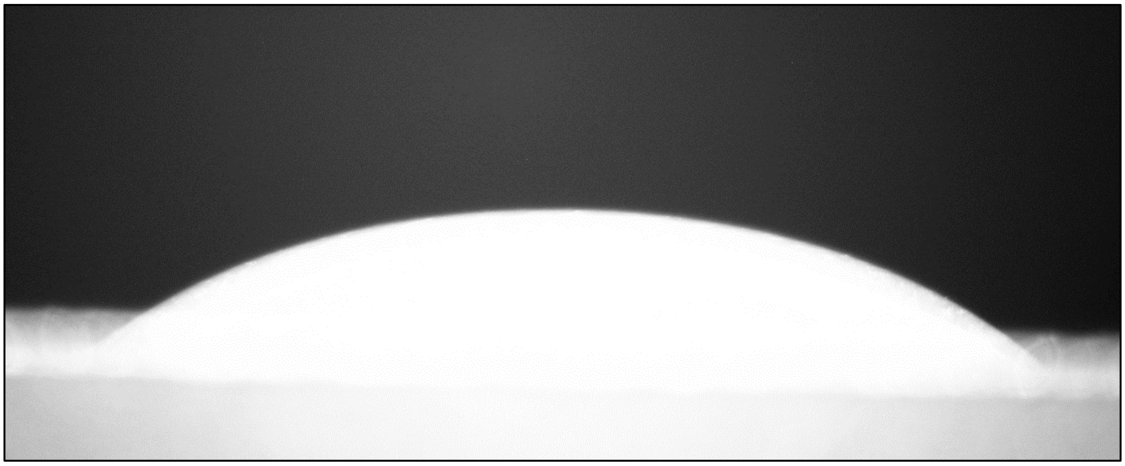

Figure 32. Profile of water droplet on moderate aluminum for measuring the water contact angle

Trial	**WCA (degrees °) (Aluminum - Moderate)**
1	38.5
2	37
3	39
Average	**38.1**
Std. Dev.	**1.04**

Table 7. Summary of water contact angle measurements on moderate aluminum

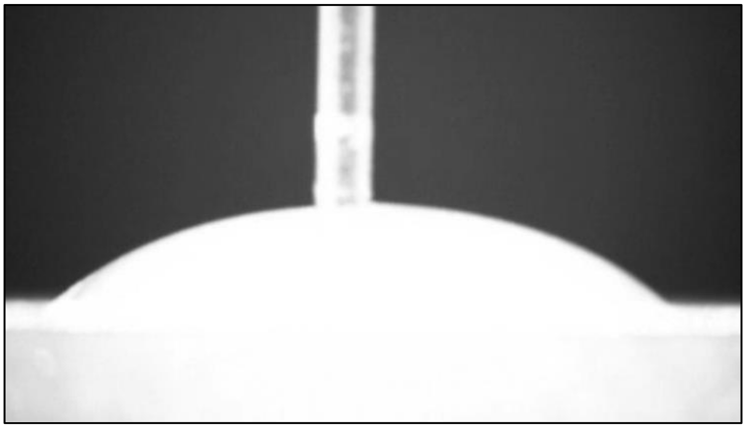

Figure 33. Profile of advancing water droplet on moderate aluminum for measuring the water contact angle hysteresis

Figure 34. Profile of receding water droplet on moderate aluminum for measuring the water contact angle hysteresis

Hysteresis (degrees °) (Aluminum - Moderate)			
Trial	**Advancing Angle**	**Receding Angle**	**Hysteresis Angle**
1	41.5	16	25.5

2	39.5	12	27.5
3	38.5	11.5	27
Average			**26.67**
Std. Dev.			**0.85**

Table 8. Summary of water contact angle hysteresis measurements on moderate aluminum

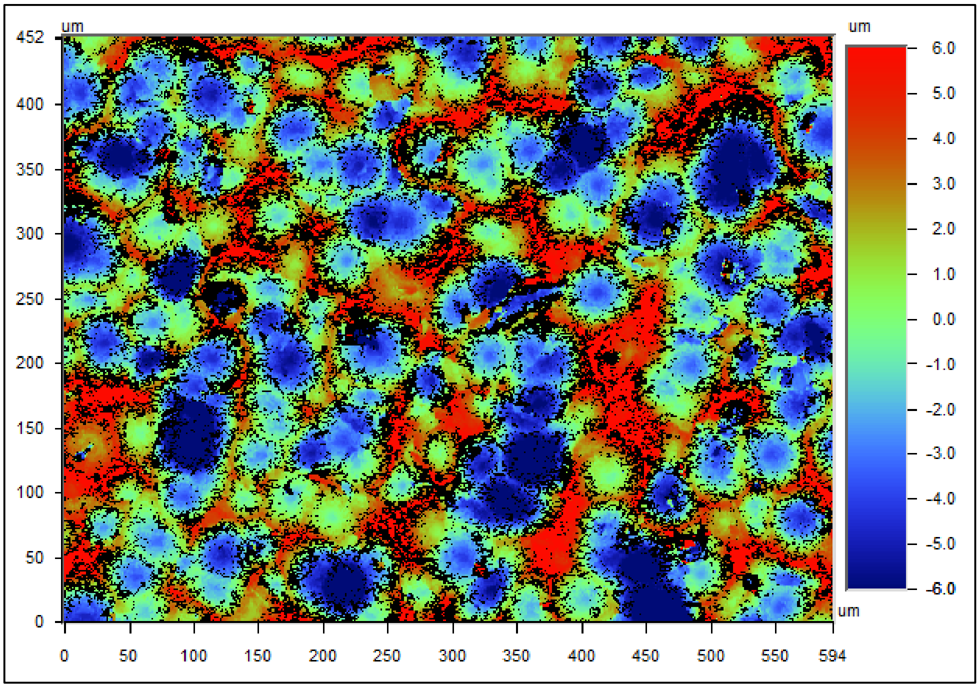

Figure 35. A two-dimensional surface profilometry scan of the surface of the moderate aluminum sample, shown at 10X magnification

The moderate aluminum samples used had an average surface roughness of 3.04 µm, a root-mean-square value of 3.82 µm, and the peak-to-valley difference calculated over the entire measured array was 38.93 µm.

Rough Aluminum

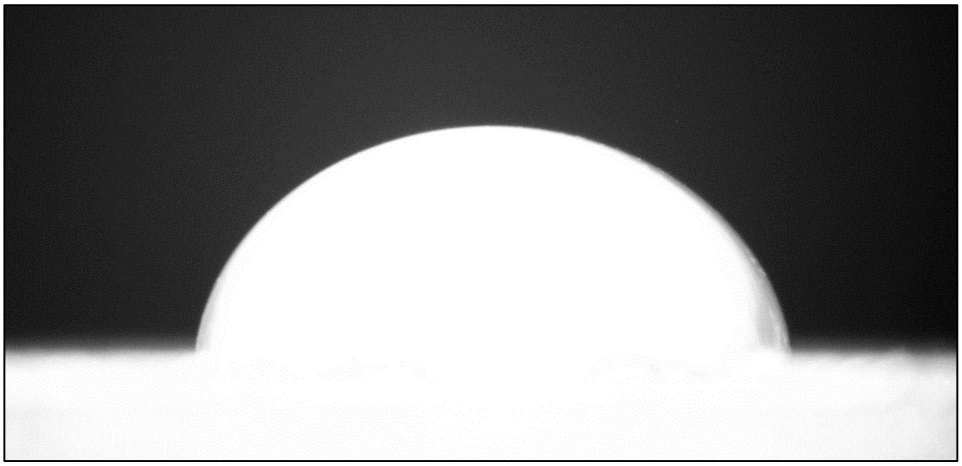

Figure 36. Profile of water droplet on rough aluminum for measuring the water contact angle

Trial	**WCA (degrees °) (Aluminum - Rough)**
1	83
2	90.5
3	87
Average	**86.83**
Std. Dev.	**3.75**

Table 9. Summary of water contact angle measurements on rough aluminum

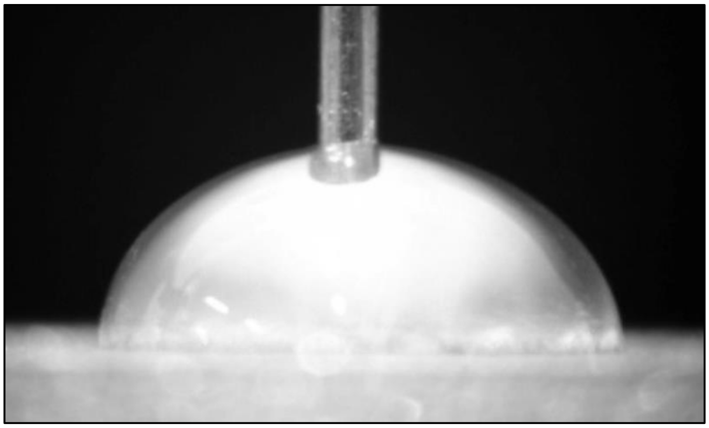

Figure 37. Profile of advancing water droplet on rough aluminum for measuring the water contact angle hysteresis

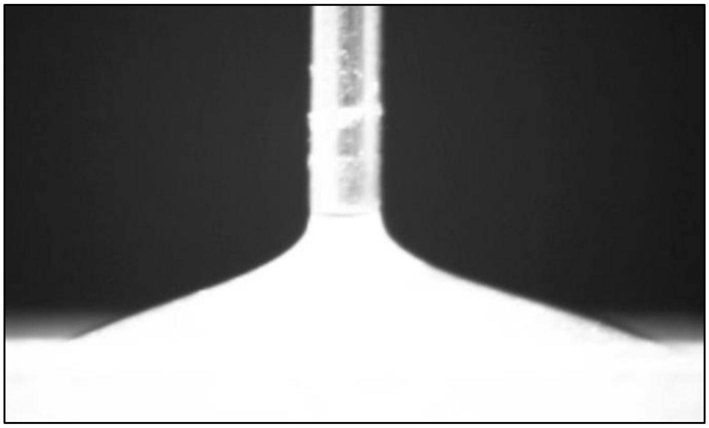

Figure 38. Profile of receding water droplet on rough aluminum for measuring the water contact angle hysteresis

Hysteresis (degrees °) (Aluminum - Rough)			
Trial	**Advancing Angle**	**Receding Angle**	**Hysteresis Angle**
1	84.5	27.5	57

2	70.5	15	55.5
3	73	21.5	51.5
Average			**54.67**
Std. Dev.			**2.32**

Table 10. Summary of water contact angle hysteresis measurements on rough aluminum

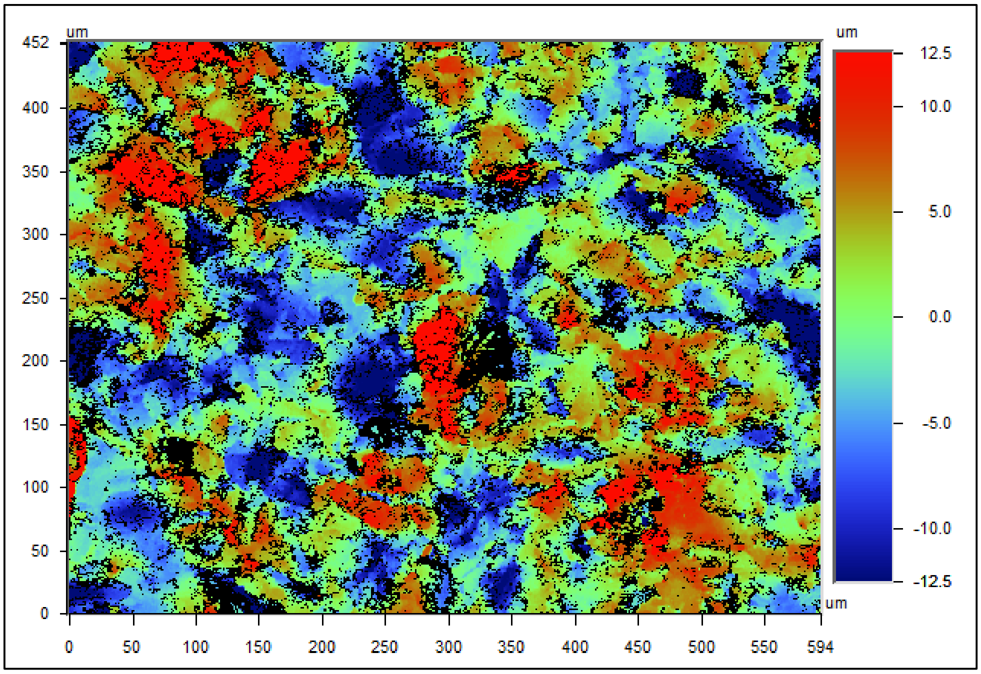

Figure 39. A two-dimensional surface profilometry scan of the surface of the rough aluminum sample, shown at 10X magnification

The rough aluminum samples used had an average surface roughness of 5.06 µm, a root-mean-square value of 6.46 µm, and the peak-to-valley difference calculated over the entire measured array was 60.04 µm.

Stainless Steel Samples

Because of the need for the solar panel arrays to have access to sunlight and need to be raised up off the ground they often need to be built with materials that have superior structural strength and integrity. Combine this structural strength with durability and cost efficiency and it becomes easy to understand why steel is so widely used. Due to the wide use of steel in solar panel arrays and the prevalence of icing conditions in temperate climates, it is important to understand the interaction occurring between ice and steel. To investigate the adhesion properties of ice to steel, small steel sample slides were manufactured and used. The slides dimensions were 25mm x 75mm x 1mm and were made of stainless steel. Three surface conditions were prepared to simulate and test the effects that surface morphology will have on the adhesion of ice to the aluminum. Of the three samples, one sample is mirror polished, the second is moderately textured using a moderate grit with sandblasting, and the third is roughly textured using a rough grit with sandblasting.

Polished Stainless Steel

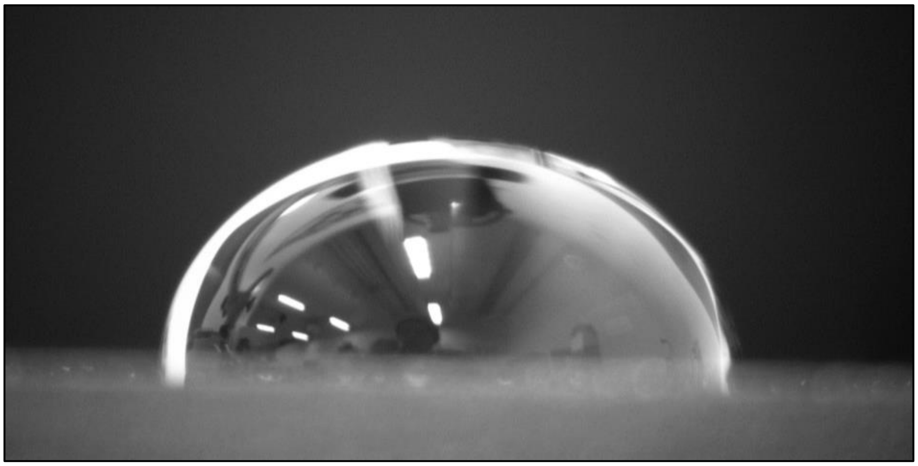

Figure 40. Profile of water droplet on polished stainless steel for measuring the water contact angle

Trial	WCA (degrees °) (Stainless Steel - Polished)
1	98
2	97
3	96.5
Average	**97.17**
Std. Dev.	**0.76**

Table 11. Summary of water contact angle measurements on polished stainless steel

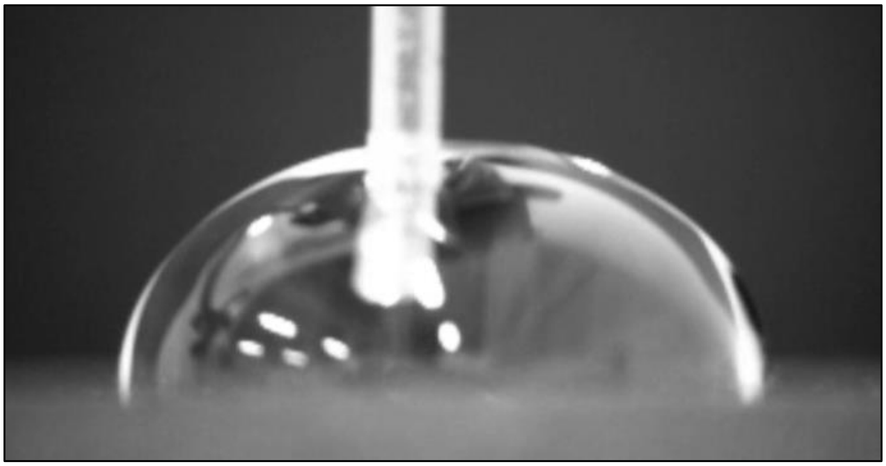

Figure 41. Profile of advancing water droplet on polished stainless steel for measuring the water contact angle hysteresis

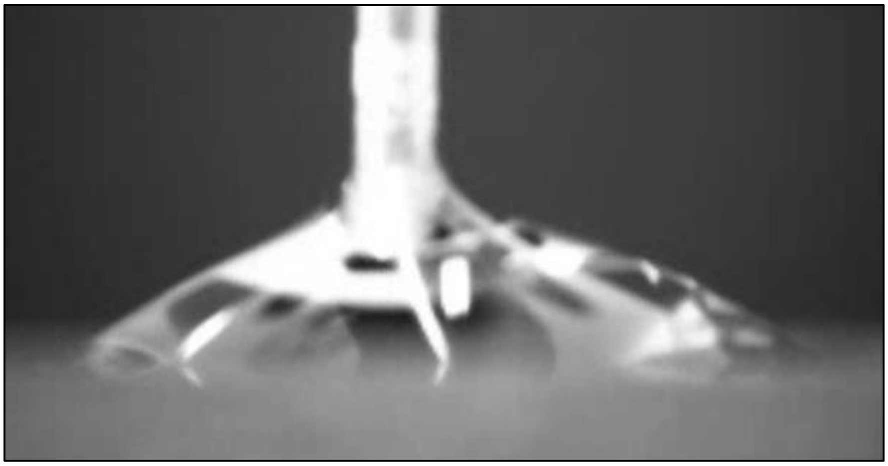

Figure 42. Profile of receding water droplet on polished stainless steel for measuring the water contact angle hysteresis

Hysteresis (degrees °) (Stainless Steel - Polished)			
Trial	**Advancing Angle**	**Receding Angle**	**Hysteresis Angle**
1	95.5	38.5	57
2	101	40	61
3	105.5	49	56.5
Average			**58.17**
Std. Dev.			**2.01**

Table 12. Summary of water contact angle hysteresis measurements on polished stainless steel

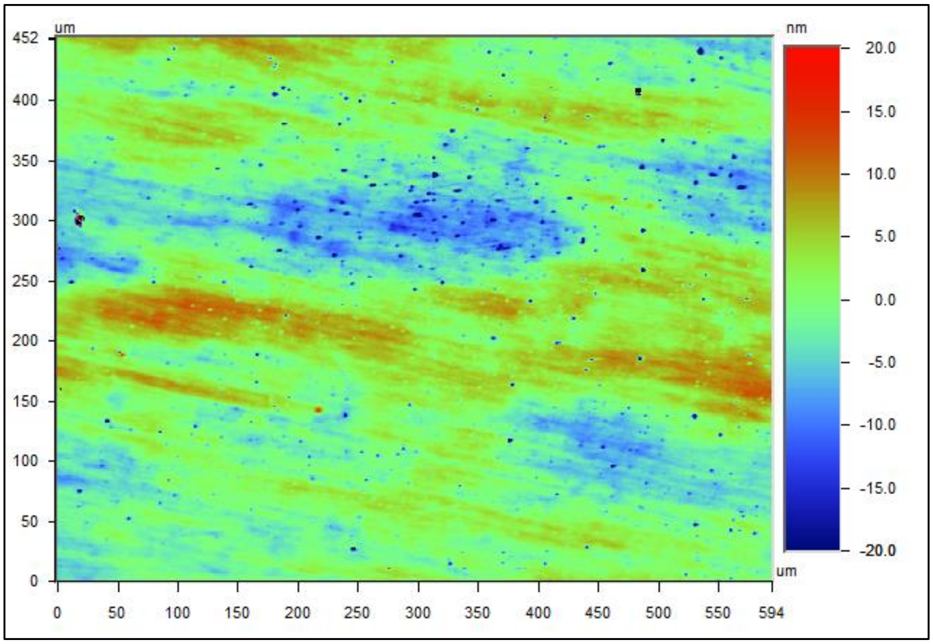

Figure 43. A two-dimensional surface profilometry scan of the surface of the polished stainless steel sample, shown at 10X magnification

The polished stainless steel samples used had an average surface roughness of 2.74 nm, a root-mean-square value of 3.55 nm, and the peak-to-valley difference calculated over the entire measured array was 155.2 nm.

<u>Moderate Stainless Steel</u>

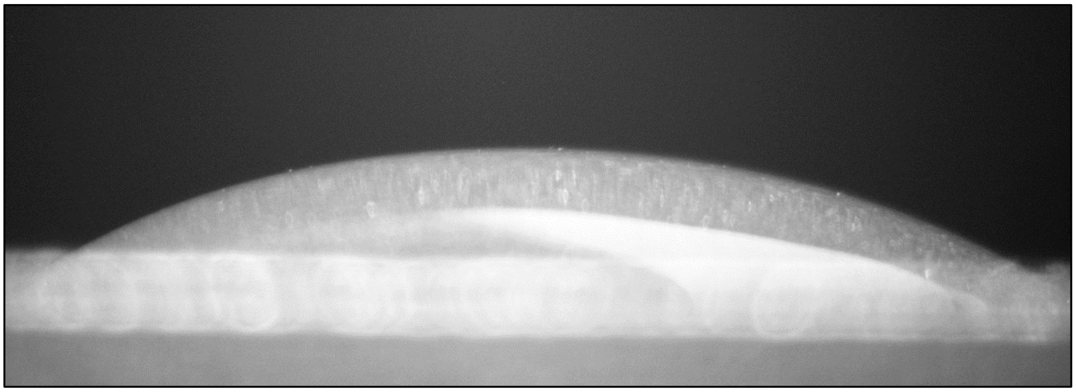

Figure 44. Profile of water droplet on moderate stainless steel for measuring the water contact angle

Trial	**WCA (degrees °) (Stainless Steel - Moderate)**
1	38
2	27
3	27
Average	**30.67**
Std. Dev.	**6.35**

Table 13. Summary of water contact angle measurements on moderate stainless steel

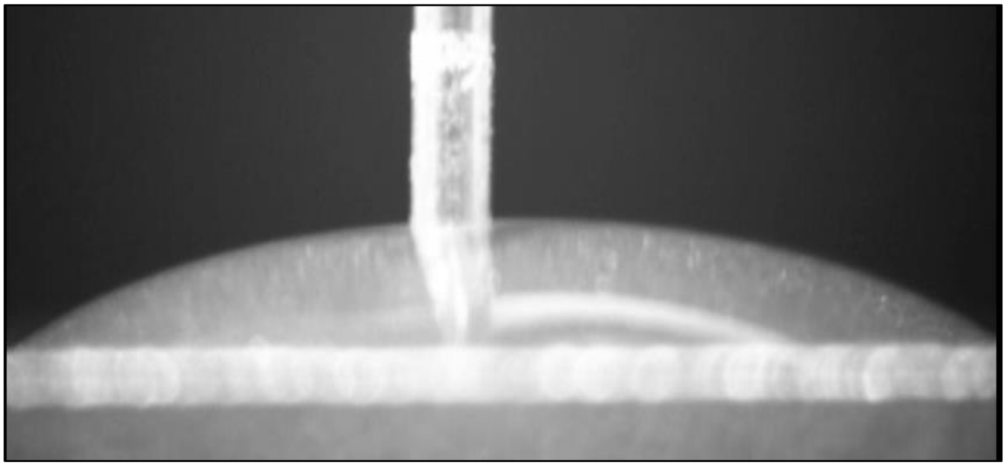

Figure 45. Profile of advancing water droplet on moderate stainless steel for measuring the water contact angle hysteresis

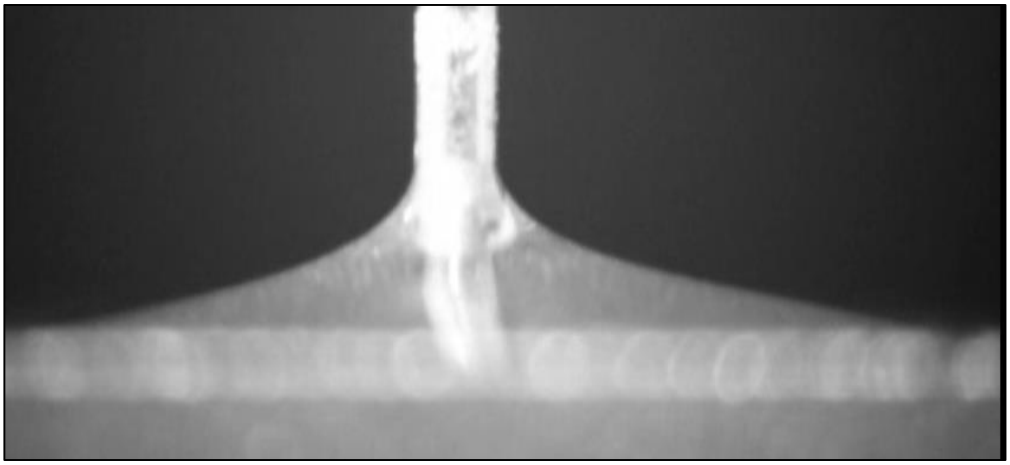

Figure 46. Profile of receding water droplet on moderate stainless steel for measuring the water contact angle hysteresis

Hysteresis (degrees °) (Stainless Steel - Moderate)			
Trial	**Advancing Angle**	**Receding Angle**	**Hysteresis Angle**
1	27	16.5	10.5
2	28	10	18
3	29.5	9.5	20
Average			**16.17**
Std. Dev.			**4.09**

Table 14. Summary of water contact angle hysteresis measurements on moderate stainless steel

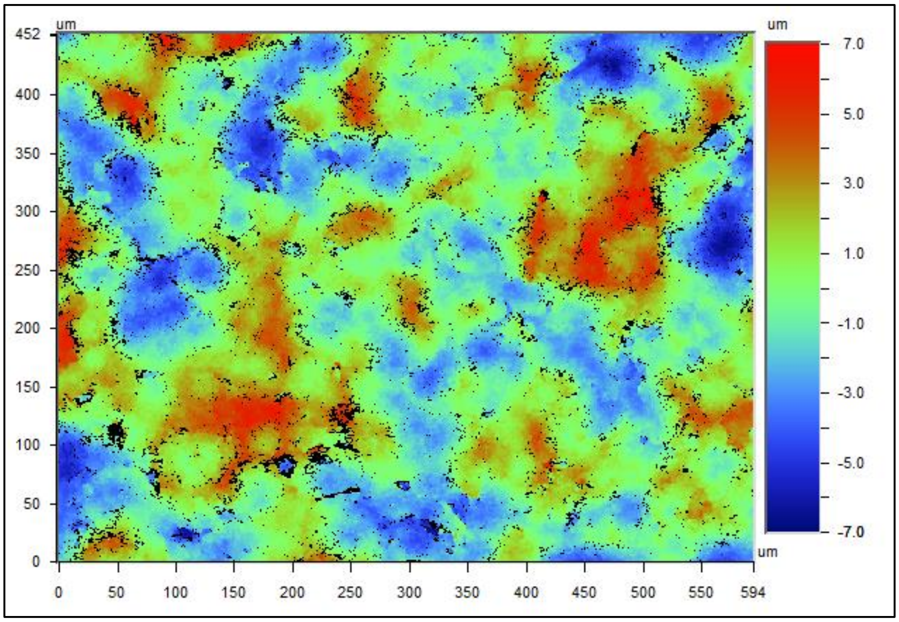

Figure 47. A two-dimensional surface profilometry scan of the surface of the moderate stainless steel sample, shown at 10X magnification

The moderate stainless steel samples used had an average surface roughness of 1.94 µm, a root-mean-square value of 2.42 µm, and the peak-to-valley difference calculated over the entire measured array was 20.41 µm.

Rough Stainless Steel

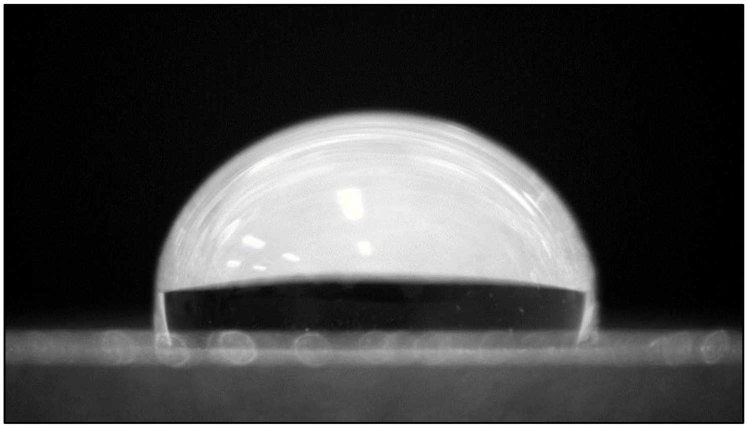

Figure 48. Profile of water droplet on rough stainless steel for measuring the water contact angle

Trial	**WCA (degrees °) (Stainless Steel - Rough)**
1	102
2	119
3	109.75
Average	**110.25**
Std. Dev.	**8.5**

Table 15. Summary of water contact angle measurements on rough stainless steel

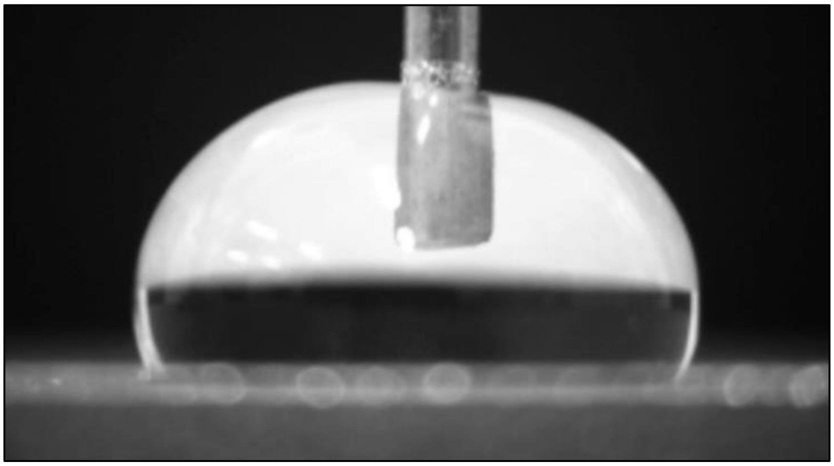

Figure 49. Profile of advancing water droplet on rough stainless steel for measuring the water contact angle hysteresis

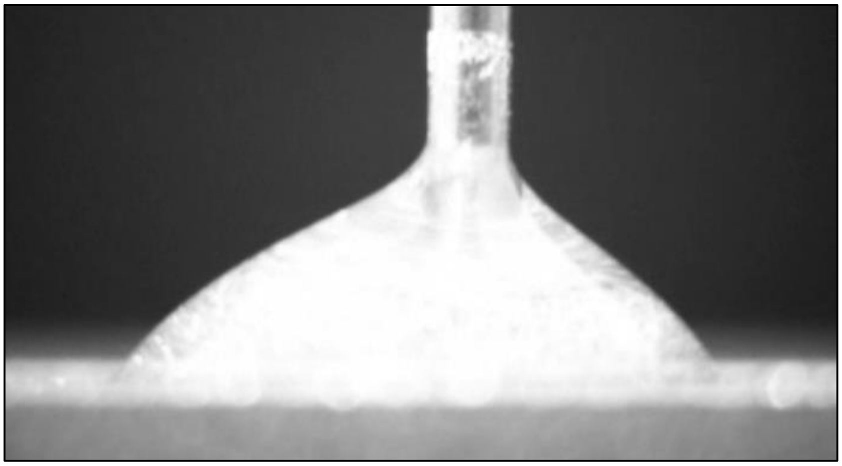

Figure 50. Profile of receding water droplet on rough stainless steel for measuring the water contact angle hysteresis

Hysteresis (degrees °) (Stainless Steel - Rough)			
Trial	**Advancing Angle**	**Receding Angle**	**Hysteresis Angle**
1	120	47.5	72.5
2	117	39	78
3	113.5	51	62.5
Average			**71**
Std. Dev.			**6.42**

Table 16. Summary of water contact angle hysteresis measurements on rough stainless steel

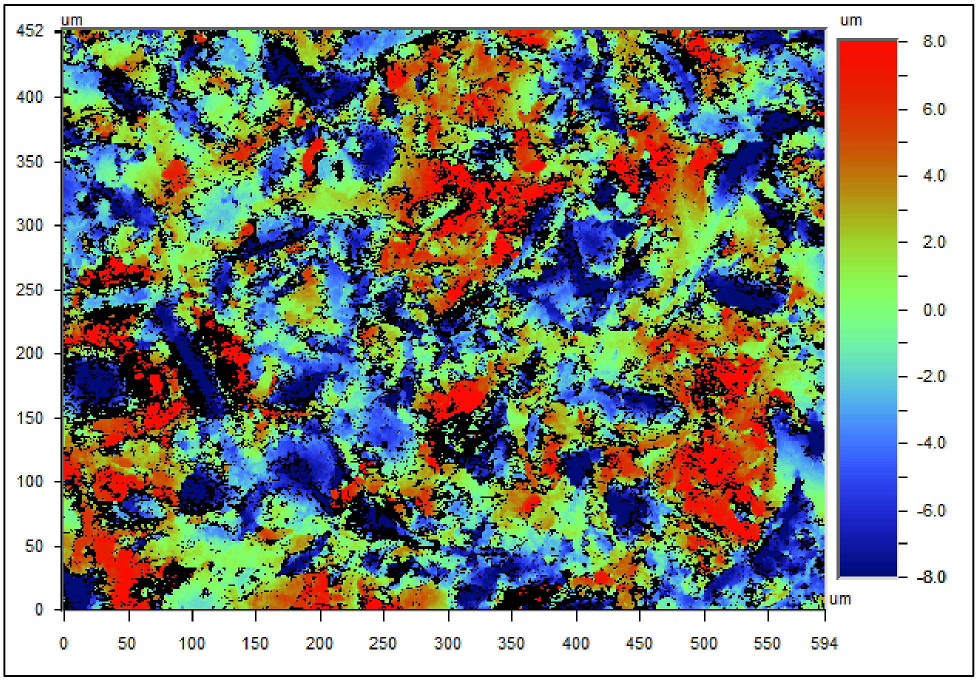

Figure 51. A two-dimensional surface profilometry scan of the surface of the rough stainless steel sample, shown at 10X magnification

The rough stainless steel samples used had an average surface roughness of 3.74 µm, a root-mean-square value of 4.8 µm, and the peak-to-valley difference calculated over the entire measured array was 61.28 µm.

	Glass	**Aluminum**			**Stainless Steel**		
	As-Received	**Polished**	**Moderate**	**Rough**	**Polished**	**Moderate**	**Rough**
R_a	11.27 nm	22.2 nm	3.04 µm	5.06 µm	2.74 nm	1.94 µm	3.74 µm
R_q	24.51 nm	27.9 nm	3.82 µm	6.46 µm	3.55 nm	2.42 µm	4.8 µm
R_t	1.90 µm	243.3 nm	38.93 µm	60 µm	155.2 nm	20.41 µm	61.3 µm

Table 17. Summary of roughness measurements on glass, aluminum, and stainless steel samples where R_a is the average surface roughness, R_q is the root-mean-square value, and R_t is the peak-to-valley difference, all calculated over the entire measured array.

Wettability Characterization

It is necessary to measure the water contact angle of surfaces that are of interest for study of ice adhesion. Hydrophobicity refers to the physical property of a material that repels a mass of water. A water droplet being repelled by the material will not touch a large area of the surface and will take a spherical shape, thus making the water contact angle very large. The evaluation of hydrophilicity and hydrophobicity are made through measuring the angle at which water contacts a surface. A surface with a water contact angle greater than 90° is usually referred to as hydrophobic, and one with a water contact angle higher than 140° is qualified as ultra-hydrophobic. The surfaces with very high water contact angles, particularly greater than 150°, are usually called superhydrophobic surfaces. The contact angle of water has been commonly used as a criterion to evaluate the static hydrophobicity of a surface. Currently, there is no known material that can completely prevent ice or snow from accumulating on its surface, however, some coatings are believed to provide reduced adhesion (18) and for smooth surfaces, there is a clear trend that the ice adhesion strength decreases as the surface becomes more hydrophobic (121).

Alone, however, the measurement of the water contact angle is not adequate for the evaluation of dynamic hydrophobicity, which is the sliding of water droplets. Dynamic hydrophobicity is describing a surface's ability to shed water. Furthermore, to completely describe a superhydrophobic state, the contact angle hysteresis should also be measured. The contact angle hysteresis is the difference between the advancing and receding contact angles. The sliding angle and/or the contact angle hysteresis are commonly utilized as criteria for dynamic hydrophobicity on a solid hydrophobic surface. For an optimal superhydrophobic state, the static contact angle should be maximized, and the contact angle hysteresis minimized (26). It was shown that the ice adhesion strength on a rough hydrophobic surface is not correlated with the water contact angle but is correlated with the contact angle hysteresis, or dynamic hydrophobicity. It was also shown that despite the rough surface of a superhydrophobic coating, it will reduce the adhesion of ice more than a smooth hydrophobic surface of the same chemical composition, and superhydrophobic coatings exhibiting a contact angle hysteresis lower than 5° lead to very high icephobic properties (18) (20) (21). The continuing research in the ice resistance of superhydrophobic coatings further revealed that only the receding contact angle was important in matters of ice adhesion (114).

Hysteresis is a phenomenon that can arise from the molecular interactions between the solid and liquid or from irregularities in the surface, such as roughness or heterogeneities. In the case of a sessile drop: when further liquid is added, the contact line advances forward. When the motion of the drop stops it exhibits an advancing contact angle, θ_A. However, if liquid is removed from the sessile drop, the contact angle decreases before the contact line retreats back to a receding value, θ_R. The contact angle hysteresis is referred to as the difference between θ_A and θ_R. Furthermore, in the case of a droplet moving along the solid surface, the contact angle that appears at the front of the droplet, θ_A, will be greater than that at the back of the droplet, θ_R. This is due to roughness and surface heterogeneity, resulting in the contact angle hysteresis (27) (28).

Goniometer Design Requirements

In order to measure the water contact angle and hysteresis of the surfaces that will be studied it was necessary to design and fabricate a device referred to as a goniometer for its ability and purpose of measuring angles. This goniometer, however, is specially adapted to measure the angle that a droplet of liquid makes contact with the surface. The design requirements of the goniometer include the need to be able to capture and save images of the droplet profile while resting on the sample surface. The goniometer must be capable of recording videos of the addition and withdrawal of liquid to and from the droplets resting on the sample surface. It must be capable of sharing information through a computer interface to work with electronic data. The device needed to be able to deposit and withdrawal very precise volumes of water, down to the microliter. Lastly, the device needs a method of determining the angle with which the droplet of water meets the sample surface which will indicate the water contact angle, and allow the calculation of the water contact angle hysteresis.

The final design for the goniometer utilizes a horizontal microscope to measure the water contact angles. The samples are placed on the horizontal microscope stage and images can be captured using the digital camera that is installed on the eyepiece of the horizontal microscope. The digital camera captures the visual information and converts it to be manipulated and saved on a nearby connected personal computer. The droplets are placed on the stage using an automatic syringe controlled by a computer. The computer is capable of carrying out tasks including the deposition and withdrawal of precise amounts of liquid, to the microliter. The automatic syringe is mounted on an adjustable microscope boom stand for maneuverability and support. Once the images are capture by the digital camera and sent to the personal computer they are analyzed using the computer interface software Toup View which allows the images and video recordings of the droplet profiles on the microscope stage be saved in an electronic format to be measured. The images are uploaded into Drop Analysis software and a program is used to map the profile of the droplet and when this is complete it will calculate the angle that the droplet meets the surface.

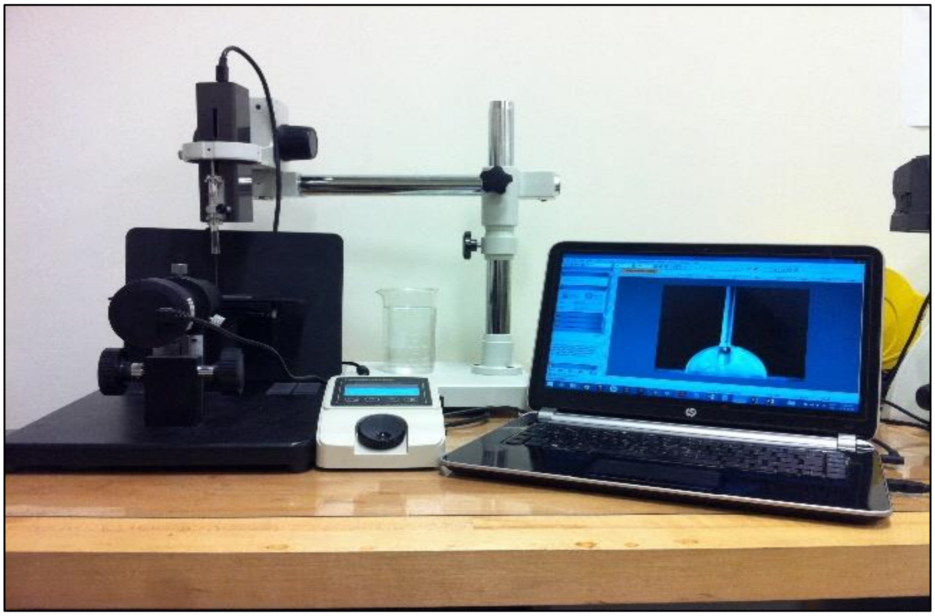

Figure 52. An image of the completed goniometer in operation

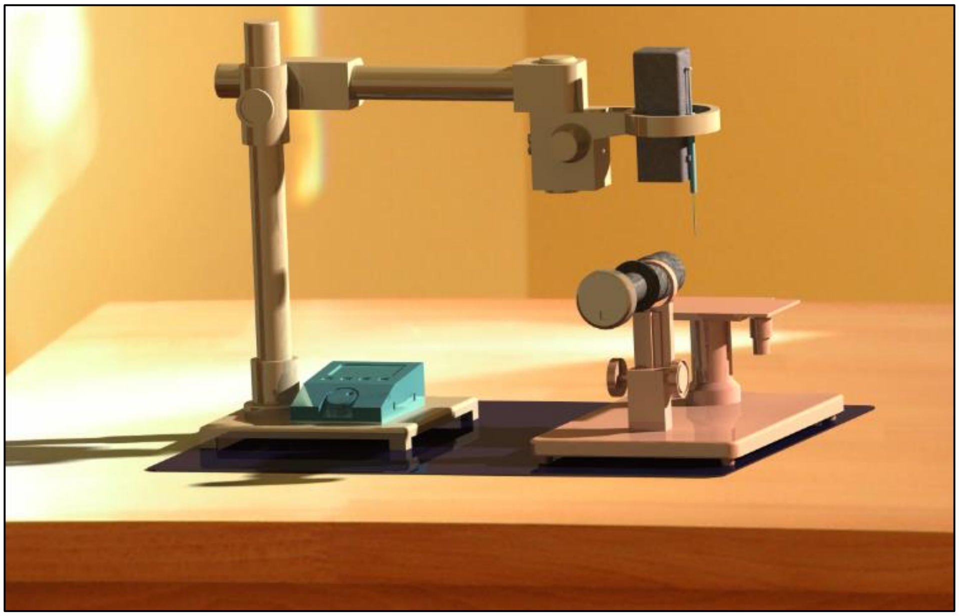

Figure 53. An image of the computer modeled goniometer from the designs used for fabrication

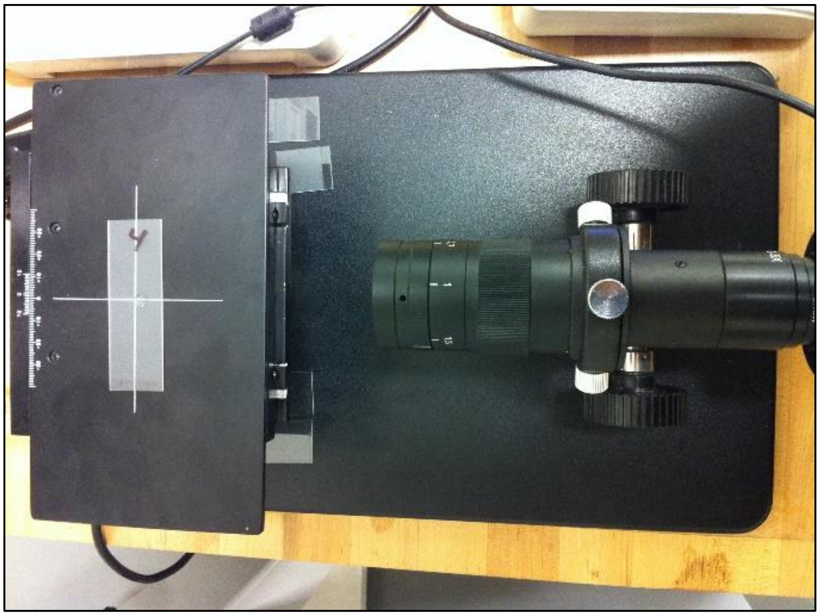

Figure 54. The horizontal microscope stage used in the construction of the goniometer

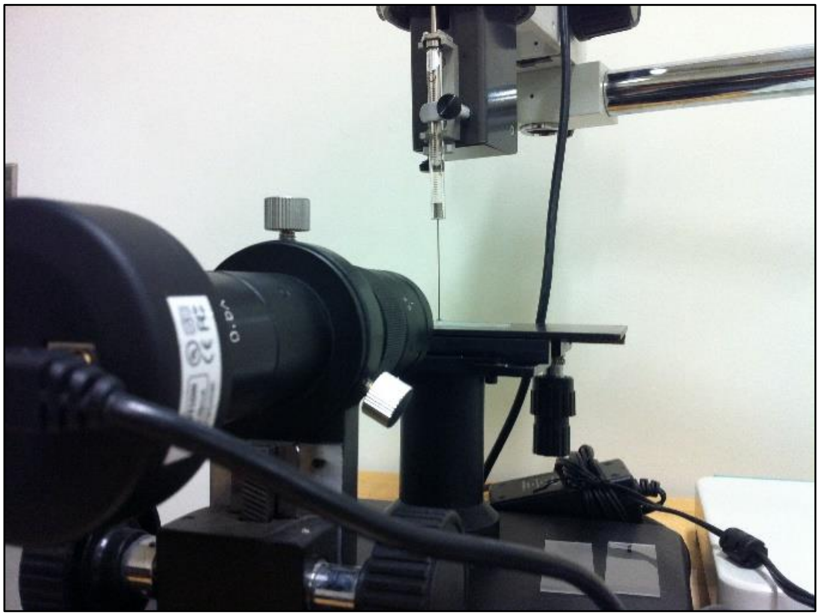

Figure 55. A view down the optical scope showing the location of the water droplet on the microscope slide

Figure 56. The computer operated driver of the syringe supported by the boom stand

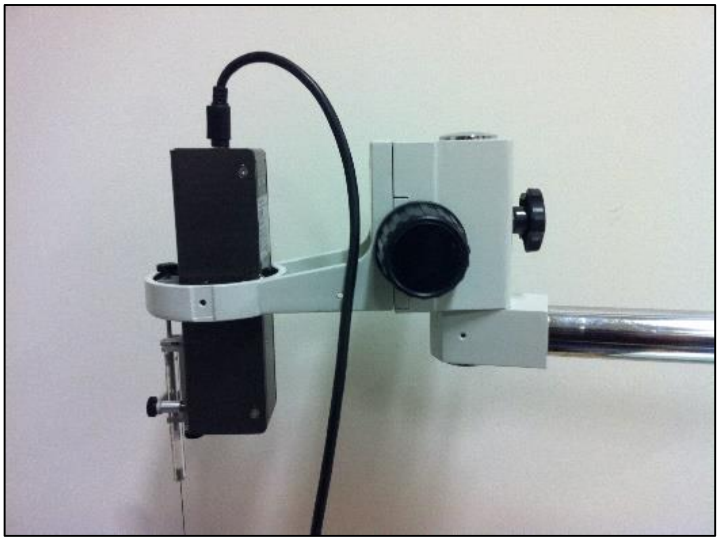

Figure 57. The rack-and-pinion mechanism allowed for repeatable precise maneuvering

Figure 58. The boom stand could be adjusted and fixed in any convenient location

WCA and Hysteresis Measuring Procedure

To measure the water contact angle the sample slide is carefully loaded in place onto the microscope stage of the goniometer. The automatic syringe is centered in the frame of the camera and is maneuvered to within 2 mm of the sample surface. The syringe then places 10 µL of distilled water slowly onto the sample surface in the form of a droplet. The computer interface Toup View is then used to capture the image for measurement. Later the image is uploaded into Drop Analysis software and the profile of the droplet is mapped and the water contact angle measured.

To measure the water contact angle hysteresis the sample slide is carefully loaded in place onto the microscope stage of the goniometer. The automatic syringe is centered in the frame of the camera and is maneuvered to within 2 mm of the sample surface. The syringe then places 10 µL of distilled water slowly onto the sample surface in the form of a droplet. The computer interface Toup View is then used to record a video while 5 µL is subsequently added, followed by 10 µL being finally withdrawn from the droplet. This addition and withdrawal of water from the droplet causes the contact line between the droplet and the sample surface to advance and subsequently recede. Image are taken for measurement of the droplets immediately prior to contact line advancement and recession. By uploading these images into Drop Analysis software, the advancing and receding contact angles are calculated and the difference taken between them to produce the contact angle hysteresis.

Ice Adhesion

It is necessary to measure the ice adhesion because in many places where renewable energy systems are used, climactic conditions are severe and icing is prevalent. This is a problem because the efficiency of wind turbines and solar devices is greatly reduced due to icing and snow accumulation; it may even stop the production of energy all together (1) (14) (15) (16). Due to the crippling effect ice accretion has on the ability of solar devices to produce electricity, many researchers have been turning their attention to designing systems of ice removal. Passive methods of ice removal represent a cheaper option than active methods which are energy hungry and can be expensive to produce and operate (17). One such possible passive solution may lie in hydrophobic coatings. Currently, there is no known material that can completely prevent ice or snow from accumulating on its surface, however, some coatings are believed to provide reduced adhesion (18) and for smooth surfaces, there is a clear trend that the ice adhesion strength decreases as the surface becomes more hydrophobic (121). In order to test the affect that the outlined variables in the study (surface condition, material, coating properties) have on the adhesion of ice to that substrate surface, it is necessary to be capable of accurately measuring the ice adhesion to given surfaces.

It is necessary to measure the adhesion of ice to differing materials such as glass, aluminum, and stainless steel because there are three physical mechanisms involved in the adhesion of ice to a surface, specifically, hydrogen bonding, van der Waals forces, and direct electrostatic interactions. Of these three, the direct electrostatic interactions have been found to be the dominant factor (115) (116). Charges on ice induce equal and opposite charges on metals, whereas on dielectrics, the induced charge is smaller and is related to the dielectric constant. Do to the fact that differing chemistry affects the adhesion of ice to a substrate and that different materials are used in the construction of the protective case assembly used to shield the photvoltaic cells from the outdoor climactic conditions it is necessary to test the adhesion of ice to the materials to determine its behavior and why this behavior is occuring.

It is necessary to measure the adhesion of ice for different roughness and surface conditions because the materials used in the construction of the protective solar panel case (glass, aluminum, steel) are prepared in a variety of methods and each one will leave the material with a distinctive surface condition and roughness. Knowing that the protective casing and variety of materials composing it will be regularly exposed to climactic icing events it is important that the effect of the surface condition and roughness on the adhesion of ice be understood to ensure that the design of the proposed system is repeatable and reliable.

Lastly, it is necessary to measure the adhesion of ice under ultrasonic vibration because it is important to understand how the power, frequency, and orientation of the ultrasonic vibration affect the ice adhesion. In order to create a highly efficient system, it should use as little power as is needed. By understanding how the ultrasonic vibration decreased the ice adhesion and by how much under certain conditions, the vibrations can be fine-tuned to delaminated accreted ice with minimal energy input.

Ice Adhesion Measurement Method

The adhesion of ice to a substrate is measured by freezing a known surface area of water into ice on the substrate. Next, a force is applied strictly to the ice in strictly a shearing motion along the ice/substrate interface. The force can be applied by means of actuators and centrifuges, in either event, the shear force applied to the ice can be calculated or measured directly with a load cell. Having the shear force that was sufficient to break the bonds of the ice to the substrate, and knowing the area of ice frozen to the substrate, the ice adhesion can be calculated by dividing the shear force by the area. The ice adhesion can be measured for different materials, such as glass, metals, and polymers by substituting the substrate surface with the desired material to be studies. The ice adhesion of different roughness can be measured by substituting the substrate surface with a surface that has undergone surface preparation of varying magnitudes. Lastly, the ice adhesion under ultrasonic vibration can be calculated by introducing ultrasonic transducers to the testing procedure to input ultrasonic vibration. The orientation of the ultrasonic input can be adjusted by adjusting the positioning of the transducers, and the power and frequency can be adjusted by substituting different sizes of transducers.

Ice Adhesion Tester Design Requirements

In order to measure the ice adhesion for different materials, roughness, and under ultrasonic vibration it was necessary to design and fabricate a device that will be referred to as the Ice Adhesion Tester (IAT). The design requirements of the IAC include the need to be able to hold interchangeable samples, in order to change the material being tested and/or the surface conditions of the sample. It needs to include a feature that allows known surface areas of ice to be frozen to the samples. It needs to have the ability to apply strictly shearing forces to only the ice in sufficient quantities capable of breaking the bonds of ice to the sample. It also will be required to have a means of calculating or measuring the shearing force that was required to debond the ice from the sample. The IAC will need a computer interface for operation, and an electronic data acquisition system for the accumulation and interpretation of the data obtained. It must possess the ability to mount ultrasonic transducers of varying power in both the normal and transverse direction to the ice/substrate interface and be able to remotely operate it. Finally, the IAC will need to be able to control the climate conditions that the tests are exposed to and be capable of measuring and monitoring these conditions.

The final design of the IAC utilizes an aluminum stage as a base to hold interchangeable substrate samples, a linear actuator, horizontal low-friction sliders, and replaceable ultrasonic transducers. The horizontal low-friction sliders hold a polycarbonate cylinder directly over the sample substrate and is attached to the linear actuator through an S-type load cell (LC101 Omega Scientific). A K-type thermocouple (Omega Scientific) is located next to the sample substrate in order to monitor the temperature near the ice/substrate interface to ensure proper experimental conditions. This whole apparatus is located inside a climate control unit capable of holding the ambient temperatures at -20°C. The linear actuator is controlled through a computer interface (CRK Motion

Creator) and data acquisition (InstruNet) is conducted for the load cell through each trial and the data saved to the computer interface for later retrieval and analysis.

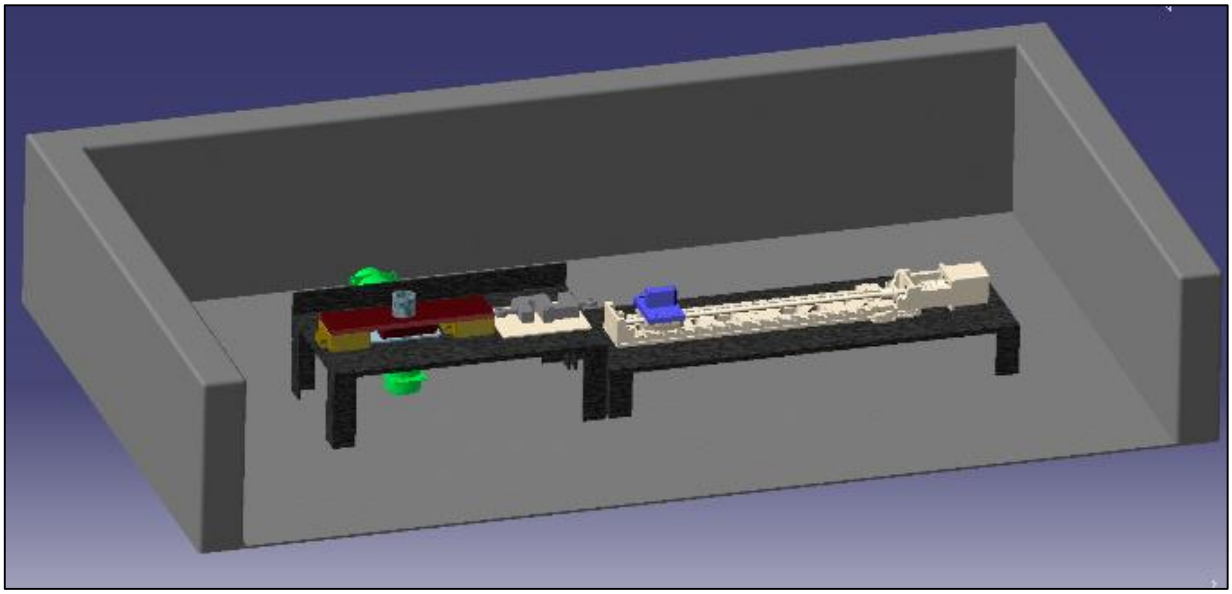

Figure 59. A view of the computer modeled Ice Adhesion Tester (IAC) in climate control chamber

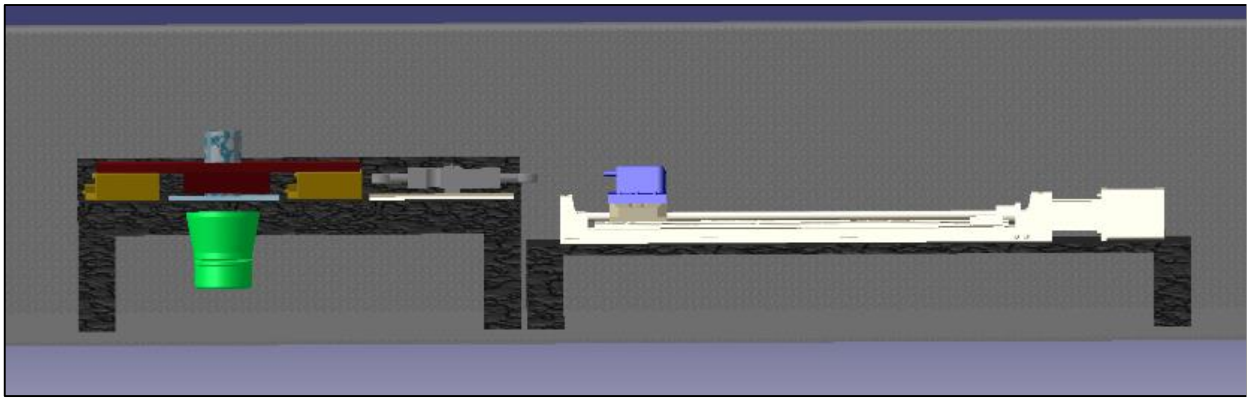

Figure 60. A horizontal view of the computer modeled IAC

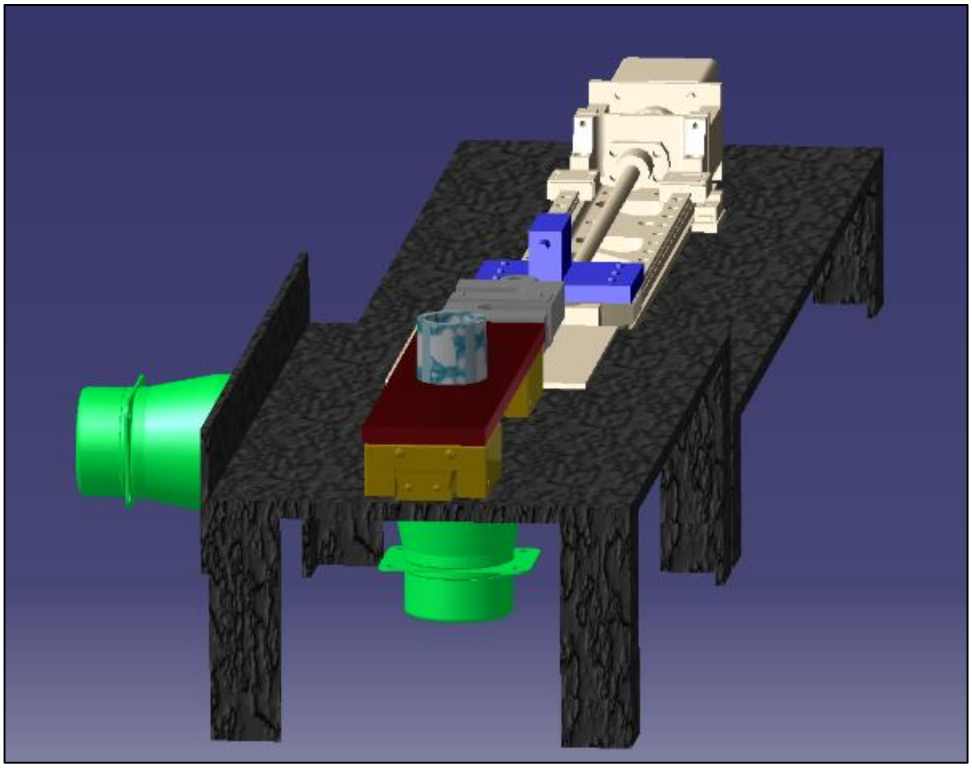

Figure 61. An isometric view of the computer modelled IAC showing the mounted ultrasonic transducers, linear actuator, and horizontal low-friction sliders

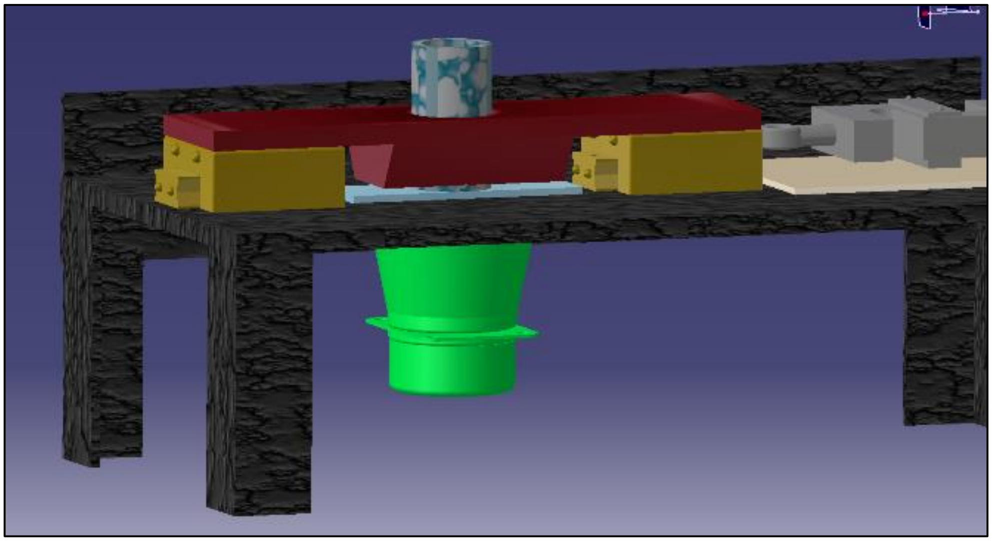

Figure 62. A close-up image of the computer modelled IAC showing the mounted ultrasonic transducer beneath the stage and the low-friction sliders holding the polycarbonate mold being pulled by the S-type load cell

Figure 63. An overhead optical image of the Ice Adhesion Tester in the climate control chamber

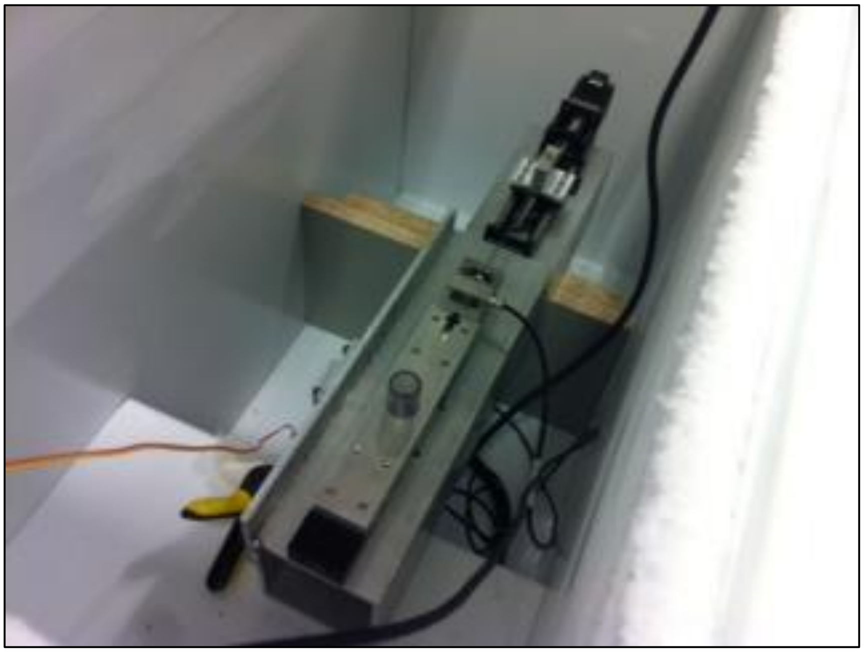

Figure 64. An isometric view of the Ice Adhesion Tester in the climate control chamber

Using the Ice Adhesion Tester (IAC) to Measure Ice Adhesion

The IAC measures ice adhesion by freezing distilled water in the polycarbonate mold (1.905 cm or 0.75 in. internal diameter) to a sample substrate originally at standard temperature and pressure

(STP) being tested. The sample substrate is secured to the aluminum stage of the machine and is immobile. 10mL of STP water is added to the polycarbonate mold and allowed to freeze solid for 30 minutes. After this time the computer interface CRK Motion Creator is used to control the linear actuator and apply a tensile force to the horizontal low-friction sliders that hold the polycarbonate cylinder mold which in turns holds the ice against the sample substrate. This generates a strictly shearing force in the ice/substrate interface that is measured by the S-type load cell and uploaded to the data acquisition software InstruNet. As the linear actuator increasingly applies more tension on the cable, more shearing force is concentrated at the ice/substrate interface, eventually, a critical shearing force is achieved and the ice is removed from the surface of the sample substrate. Using the known area of ice frozen to the sample substrate in the mold, and the critical shearing force needed to remove the ice the adhesion of the ice to that substrate can be calculated simply by dividing the critical shearing force by the area of frozen ice.

The IAC can measure the ice adhesion of any sample substrate under ultrasonic vibration by using the same method as previously explained with one additional step. When the linear actuator is started and applying in turn apply the shearing force to the ice/substrate interface, the ultrasonic transducer which can be installed in one of two positions, will be activated and will send vibrations through the ice/substrate interface at 20,000 cycles per second to break or weaken the bonds.

The IAC can also be used to investigate the influence of ice/substrate/apparatus thermal gradients on the standard deviation of ice adhesion tests. Three possible combinations exist for the thermal starting points of the sample substrate and the distilled water to be frozen: 1) the experiment can be run using a sample substrate at -20°C and STP water, 2) The experiment can be run using a sample substrate at -20°C and icy water at ~1-3°C, 3) the experiment can be run using a sample substrate and water at STP. The significance of these experimental scenarios is that each will affect the ice/substrate interface differently due to the differing rates at which the heat is removed from the water to be frozen, and the sample substrate because of the difference in thermal gradient. Since it is not the aim of this study to accurately determine the effect of thermal heat transfer rates on the nucleation of ice and structure of ice, this thermal investigation will be limited to the effect it has on the standard deviation and repeatability of the IAC.

Hydrophobic Coating

It is necessary to test the ice adhesion of hydrophobic coatings because of the potential they show for reducing ice adhesion and preventing ice accumulation. Because active methods of ice removal (thermal, mechanical, chemical fluids) are energy hungry and expensive passive methods represent a cheaper option (17). Although, currently there is no known material that can completely prevent ice or snow from accumulating on its surface, hydrophobic coatings can provide reduced adhesion, and as the hydrophobicity of the surface increases, the ice adhesion decreases (18) (121). Due to the current inability of the hydrophobic coatings to consistently prevent any adherence of ice it is necessary to couple the hydrophobic coatings with an ultrasonic transducer to mechanically break what weak bonds may have been able to form between the coating/substrate and the ice. This then dictates the necessity to measure the ice adhesion of candidate hydrophobic coatings in order to determine which can most prevent the adhesion of ice while maintaining the other necessary factors for a coating to be used in photovoltaic device applications (transparency, durability, etc). This characterization of the coating will also allow for the selection of a transducer which will use as little energy as is needed to remove the ice because it has been intelligently coupled with the hydrophobic coating. Without proper understanding of how the hydrophobic coating will affect the ice adhesion an ultrasonic transducer may be used that is not optimized and over the lifetime of the system it will use many time more energy than would be needed.

It is necessary to test both smooth and rough hydrophobic coatings because despite the rough surface of a superhydrophobic coating, it will reduce the adhesion of ice more than a smooth hydrophobic surface of the same chemical composition, and superhydrophobic coatings exhibiting a contact angle hysteresis lower than 5° lead to very high icephobic properties (18) (20) (21). However, the durability and mechanical robustness of the coating are particularly important to consider because the fragile hierarchical roughness can be irreversibly destroyed, which will inevitably lead to an increase in the contact angle hysteresis and a rapid decrease in the static contact angle (22). Rough superhydrophobic coatings offer attractive drastic ice adhesion reductions but come at the price of durability, whereas, the smooth hydrophobic coatings do not provide as much ice reduction but can provide a much more durable and transparent coating. Both must be tested in order to make an informed choice on which will be best coupled with ultrasonic transducers to remove the ice.

Coating Selection

A suitable hydrophobic coating will be selected on the basis of ice adhesion reduction, transparency, durability, method of application, and environmental toxicity. The coating must be able to significantly decrease the adhesion of ice that accumulates, it must be capable of allowing the large majority of light through (~90%) in order not to interfere with the photovoltaic production of electricity, it must be durable enough to withstand repeated ice shedding events without beneficial property reductions, and finally it must meet standards of safety for the care of our environment.

After reviewing 39 potential candidate hydrophobic coatings in literature, the list has been narrowed down to 3 for serious consideration to investigate in this ice adhesion study. These candidate coatings are described in detail in literature (Hwang et al. (92), Kavale et al. (65), and

Manca et al. (84)), however, for quick reference important qualities of the coatings have been highlighted in Table. 17. The first factor that needs to be considered is the substrate to be coated, for the considered coatings, each has been successfully used in conjunction with glass which is the primary material under consideration and therefore all conform to the needs of this study. Secondly there is the reported contact angle and sliding angle which are indicators of the coatings ice adhesion reducing potential, the larger the contact angle and the smaller the sliding angle the more likely the coating is to maintain a composite wetting state (Cassie-Baxter) and not allow the penetration of moisture into the roughness and will therefore significantly reduce the adhesion. The third factor is the method that the coating can be applied. For industry use it is imperative that the method be simple, affordable, and scalable to large production capacity. Fourth, and lastly, the coating must be transparent in order to allow the light waves to penetrate which is necessary for the photovoltaic device to produce electricity.

Author	**Year**	**Composition**	**Substrate**	**Contact Angle**	**Sliding Angle**	**Method of Application**	**Transparency**
Hwang et al. (92)	2011	3-[tris[(trimethylsilyl)oxy]-silyl]propyl methacrylate	Glass	178°	1°	Spray Coated	Yes
Kavale et al. (65)	2011	Methyltrimethyloxysilane	Glass	171°	2°	Dip Coated	Yes
Manca et al. (84)	2009	Trimethylsiloxane (TMS) and Methyltriethoxysilane (MTEOS)	Glass	168°	3°	Spin Coated	Yes

Table 18. Summary of the top 3 candidates for coating study

After careful consideration of the former factors mentioned above, the coating reported by Hwang et al. (92) was chosen for this study. The advantages of this coating are that it has been designed for glass, the contact angle is 178° which is just 2° less than the theoretical maximum. Also the sliding angle is extremely low, just 1°, indicating that the water has very low adhesion to the coating which also indicates its potential for ice adhesion reduction. Lastly, the reported coating is sufficiently transparent as to not interfere with the capture of light photons by the photovoltaic cells for the production of electricity.

Coating Synthesis

This coating is a statistical copolymer synthesised of 3-[tris[(trimethylsilyl)oxy]-sily]propyl (SiMA) which imparts the final coating with a low surface energy, methyl methacrylate (MMA) which add rigidity to the coating, and 2, 2' –azobis(isobutyronitrile) (AIBN) which is used as an initiator of the free-radical polymerization process. First the chemicals were precisely weighed using a high accuracy balance (Cole Parmer Symmetry). 2g of MMA, 2g of SiMA, and 0.04g of AIBN were weighed out.

Figure 65. High accuracy balance used to precisely measure the weight of precursor chemicals

Figure 66. Chemical precursors were mixed in glove bag under argon atmosphere

Figure 67. Combined chemicals were heated at 70°C for 6 hours to facilitate free-radical polymerization

Additionally, 4mL of toluene was measured using a 10 mL graduated cylinder. These portioned chemicals were then placed in a glove bag (Omega Scientific) flushed with argon to remove oxygen from the glove bag environment. Under the argon atmosphere, the carefully portioned chemicals were placed in a 25 mL Erlenmeyer flask and then sealed with a glass stopper. The Erlenmeyer flask was then set on a hot plate at 70°C for 6 hours to facilitate the free-radical polymerization reaction. Once finished the end result is that of a hydrophobic coating solution of 3-[tris[(trimethylsilyl)oxy]-silyl]propyl methacrylate.

Coating Application

To create a smooth hydrophobic coating, 5g of coating solution is added to 200g of acetone (solvent) in a 50mL beaker to form a 2.5% copolymer-solvent solution by weight. The beaker is placed in an ultrasonic bath for 8 minutes ensuring thorough mixing of the coating solution into the acetone. The beaker is then loaded into the dip-coater. Pre-cleaned glass microscope slides are fastened into the dipping stage of the dip-coater and the stage is lowered and retracted at constant speeds (5, 50, 100, 150, and 200 mm/min) to smoothly deposit the solution which is then allowed to dry at room temperature for 24 hours.

Figure 68. MTS climate controlled variable-speed dip-coater used throughout the study

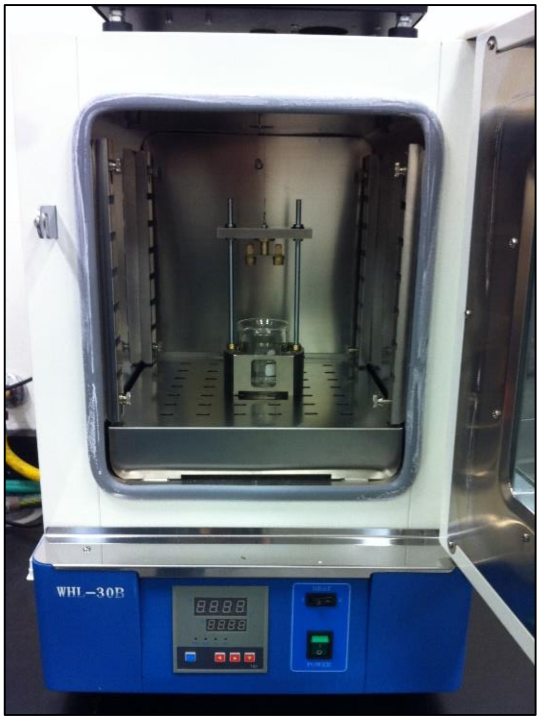

Figure 69. A view inside the MTS climate controlled variable-speed dip-coater showing the retractable dipping stage

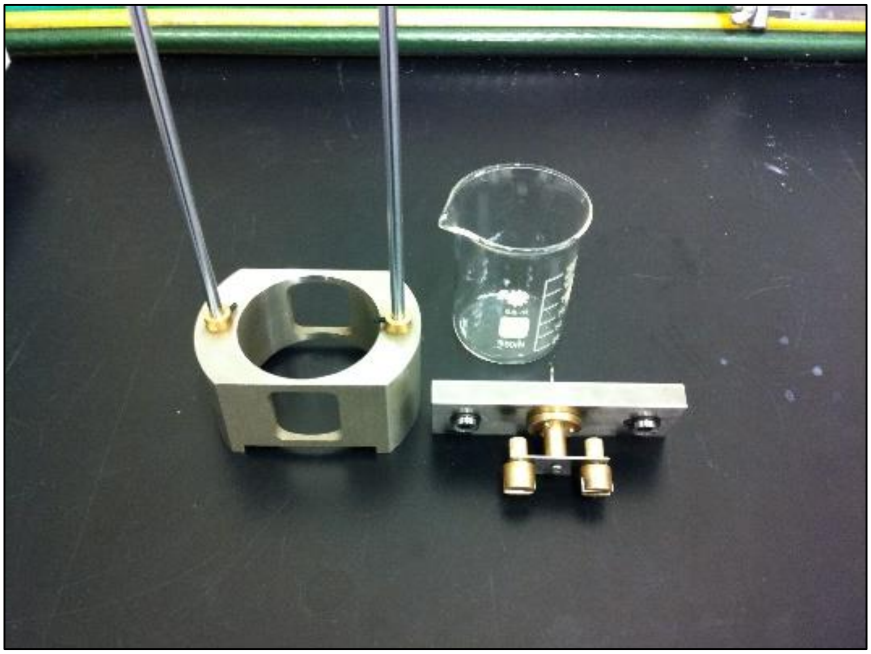

Figure 70. A close-up image of the coating solution beaker, the beaker holder with guide rails, and the mounting stage for fastening test slides

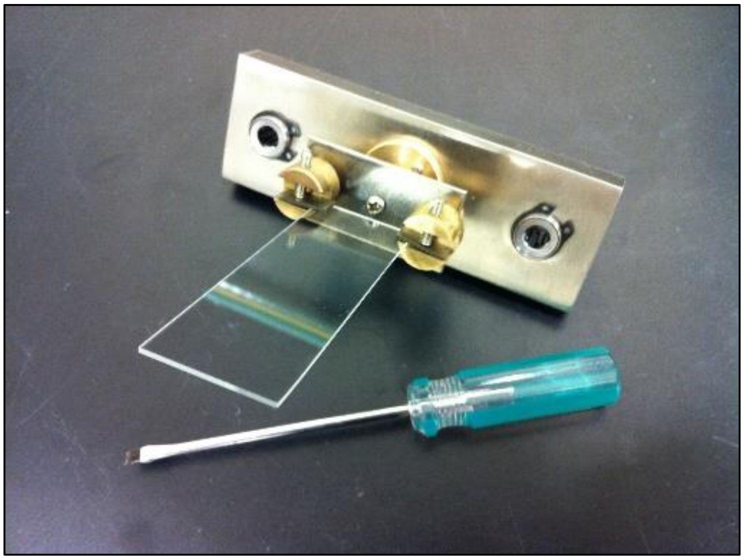

Figure 71. A close-up image of the mounting stage with a glass microscope slide mounted

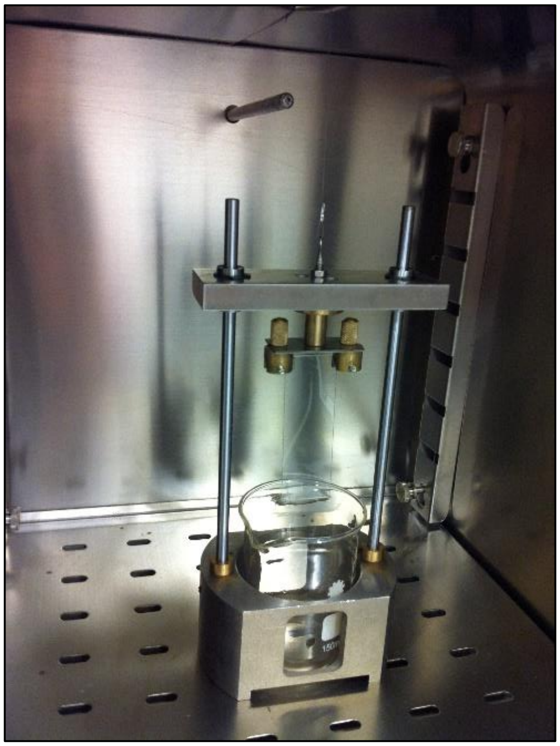

Figure 72. A close-up view inside the dip-coater showing the stage lowering a glass slide into the solution beaker

To create a rough hydrophobic coating, 1g of coating solution was added to 200g of acetone (solvent) in a 50mL beaker to form a 0.5% copolymer solution by weight. The beaker is placed in an ultrasonic bath for 8 minutes ensuring thorough mixing of the coating solution into the acetone. The solution is then added to the canister of an airbrush (Earlex HV5000). Pre-cleaned glass microscope slides are fastened to a disposable recyclable backdrop (cardboard) for spray coating. The solution was sprayed toward the glass slide from a distance of 10cm or 20cm with 2, 4, or 6 passes at 2psi.

Figure 73. The Earlex spray-coater used to deposit the rough sprayed coatings

Coating Design Requirements

The design requirements of the smooth hydrophobic coating are full and complete coverage of the glass surface with no exposure of the glass. It requires a consistently smooth and level surface throughout the area of the glass microscope slide. It will require wettability properties that exhibit a high water contact angle indicating low surface energy and a very low water contact angle which indicates low adhesion of water to the coating. Finally, it requires good adhesion to the glass substrate and the durability to endure multiple violent ice shedding events.

The design requirements of the rough hydrophobic coating are likewise to achieve full and complete coverage of the glass surface with no exposure of the glass. Unlike its smooth counterpart, the rough coating requires roughness not on one but two scales. Hierarchical roughness composed of micro- peaks and valleys, and nano- peaks and valleys are required for the ice adhesion reducing properties sought after. Cao et al. (23) demonstrated that the probability of icing occurring on the coating increased remarkably when the nano-scale roughness is greater than 50nm when the micro-scale roughness is 10µm. This indicates that the rough coating should also conform to nano-scale roughness of less than 50nm to achieve best ice adhesion reducing properties from the coating. It will require wettability properties that exhibit a high water contact angle indicating low surface energy and a very low water contact angle which indicates low adhesion of water to the coating. Finally, it also requires good adhesion to the glass substrate and the durability to endure multiple violent ice shedding events without losing the critical roughness parameters that impart its properties. The performance results of the selected coatings will be displayed in the next chapter, and discussed in the chapter following that.

4. Results

Copolymer coating characterization testing results

Smooth dipped coating

Two variables pertaining to the dip coating of the copolymer coating onto glass slides are the number of layers applied and the speeds at which the glass microscope slide is lowered and retracted with each dip. The MTS dip coater used throughout this study has the capability of varying the dipping speed between 5 - 200 mm/min, this has been divided into 5 speeds to test the effect that the speed of dipping has on the dip coated copolymer coating. The speeds used for dip coating are indicated in Table 19. Furthermore, the number of layers of the copolymer coating is another factor that must be investigated in order to understand the effect of the amount of layers on the performance of the coating. Single layer and double layer copolymer dip coated samples have been prepared at the varied dipping speeds and the wettability, morphological, and icing properties will be investigated by measuring the static water contact angles, contact angle hysteresis, surface profilometry, environmental scanning electron microscopy, and the ice adhesion.

The design requirements of the smooth hydrophobic coating are full and complete coverage of the glass surface with no exposure of the glass. It requires a consistently smooth and level surface throughout the area of the glass microscope slide. It will require wettability properties that exhibit a high water contact angle indicating low surface energy and a very low water contact angle which indicates low adhesion of water to the coating. Finally, it requires good adhesion to the glass substrate and the durability to endure multiple violent ice shedding events.

Dip-Coated Single Layer

Dip-Coating Speeds (mm/min)				
Slow (S)	Medium/Slow (MS)	Medium (M)	Medium/Fast (MF)	Fast (F)
5	50	100	150	200

Table 19. The dipping speeds tested for applying the smooth copolymer coating

To measure the water contact angle the sample slide is carefully loaded in place onto the microscope stage of the goniometer. The automatic syringe is centered in the frame of the camera and is maneuvered to within 2 mm of the sample surface. The syringe then places 10 µL of distilled water slowly onto the sample surface in the form of a droplet. The computer interface Toup View is then used to capture the image for measurement. Later the image is uploaded into Drop Analysis software and the profile of the droplet is mapped and the water contact angle measured.

To measure the water contact angle hysteresis the sample slide is carefully loaded in place onto the microscope stage of the goniometer. The automatic syringe is centered in the frame of the camera and is maneuvered to within 2 mm of the sample surface. The syringe then places 10 µL of distilled water slowly onto the sample surface in the form of a droplet. The computer interface Toup View is then used to record a video while 5 µL is subsequently added, followed by 10 µL being finally withdrawn from the droplet. This addition and withdrawal of water from the droplet causes the contact line between the droplet and the sample surface to advance and subsequently recede. Image are taken for measurement of the droplets immediately prior to contact line advancement and recession. By uploading these images into Drop Analysis software, the advancing and receding contact angles are calculated and the difference taken between them to produce the contact angle hysteresis.

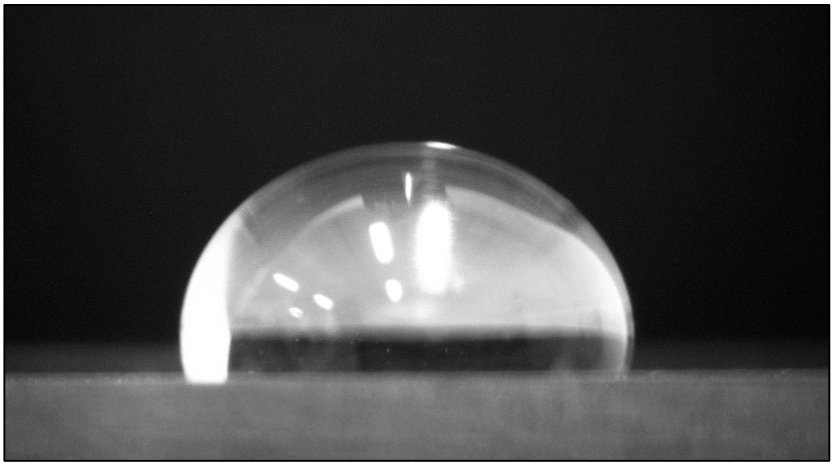

Figure 74. Profile of water droplet on slowly single dip-coated glass for measuring the water contact angle

Trial	**WCA (degrees °) (Coating – DP1L - Slow)**
1	110.5
2	105
3	107.5
Average	**107.5**
Std. Dev.	**2.75**

Table 20. Summary of water contact angle measurements on slowly single dip-coated glass

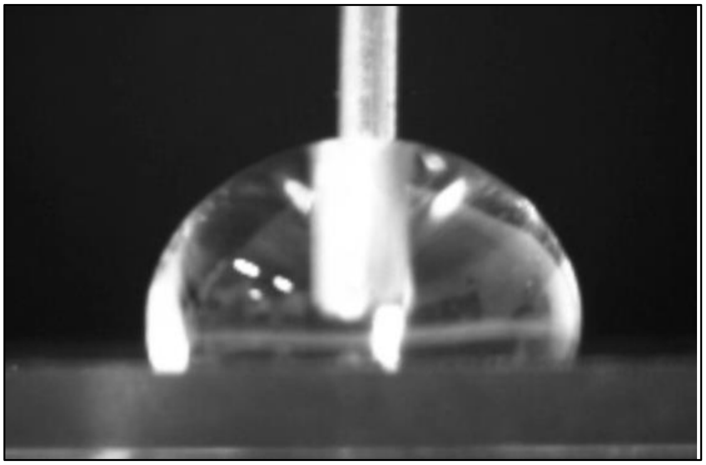

Figure 75. Profile of advancing water droplet on slowly single dip-coated glass for measuring the water contact angle hysteresis

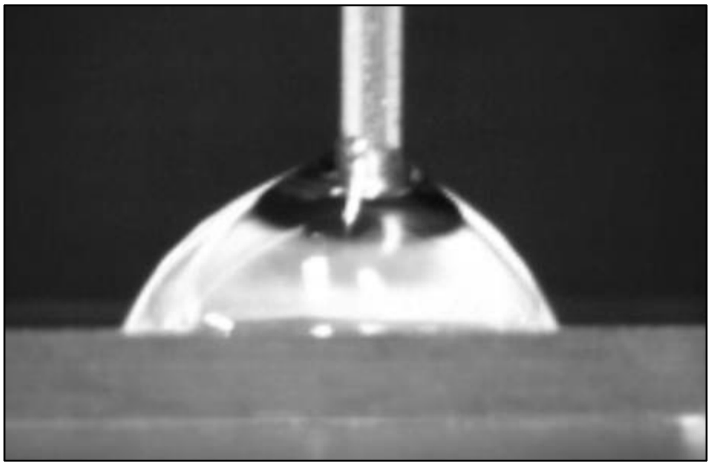

Figure 76. Profile of receding water droplet on slowly single dip-coated glass for measuring the water contact angle hysteresis

Hysteresis (degrees °) (Coating – DP1L - S)			
Trial	**Advancing Angle**	**Receding Angle**	**Hysteresis Angle**
1	108.5	71	37.5
2	107	72.5	34.5
3	107	71	36

Average			**36**
Std. Dev.			**1.22**

Table 21. Summary of water contact angle hysteresis measurements on slowly single dip-coated glass

Trial	**WCA (degrees °) (Coating – DP1L - MS)**
1	108.5
2	108.5
3	109
Average	**108.67**
Std. Dev.	**0.29**

Table 22. Summary of water contact angle measurements on medium-slow single dip-coated glass

Hysteresis (degrees °) (Coating – DP1L - MS)			
Trial	**Advancing Angle**	**Receding Angle**	**Hysteresis Angle**
1	107.5	70.5	37
2	104	69.5	34.5
3	107	68	39

Average			**36.83**
Std. Dev.			**1.84**

Table 23. Summary of water contact angle hysteresis measurements on medium-slow single dip-coated glass

Trial	**WCA (degrees °) (Coating – DP1L - M)**
1	105
2	110
3	110.5
Average	**108.5**
Std. Dev.	**3.04**

Table 24. Summary of water contact angle measurements on medium single dip-coated glass

Hysteresis (degrees °) (Coating – DP1L - M)			
Trial	**Advancing Angle**	**Receding Angle**	**Hysteresis Angle**
1	105	72	33
2	108	75.5	32.5
3	109.5	76	33.5

Average			**33**
Std. Dev.			**0.41**

Table 25. Summary of water contact angle hysteresis measurements on medium single dip-coated glass

Trial	**WCA (degrees °) (Coating – DP1L - MF)**
1	114
2	111.5
3	111
Average	**112.17**
Std. Dev.	**1.61**

Table 26. Summary of water contact angle measurements on medium-fast single dip-coated glass

Hysteresis (degrees °) (Coating – DP1L - MF)			
Trial	**Advancing Angle**	**Receding Angle**	**Hysteresis Angle**
1	112	80	32
2	111	76.5	34.5
3	109	77.5	31.5
Average			**32.67**

Std. Dev.			**1.31**

Table 27. Summary of water contact angle hysteresis measurements on medium-fast single dip-coated glass

Trial	**WCA (degrees °) (Coating – DP1L - F)**
1	107
2	106
3	111
Average	**108**
Std. Dev.	**2.65**

Table 28. Summary of water contact angle measurements on fast single dip-coated glass

Hysteresis (degrees °) (Coating – DP1L - F)			
Trial	**Advancing Angle**	**Receding Angle**	**Hysteresis Angle**
1	110	77	33
2	112	78	34
3	108	79.5	28.5
Average			**31.83**
Std. Dev.			**2.4**

Table 29. Summary of water contact angle hysteresis measurements on fast single dip-coated glass

Dip-Coated 1 Layer		
Speed (mm/min)	**WCA (degrees)**	**Hysteresis (degrees)**
5 (S)	107.7	36
50 (MS)	108.7	36.8
100 (M)	108.5	33
150 (MF)	112.2	32.7
200 (F)	108	31.8
Average	**109**	**34**
Std. Dev.	**1.63**	**1.97**

Table 30. Summary of water contact angle and hysteresis measurements on the speed varied single dip-coated glass

The series of coatings created with one layer by varying the speed of dipping have all performed very similarly in regards to wettability. The five coatings deposited at speeds ranging from 5 – 200 mm/min exhibited an average water contact angle of 109°, ranging from 107° - 112° with a standard deviation of only 1.63°. Likewise, the contact angle hysteresis of the coatings were remarkably similar with an average of 34°, ranging from 32° - 36° with a standard deviation of only 1.97°.

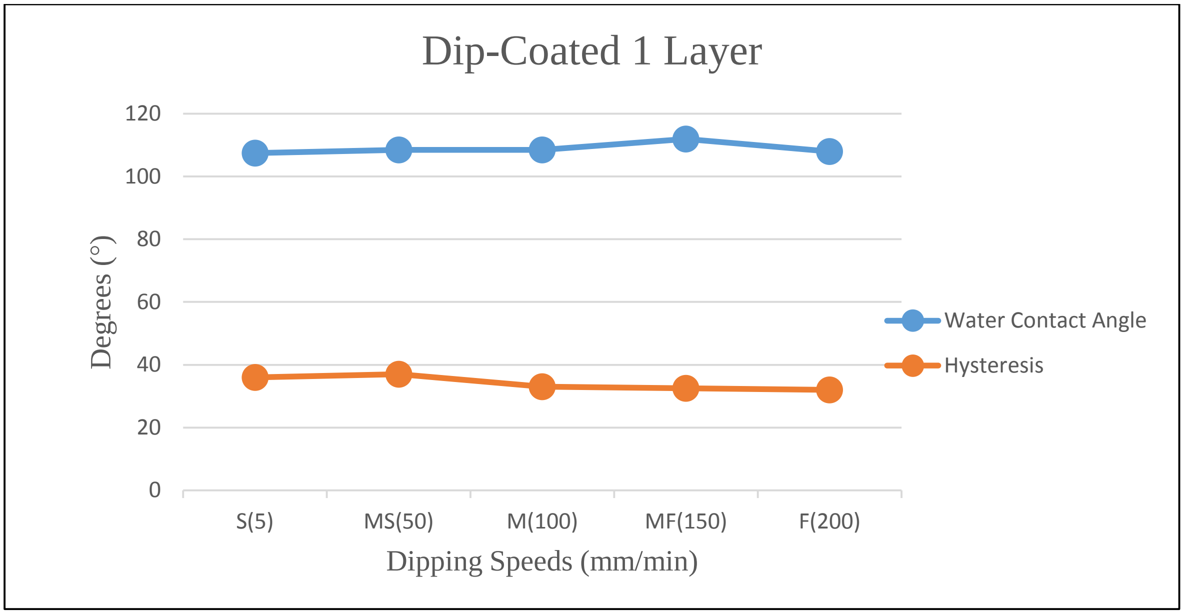

Figure 77. The WCA and Hysteresis plotted against dipping speed for single dipped coatings

Dip-Coated Double Layer

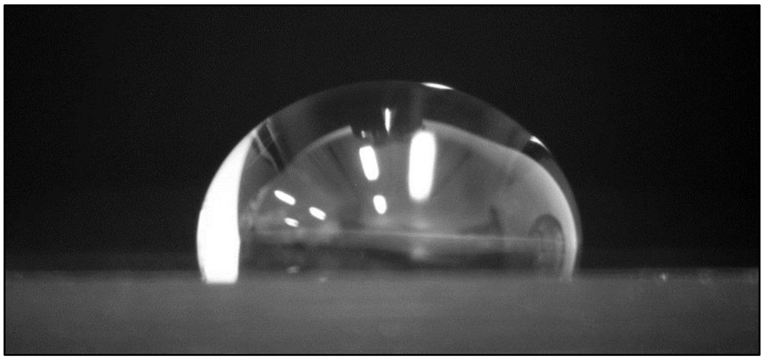

Figure 78. Profile of water droplet on slowly double dip-coated glass for measuring the water contact angle

Trial	**WCA (degrees °) (Coating – DP2L - S)**
1	109
2	110.5
3	108

Average	**109.17**
Std. Dev.	**1.26**

Table 31. Summary of water contact angle measurements on slowly double dip-coated glass

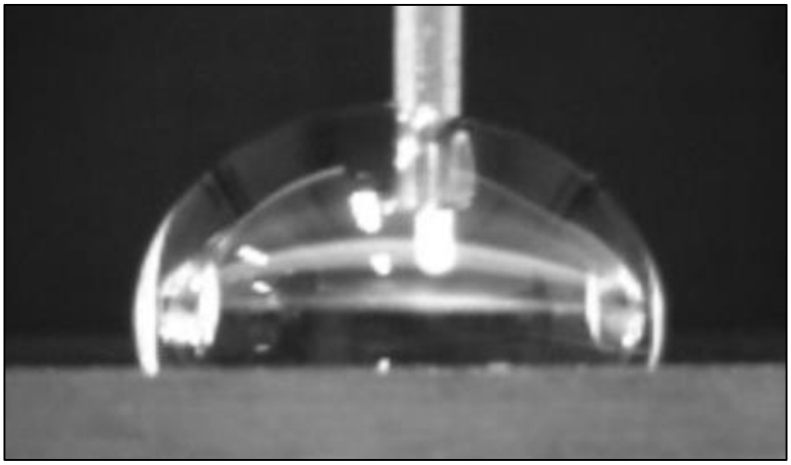

Figure 79. Profile of advancing water droplet on slowly double dip-coated glass for measuring the water contact angle hysteresis

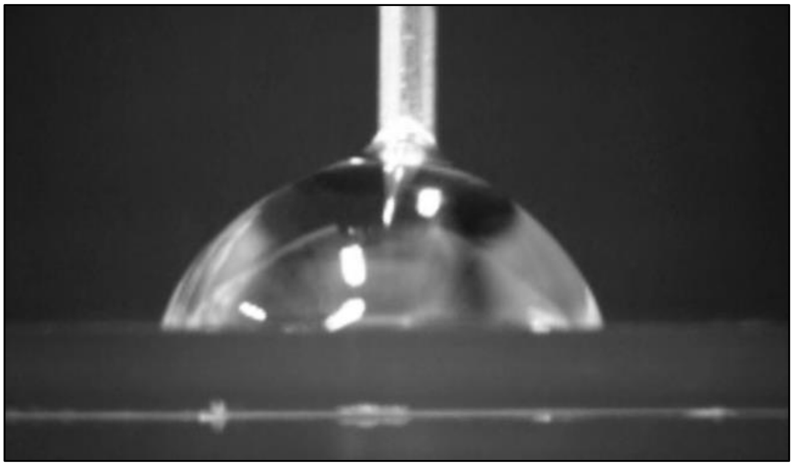

Figure 80. Profile of receding water droplet on slowly double dip-coated glass for measuring the water contact angle hysteresis

Hysteresis (degrees °) (Coating – DP2L - S)			
Trial	**Advancing Angle**	**Receding Angle**	**Hysteresis Angle**
1	105	70	35
2	106	69	37
3	106	70.5	35.5
Average			**35.83**
Std. Dev.			**0.85**

Table 32. Summary of water contact angle hysteresis measurements on slowly double dip-coated glass

Trial	**WCA (degrees °) (Coating – DP2L - MS)**
1	104
2	104.5
3	104.5
Average	**104.33**
Std. Dev.	**0.29**

Table 33. Summary of water contact angle measurements on medium-slow double dip-coated glass

Hysteresis (degrees °) (Coating – DP2L - MS)			
Trial	**Advancing Angle**	**Receding Angle**	**Hysteresis Angle**
1	108	75.5	32.5
2	109.5	74	35.5
3	108	72	36
Average			**34.67**
Std. Dev.			**1.55**

Table 34. Summary of water contact angle hysteresis measurements on medium-slow double dip-coated glass

Trial	**WCA (degrees °) (Coating – DP2L - M)**
1	104.5
2	111
3	108
Average	**107.83**
Std. Dev.	**3.25**

Table 35. Summary of water contact angle measurements on medium double dip-coated glass

Hysteresis (degrees °) (Coating – DP2L - M)			
Trial	**Advancing Angle**	**Receding Angle**	**Hysteresis Angle**
1	103	70.5	32.5
2	103	74	29
3	106	70	36
Average			**32.5**
Std. Dev.			**2.86**

Table 36. Summary of water contact angle hysteresis measurements on medium double dip-coated glass

Trial	WCA (degrees °) (Coating – DP2L - MF)
1	107.5
2	108.5
3	108.5
Average	**108.17**
Std. Dev.	**0.58**

Table 37. Summary of water contact angle measurements on medium-fast double dip-coated glass

Hysteresis (degrees °) (Coating – DP2L - MF)			
Trial	**Advancing Angle**	**Receding Angle**	**Hysteresis Angle**
1	107.5	75.5	32
2	110	77.5	32.5
3	111.5	77.5	34
Average			**32.83**
Std. Dev.			**0.85**

Table 38. Summary of water contact angle hysteresis measurements on medium-fast double dip-coated glass

Trial	**WCA (degrees °) (Coating – DP2L - F)**
1	106
2	107
3	105
Average	**106**
Std. Dev.	**1**

Table 39. Summary of water contact angle measurements on fast double dip-coated glass

Hysteresis (degrees °) (Coating – DP2L - F)			
Trial	**Advancing Angle**	**Receding Angle**	**Hysteresis Angle**
1	104	76	28
2	110	76.5	33.5
3	108.5	77	31.5
Average			**31**
Std. Dev.			**2.27**

Table 40. Summary of water contact angle hysteresis measurements on fast double dip-coated glass

Dip-Coated 2 Layer		
Speed (mm/min)	**WCA (degrees)**	**Hysteresis (degrees)**
5 (S)	109.2	35.8
50 (MS)	104.3	34.7
100 (M)	107.8	32.5
150 (MF)	108.2	32.8
200 (F)	106	31
Average	**107.1**	**33.4**
Std. Dev.	**1.74**	**1.7**

Table 41. Summary of water contact angle and hysteresis measurements on the speed varied double dip-coated glass

The series of coatings created with two layers by varying the speed of dipping have all performed very similarly in regards to wettability. The five coatings deposited at speeds ranging from 5 – 200 mm/min exhibited an average water contact angle of 107.1°, ranging from 104.3° - 109.2° with a standard deviation of only 1.74°. Likewise, the contact angle hysteresis of the coatings were remarkably similar with an average of 33.4°, ranging from 31° - 35.8° with a standard deviation of only 1.7°.

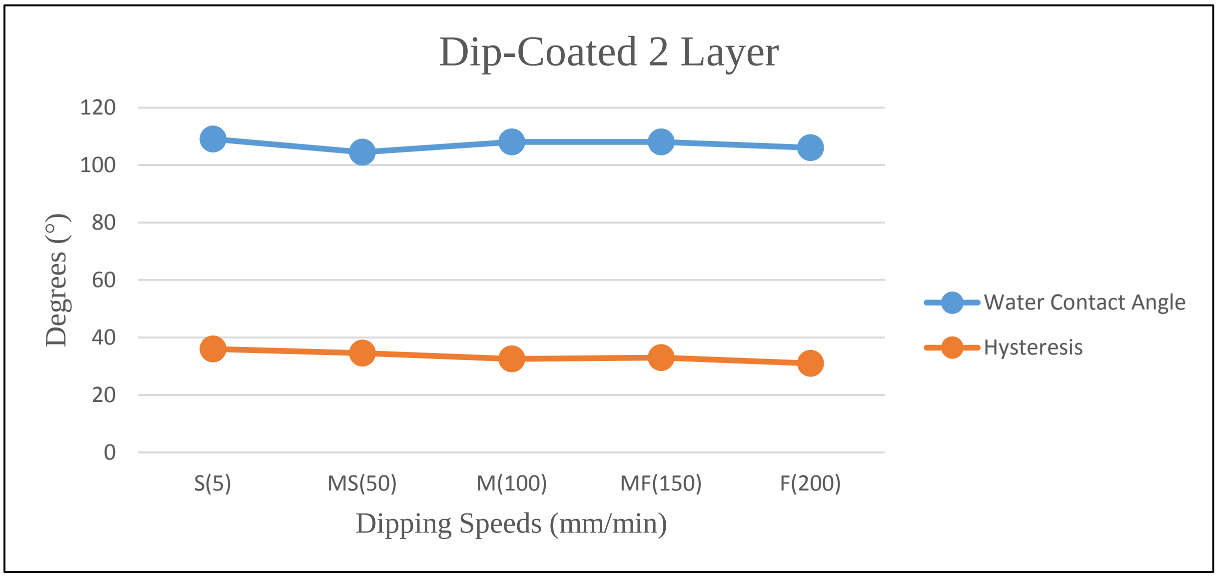

Figure 81. The WCA and Hysteresis plotted against dipping speed for double dipped coatings

Dip-Coated 1 & 2 Layer Comparison		
Sample	**Average WCA (degrees)**	**Average Hysteresis (degrees)**
1 Layer	109	34
2 Layer	107.1	33.4

Table 42. Summary of water contact angle and hysteresis measurements on the speed varied single dip-coated glass

It has been shown previously that the speed of dipping does not have a significant effect on the wettability properties on the dip-coated copolymer coatings of one or two layers. Likewise, the comparison of the average water contact angle and average water contact angle hysteresis of the one and two layer dip-coated copolymer coatings are very similar. The single layer coatings showed an average water contact angle of 109°, while the two layer coating showed an average water contact angle of 107.1°, a difference of only 1.9°. The single layer coating also showed an average contact angle hysteresis of 34°, while the two layer coating showed an average water contact angle hysteresis of 33.4°, a difference of only 0.6°. Furthermore, Figure 82. highlights the uniformity in wettability behavior of the dip-coated copolymer coatings created by varying the dipping speeds and coating layers.

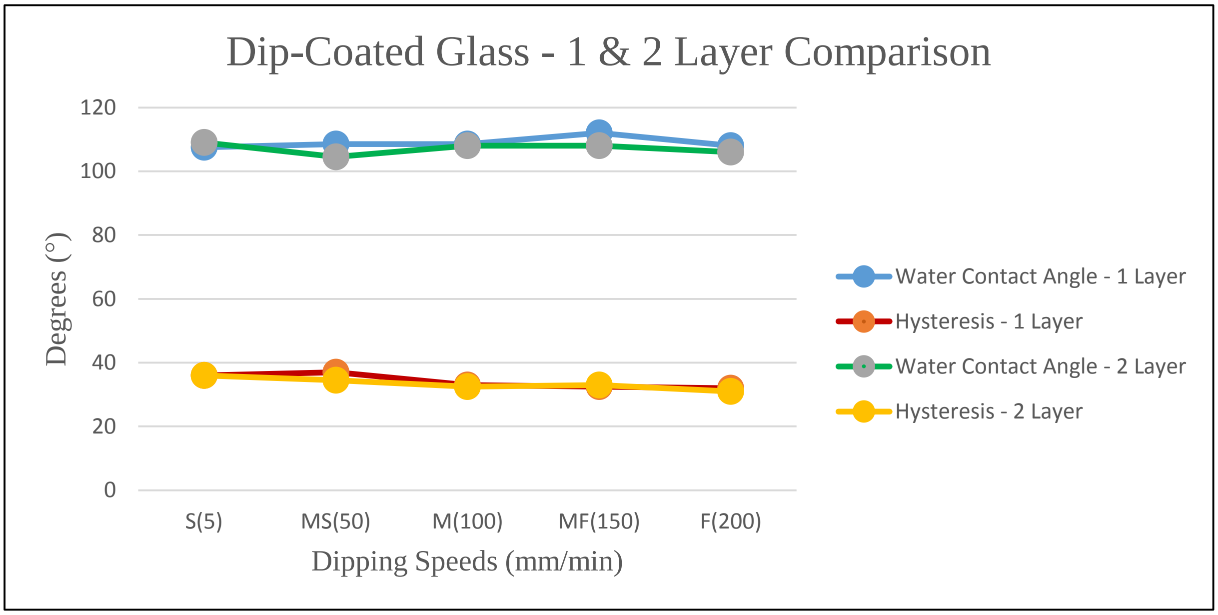

Figure 82. The WCA and Hysteresis plotted against dipping speeds for both single and double layer dipped coatings for comparison

Surface of Dip-Coated Samples:

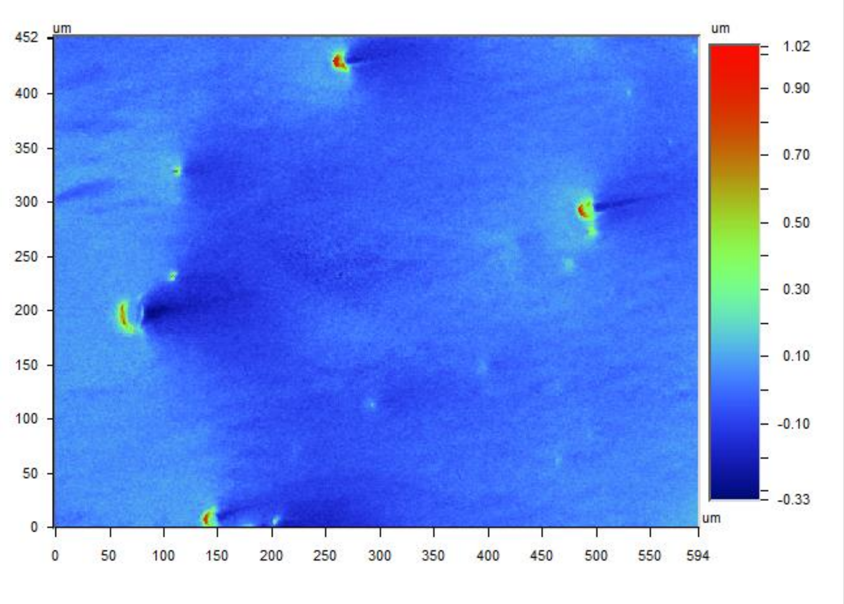

Figure 83. A two-dimensional surface profilometry scan of the surface of the dip-coated glass sample, shown at 10X magnification

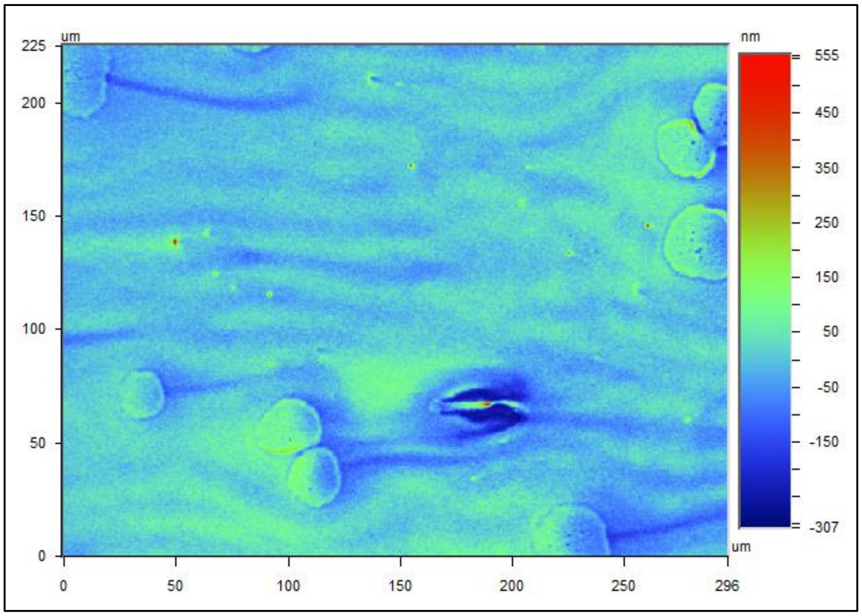

Figure 84. A two-dimensional surface profilometry scan of the surface of the dip-coated glass sample, shown at 20X magnification

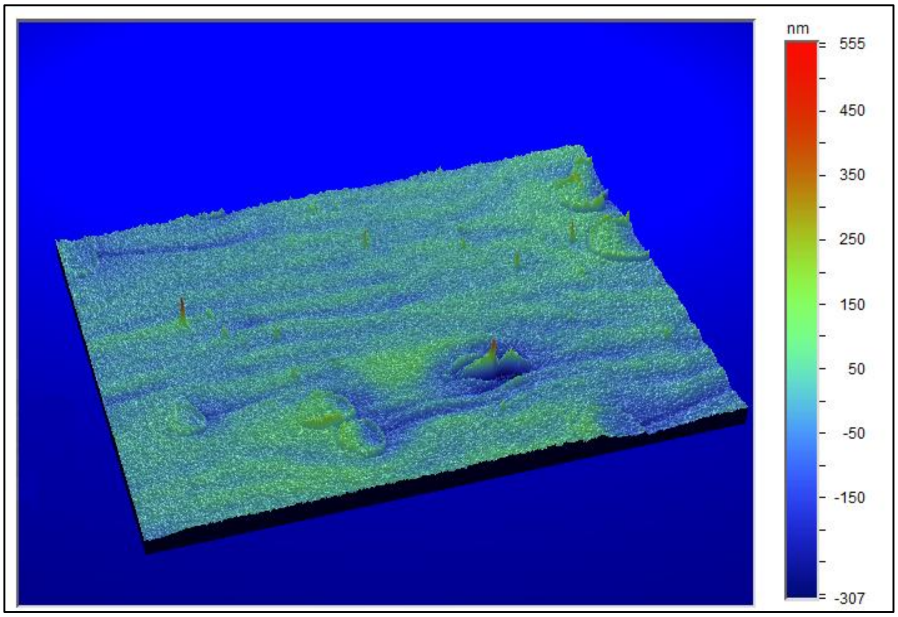

Figure 85. A three-dimensional surface profilometry scan of the surface of the dip-coated glass sample, shown at 20X magnification

Surface profilometry scans of the dip-coated samples (Figures 83. – 85.) reveal uniform topography comprised of a gentle flow morphology with dispersed 'island' features of low roughness. The surface of the dip-coated samples are very smooth with an average roughness of only 31 nm. Similarly, the root-mean-squared roughness calculated over the entire measured array is 43 nm and the average peak-to-valley difference calculated over the entire measured array is 862 nm. The environmental scanning electron microscopy images (Figures 86. & 87.) show the uniformly smooth surface of the dip-coated samples, at 8000X magnification, the 'island' morphology can be seen on the surface, at magnifications up to 30,000X no defined morphology can be distinguished on the surface.

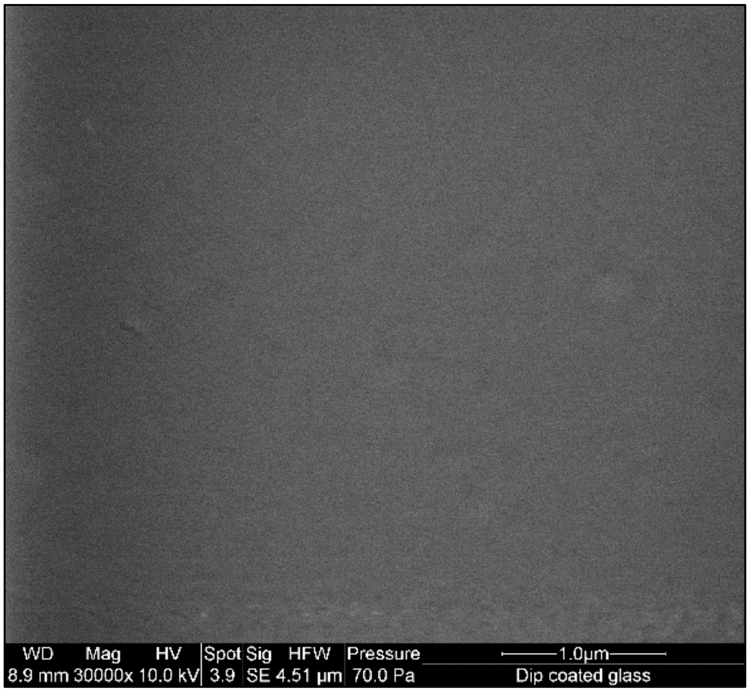

Figure 86. An ESEM image of the surface of the dip-coated glass sample, the surface appears nearly featureless even at 30,000X magnification

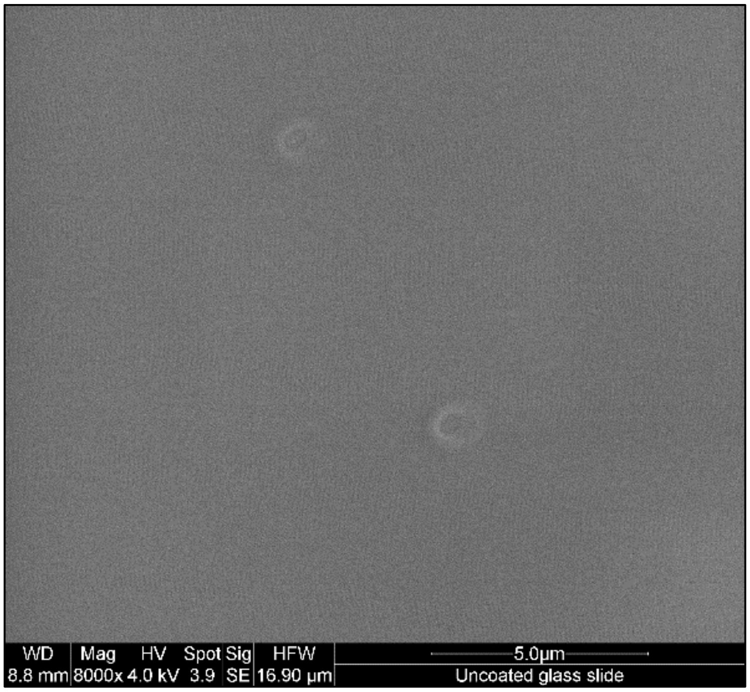

Figure 87. An ESEM image of the surface of the dip-coated glass sample, the surface exhibits small ‘island’ morphology at 8000X magnification

Rough Sprayed Coating

It is necessary to test both smooth and rough hydrophobic coatings because despite the rough surface of a superhydrophobic coating, it will reduce the adhesion of ice more than a smooth hydrophobic surface of the same chemical composition, and superhydrophobic coatings exhibiting a contact angle hysteresis lower than 5° lead to very high icephobic properties (18) (20) (21). However, the durability and mechanical robustness of the coating are particularly important to consider because the fragile hierarchical roughness can be irreversibly destroyed, which will inevitably lead to an increase in the contact angle hysteresis and a rapid decrease in the static contact angle (22). Rough superhydrophobic coatings offer attractive drastic ice adhesion reductions but come at the price of durability, whereas, the smooth hydrophobic coatings do not provide as much ice reduction but can provide a much more durable and transparent coating. Both must be tested in order to make an informed choice on which will be best coupled with ultrasonic transducers to remove the ice.

The design requirements of the rough hydrophobic coating are likewise to achieve full and complete coverage of the glass surface with no exposure of the glass. Unlike its smooth counterpart, the rough coating requires roughness not on one but two scales. Hierarchical roughness composed of micro- peaks and valleys, and nano- peaks and valleys are required for the ice adhesion reducing properties sought after. Cao et al. (23) demonstrated that the probability of icing occurring on the coating increased remarkably when the nano-scale roughness is greater than 50nm when the micro-scale roughness is 10µm. This indicates that the rough coating should also conform to nano-scale roughness of less than 50nm to achieve best ice adhesion reducing properties from the coating. It will require wettability properties that exhibit a high water contact angle indicating low surface energy and a very low water contact angle which indicates low adhesion of water to the coating. Finally, it also requires good adhesion to the glass substrate and the durability to endure multiple violent ice shedding events without losing the critical roughness parameters that impart its properties.

Two variables pertaining to the spray coating of the copolymer coating onto glass slides are the number of layers applied and the size of the nozzle used for spraying the coating solution. The Earlex HV5000 pressure sprayer has the ability to interchange the size of the spray nozzle between 1mm and 2mm. The size of the nozzle is an important factor to investigate as it dictates the size of the coating particles that are propelled towards the surface of the glass microscope slide. The size of the these coating projectiles will determine the rate at which they dry passing through the air and their subsequent dynamics with the glass surface, creating either the desired topography for superhydrophobicity and icephobicity, or an underachieving hydrophobic coating with poor icing properties. The number of passes with the pressure sprayer is another factor that must be considered, complete coverage of the surface is required in the design of a superhydrophobic coating with icephobic properties, however, the greater the number of passes used to create the coating the thicker the coating becomes and scatters more light leading to lower transmission in the visible light range. As Table 43. highlights, three variations have been used in the number of passes used in depositing the spray coating. First is lightly coated with only two full passes, the next is medium coated with four full passes, and finally the third is heavily coated with six full passes. Spray coated samples varying between two, four, and six passes with a 2mm and 1mm nozzle have been prepared and the wettability, morphological, and icing properties will be investigated by measuring the static water contact angles, contact angle hysteresis, surface profilometry, environmental scanning electron microscopy, and the ice adhesion.

Spray-Coated Variants (No. of Passes)		
Light (L)	Medium (M)	Heavy (H)
2 passes	4 passes	6 passes

Table 43. The number of passes tested during spray coating

Spray-Coated with 2mm nozzle:

Light (2mm)

To create a rough hydrophobic coating, 1g of coating solution was added to 200g of acetone (solvent) in a 50mL beaker to form a 0.5% copolymer solution by weight. The beaker is placed in an ultrasonic bath for 8 minutes ensuring thorough mixing of the coating solution into the acetone. The solution is then added to the canister of an airbrush (Earlex HV5000). Pre-cleaned glass microscope slides are fastened to a disposable recyclable backdrop (cardboard) for spray coating. The solution was sprayed toward the glass slide from a distance of 10cm or 20cm with 2, 4, or 6 passes at 2psi. The first combination of variables investigated for the spray coating was using the 2mm nozzle lightly coated at 2 passes.

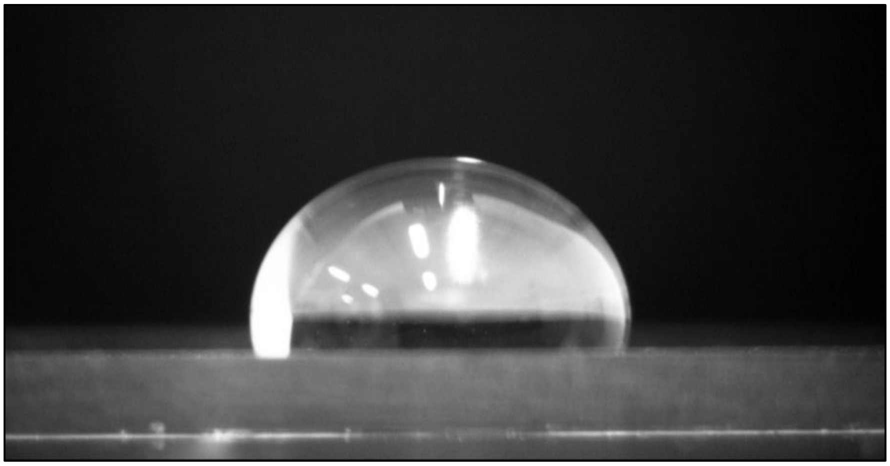

Figure 88. Profile of water droplet on lightly spray-coated glass with 2mm nozzle for measuring the water contact angle

Trial	**WCA (degrees °) (Coating – SPC - L)**
1	109
2	108.5
3	110
Average	**109.17**
Std. Dev.	**0.76**

Table 44. Summary of water contact angle measurements on lightly spray-coated glass with 2mm nozzle

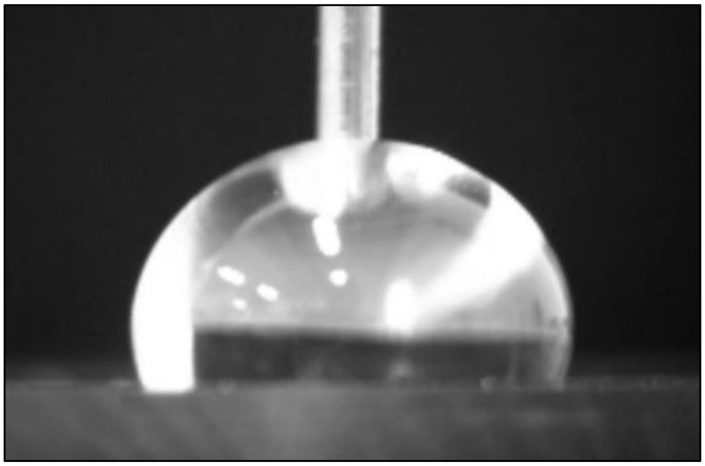

Figure 89. Profile of advancing water droplet on lightly spray-coated glass with 2mm nozzle for measuring the water contact angle hysteresis

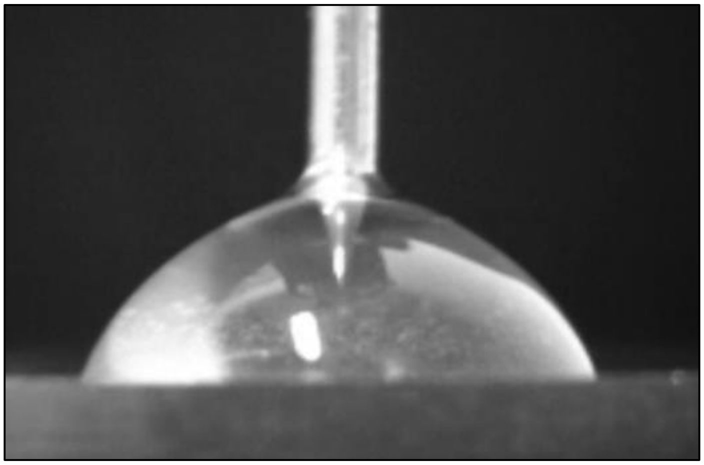

Figure 90. Profile of receding water droplet on lightly spray-coated glass with 2mm nozzle for measuring the water contact angle hysteresis

Hysteresis (degrees °) (Coating – SPC - L)			
Trial	**Advancing Angle**	**Receding Angle**	**Hysteresis Angle**
1	109.5	69.5	40
2	110	71	39
3	111.5	67.5	44
Average			**41**
Std. Dev.			**2.16**

Table 45. Summary of water contact angle hysteresis measurements on lightly spray-coated glass with 2mm nozzle

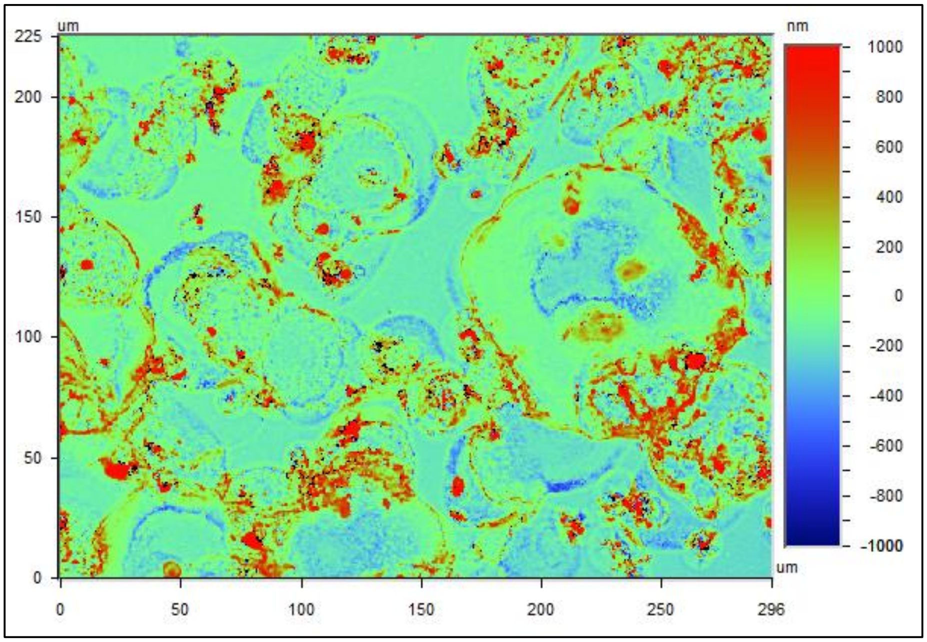

Figure 91. A two-dimensional surface profilometry scan of the surface of the lightly spray-coated glass with 2mm nozzle sample, shown at 10X magnification

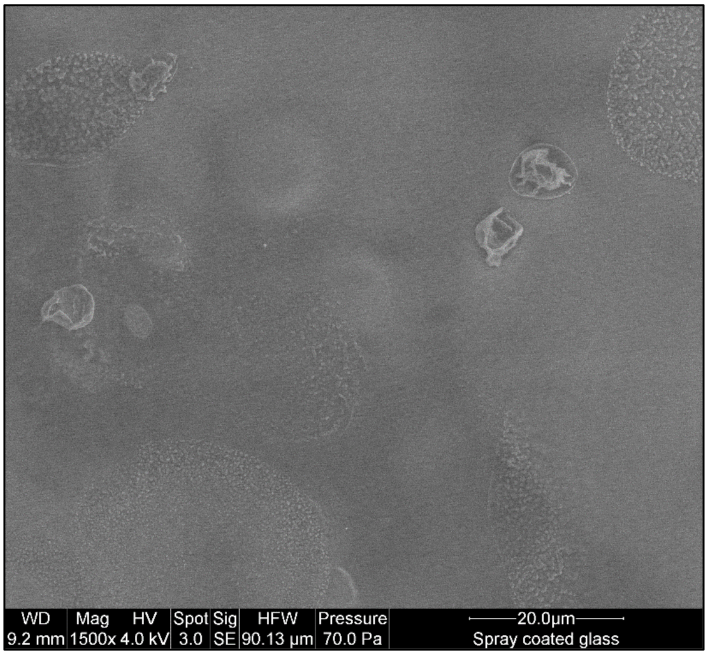

Figure 92. An ESEM image of the surface of the lightly spray-coated glass with 2mm nozzle sample at 1500X magnification

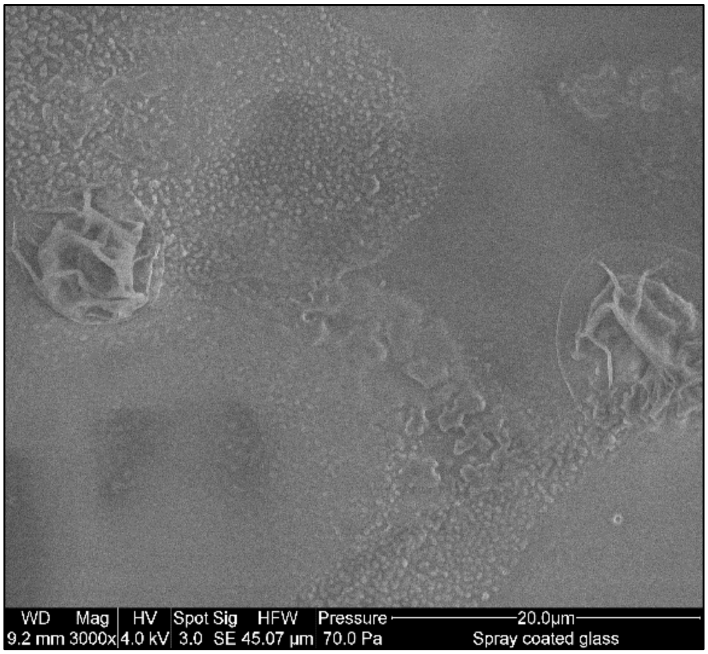

Figure 93. An ESEM image of the surface of the lightly spray-coated glass with 2mm nozzle sample at 3000X magnification

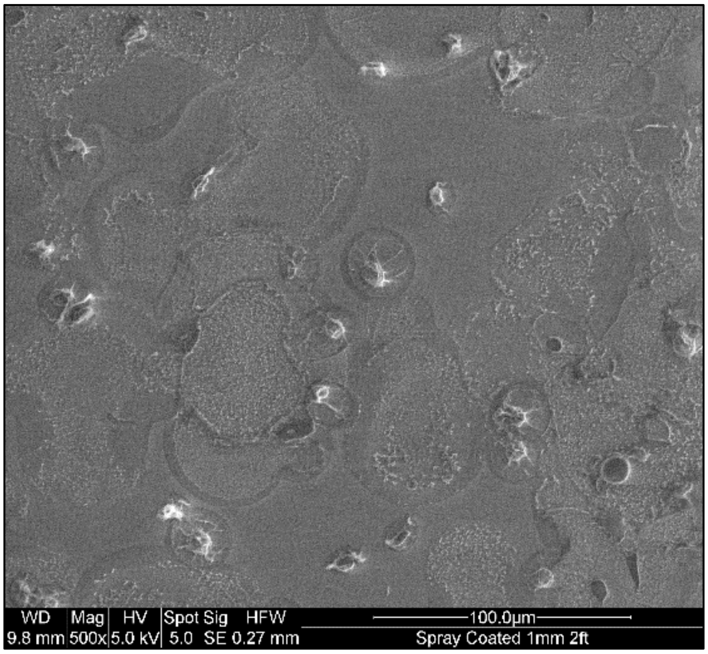

Figure 94. An ESEM image of the surface of the lightly spray-coated glass with 2mm nozzle sample at 500X magnification

The average water contact angle of the lightly sprayed coating with a 2mm nozzle was measured at 109.2° over three trials with a standard deviation of only 0.76° and the average water contact angle hysteresis was measured at 41° over three trials with a standard deviation of 2.2°. The optical image of the sample shows that the coating is visibly smooth and transparent with only a slight haze with inspection. The surface profilometry scans of the coating reveal that the surface of the slide is not completely coated, there are small areas of exposed glass throughout the sample surface. Surface profilometry scans of the spray coated samples (Figure 91.) reveal rough and sporadic topography comprised of large splats of coating overlaid on top of each other with some bare spots. The surface of the lightly spray coated samples are rough with an average roughness of 203 nm. Similarly, the root-mean-squared roughness calculated over the entire measured array is 322 nm and the average peak-to-valley difference calculated over the entire measured array is 41.5 µm. At 500X magnification using environmental scanning electron microscopy two types of coating solution splats are visible on the surface. The first type of splat exhibits the appearance of relatively large droplets of approximately 10 µm in diameter that formed a dried layer on its outside and subsequently evaporated and shriveled on the surface. The second type of splat is larger, being 20 – 30 µm in diameter, and shows uniform fine roughness within the boundaries of the splat.

Medium (2mm)

Trial	**WCA (degrees °) (Coating – SPC - M)**
1	106.5
2	111

3	103.5
Average	**107**
Std. Dev.	**3.78**

Table 46. Summary of water contact angle measurements on medium spray-coated glass with 2mm nozzle

Hysteresis (degrees °) (Coating – SPC - M)			
Trial	**Advancing Angle**	**Receding Angle**	**Hysteresis Angle**
1	107	70.5	36.5
2	109.5	71	38.5
3	109	72	37
Average			**37.33**
Std. Dev.			**0.85**

Table 47. Summary of water contact angle hysteresis measurements on medium spray-coated glass with 2mm nozzle

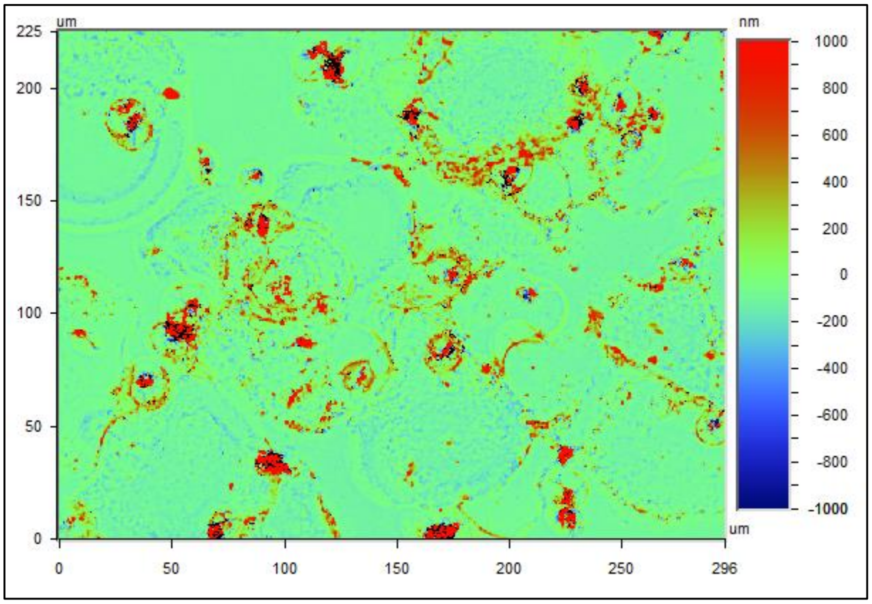

Figure 95. A two-dimensional surface profilometry scan of the surface of the medium spray-coated glass with 2mm nozzle sample, shown at 20X magnification

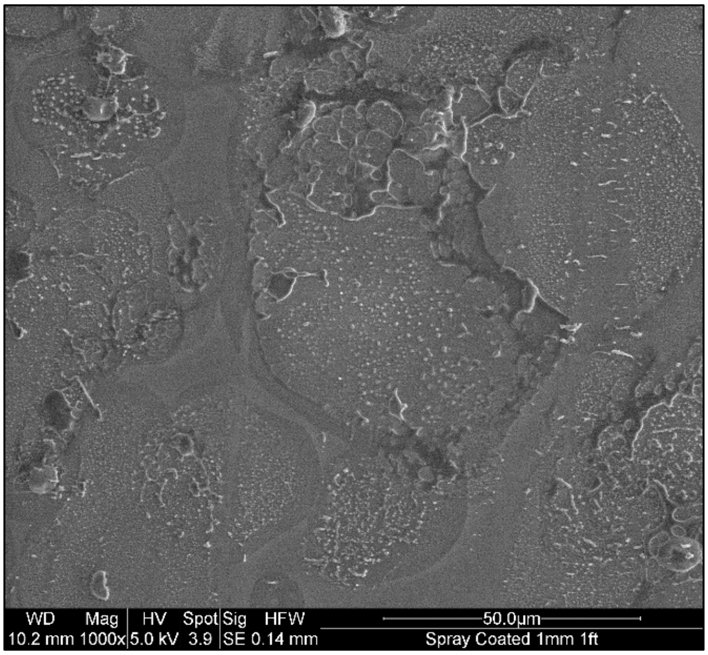

Figure 96. An ESEM image of the surface of the medium spray-coated glass with 2mm nozzle sample at 1000X magnification

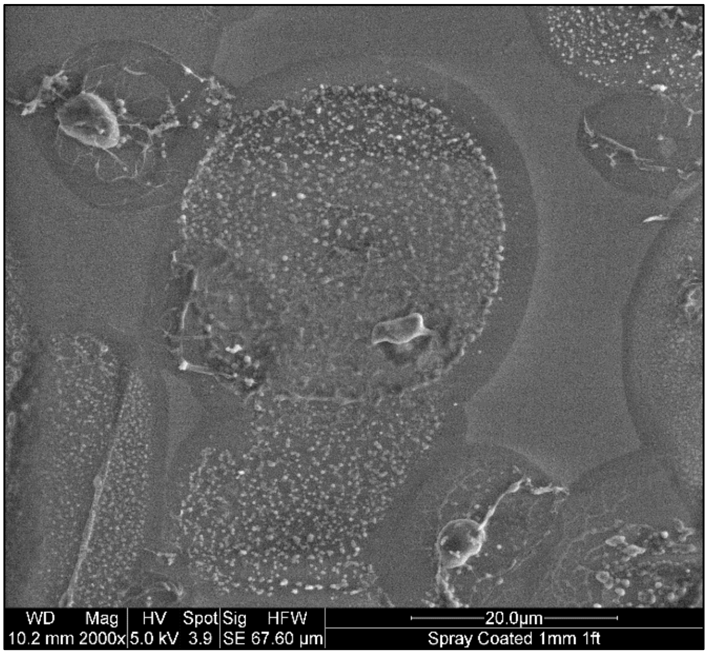

Figure 97. An ESEM image of the surface of the medium spray-coated glass with 2mm nozzle sample at 2000X magnification

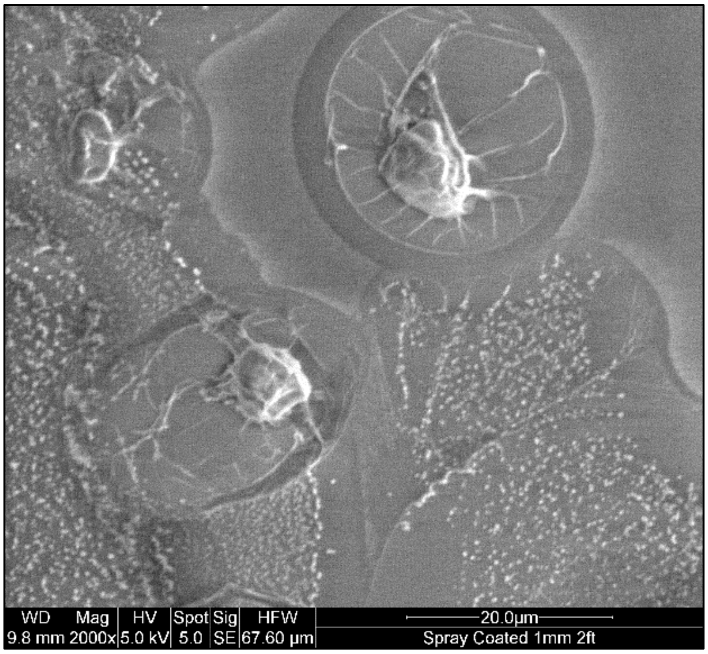

Figure 98. An ESEM image of the surface of the medium spray-coated glass with 2mm nozzle sample at 2000X magnification

The average water contact angle of the medium sprayed coating with a 2mm nozzle was measured at 107° over three trials with a standard deviation of only 3.78° and the average water contact angle hysteresis was measured at 37.3° over three trials with a standard deviation of 0.85°. The coating is visibly smooth and transparent with only a slight haze with inspection. The surface profilometry scans of the coating reveal that the surface of the slide is not completely coated, there are very small areas of exposed glass that appear rarely throughout the sample surface. Surface profilometry scans of the spray coated samples (Figure 95.) reveal rough and sporadic topography comprised of large splats of coating overlaid on top of each other with some rare bare spots. The surface of the medium spray coated samples are rough with an average roughness of 155 nm. Similarly, the root-mean-squared roughness calculated over the entire measured array is 473 nm and the average peak-to-valley difference calculated over the entire measured array is 45 µm. At 2000X magnification using environmental scanning electron microscopy two types of coating solution splats are visible on the surface. The first type of splat exhibits the appearance of relatively large droplets of approximately 10 µm in diameter that formed a dried layer on its outside and subsequently evaporated and shriveled on the surface, it appears less often and less formed in the medium sprayed than the lightly sprayed. The second type of splat is larger, being 20 – 30 µm in diameter, and shows uniform fine roughness within the boundaries of the splat.

Heavy (2mm)

Trial	**WCA (degrees °) (Coating – SPC - H)**
1	108
2	104.5
3	109.5
Average	**107.33**
Std. Dev.	**2.57**

Table 48. Summary of water contact angle measurements on heavily spray-coated glass with 2mm nozzle

Hysteresis (degrees °) (Coating – SPC - H)			
Trial	**Advancing Angle**	**Receding Angle**	**Hysteresis Angle**
1	108	63	45
2	114	69.5	44.5
3	111.5	69	42.5
Average			**44**
Std. Dev.			**1.08**

Table 49. Summary of water contact angle hysteresis measurements on heavily spray-coated glass with 2mm nozzle

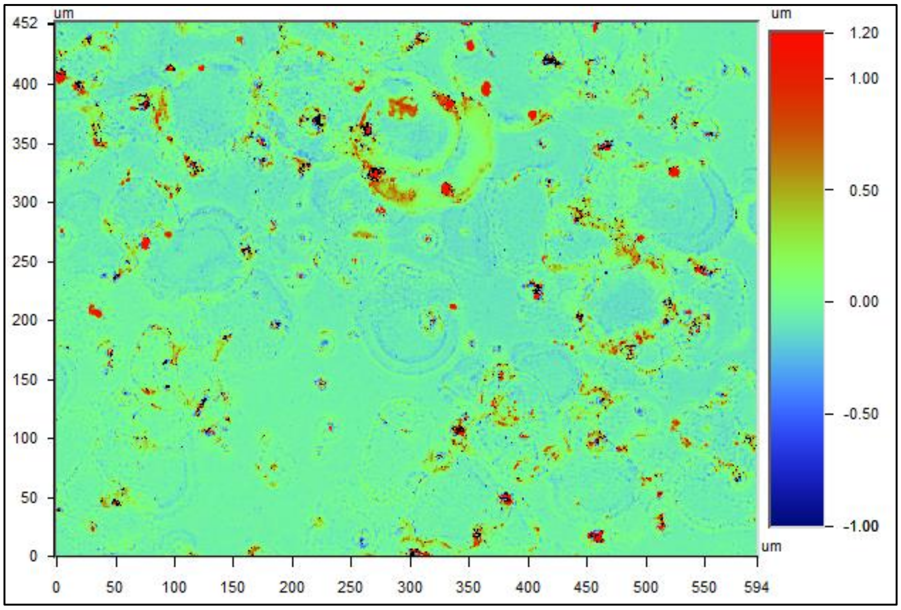

Figure 99. A two-dimensional surface profilometry scan of the surface of the heavily spray-coated glass with 2mm nozzle sample, shown at 10X magnification

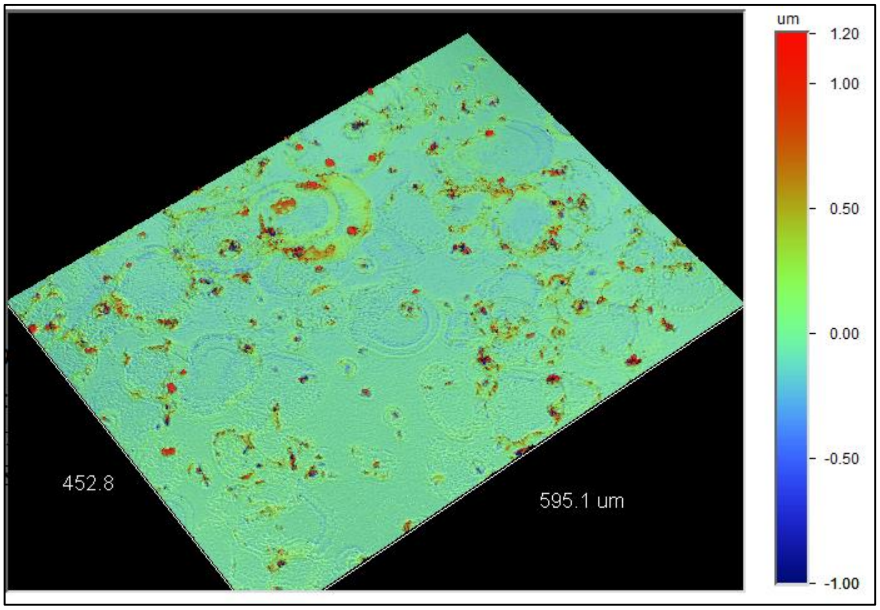

Figure 100. A three-dimensional surface profilometry scan of the surface of the heavily spray-coated glass with 2mm nozzle sample, shown at 10X magnification

Figure 101. An ESEM image of the surface of the heavily spray-coated glass with 2mm nozzle sample at 4000X magnification

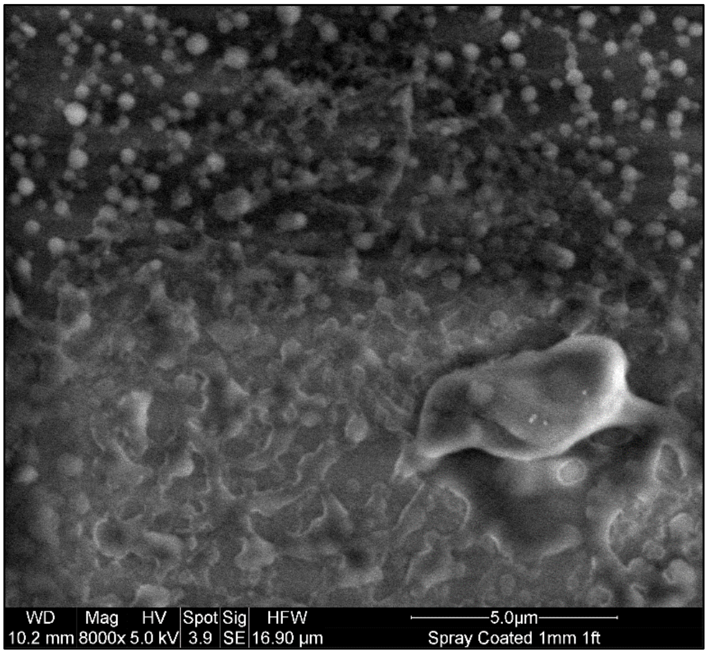

Figure 102. An ESEM image of the surface of the heavily spray-coated glass with 2mm nozzle sample at 8000X magnification

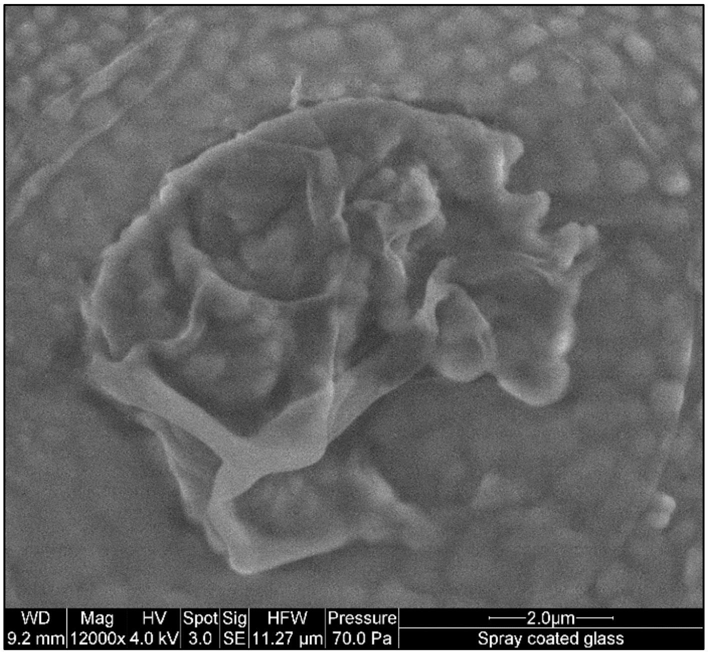

Figure 103. An ESEM image of the surface of the heavily spray-coated glass with 2mm nozzle sample at 12000X magnification

The average water contact angle of the heavily sprayed coating with a 2mm nozzle was measured at 107.3° over three trials with a standard deviation of only 2.57° and the average water contact angle hysteresis was measured at 44° over three trials with a standard deviation of 1.08°. The optical image of the sample shows that the coating is visibly smooth and transparent with only a slight haze with inspection, slightly more than the lightly or medium sprayed coating. The surface profilometry scans of the coating reveal that the surface of the slide is completely coated, there are no areas of exposed glass that appear throughout the sample surface. Surface profilometry scans of the spray coated samples (Figures 99 & 100.) reveal very rough and sporadic topography comprised of large splats of coating overlaid on top of each other with some no bare spots. The surface of the heavily spray coated samples are rough with an average roughness of 137 nm. Similarly, the root-mean-squared roughness calculated over the entire measured array is 217 nm and the average peak-to-valley difference calculated over the entire measured array is 5.5 µm. At 12,000X magnification using environmental scanning electron microscopy two types of coating solution splats are visible on the surface. The first type of splat exhibits the appearance of relatively large droplets of approximately 5 -10 µm in diameter that formed a dried layer on its outside and subsequently evaporated and shriveled on the surface, it appears less often and less formed in the heavily sprayed than the lightly or medium sprayed. The second type of splat is larger, being 20 – 30 µm in diameter, and shows uniform fine roughness within the boundaries of the splat and appears most uniformly and often in the heavily sprayed coating.

Spray-Coated with 1mm nozzle:

Light (1mm)

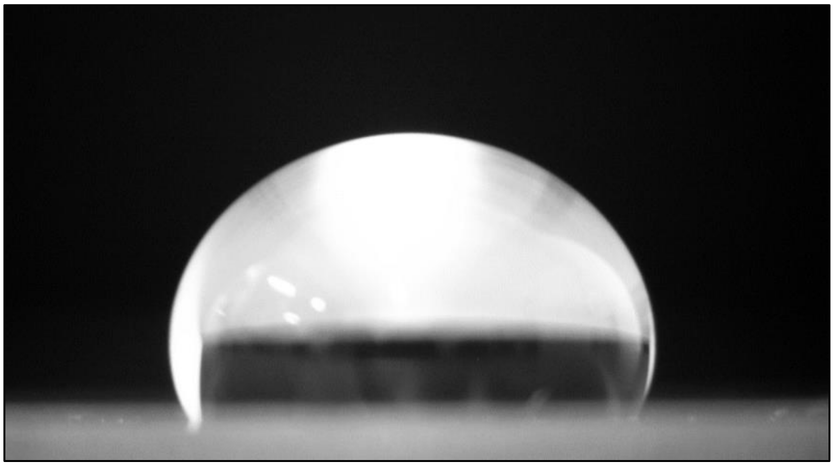

Figure 104. Profile of water droplet on lightly spray-coated glass with 1mm nozzle for measuring the water contact angle

Trial	**WCA (degrees °) (Coating – SPC – 1 - L)**
1	117
2	114
3	124
Average	**118.33**
Std. Dev.	**5.13**

Table 50. Summary of water contact angle measurements on lightly spray-coated glass with 1mm nozzle

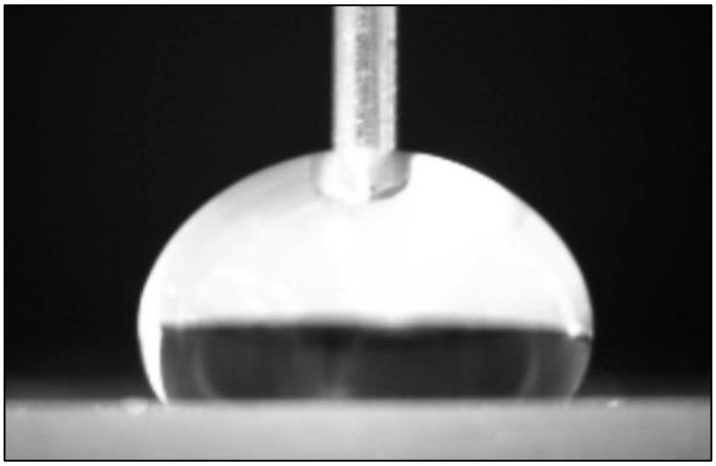

Figure 105. Profile of advancing water droplet on lightly spray-coated glass with 1mm nozzle for measuring the water contact angle hysteresis

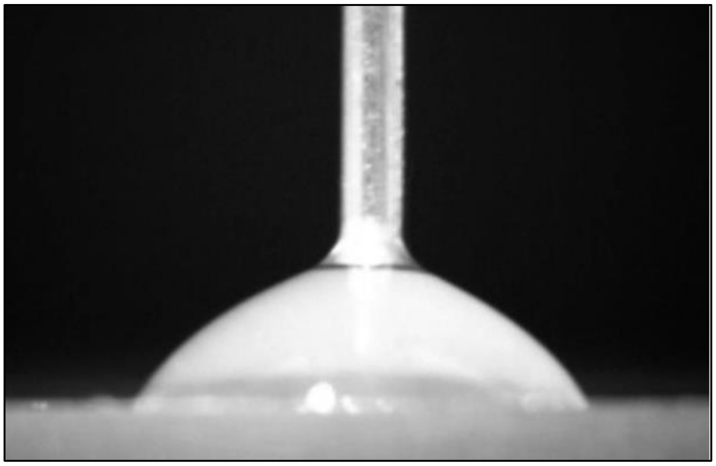

Figure 106. Profile of receding water droplet on lightly spray-coated glass with 1mm nozzle for measuring the water contact angle hysteresis

Hysteresis (degrees °) (Coating – SPC – 1 - L)			
Trial	**Advancing Angle**	**Receding Angle**	**Hysteresis Angle**
1	118.5	62	56.5
2	126	54	72
3	120.5	53.5	67
Average			**65.17**
Std. Dev.			**6.46**

Table 51. Summary of water contact angle hysteresis measurements on lightly spray-coated glass with 1mm nozzle

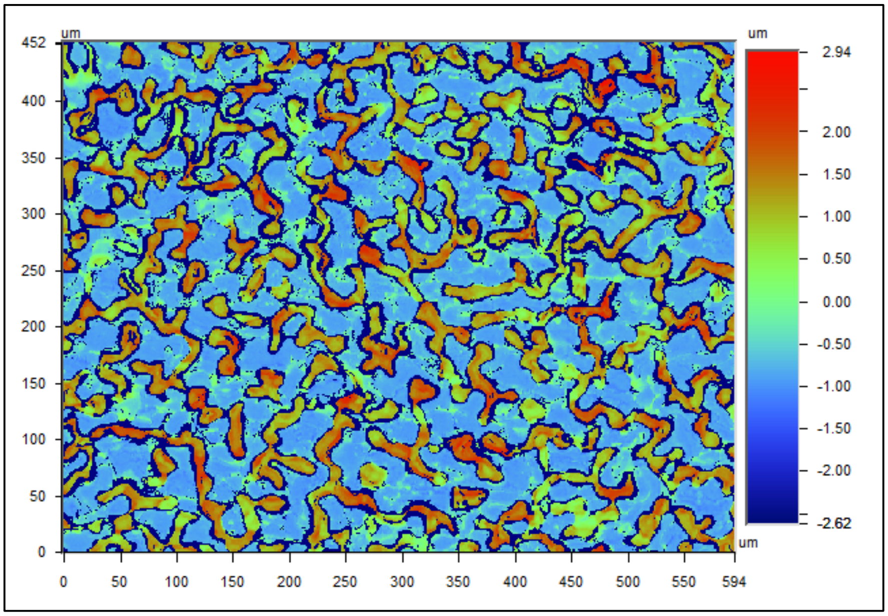

Figure 107. A two-dimensional surface profilometry scan of the surface of the lightly spray-coated glass with 1mm nozzle sample, shown at 10X magnification

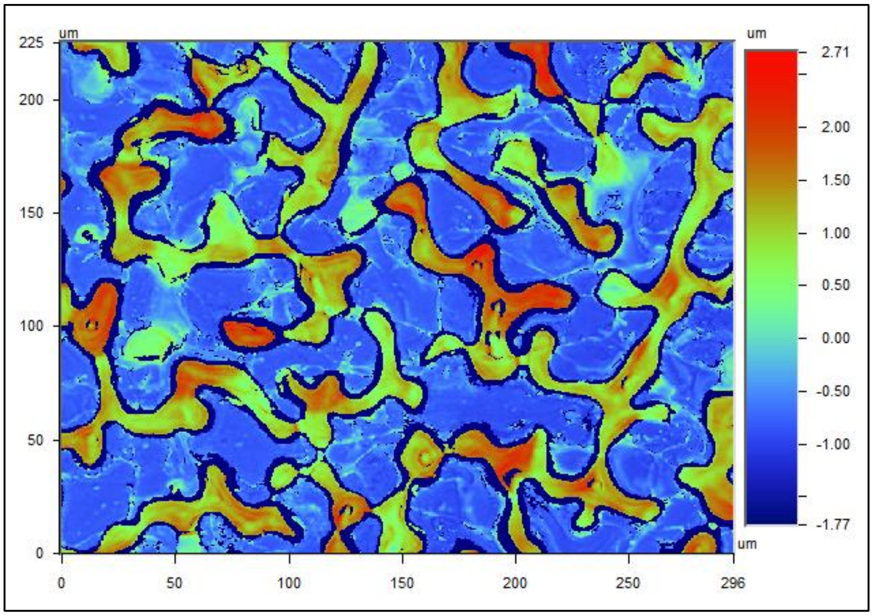

Figure 108. A two-dimensional surface profilometry scan of the surface of the lightly spray-coated glass with 1mm nozzle sample, shown at 20X magnification

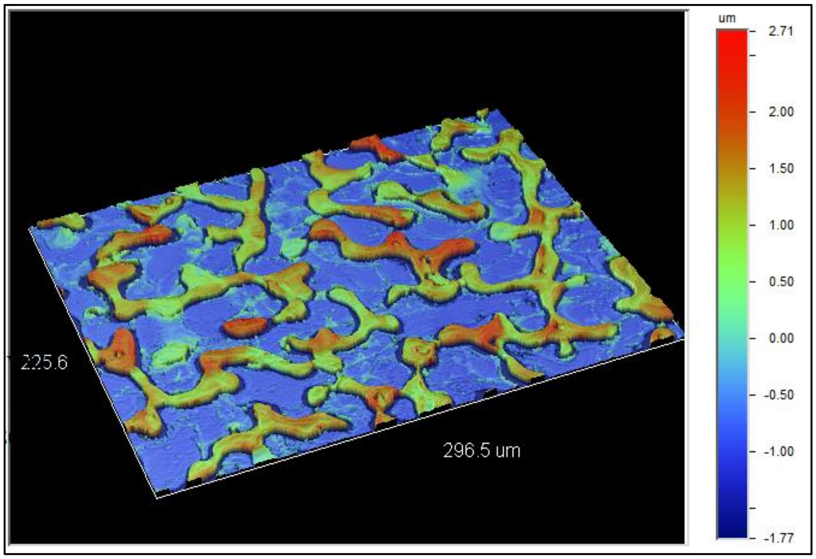

Figure 109. A three-dimensional surface profilometry scan of the surface of the lightly spray-coated glass with 1mm nozzle sample, shown at 20X magnification

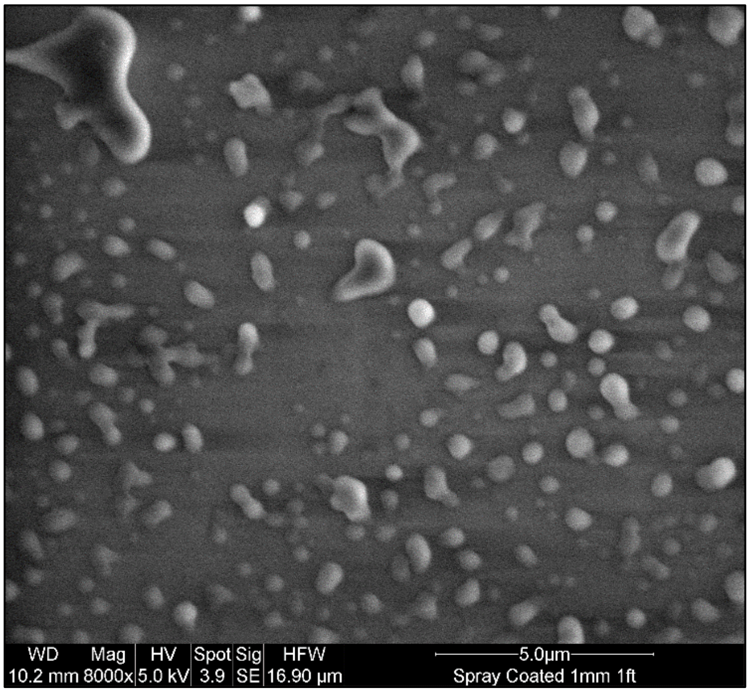

Figure 110. An ESEM image of the surface of the lightly spray-coated glass with 1mm nozzle sample at 8000X magnification

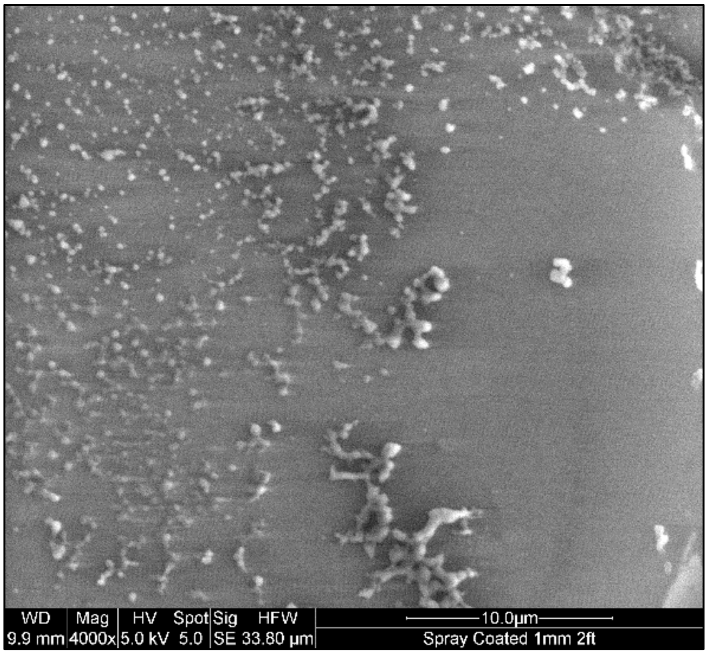

Figure 111. An ESEM image of the surface of the lightly spray-coated glass with 1mm nozzle sample at 4000X magnification

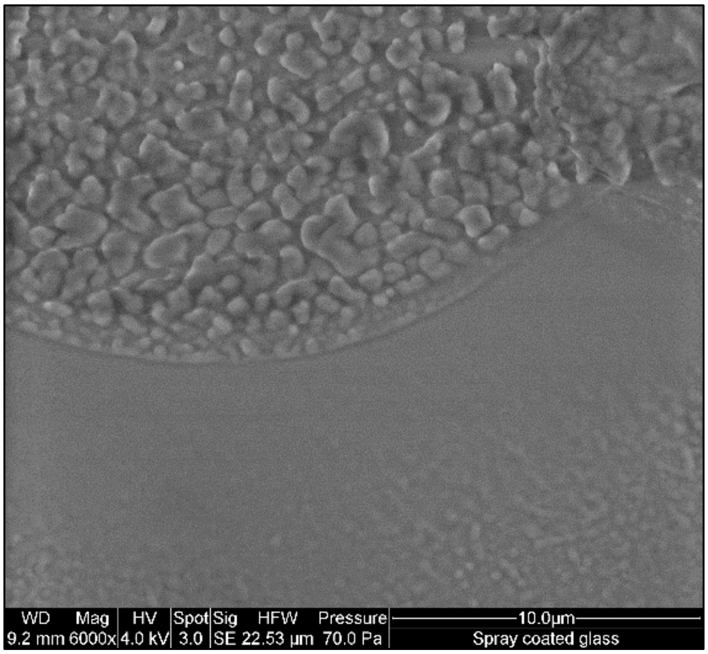

Figure 112. An ESEM image of the surface of the lightly spray-coated glass with 1mm nozzle sample at 6000X

The average water contact angle of the lightly sprayed coating with a 1mm nozzle was measured at 118.3° over three trials with a standard deviation of only 5.13° and the average water contact angle hysteresis was measured at 65.2° over three trials with a standard deviation of 6.5°. The optical image of the sample shows that the coating is visibly smooth and transparent with only a slight haze with inspection. The surface profilometry scans of the coating reveal that the surface of the slide is not completely coated, there are very small areas of exposed glass that appear rarely throughout the sample surface. Surface profilometry scans of the spray coated samples (Figures 108 & 109.) reveal rough and relatively uniform topography comprised of large splats comprised of small globular roughness with some rare bare spots. The surface of the lightly spray coated samples are very rough with an average roughness of 900 nm. Similarly, the root-mean-squared roughness calculated over the entire measured array is 990 nm and the average peak-to-valley difference calculated over the entire measured array is 5.5 µm. At 6000X magnification using environmental scanning electron microscopy mainly one types of coating solution splat is visible on the surface. The type of splat that is visible is larger, being 20 – 30 µm in diameter, and shows uniform fine globular roughness within the boundaries of the splat.

Spray Coating Summary		
Sample	**WCA (degrees)**	**Hysteresis (degrees)**
SPC – L (2mm nozzle)	109.2	41
SPC – M (2mm nozzle)	107	37.3
SPC – H (2mm nozzle)	107.3	44
Average	107.8	40.8
Std. Dev.	0.97	2.74
SPC – L (1mm nozzle)	118.3	65.2

Table 52. Summary of water contact angle and hysteresis measurements on the variety of spray-coated glass

The comparison drawn in Table 52 and Figure 113. shows that when using the 2mm nozzle, using 2, 4, or 6 passes will not significantly affect the static water contact angle, with a deviation of less 1°, or the contact angle hysteresis, with a deviation of only 2.74°. The lightly sprayed coating of 2 passes with a 1mm nozzle showed an increase in static water contact angle over the 2mm nozzle, being 118.3°. The water contact angle hysteresis, however, has increased significantly using the 1mm nozzle, being 65.2°.

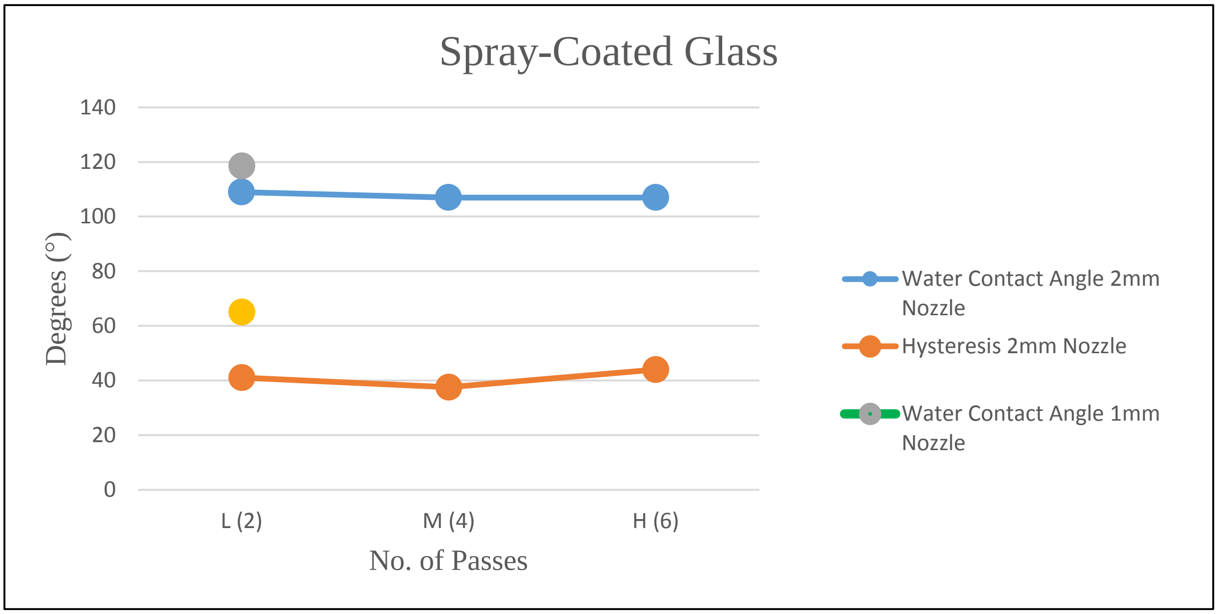

Figure 113. The WCA and Hysteresis plotted against the number of passes for both 2mm and 1mm nozzle sprayed coatings for comparison

Ice Adhesion

The adhesion of ice to a substrate is measured by freezing a known surface area of water into ice on the substrate. Next, a force is applied strictly to the ice in strictly a shearing motion along the ice/substrate interface. The force can be applied by means of actuators and centrifuges, in either event, the shear force applied to the ice can be calculated or measured directly with a load cell. Having the shear force that was sufficient to break the bonds of the ice to the substrate, and knowing the area of ice frozen to the substrate, the ice adhesion can be calculated by dividing the shear force by the area. The ice adhesion can be measured for different materials, such as glass, metals, and polymers by substituting the substrate surface with the desired material to be studies. The ice adhesion of different roughnesses can be measured by substituting the substrate surface with a surface that has undergone surface preparation of varying magnitudes. Lastly, the ice adhesion under ultrasonic vibration can be calculated by introducing ultrasonic transducers to the testing procedure to input ultrasonic vibration. The orientation of the ultrasonic input can be adjusted by adjusting the positioning of the transducers, and the power and frequency can be adjusted by substituting different sizes of transducers.

Ice Adhesion Calculation

To calculate the ice adhesion in kPa from the resistance load data measured using the IAC. Knowing that the inside diameter of the polycarbonate cylinder used as a mold for the water to freeze was 0.75 inches or 0.01905 meters, the area of ice frozen to the sample is equal to the surface area inside the polycarbonate cylinder, or $A = \frac{1}{4}\pi d^2$, where d = 0.01905m. Furthermore, the max resistance load can be converted from kg to N by multiplying by a factor of 9.80665. This allows the ice adhesion to be calculated as the shear stress experienced by the ice/substrate interface which is simply the max load (N) divided by the area of frozen ice (m^2).

Effect of thermal gradients on ice adhesion repeatability

The IAC can also be used to investigate the influence of ice/substrate/apparatus thermal gradients on the standard deviation of ice adhesion tests. Three possible combinations exist for the thermal starting points of the sample substrate and the distilled water to be frozen: 1) the experiment can be run using a sample substrate at -20°C and STP water, 2) The experiment can be run using a sample substrate at -20°C and icy water at ~1-3°C, 3) the experiment can be run using a sample substrate and water at STP. The significance of these experimental scenarios is that each will affect the ice/substrate interface differently due to the differing rates at which the heat is removed from the water to be frozen, and the sample substrate because of the difference in thermal gradient. Since it is not the aim of this study to accurately determine the effect of thermal heat transfer rates on the nucleation of ice and structure of ice, this thermal investigation will be limited to the effect it has on the standard deviation and repeatability of the IAC.

Frozen Sample & Ice Water – Ice Adhesion

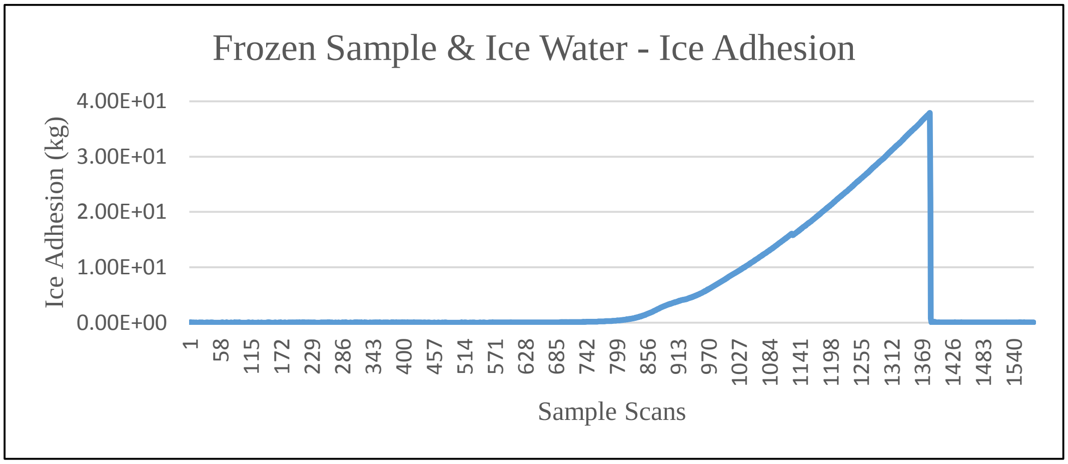

Figure 114. Graph of the resistance load due to ice adhesion vs. sample scans at a rate of 1/ 0.01405s. Max load = 37.9 kg

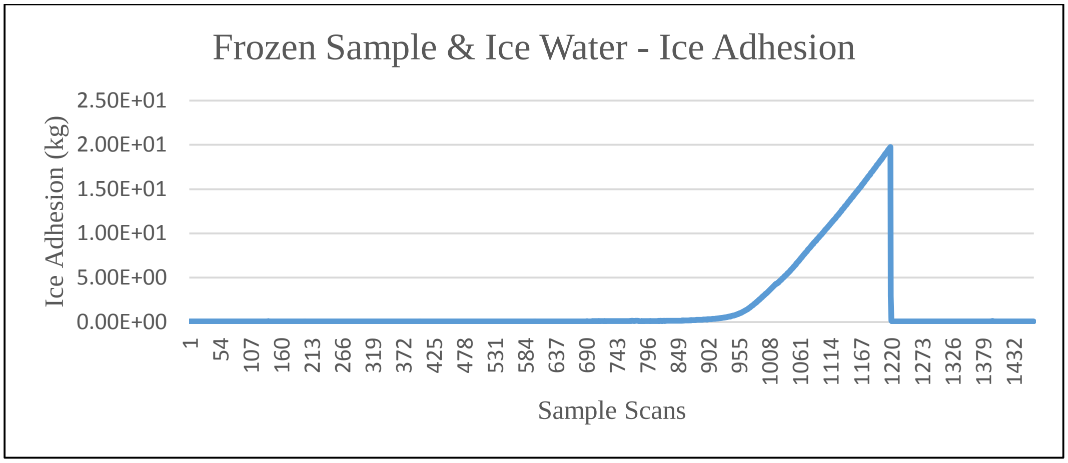

Figure 115. Graph of the resistance load due to ice adhesion vs. sample scans at a rate of 1/ 0.01405s. Max load = 19.8 kg

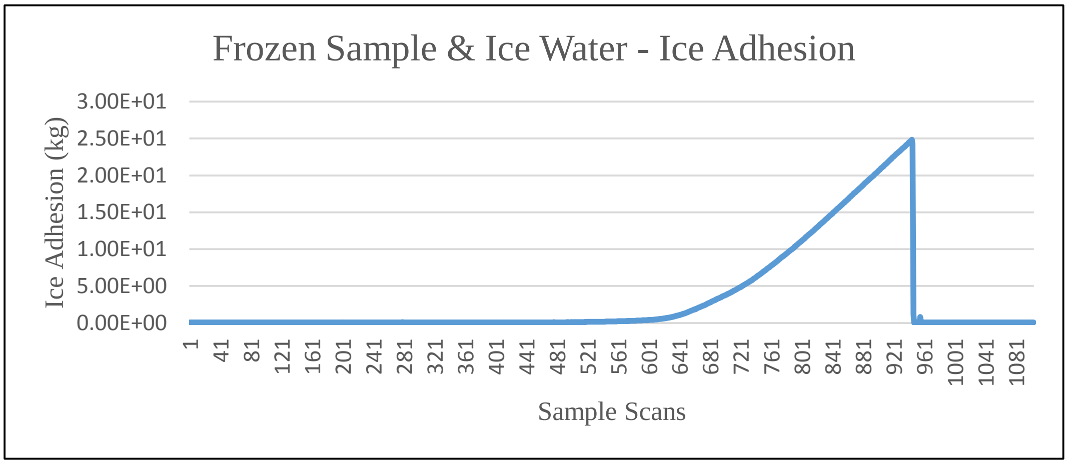

Figure 116. Graph of the resistance load due to ice adhesion vs. sample scans at a rate of 1/ 0.01405s. Max load = 24.8 kg

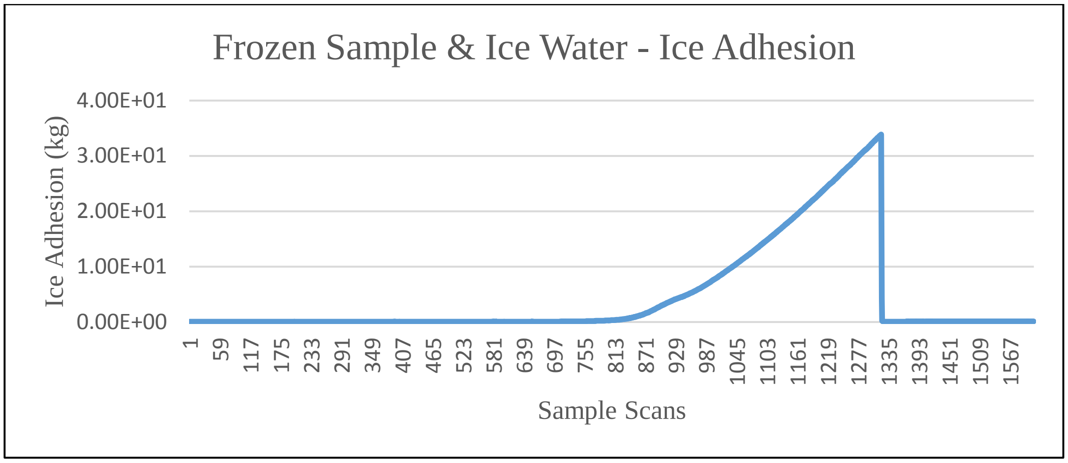

Figure 117. Graph of the resistance load due to ice adhesion vs. sample scans at a rate of 1/ 0.01405s. Max load = 33.9 kg

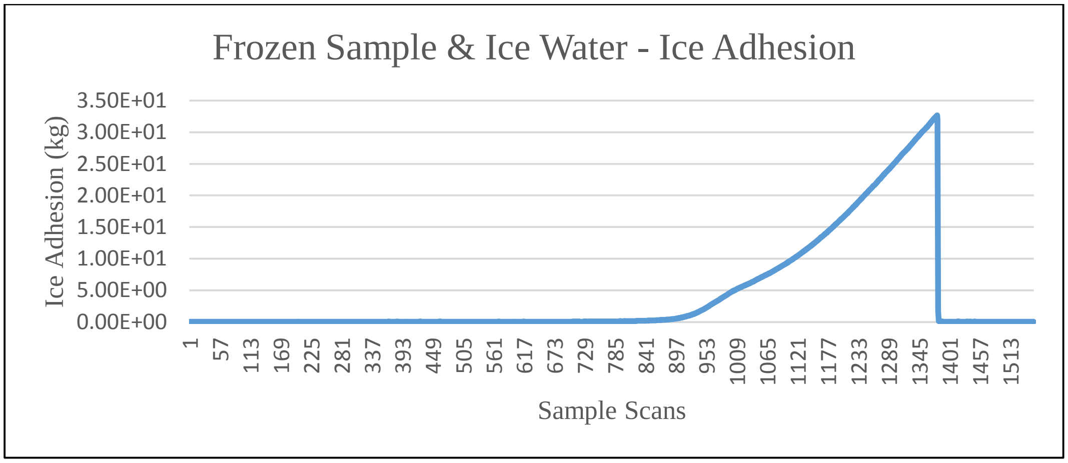

Figure 118. Graph of the resistance load due to ice adhesion vs. sample scans at a rate of 1/ 0.01405s. Max load = 32.7 kg

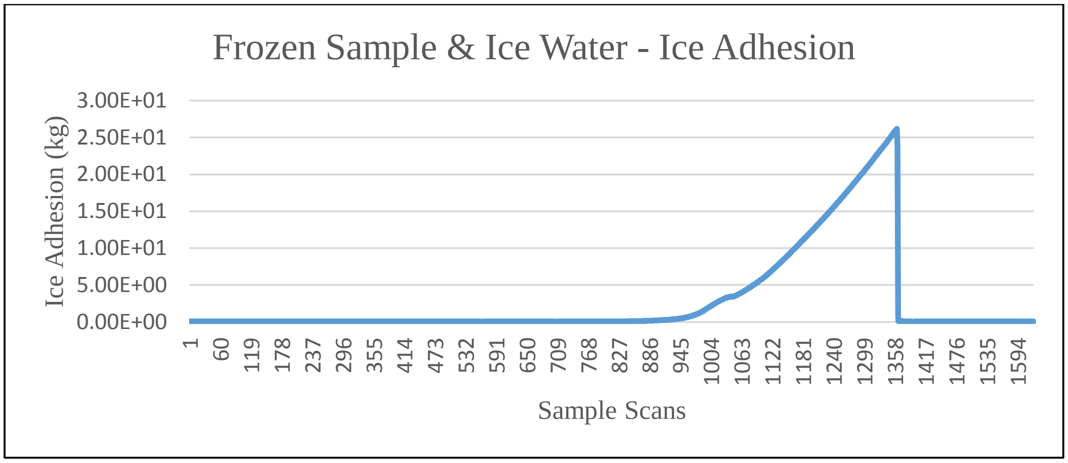

Figure 119. Graph of the resistance load due to ice adhesion vs. sample scans at a rate of 1/ 0.01405s. Max load = 26.2 kg

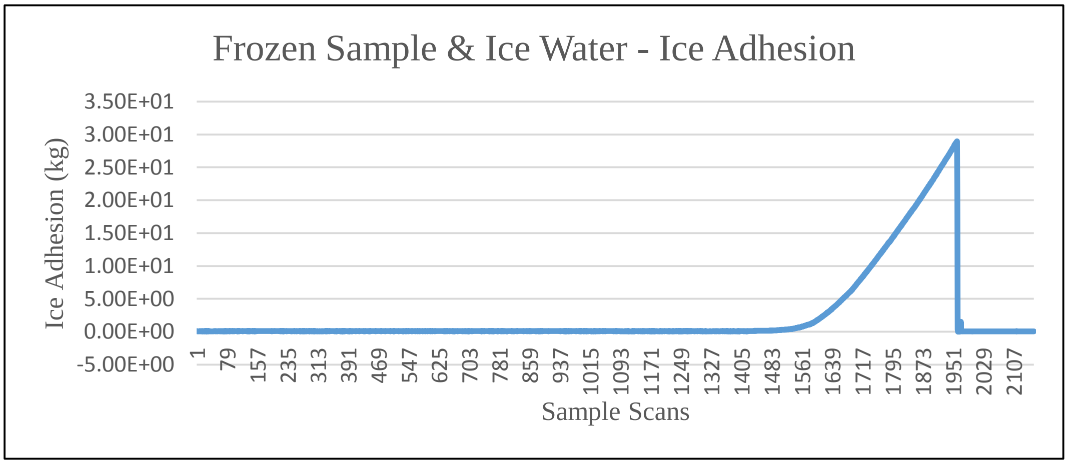

Figure 120. Graph of the resistance load due to ice adhesion vs. sample scans at a rate of 1/ 0.01405s. Max load = 29 kg

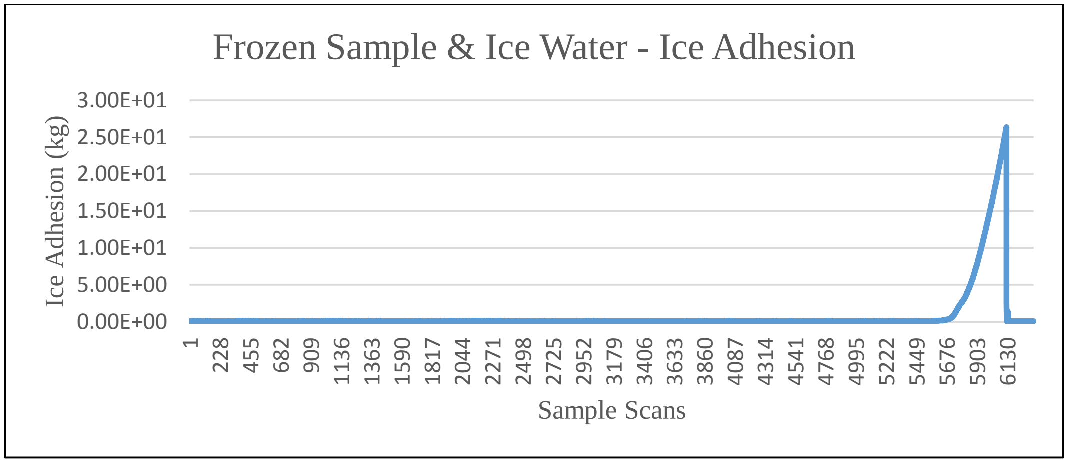

Figure 121. Graph of the resistance load due to ice adhesion vs. sample scans at a rate of 1/ 0.01405s. Max load = 26.4 kg

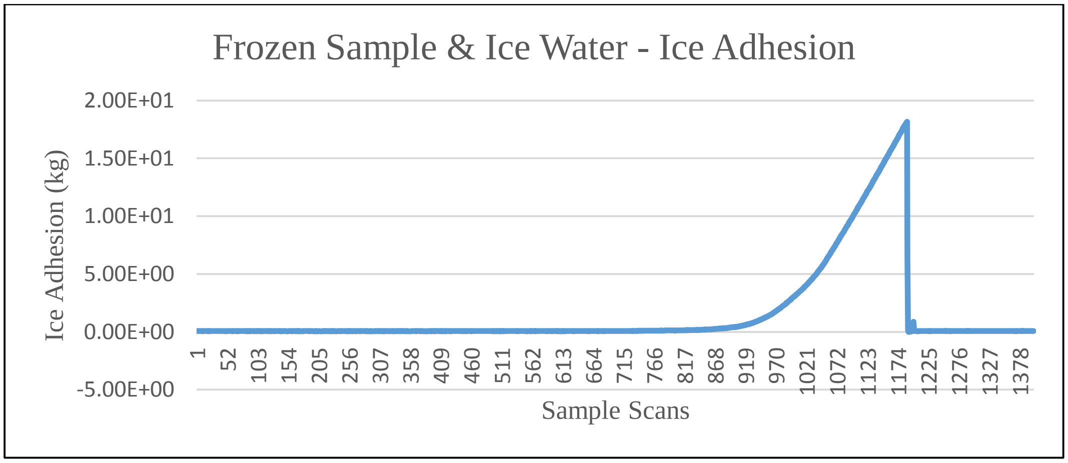

Figure 122. Graph of the resistance load due to ice adhesion vs. sample scans at a rate of 1/ 0.01405s. Max load = 18.2 kg

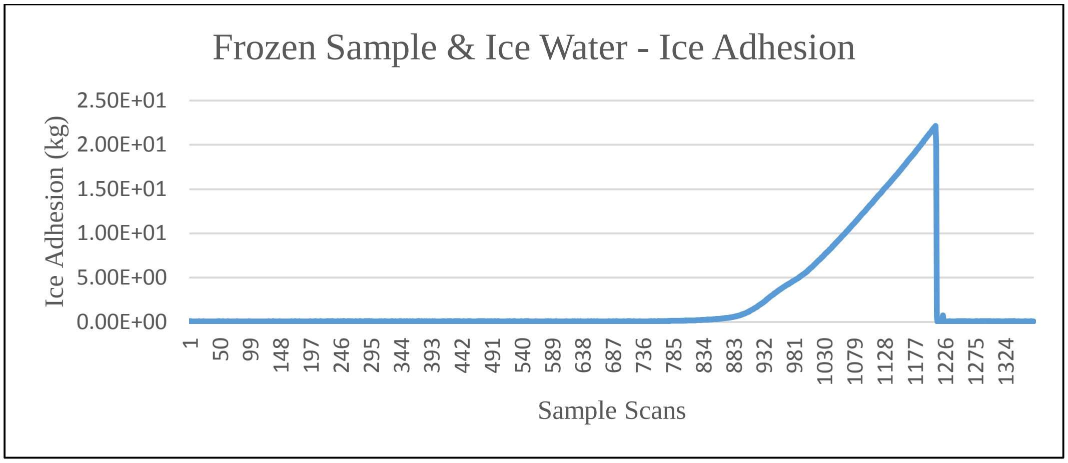

Figure 123. Graph of the resistance load due to ice adhesion vs. sample scans at a rate of 1/ 0.01405s. Max load = 22.1 kg

Frozen Sample & Ice Water – Ice Adhesion (kPa)	
Trial 1	1304.1
Trial 2	681.3
Trial 3	853.4
Trial 4	1166.5
Trail 5	1125.2
Trial 6	901.5
Trial 7	997.9
Trial 8	908.4
Trial 9	626.3
Trial 10	760.5
Average	**932.5**
Std. Dev.	**207**

Table 53. Summary of the ice adhesion measurements on stainless steel with a frozen sample and ice water

The ice adhesion using the frozen sample and ice water averaged over ten trials was 932.5 kPa, ranging from 626.3 kPa to 1304.1 kPa with a standard deviation of 207 kPa. The standard deviation is high at 22.2%.

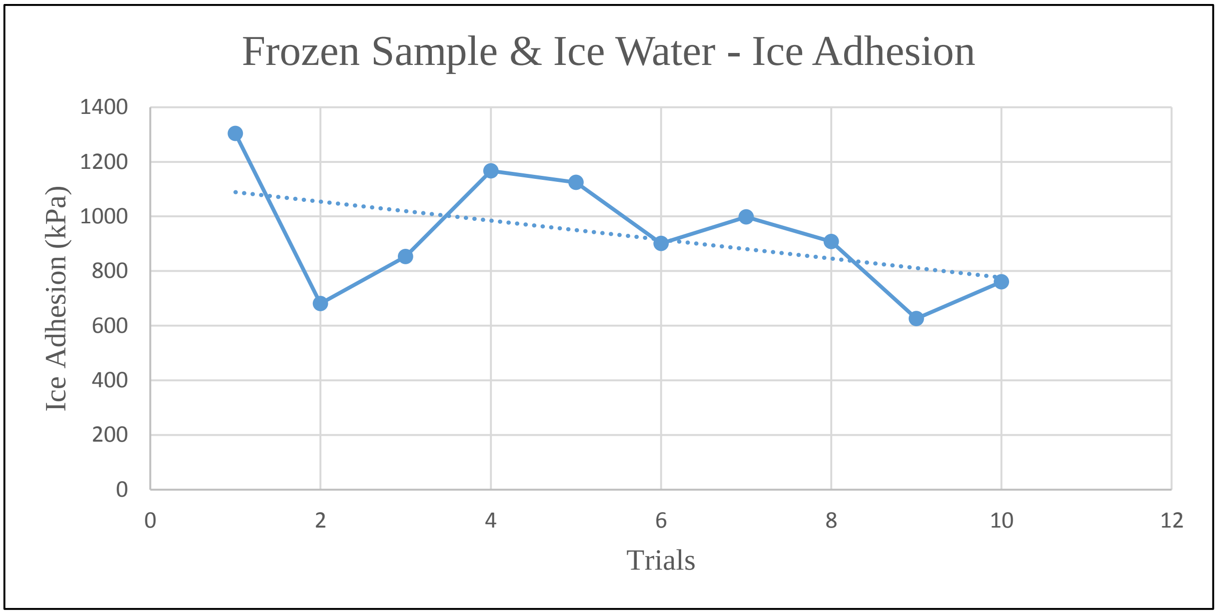

Figure 124. A scatter plot of the ice adhesion over ten trials testing the effect of a frozen sample and ice water on repeatability of ice adhesion measurements

Frozen Sample & S.T.P. Water – Ice Adhesion (kPa)	
Trial 1	1108
Trial 2	736.4
Trial 3	963.5
Trial 4	722.6
Trail 5	956.6
Trial 6	516.1
Trial 7	426.7
Trial 8	915.3

Trial 9	767.3
Trial 10	836.2
Average	**794.9**
Std. Dev.	**197.9**

Table 54. Summary of the ice adhesion measurements on stainless steel with a frozen sample and water at standard temperature and pressure

The ice adhesion using the frozen sample and water at standard temperature and pressure averaged over ten trials was 794.9 kPa, ranging from 516.1 kPa to 1108 kPa with a standard deviation of 197.9 kPa. The standard deviation is high at 24.9%.

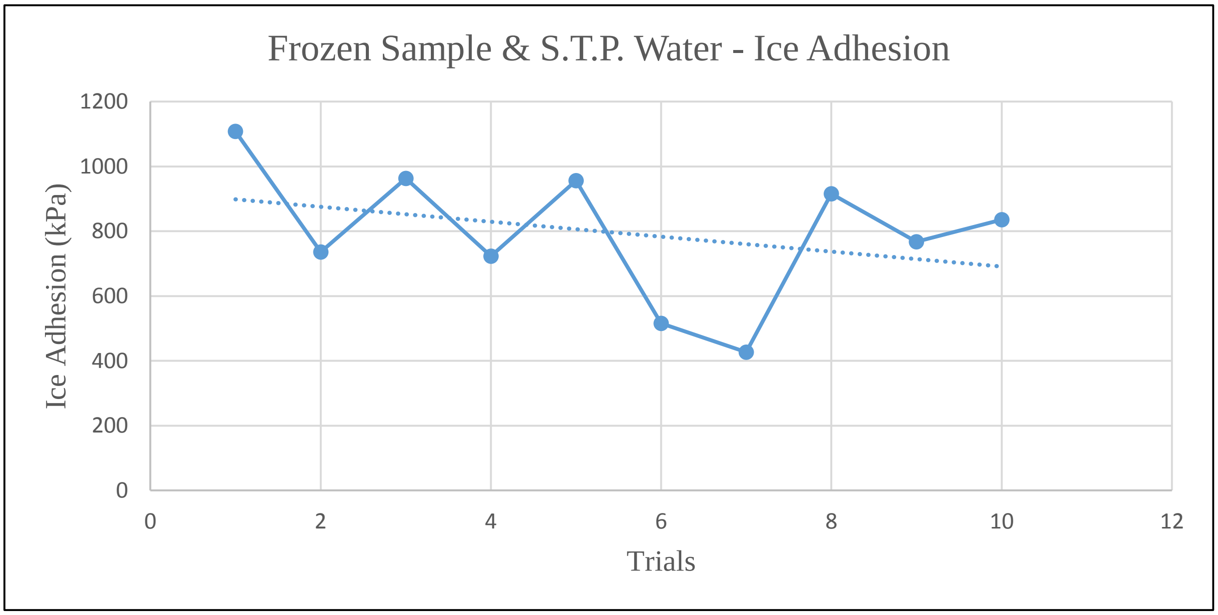

Figure 125. A scatter plot of the ice adhesion over ten trials testing the effect of a frozen sample and water at standard temperature and pressure on repeatability of ice adhesion measurements

S.T.P. Sample & Water – Ice Adhesion (kPa)	
Trial 1	1211.2
Trial 2	1225
Trial 3	1118.3
Trial 4	1311
Trail 5	1331.6
Trial 6	1259.4
Trial 7	1321.3
Trial 8	1073.6
Trial 9	1039.2
Trial 10	1496.8
Average	**1238.7**
Std. Dev.	**130.5**

Table 55. Summary of the ice adhesion measurements on stainless steel with the sample and water at standard temperature and pressure

The ice adhesion using the sample and water at standard temperature and pressure averaged over ten trials was 1238.7 kPa, ranging from 1039.2 kPa to 1496.8 kPa with a standard deviation of 130.5 kPa. The standard deviation is acceptable at 10.5%.

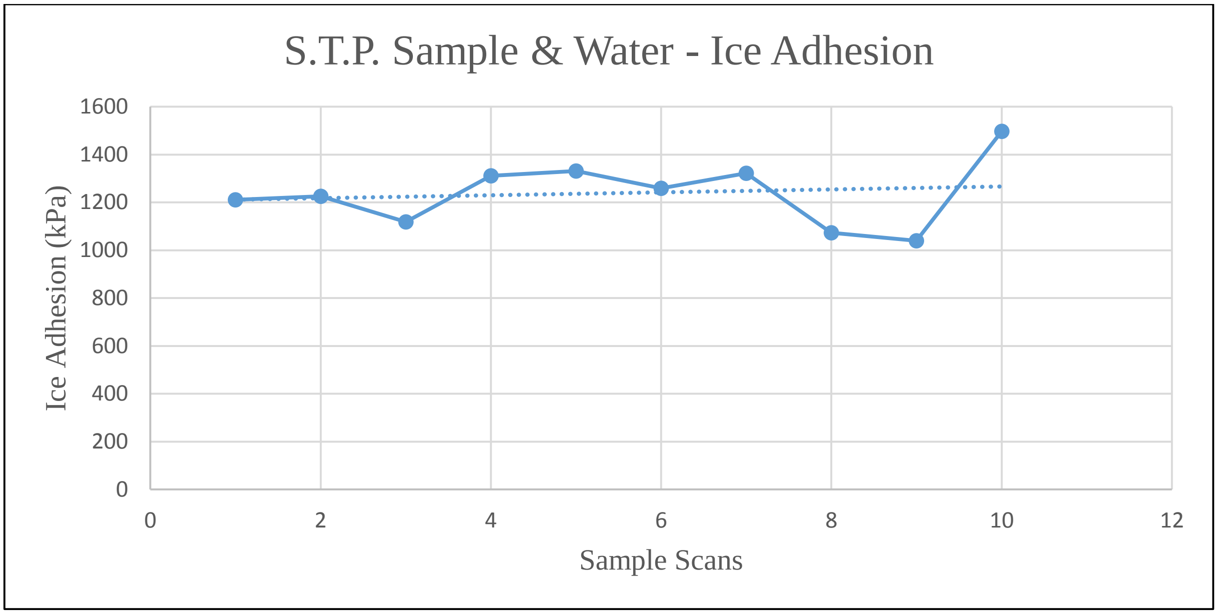

Figure 126. A scatter plot of the ice adhesion over ten trials testing the effect of the sample and water at standard temperature and pressure on repeatability of ice adhesion measurements

	Variations		
	Frozen Sample & S.T.P. Water	**Frozen Sample & Ice Water**	**S.T.P. Sample & Water**
Average Ice Adhesion (kPa)	794.9	932.5	1238.7
Standard Deviation (kPa)	197.9	207	130.5

Table 56. Summary of the average ice adhesion and standard deviation measurements on stainless steel while varying the starting temperatures for the sample and water

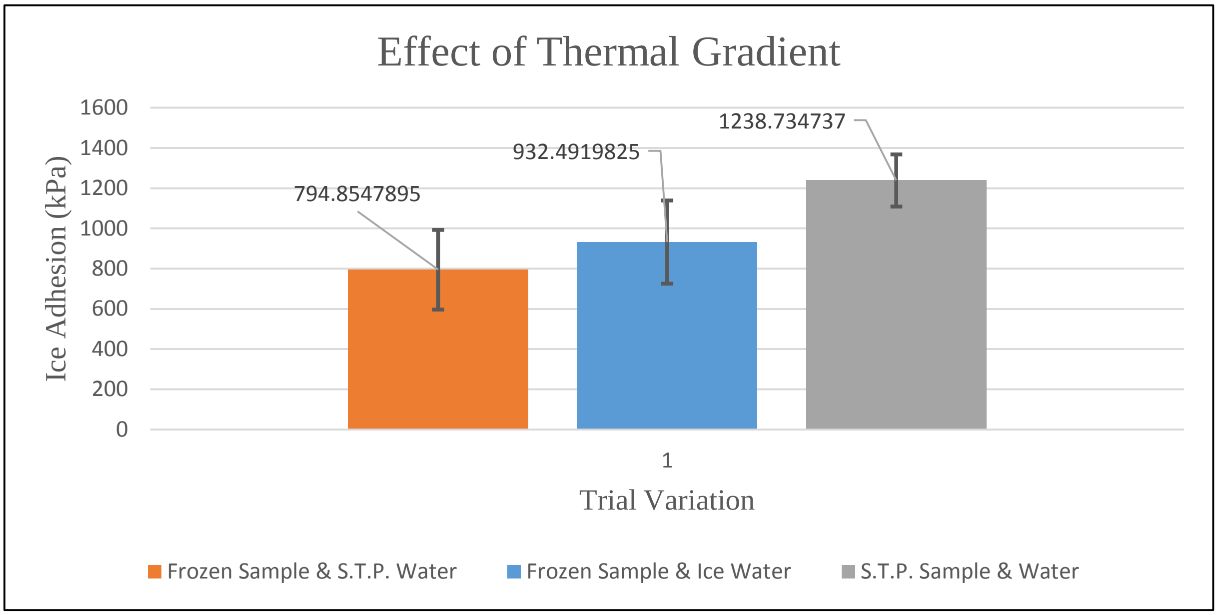

Figure 127. A histogram showing the ice adhesion and standard deviation while varying the starting temperatures for the sample and water

As Table 56 and Figure 127. Show, there is a large difference in the accuracy and repeatability of the ice adhesion measurements when the initial starting temperatures of the water and sample are varied to create varying degrees of thermal gradients between the water and the sample, and the sample and the stage of the ice adhesion tester creating different conditions for ice nucleation and ice adhesion. The tests run using the frozen sample and ice water, and the frozen sample and water at standard temperature and pressure showed the highest standard deviations at 22.2% and 24.9%, both of these freezing conditions allow for a very rapid transfer of heat from the water/sample interface which will result in rapid ice nucleation and freezing. The test run using a sample and water at standard temperature and pressure exhibited markedly decreased standard deviation of only 10.5% and represents the condition in which heat will be transferred away from the water/sample interface the slowest and slows the rate of ice nucleation and freezing. The lowest thermal gradient between the water and the sample has exhibited the smallest standard deviation and represents the combination of initial starting temperatures for the water and sample that will give the most accurate results and will be used throughout the remainder of this investigation.

Ice adhesion of different materials of varying roughness

It is necessary to measure the adhesion of ice to differing materials such as glass, aluminum, and stainless steel because there are three physical mechanisms involved in the adhesion of ice to a surface, specifically, hydrogen bonding, van der Waals forces, and direct electrostatic interactions. Of these three, the direct electrostatic interactions have been found to be the dominant factor (115) (116). Charges on ice induce equal and opposite charges on metals, whereas on dielectrics, the induced charge is smaller and is related to the dielectric constant. Do to the fact that differing chemistry affects the adhesion of ice to a substrate and that different materials are used in the construction of the protective case assembly used to shield the photvoltaic cells from the outdoor climactic conditions it is necessary to test the adhesion of ice to the materials to determine its behavior and why this behavior is occuring.

It is necessary to measure the adhesion of ice for different roughness and surface conditions because the materials used in the construction of the protective solar panel case (glass, aluminum, steel) are prepared in a variety of methods and each one will leave the material with a distinctive surface condition and roughness. Knowing that the protective casing and variety of materials composing it will be regularly exposed to climactic icing events it is important that the effect of the surface condition and roughness on the adhesion of ice be understood to ensure that the design of the proposed system is repeatable and reliable.

Ice adhesion of glass

Glass – Ice Adhesion (kPa)	
Trial 1	1596.6
Trial 2	1338.5
Trial 3	1579.4
Trial 4	1576
Trail 5	1455.5
Trial 6	1462.4
Trial 7	1551.9
Trial 8	1692.9
Trial 9	1610.4
Trial 10	1748
Average	**1561.5**
Std. Dev.	**112.8**

Table 57. Summary of the ice adhesion measurements on glass

The ice adhesion using the glass sample averaged over ten trials was 1561.5 kPa, ranging from 1338.5 kPa to 1748 kPa with a standard deviation of 112.8 kPa or 7.2%.

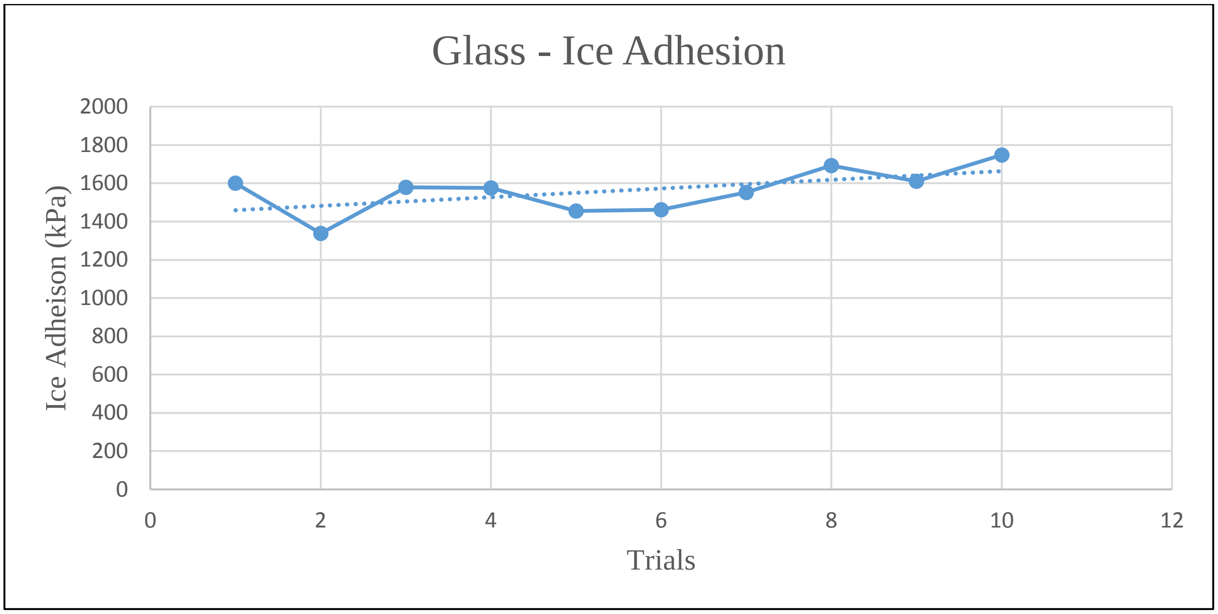

Figure 128. Scatter plot of the ice adhesion over ten trials on glass

Ice Adhesion of Aluminum

Polished Aluminum

Aluminum – Polished – Ice Adhesion (kPa)	
Trial 1	843
Trial 2	1166.5
Trial 3	1059.8
Trial 4	1190.6
Trail 5	915.3
Trial 6	929.1
Trial 7	1080.5
Trial 8	956.6
Trial 9	1187.1
Trial 10	1063.3

Average	**1039.2**
Std. Dev.	**116.8**

Table 58. Summary of the ice adhesion measurements on polished aluminum

The ice adhesion using the polished aluminum sample averaged over ten trials was 1039.2 kPa, ranging from 843 kPa to 1190.6 kPa with a standard deviation of 116.8 kPa or 11.2%.

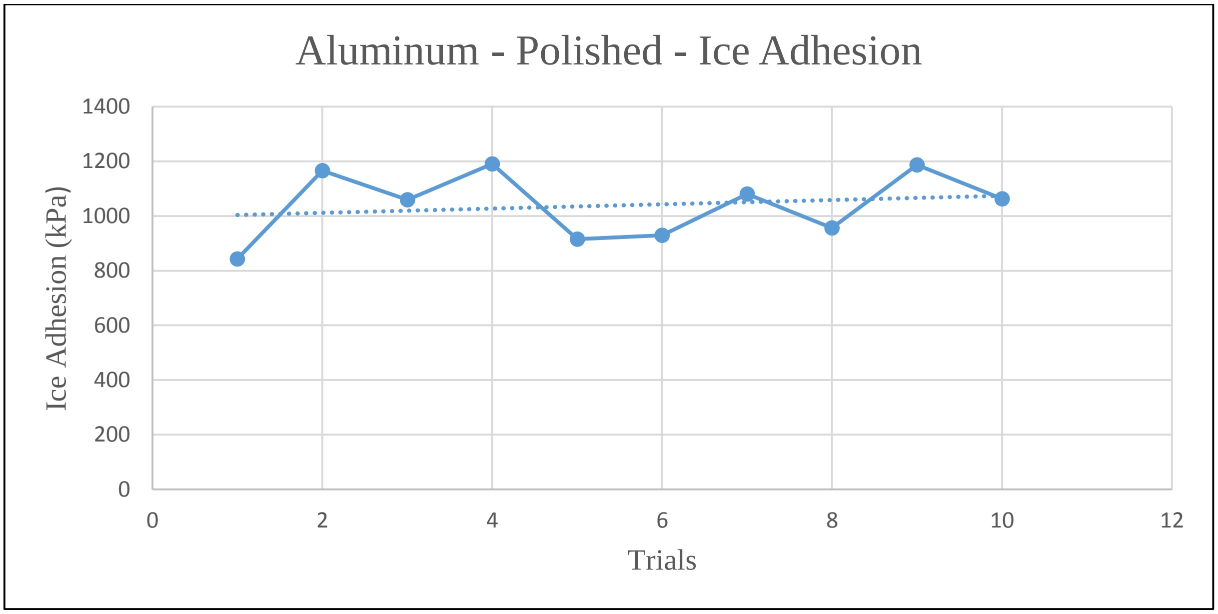

Figure 129. Scatter plot of the ice adhesion over ten trials on polished aluminum

Moderate Aluminum

Aluminum – Moderate – Ice Adhesion (kPa)	
Trial 1	1383.3
Trial 2	1249.1
Trial 3	1276.6
Trial 4	1441.8
Trail 5	1235.3
Trial 6	1589.7
Trial 7	1262.8
Trial 8	1441.8
Trial 9	1582.8
Trial 10	1266.3
Average	**1372.9**
Std. Dev.	**129.5**

Table 59. Summary of the ice adhesion measurements on moderate aluminum

The ice adhesion using the moderate aluminum sample averaged over ten trials was 1379.9 kPa, ranging from 1235.3 kPa to 1589.7 kPa with a standard deviation of 129.5 kPa or 9.4%.

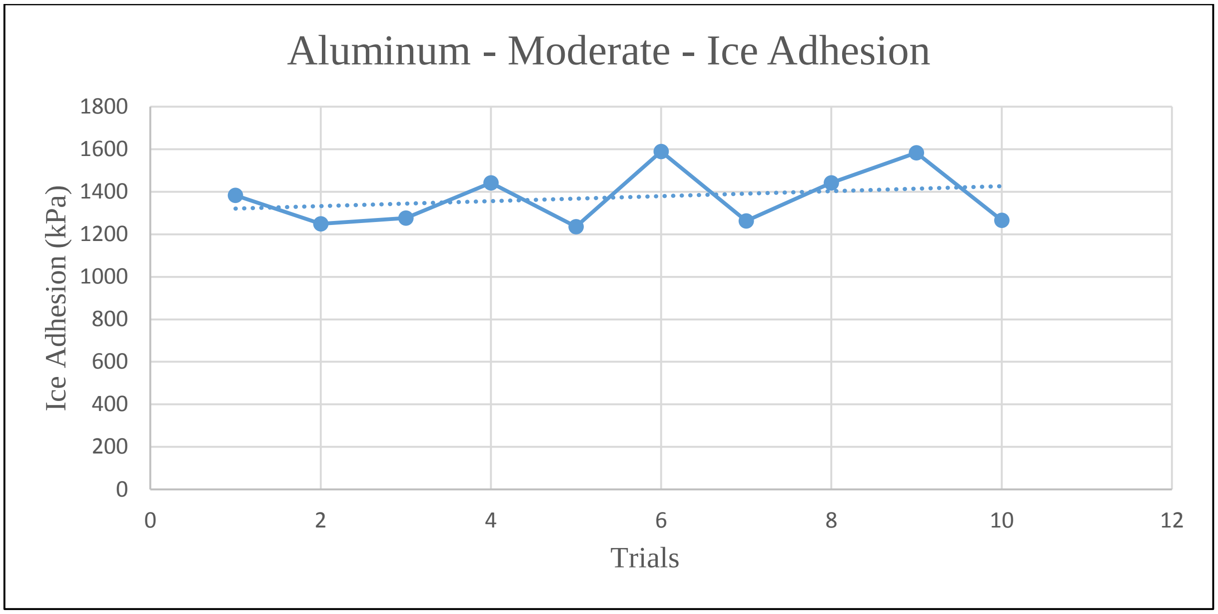

Figure 130. Scatter plot of the ice adhesion over ten trials on moderate aluminum

Rough Aluminum

Aluminum – Rough – Ice Adhesion (kPa)	
Trial 1	1510.6
Trial 2	1627.6
Trial 3	1465.8
Trial 4	1692.9
Trail 5	1803.1
Trial 6	1397
Trial 7	1472.7
Trial 8	1493.4
Trial 9	1675.7
Trial 10	1689.5

Average	**1582.8**
Std. Dev.	**125**

Table 60. Summary of the ice adhesion measurements on rough aluminum

The ice adhesion using the rough aluminum sample averaged over ten trials was 1582.8 kPa, ranging from 1397 kPa to 1803.1 kPa with a standard deviation of 125 kPa or 7.9%.

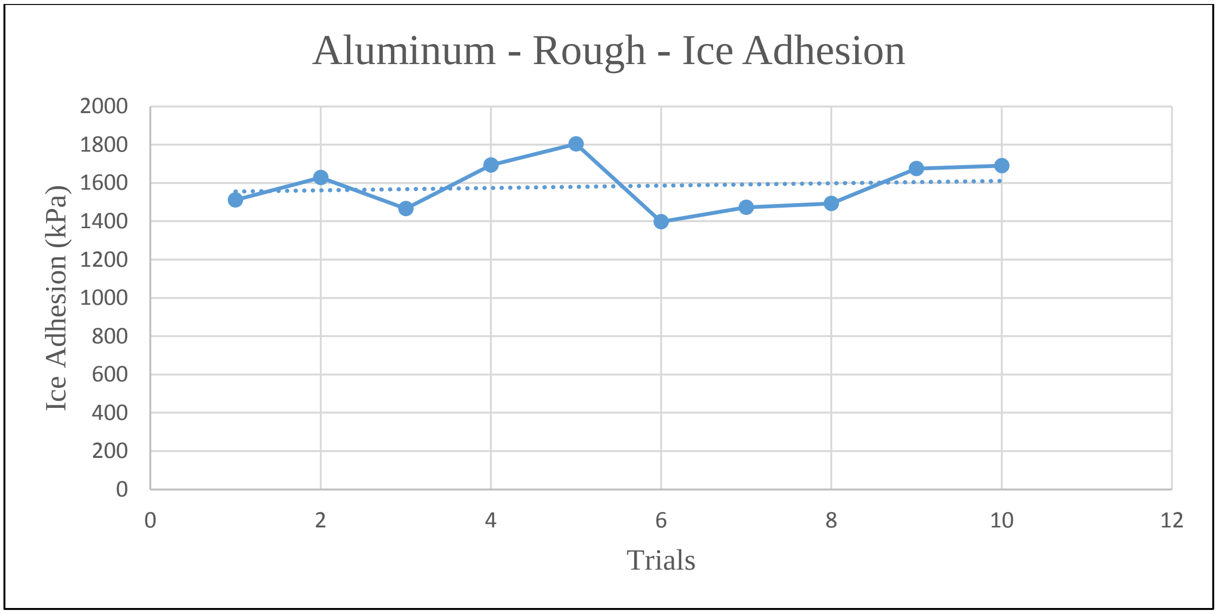

Figure 131. Scatter plot of the ice adhesion over ten trials on rough aluminum

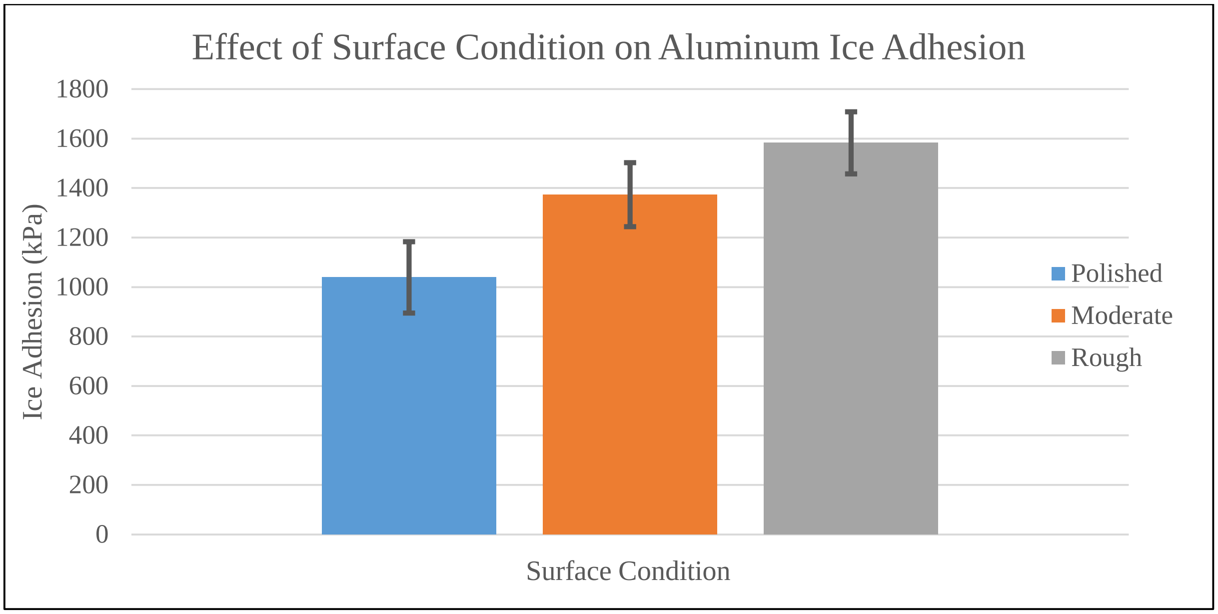

Figure 132. A comparison of the average ice adhesion and standard deviation of the aluminum samples with different surface conditions

	Aluminum Sample Variations		
	Polished	**Moderate**	**Rough**
Roughness	**(nm)**	**(µm)**	**(µm)**
R_a	22.2	3.04	5.06
R_q	27.9	3.82	6.46
R_t	243.3	38.9	60
Average Ice Adhesion (kPa)	1039.2	1372.9	1582.8
Standard Deviation (kPa)	116.8	129.5	125

Table 61. Summary of roughness measurements on aluminum samples compared to the ice adhesion and standard deviation, where R_a is the average surface roughness, R_q is the root-mean-square value, and R_t is the peak-to-valley difference, all calculated over the entire measured array.

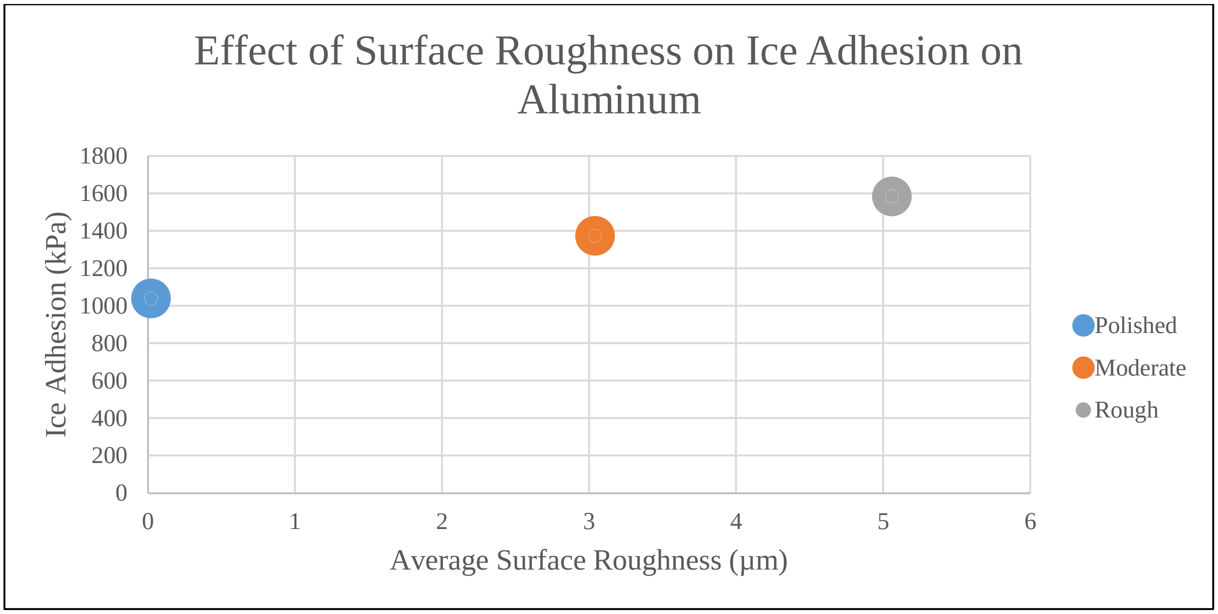

Figure 133. Scatter plot showing the effect of average surface roughness on ice adhesion

As Figure 132. shows, the ice adhesion on aluminum of different surface conditions shows a clear trend with the ice adhesion increasing as the surface condition includes a higher roughness. It can be seen from Table 61 and Figure 133. that when the average surface roughness of the samples are measured and plotted against the ice adhesion they behave in a linearly proportional manner. As the average surface roughness of the aluminum sample increased, so did the ice adhesion.

Ice adhesion of stainless steel

Polished Stainless Steel

Stainless Steel - Polished – Ice Adhesion (kPa)	
Trial 1	1176.8
Trial 2	901.5
Trial 3	1087.3
Trial 4	1059.8
Trail 5	1135.5
Trial 6	1125.2
Trial 7	825.8
Trial 8	994.4
Trial 9	1049.5
Trial 10	863.7
Average	**1022**
Std. Dev.	**115.2**

Table 62. Summary of the ice adhesion measurements on polished stainless steel

The ice adhesion using the polished stainless steel sample averaged over ten trials was 1022 kPa, ranging from 825.8 kPa to 1176.8 kPa with a standard deviation of 115.2 kPa or 11.3%.

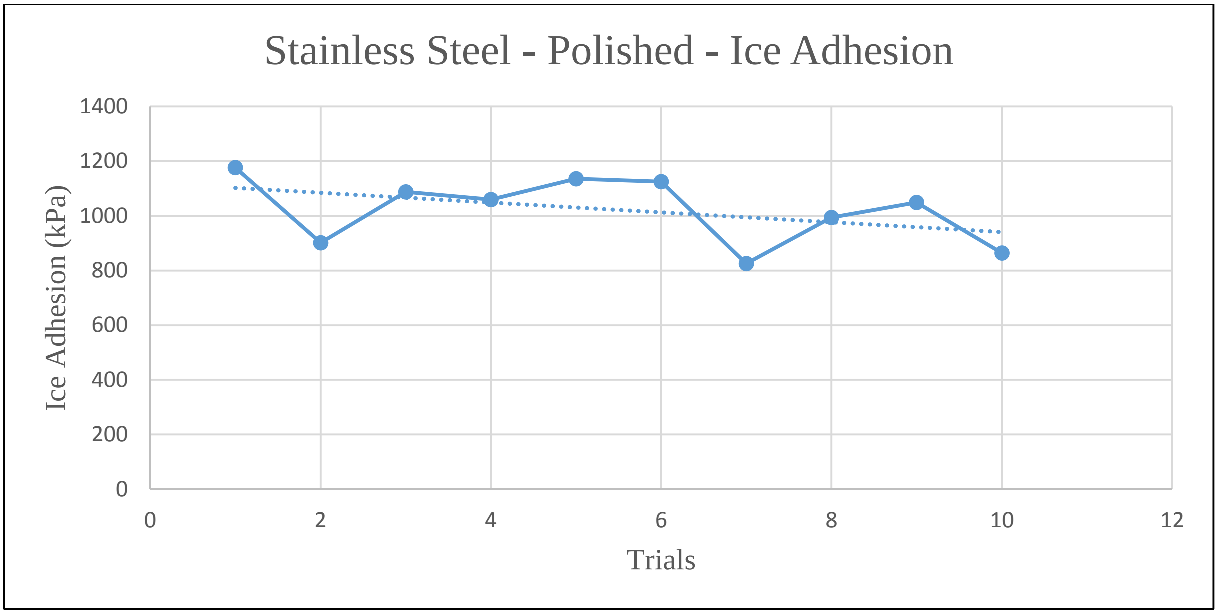

Figure 134. Scatter plot of the ice adhesion over ten trials on polished stainless steel

Moderate Stainless Steel

Stainless Steel - Moderate – Ice Adhesion (kPa)	
Trial 1	1345.4
Trial 2	1483
Trial 3	1331.6
Trial 4	1414.2
Trail 5	1207.8
Trial 6	1524.3
Trial 7	1355.7
Trial 8	1197.4
Trial 9	1139
Trial 10	1472.7

Average	**1347.1**
Std. Dev.	**124.8**

Table 63. Summary of the ice adhesion measurements on moderate stainless steel

The ice adhesion using the moderate stainless steel sample averaged over ten trials was 1347.1 kPa, ranging from 1139 kPa to 1524.3 kPa with a standard deviation of 124.8 kPa or 9.3%.

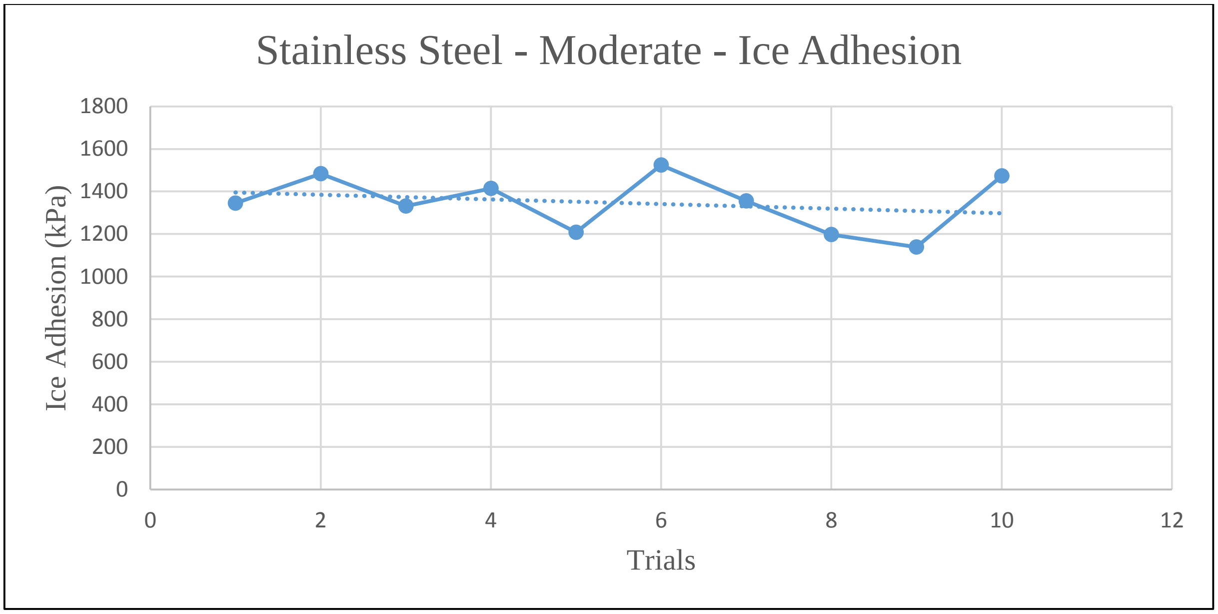

Figure 135. Scatter plot of the ice adhesion over ten trials on moderate stainless steel

Rough Stainless Steel

Stainless Steel - Rough – Ice Adhesion (kPa)	
Trial 1	1758.3
Trial 2	1551.9
Trial 3	1737.7
Trial 4	1476.2
Trail 5	1579.4
Trial 6	1510.6
Trial 7	1675.7
Trial 8	1417.7
Trial 9	1668.9
Trial 10	1706.7
Average	**1608.3**
Std. Dev.	**111.6**

Table 64. Summary of the ice adhesion measurements on rough stainless steel

The ice adhesion using the rough stainless steel sample averaged over ten trials was 1608.3 kPa, ranging from 1417.7 kPa to 1758.3 kPa with a standard deviation of 111.6 kPa or 6.9%.

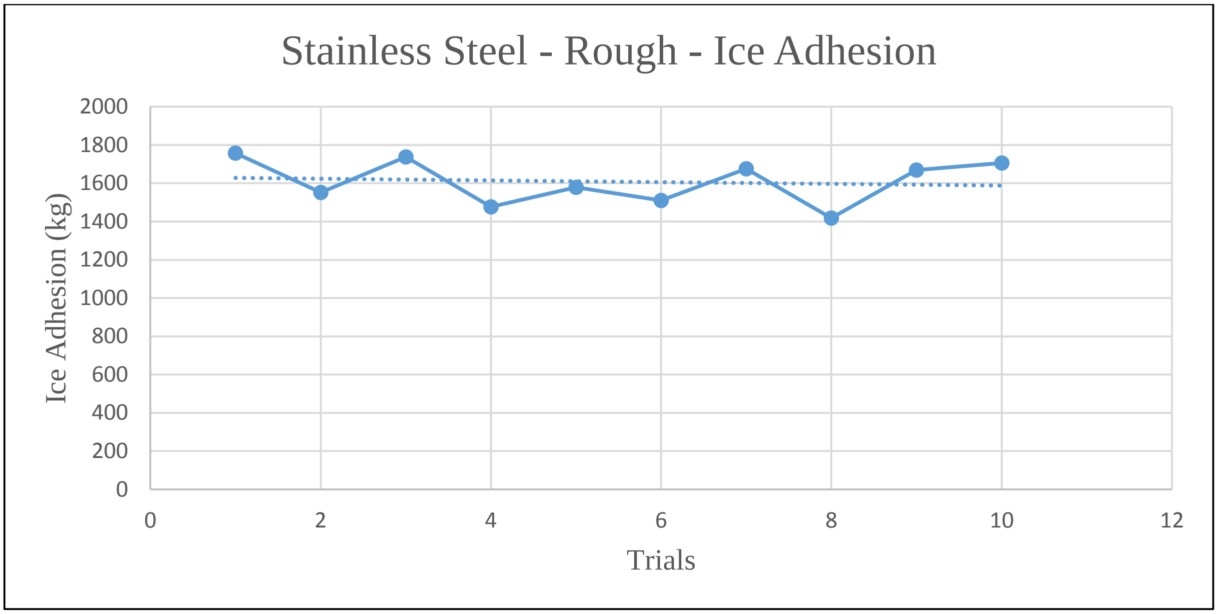

Figure 136. Scatter plot of the ice adhesion over ten trials on rough stainless steel

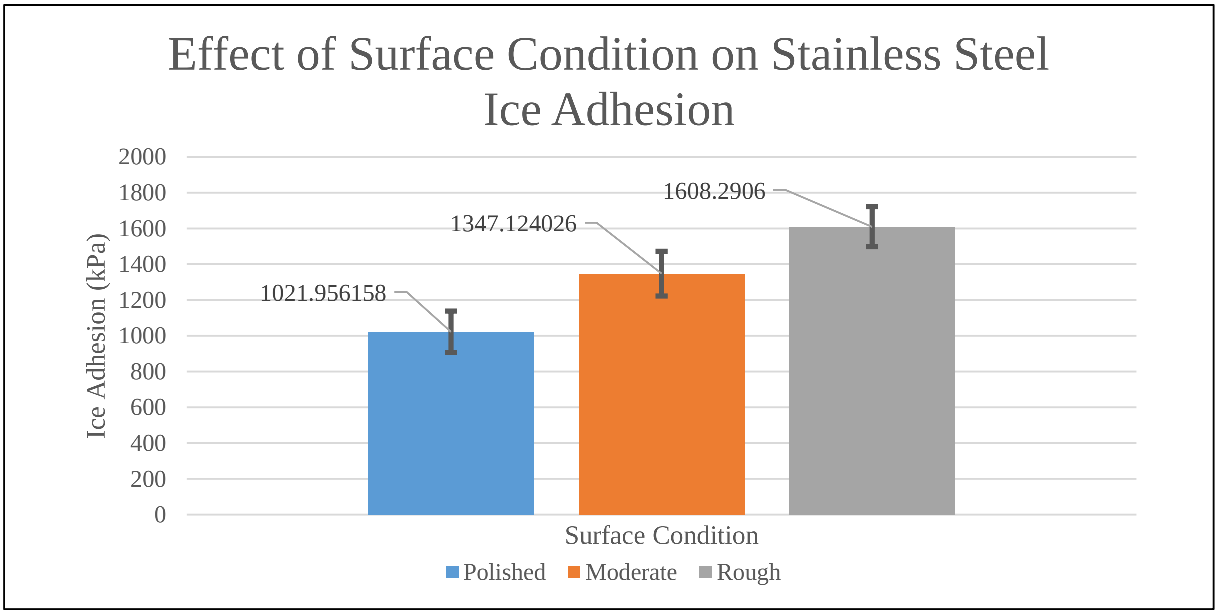

Figure 137. A comparison of the average ice adhesion and standard deviation of the aluminum samples with different surface conditions

	Stainless Steel Sample Variations		
	Polished	**Moderate**	**Rough**
Roughness	**(nm)**	**(µm)**	**(µm)**
R_a	2.74	1.94	3.74
R_q	3.55	2.42	4.81
R_t	155.2	20.4	61.3
Average Ice Adhesion (kPa)	1022	1347.1	1608.3
Standard Deviation (kPa)	115.2	124.8	111.6

Table 65. Summary of roughness measurements on stainless steel samples compared to the ice adhesion and standard deviation, where R_a is the average surface roughness, R_q is the root-mean-square value, and R_t is the peak-to-valley difference, all calculated over the entire measured array.

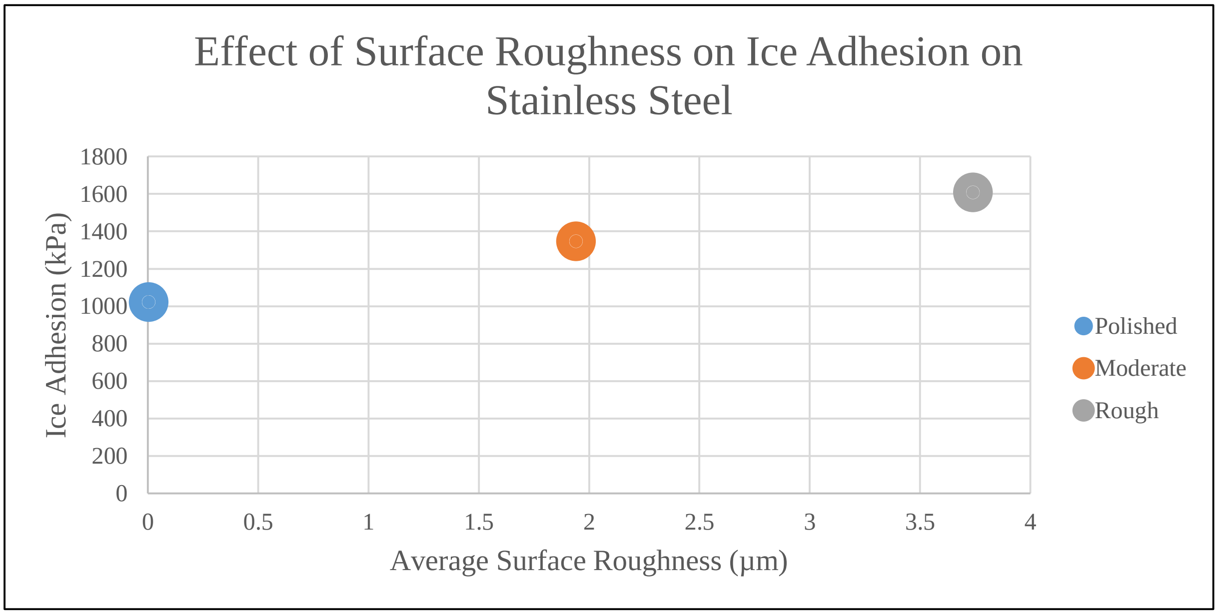

Figure 138. Scatter plot showing the effect of average surface roughness on ice adhesion

As Figure 137. shows, the ice adhesion on stainless steel of different surface conditions shows a clear trend with the ice adhesion increasing as the surface condition includes a higher roughness. It can be seen from Table 65 and Figure 138. that when the average surface roughness of the samples are measured and plotted against the ice adhesion they behave in a linearly proportional manner. As the average surface roughness of the stainless steel sample increased, so did the ice adhesion.

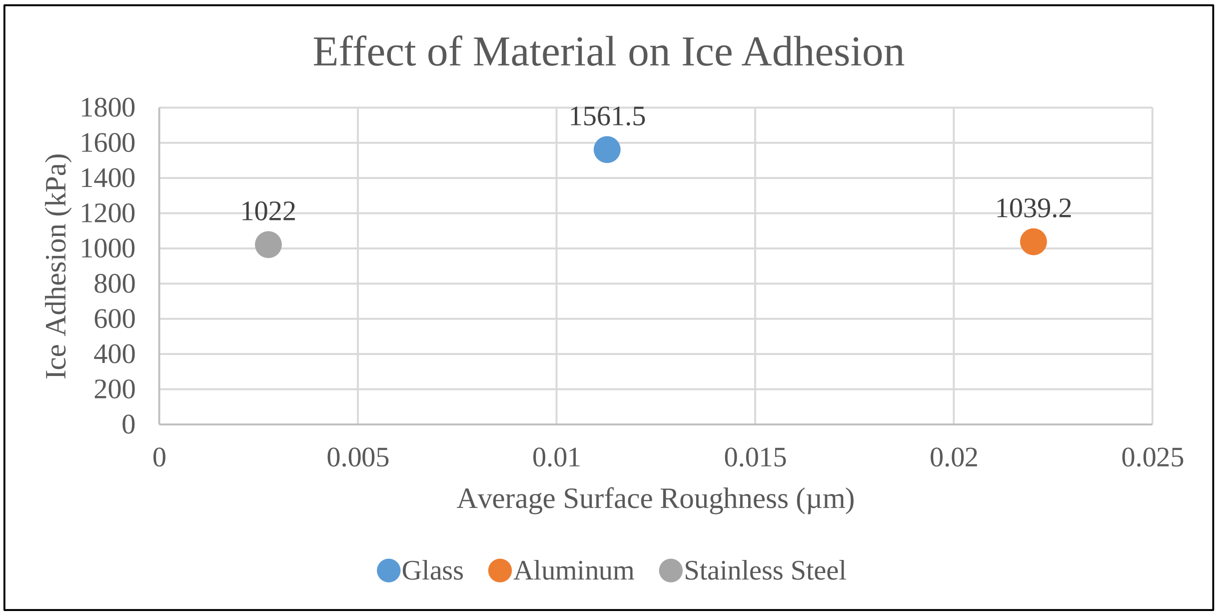

Figure 139. A comparison showing the effect of material on the average ice adhesion

Figure 139. shows that despite a small difference in average surface roughness between the polished metal samples of aluminum and stainless steel (22.2 nm and 2.74 nm) there is very little difference in average ice adhesion (1039.2 kPa and 1022 kPa). This is in stark contrast, however, to the large difference in average ice adhesion of the polished metal samples with the smooth glass sample of similar roughness. The average adhesion varies from 1022/1039.2 kPa to 1561.5

kPa when the surface roughness of the glass lies between that of the aluminum and stainless steel samples, 11.27 nm. This demonstrates that the average ice adhesion does not vary significantly between metallic samples of aluminum and stainless steel provided their surface roughness is similar. The average ice adhesion between ceramic materials and metallic materials varies considerably, however, despite the same similarity in surface roughness.

Ice adhesion of copolymer coating

It is necessary to test the ice adhesion of hydrophobic coatings because of the potential they show for reducing ice adhesion and preventing ice accumulation. Because active methods of ice removal (thermal, mechanical, chemical fluids) are energy hungry and expensive passive methods represent a cheaper option (17). Although, currently there is no known material that can completely prevent ice or snow from accumulating on its surface, hydrophobic coatings can provide reduced adhesion, and as the hydrophobicity of the surface increases, the ice adhesion decreases (18) (121).

Dip Coated Copolymer Coating – Ice Adhesion (kPa)	
Trial 1	970.3
Trial 2	1486.5
Trial 3	1211.2
Trial 4	1245.6
Trail 5	1507.1
Average	**1248.2**
Std. Dev.	**198**

Table 66. Summary of the ice adhesion measurements on the dip coated copolymer coating

The ice adhesion using the dip coated copolymer coating on glass sample averaged over five trials was 1248.2 kPa, ranging from 970.3 kPa to 1507.1 kPa with a standard deviation of 198 kPa or 15.9%.

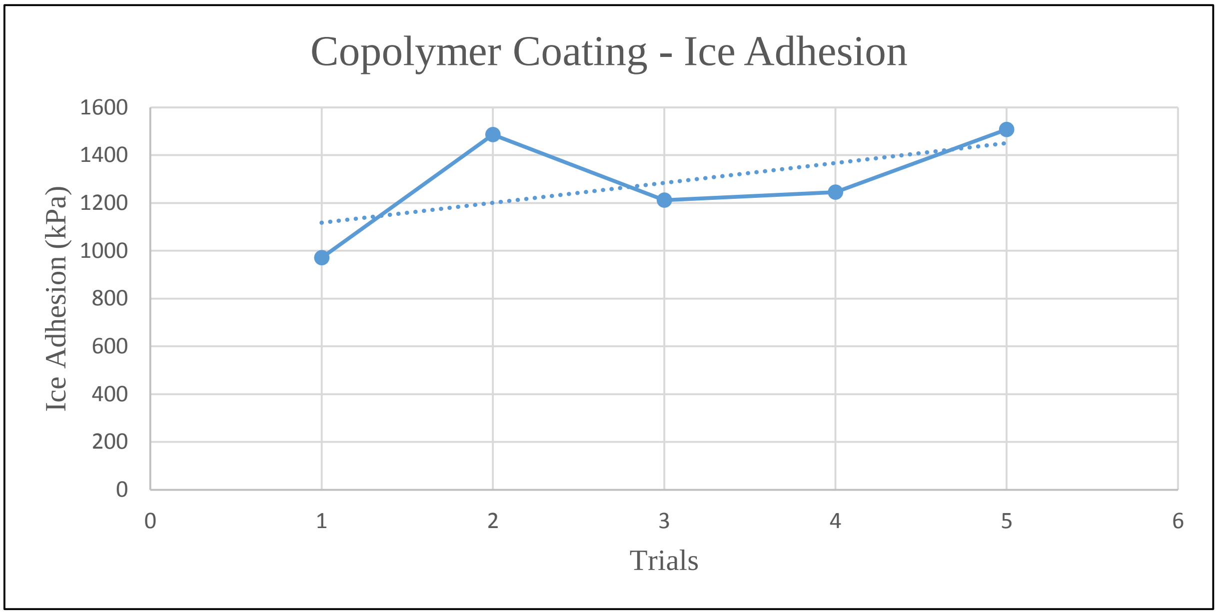

Figure 140. Scatter plot of the ice adhesion over ten trials on the dip coated copolymer coating

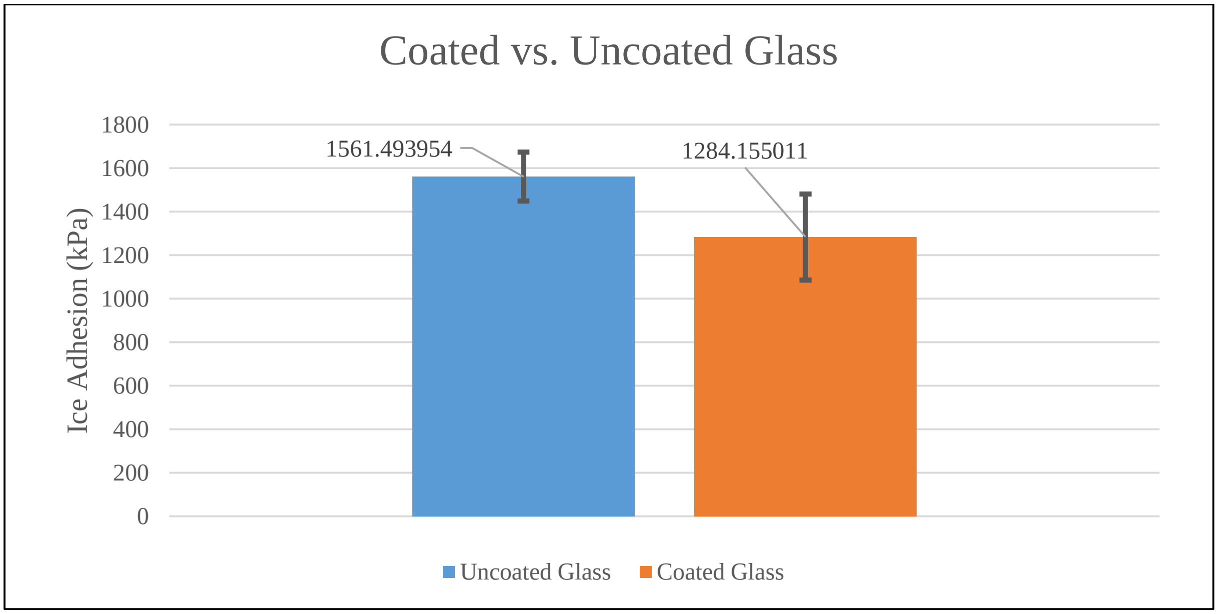

Figure 141. A comparison of the average ice adhesion and standard deviation between the uncoated glass and the dip-coated copolymer glass samples

From figure 141. it can be seen that the addition of the dip-coated copolymer coating to the glass did not make a significant reduction in the ice adhesion (1561.5 to 1248.2 kPa), and resulted in an increase of the standard deviation (112.8 to 198 kPa).

Ice adhesion of glass with ultrasound

The IAC can measure the ice adhesion of any sample substrate under ultrasonic vibration by using the same method as previously explained method with one additional step. When the linear actuator is started and applying in turn apply the shearing force to the ice/substrate interface, the ultrasonic transducer which can be installed in one of two positions, will be activated and will send vibrations through the ice/substrate interface at 20,000 cycles per second to break or weaken the bonds. Due to the current inability of the hydrophobic coatings to consistently prevent any adherence of ice it is necessary to couple the hydrophobic coatings with an ultrasonic transducer to mechanically break what weak bonds may have been able to form between the coating/substrate and the ice. This then dictates the necessity to measure the ice adhesion of candidate hydrophobic coatings in order to determine which can most prevent the adhesion of ice while maintaining the other necessary factors for a coating to be used in photovoltaic device applications (transparency, durability, etc). This characterization of the coating will also allow for the selection of a transducer which will use as little energy as is needed to remove the ice because it has been intelligently coupled with the hydrophobic coating. Without proper understanding of how the hydrophobic coating will affect the ice adhesion an ultrasonic transducer may be used that is not optimized and over the lifetime of the system it will use many time more energy than would be needed.

<table>
<tr><th colspan="2">Glass – Ultrasound (20 kHz, 700W, Transverse) – Ice Adhesion (kPa)</th></tr>
<tr><td>Trial 1</td><td>182.4</td></tr>
<tr><td>Trial 2</td><td>0</td></tr>
<tr><td>Trial 3</td><td>0</td></tr>
<tr><td>Trial 4</td><td>0</td></tr>
<tr><td>Trail 5</td><td>110.1</td></tr>
<tr><td>Average</td><td>58.5</td></tr>
<tr><td>Std. Dev.</td><td>75.2</td></tr>
</table>

Table 67. Summary of the ice adhesion measurements on glass with ultrasound (20 kHz, 700W, Transverse)

The ice adhesion on glass using ultrasonic vibration at 20 kHz at 700W in the transverse direction to the ice/sample interface averaged over ten trials was 58.5 kPa, ranging from 0 kPa to 182.4 kPa with a standard deviation of 75.2 kPa or 128.5%.

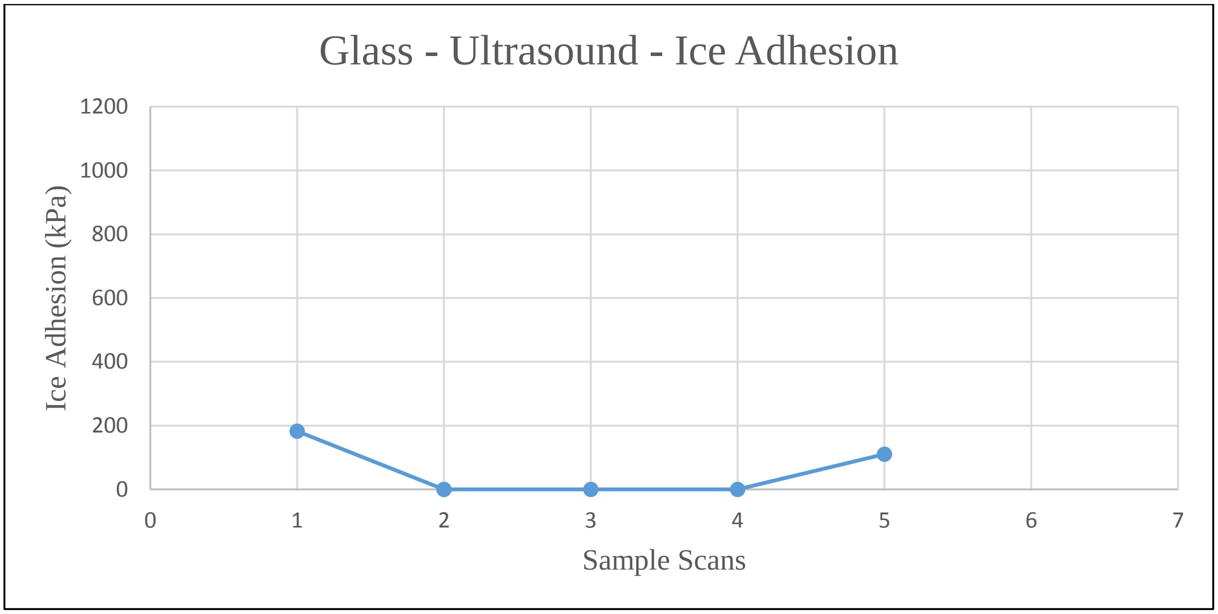

Figure 142. Scatter plot of the ice adhesion over ten trials on glass with ultrasound (20 kHz, 700W, Transverse)

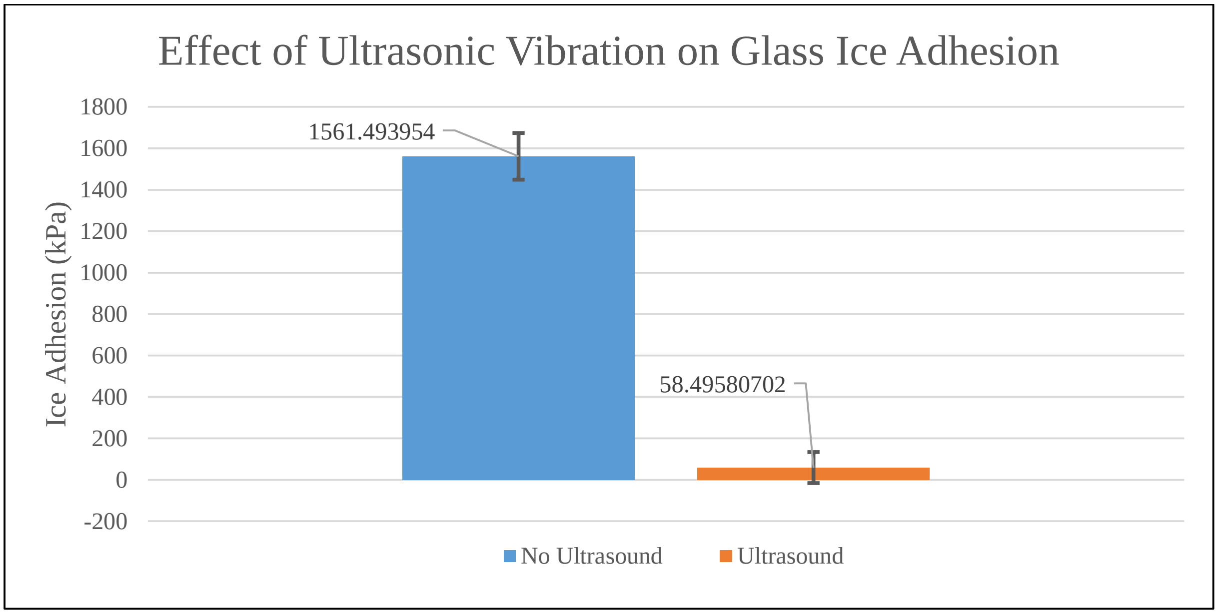

Figure 143. A comparison showing the effect of ultrasonic vibration (700W, 20 kHz, transverse) on glass ice adhesion. The ultrasonic vibration reduced the average ice adhesion by 96.3% from 1561.5 kPa to 58.5 kPa.

From figure 143. It can be seen that the introduction of the ultrasonic vibration (700W, 20 kHz, transverse direction) during ice adhesion testing on glass has drastically decreased the adhesion with which ice can adhere, from 1561.5 to 58.5 kPa on average, a decrease of 96.3%.

Surface of Coating After Ice Shedding Event

Surface Profilometry

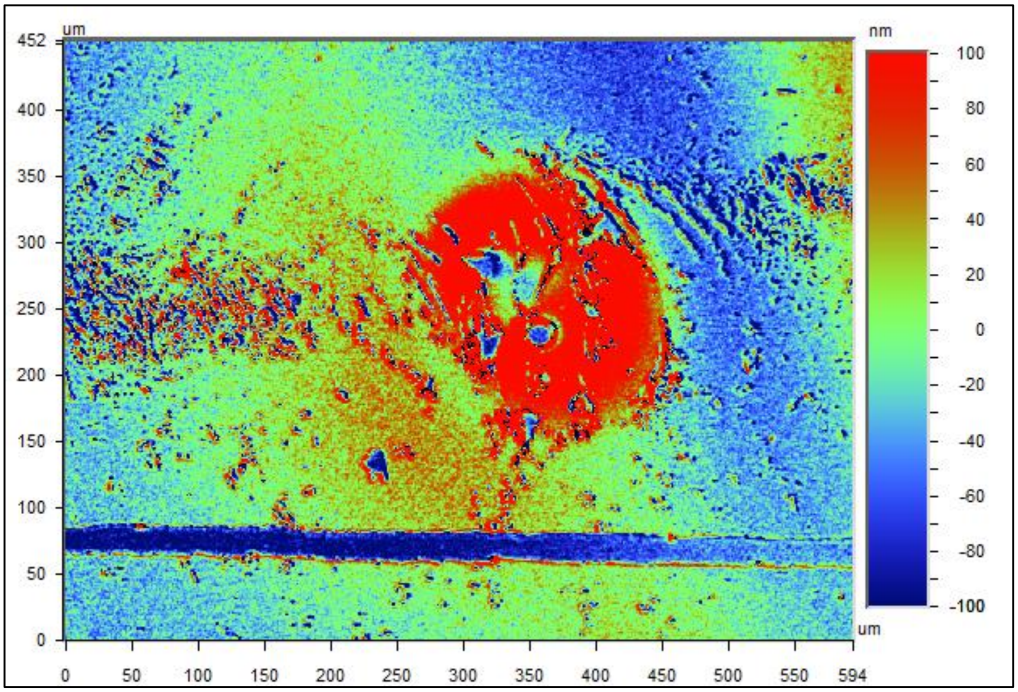

Figure 144. A two-dimensional surface profilometry scan of the surface of the dip coated copolymer coating after ice shedding event, shown at 10X magnification

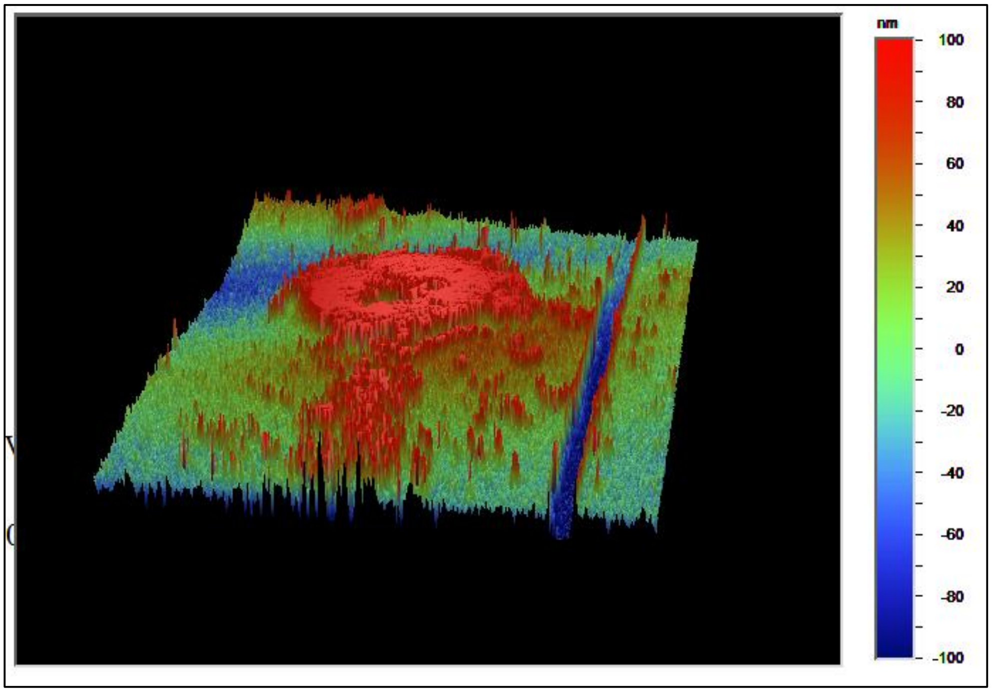

Figure 145. A three-dimensional surface profilometry scan of the surface of the dip coated copolymer coating after ice shedding event, shown at 10X magnification

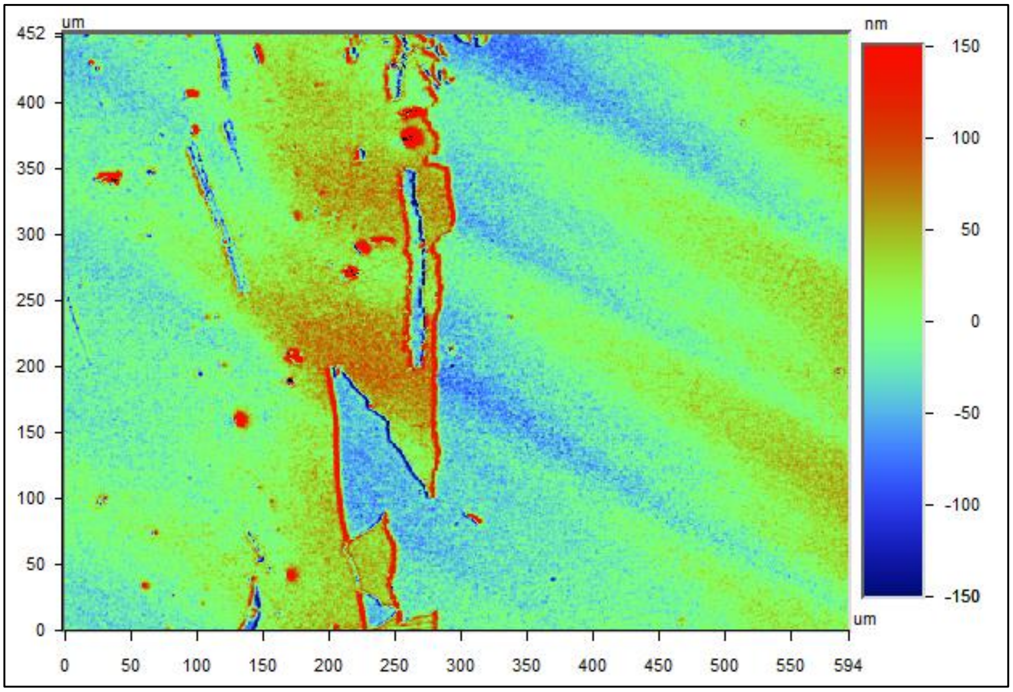

Figure 146. A two-dimensional surface profilometry scan of the surface of the dip coated copolymer coating after ice shedding event, shown at 10X magnification

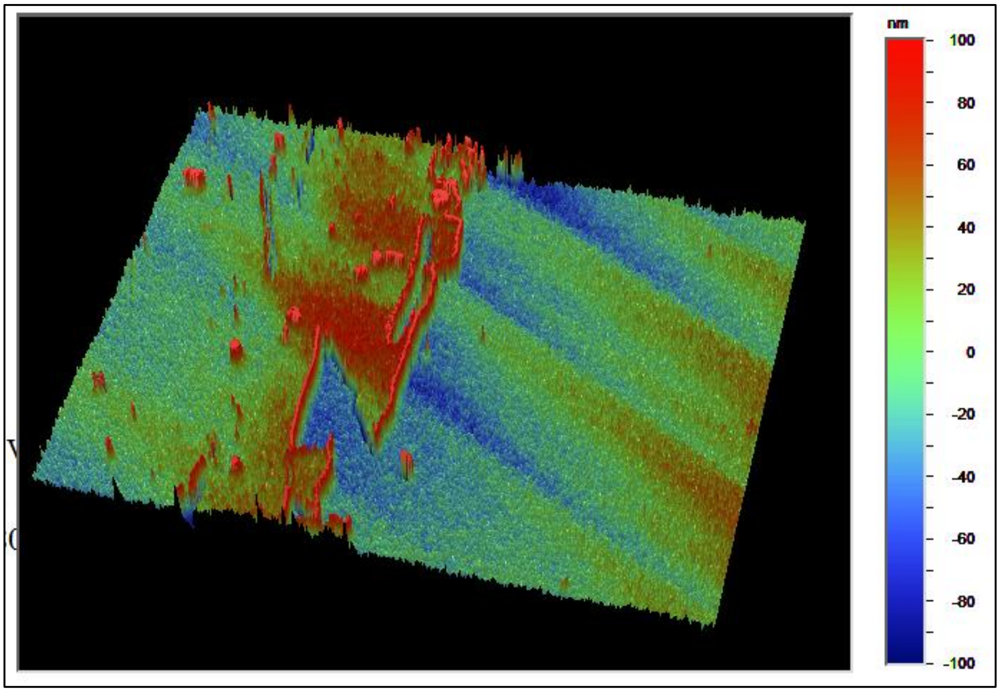

Figure 147. A three-dimensional surface profilometry scan of the surface of the dip coated copolymer coating after ice shedding event, shown at 10X magnification

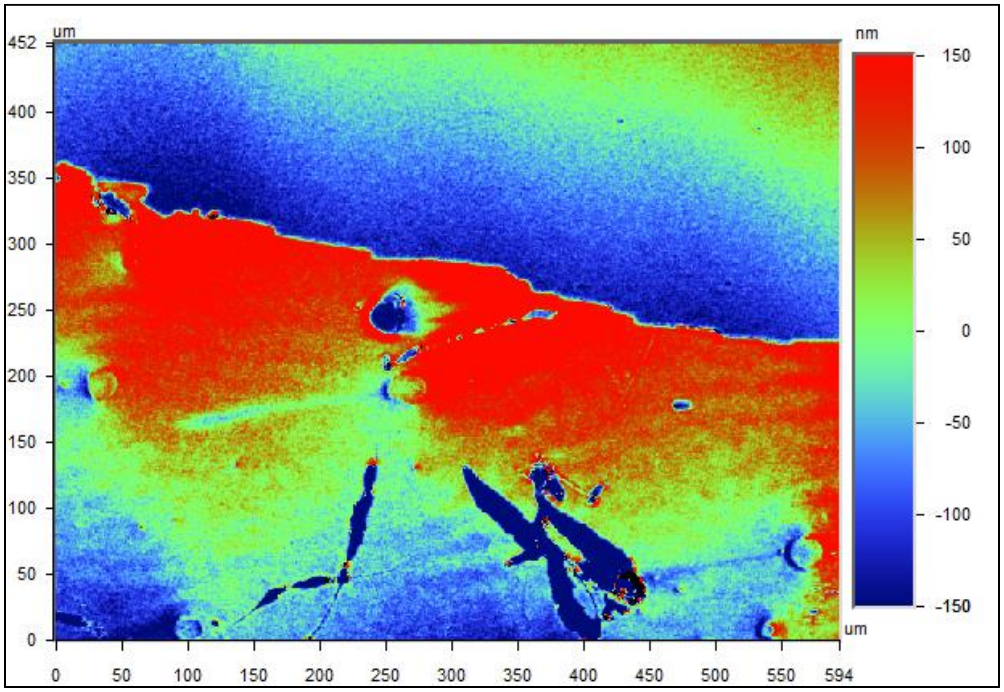

Figure 148. A two-dimensional surface profilometry scan of the surface of the dip coated copolymer coating after ice shedding event, shown at 10X magnification

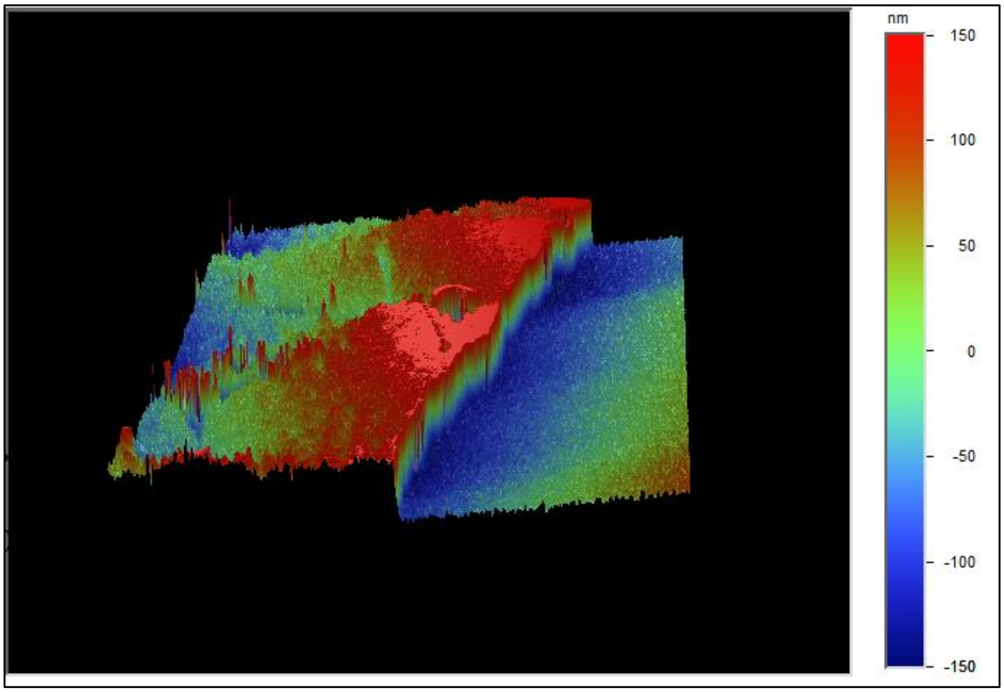

Figure 149. A three-dimensional surface profilometry scan of the surface of the dip coated copolymer coating after ice shedding event, shown at 10X magnification

The surface profilometry scans of the surface of the dip coated copolymer coating sample that has undergone an ice shedding event showed extensive damage to the coating surface. The scans show damage in the forms of linear gouges (Figures 144 & 145) creating troughs of exposed glass surface, they also show the jagged edges of the coating where large areas of the coating have been delaminated (Figure 146 – 149) with the ice exposing large areas of glass throughout the sample. Some have the appearance of brittle fracture.

Environmental Scanning Electron Microscopy

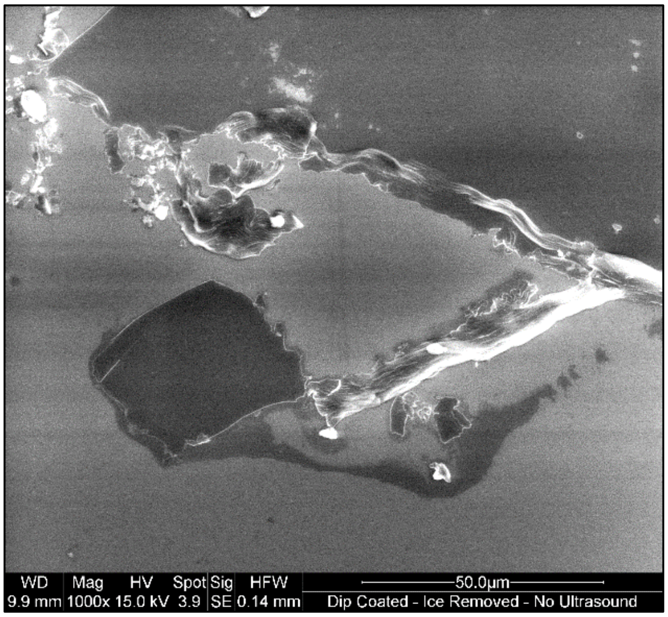

Figure 150. An ESEM image of the surface of the dip-coated glass sample after ice shedding event at 1000X magnification

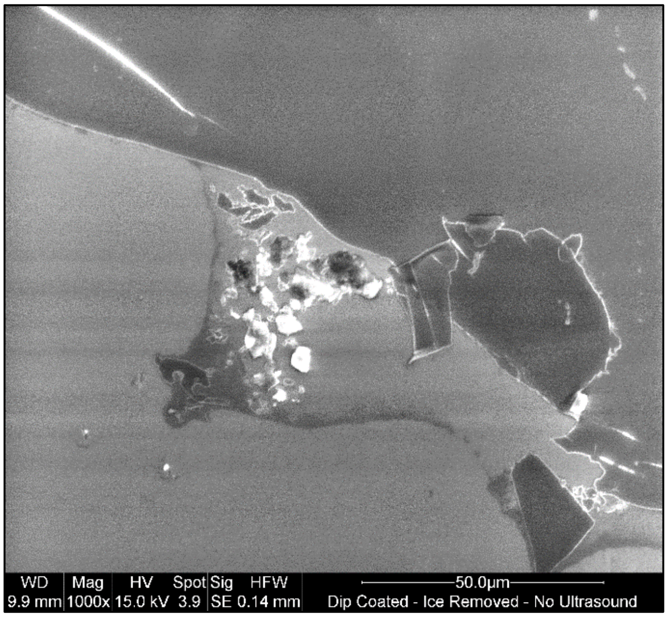

Figure 151. An ESEM image of the surface of the dip-coated glass sample after ice shedding event at 1000X magnification

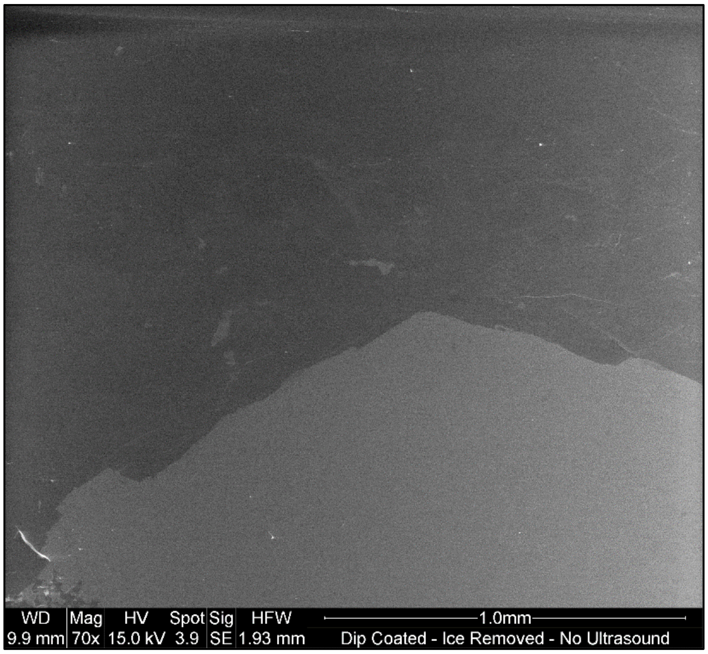

Figure 152. An ESEM image of the surface of the dip-coated glass sample after ice shedding event at 70X magnification

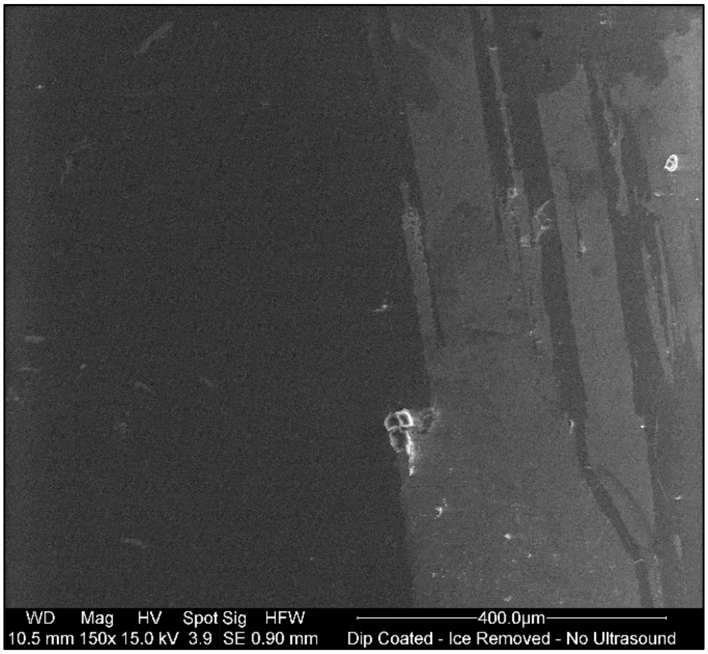

Figure 153. An ESEM image of the surface of the dip-coated glass sample after ice shedding event at 150X magnification

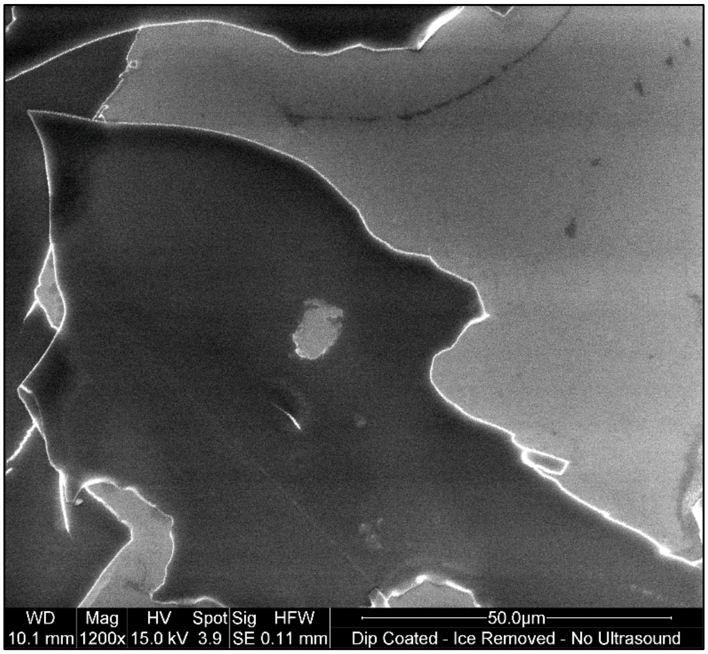

Figure 154. An ESEM image of the surface of the dip-coated glass sample after ice shedding event at 1200X magnification

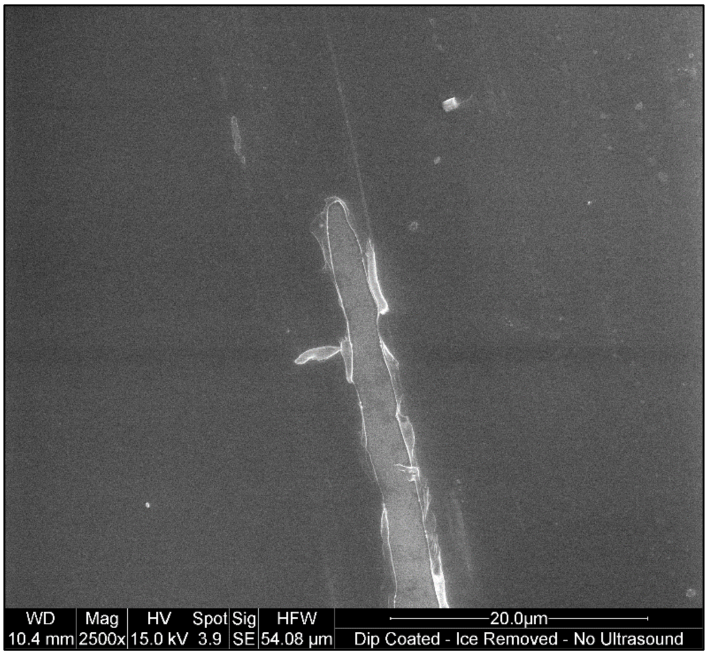

Figure 155. An ESEM image of the surface of the dip-coated glass sample after ice shedding event at 2500X magnification

The environmental electron scanning electron microscopy images of the surface of the dip coated copolymer coating sample that has undergone an ice shedding event showed extensive damage to the coating surface. The images also show damage in the forms of linear gouges (Figure 155) creating troughs of exposed glass surface, they also show the jagged edges of the coating where large areas of the coating have been delaminated (Figure 150 - 154) with the ice exposing large areas of glass throughout the sample. Some have the appearance of brittle fracture.

5. Discussion

Effect of thermal gradients on ice adhesion testing repeatability

The IAC can also be used to investigate the influence of ice/substrate/apparatus thermal gradients on the standard deviation of ice adhesion tests. Three possible combinations exist for the thermal starting points of the sample substrate and the distilled water to be frozen: 1) the experiment can be run using a sample substrate at -20°C and STP water, 2) The experiment can be run using a sample substrate at -20°C and icy water at ~1-3°C, 3) the experiment can be run using a sample substrate and water at STP. The significance of these experimental scenarios is that each will affect the ice/substrate interface differently due to the differing rates at which the heat is removed from the water to be frozen, and the sample substrate because of the difference in thermal gradient. Since it is not the aim of this study to accurately determine the effect of thermal heat transfer rates on the nucleation of ice and structure of ice, this thermal investigation will be limited to the effect it has on the standard deviation and repeatability of the IAC.

The ice adhesion using the frozen sample and ice water averaged over ten trials was 932.5 kPa, ranging from 626.3 kPa to 1304.1 kPa with a standard deviation of 207 kPa. The standard deviation is high at 22.2%.

The ice adhesion using the frozen sample and water at standard temperature and pressure averaged over ten trials was 794.9 kPa, ranging from 516.1 kPa to 1108 kPa with a standard deviation of 197.9 kPa. The standard deviation is high at 24.9%.

The ice adhesion using the sample and water at standard temperature and pressure averaged over ten trials was 1238.7 kPa, ranging from 1039.2 kPa to 1496.8 kPa with a standard deviation of 130.5 kPa. The standard deviation is acceptable at 10.5%.

As Table 56 and Figure 127. Show, there is a large difference in the accuracy and repeatability of the ice adhesion measurements when the initial starting temperatures of the water and sample are varied to create varying degrees of thermal gradients between the water and the sample, and the sample and the stage of the ice adhesion tester creating different conditions for ice nucleation and ice adhesion. The tests run using the frozen sample and ice water, and the frozen sample and water at standard temperature and pressure showed the highest standard deviations at 22.2% and 24.9%, both of these freezing conditions allow for a very rapid transfer of heat from the water/sample interface which will result in rapid ice nucleation and freezing. The test run using a sample and water at standard temperature and pressure exhibited markedly decreased standard deviation of only 10.5% and represents the condition in which heat will be transferred away from the water/sample interface the slowest and slows the rate of ice nucleation and freezing. The lowest thermal gradient between the water and the sample has exhibited the smallest standard deviation and represents the combination of initial starting temperatures for the water and sample that will give the most accurate results and will be used throughout the remainder of this investigation.

Effect of varying material on ice adhesion

It is necessary to measure the adhesion of ice to differing materials such as glass, aluminum, and stainless steel because there are three physical mechanisms involved in the adhesion of ice to a surface, specifically, hydrogen bonding, van der Waals forces, and direct electrostatic interactions. Of these three, the direct electrostatic interactions have been found to be the dominant factor (115)

(116). Charges on ice induce equal and opposite charges on metals, whereas on dielectrics, the induced charge is smaller and is related to the dielectric constant. Do to the fact that differing chemistry affects the adhesion of ice to a substrate and that different materials are used in the construction of the protective case assembly used to shield the photvoltaic cells from the outdoor climactic conditions it is necessary to test the adhesion of ice to the materials to determine its behavior and why this behavior is occuring.

The soda-lime glass microscope slides used had an average surface roughness of 11.27 nm, a root-mean-square value of 24.51 nm, and the peak-to-valley difference calculated over the entire measured array was 1.90 µm. The ice adhesion using the glass sample averaged over ten trials was 1561.5 kPa, ranging from 1338.5 kPa to 1748 kPa with a standard deviation of 112.8 kPa or 7.2%.

The polished aluminum samples used had an average surface roughness 22.2 of nm, a root-mean-square value of 27.9 nm, and the peak-to-valley difference calculated over the entire measured array was 243.3 nm. The ice adhesion using the polished aluminum sample averaged over ten trials was 1039.2 kPa, ranging from 843 kPa to 1190.6 kPa with a standard deviation of 116.8 kPa or 11.2%.

The polished stainless steel samples used had an average surface roughness of 2.74 nm, a root-mean-square value of 3.55 nm, and the peak-to-valley difference calculated over the entire measured array was 155.2 nm. The ice adhesion using the polished stainless steel sample averaged over ten trials was 1022 kPa, ranging from 825.8 kPa to 1176.8 kPa with a standard deviation of 115.2 kPa or 11.3%.

Figure 139. shows that despite a small difference in average surface roughness between the polished metal samples of aluminum and stainless steel (22.2 nm and 2.74 nm) there is very little

difference in average ice adhesion (1039.2 kPa and 1022 kPa). This is in stark contrast, however, to the large difference in average ice adhesion of the polished metal samples with the smooth glass sample of similar roughness. The average adhesion varies from 1022/1039.2 kPa to 1561.5 kPa when the surface roughness of the glass lies between that of the aluminum and stainless steel samples, 11.27 nm. This demonstrates that the average ice adhesion does not vary significantly between metallic samples of aluminum and stainless steel provided their surface roughness is similar. The average ice adhesion between ceramic materials and metallic materials varies considerably, however, despite the same similarity in surface roughness. This outcome could be predicted as the glass displayed an average water contact angle of just 22.2° classifying it as very hydrophilic. The glass samples also displayed a very high water contact angle hysteresis for such a low water contact angle at 15.5°, or 69.8%. This demonstrates that the glass surface is attracting and transiently bonding with the water droplet and exhibits high adhesion in the liquid state which will in turn become high adhesion in the solid/ice state. The polished aluminum and stainless steel samples, in contrast, showed water contact angles of 103.5° and 97.2° respectively, and water contact angle hysteresis of 43.83° and 58.17° respectively. It can be seen that the polished metallic samples exhibited much higher water contact angles and only marginally higher water contact angle hysteresis, relative. Although there is clearly attractive forces interacting between the water and metallic samples, the wettability results demonstrate there is less adhesive force in the liquid state, resulting in less adhesive force in the solid/ice state.

Effect of varying surface condition on ice adhesion

It is necessary to measure the adhesion of ice for different roughness and surface conditions because the materials used in the construction of the protective solar panel case (glass, aluminum, steel) are prepared in a variety of methods and each one will leave the material with a distinctive surface condition and roughness. Knowing that the protective casing and variety of materials composing it will be regularly exposed to climactic icing events it is important that the effect of the surface condition and roughness on the adhesion of ice be understood to ensure that the design of the proposed system is repeatable and reliable.

Aluminum

The polished aluminum samples used had an average surface roughness 22.2 of nm, a root-mean-square value of 27.9 nm, and the peak-to-valley difference calculated over the entire measured array was 243.3 nm. The ice adhesion using the polished aluminum sample averaged over ten trials was 1039.2 kPa, ranging from 843 kPa to 1190.6 kPa with a standard deviation of 116.8 kPa or 11.2%.

The moderate aluminum samples used had an average surface roughness of 3.04 µm, a root-mean-square value of 3.82 µm, and the peak-to-valley difference calculated over the entire measured array was 38.93 µm. The ice adhesion using the moderate aluminum sample averaged over ten trials was 1379.9 kPa, ranging from 1235.3 kPa to 1589.7 kPa with a standard deviation of 129.5 kPa or 9.4%.

The rough aluminum samples used had an average surface roughness of 5.06 µm, a root-mean-square value of 6.46 µm, and the peak-to-valley difference calculated over the entire measured array was 60.04 µm. The ice adhesion using the rough aluminum sample averaged over ten trials was 1582.8 kPa, ranging from 1397 kPa to 1803.1 kPa with a standard deviation of 125 kPa or 7.9%.

As Figure 132. shows, the ice adhesion on aluminum of different surface conditions shows a clear trend with the ice adhesion increasing as the surface condition includes a higher roughness. It can be seen from Table 61 and Figure 133. that when the average surface roughness of the samples are measured and plotted against the ice adhesion they behave in a linearly proportional manner. As the average surface roughness of the aluminum sample increased, so did the ice adhesion.

Stainless Steel

The polished stainless steel samples used had an average surface roughness of 2.74 nm, a root-mean-square value of 3.55 nm, and the peak-to-valley difference calculated over the entire measured array was 155.2 nm. The ice adhesion using the polished stainless steel sample averaged over ten trials was 1022 kPa, ranging from 825.8 kPa to 1176.8 kPa with a standard deviation of 115.2 kPa or 11.3%.

The moderate stainless steel samples used had an average surface roughness of 1.94 µm, a root-mean-square value of 2.42 µm, and the peak-to-valley difference calculated over the entire measured array was 20.41 µm. The ice adhesion using the moderate stainless steel sample averaged over ten trials was 1347.1 kPa, ranging from 1139 kPa to 1524.3 kPa with a standard deviation of 124.8 kPa or 9.3%.

The rough stainless steel samples used had an average surface roughness of 3.74 µm, a root-mean-square value of 4.8 µm, and the peak-to-valley difference calculated over the entire measured array was 61.28 µm. The ice adhesion using the rough stainless steel sample averaged over ten trials was 1608.3 kPa, ranging from 1417.7 kPa to 1758.3 kPa with a standard deviation of 111.6 kPa or 6.9%.

As Figure 137. shows, the ice adhesion on stainless steel of different surface conditions shows a clear trend with the ice adhesion increasing as the surface condition includes a higher roughness. It can be seen from Table 65 and Figure 138. that when the average surface roughness of the samples are measured and plotted against the ice adhesion they behave in a linearly proportional manner. As the average surface roughness of the stainless steel sample increased, so did the ice adhesion.

Smooth copolymer coating as icephobic coating

The smooth copolymer coating (3-[tris[(trimethylsilyl)oxy]-silyl]propyl methacrylate) was synthesized and deposited on the glass microscope slides via dip-coating. Two variables pertaining to the dip coating of the copolymer coating onto glass slides are the number of layers applied and the speeds at which the glass microscope slide is lowered and retracted with each dip. The MTS dip coater used throughout this study has the capability of varying the dipping speed between 5 - 200 mm/min, this has been divided into five speeds to test the effect that the speed of dipping has on the dip coated copolymer coating. The speeds used for dip coating are indicated in Table 19. Furthermore, the number of layers of the copolymer coating is another factor that must be investigated in order to understand the effect of the amount of layers on the performance of the coating. The design requirements of the smooth hydrophobic coating are full and complete coverage of the glass surface with no exposure of the glass. It requires a consistently smooth and level surface throughout the area of the glass microscope slide. It will require wettability properties that exhibit a high water contact angle indicating low surface energy and a very low water contact angle which indicates low adhesion of water to the coating. Finally, it requires good adhesion to the glass substrate and the durability to endure multiple violent ice shedding events.

The series of coatings created with one layer by varying the speed of dipping have all performed very similarly in regards to wettability. The five coatings deposited at speeds ranging from 5 – 200 mm/min exhibited an average water contact angle of 109°, ranging from 107° - 112° with a standard deviation of only 1.63°. Likewise, the contact angle hysteresis of the coatings were remarkably similar with an average of 34°, ranging from 32° - 36° with a standard deviation of only 1.97°. The series of coatings created with two layers by varying the speed of dipping have also all performed very similarly in regards to wettability. The five coatings deposited at speeds ranging from 5 – 200 mm/min exhibited an average water contact angle of 107.1°, ranging from 104.3° - 109.2° with a standard deviation of only 1.74°. Likewise, the contact angle hysteresis of the coatings were remarkably similar with an average of 33.4°, ranging from 31° - 35.8° with a standard deviation of only 1.7°.

It has been shown previously that the speed of dipping does not have a significant effect on the wettability properties on the dip-coated copolymer coatings of one or two layers. Likewise, the comparison of the average water contact angle and average water contact angle hysteresis of the one and two layer dip-coated copolymer coatings are very similar. The single layer coatings showed an average water contact angle of 109°, while the two layer coating showed an average water contact angle of 107.1°, a difference of only 1.9°. The single layer coating also showed an average contact angle hysteresis of 34°, while the two layer coating showed an average water contact angle hysteresis of 33.4°, a difference of only 0.6°. Furthermore, Figure 82. highlights the uniformity in wettability behavior of the dip-coated copolymer coatings created by varying the dipping speeds and coating layers.

Surface profilometry scans of the dip-coated samples (Figures 83. – 85.) reveal uniform topography comprised of a gentle flow morphology with dispersed ‘island’ features of low roughness. The surface of the dip-coated samples are very smooth with an average roughness of only 31 nm. Similarly, the root-mean-squared roughness calculated over the entire measured array is 43 nm and the average peak-to-valley difference calculated over the entire measured array is 862 nm. The environmental scanning electron microscopy images (Figures 86. & 87.) show the uniformly smooth surface of the dip-coated samples, at 8000X magnification, the 'island' morphology can be seen on the surface, at magnifications up to 30,000X no defined morphology can be distinguished on the surface. The properties of the smooth coating are favorable and the ice adhesion characteristics will be discussed in a later section.

Rough copolymer coating as icephobic coating

It is necessary to test both smooth and rough hydrophobic coatings because despite the rough surface of a superhydrophobic coating, it will reduce the adhesion of ice more than a smooth hydrophobic surface of the same chemical composition, and superhydrophobic coatings exhibiting a contact angle hysteresis lower than 5° lead to very high icephobic properties (18) (20) (21). However, the durability and mechanical robustness of the coating are particularly important to consider because the fragile hierarchical roughness can be irreversibly destroyed, which will inevitably lead to an increase in the contact angle hysteresis and a rapid decrease in the static contact angle (22). Rough superhydrophobic coatings offer attractive drastic ice adhesion reductions but come at the price of durability, whereas, the smooth hydrophobic coatings do not provide as much ice reduction but can provide a much more durable and transparent coating. Both must be tested in order to make an informed choice on which will be best coupled with ultrasonic transducers to remove the ice.

The design requirements of the rough hydrophobic coating are likewise to achieve full and complete coverage of the glass surface with no exposure of the glass. Unlike its smooth counterpart, the rough coating requires roughness not on one but two scales. Hierarchical roughness composed of micro- peaks and valleys, and nano- peaks and valleys are required for the ice adhesion reducing properties sought after. Cao et al. (23) demonstrated that the probability of icing occurring on the coating increased remarkably when the nano-scale roughness is greater than 50nm when the micro-scale roughness is 10μm. This indicates that the rough coating should also conform to nano-scale roughness of less than 50nm to achieve best ice adhesion reducing properties from the coating. It will require wettability properties that exhibit a high water contact angle indicating low surface energy and a very low water contact angle which indicates low adhesion of water to the coating. Finally, it also requires good adhesion to the glass substrate and the durability to endure multiple violent ice shedding events without losing the critical roughness parameters that impart its properties.

Two variables pertaining to the spray coating of the copolymer coating onto glass slides are the number of layers applied and the size of the nozzle used for spraying the coating solution. The Earlex HV5000 pressure sprayer has the ability to interchange the size of the spray nozzle between 1mm and 2mm. The size of the nozzle is an important factor to investigate as it dictates the size of the coating particles that are propelled towards the surface of the glass microscope slide. The size of the these coating projectiles will determine the rate at which they dry passing through the air and their subsequent dynamics with the glass surface, creating either the desired topography for superhydrophobicity and icephobicity, or an underachieving hydrophobic coating with poor icing properties. The number of passes with the pressure sprayer is another factor that must be considered, complete coverage of the surface is required in the design of a superhydrophobic coating with icephobic properties, however, the greater the number of passes used to create the coating the thicker the coating becomes and scatters more light leading to lower transmission in the visible light range. As Table 43. highlights, three variations have been used in the number of passes used in depositing the spray coating. First is lightly coated with only two full passes, the next is medium coated with four full passes, and finally the third is heavily coated with six full passes. Spray coated samples varying between two, four, and six passes with a 2mm and 1mm nozzle have been prepared and the wettability, morphological, and icing properties will be investigated by measuring the static water contact angles, contact angle hysteresis, surface profilometry, environmental scanning electron microscopy, and the ice adhesion.

The average water contact angle of the lightly sprayed coating with a 2mm nozzle was measured at 109.2° over three trials with a standard deviation of only 0.76° and the average water contact angle hysteresis was measured at 41° over three trials with a standard deviation of 2.2°. The optical image of the sample shows that the coating is visibly smooth and transparent with only a slight haze with inspection. The surface profilometry scans of the coating reveal that the surface of the slide is not completely coated, there are small areas of exposed glass throughout the sample surface. Surface profilometry scans of the spray coated samples (Figure 91.) reveal rough and sporadic topography comprised of large splats of coating overlaid on top of each other with some bare spots. The surface of the lightly spray coated samples are rough with an average roughness of 203 nm. Similarly, the root-mean-squared roughness calculated over the entire measured array is 322 nm and the average peak-to-valley difference calculated over the entire measured array is 41.5 µm. At 500X magnification using environmental scanning electron microscopy two types of coating solution splats are visible on the surface. The first type of splat exhibits the appearance of relatively large droplets of approximately 10 µm in diameter that formed a dried layer on its outside and subsequently evaporated and shriveled on the surface. The second type of splat is larger, being 20 – 30 µm in diameter, and shows uniform fine roughness within the boundaries of the splat.

The average water contact angle of the medium sprayed coating with a 2mm nozzle was measured at 107° over three trials with a standard deviation of only 3.78° and the average water contact angle hysteresis was measured at 37.3° over three trials with a standard deviation of 0.85°. The coating is visibly smooth and transparent with only a slight haze with inspection. The surface profilometry scans of the coating reveal that the surface of the slide is not completely coated, there are very small areas of exposed glass that appear rarely throughout the sample surface. Surface profilometry scans of the spray coated samples (Figure 95.) reveal rough and sporadic topography comprised of large splats of coating overlaid on top of each other with some rare bare spots. The surface of the medium spray coated samples are rough with an average roughness of 155 nm. Similarly, the root-mean-squared roughness calculated over the entire measured array is 473 nm and the average peak-to-valley difference calculated over the entire measured array is 45 µm. At 2000X magnification using environmental scanning electron microscopy two types of coating solution splats are visible on the surface. The first type of splat exhibits the appearance of relatively large droplets of approximately 10 µm in diameter that formed a dried layer on its outside and subsequently evaporated and shriveled on the surface, it appears less often and less formed in the medium sprayed than the lightly sprayed. The second type of splat is larger, being 20 – 30 µm in diameter, and shows uniform fine roughness within the boundaries of the splat.

The average water contact angle of the heavily sprayed coating with a 2mm nozzle was measured at 107.3° over three trials with a standard deviation of only 2.57° and the average water contact angle hysteresis was measured at 44° over three trials with a standard deviation of 1.08°. The optical image of the sample shows that the coating is visibly smooth and transparent with only a slight haze with inspection, slightly more than the lightly or medium sprayed coating. The surface profilometry scans of the coating reveal that the surface of the slide is completely coated, there are no areas of exposed glass that appear throughout the sample surface. Surface profilometry scans of the spray coated samples (Figures 99 & 100.) reveal very rough and sporadic topography comprised of large splats of coating overlaid on top of each other with some no bare spots. The surface of the heavily spray coated samples are rough with an average roughness of 137 nm. Similarly, the root-mean-squared roughness calculated over the entire measured array is 217 nm and the average peak-to-valley difference calculated over the entire measured array is 5.5 µm. At 12,000X magnification using environmental scanning electron microscopy two types of coating solution splats are visible on the surface. The first type of splat exhibits the appearance of relatively large droplets of approximately 5 -10 µm in diameter that formed a dried layer on its outside and subsequently evaporated and shriveled on the surface, it appears less often and less formed in the heavily sprayed than the lightly or medium sprayed. The second type of splat is larger, being 20 – 30 µm in diameter, and shows uniform fine roughness within the boundaries of the splat and appears most uniformly and often in the heavily sprayed coating.

The average water contact angle of the lightly sprayed coating with a 1mm nozzle was measured at 118.3° over three trials with a standard deviation of only 5.13° and the average water contact angle hysteresis was measured at 65.2° over three trials with a standard deviation of 6.5°. The optical image of the sample shows that the coating is visibly smooth and transparent with only a slight haze with inspection. The surface profilometry scans of the coating reveal that the surface of the slide is not completely coated, there are very small areas of exposed glass that appear rarely throughout the sample surface. Surface profilometry scans of the spray coated samples (Figures 107 - 109.) reveal rough and relatively uniform topography comprised of large splats comprised of small globular roughness with some rare bare spots. The surface of the lightly spray coated samples are very rough with an average roughness of 900 nm. Similarly, the root-mean-squared roughness calculated over the entire measured array is 990 nm and the average peak-to-valley difference calculated over the entire measured array is 5.5 µm. At 6000X magnification using environmental scanning electron microscopy mainly one types of coating solution splat is visible on the surface. The type of splat that is visible is larger, being 20 – 30 µm in diameter, and shows uniform fine globular roughness within the boundaries of the splat.

The comparison drawn in Table 52 and Figure 113. shows that when using the 2mm nozzle, using 2, 4, or 6 passes will not significantly affect the static water contact angle, with a deviation of less 1°, or the contact angle hysteresis, with a deviation of only 2.74°. The lightly sprayed coating of 2 passes with a 1mm nozzle showed an increase in static water contact angle over the 2mm nozzle, being 118.3°. The water contact angle hysteresis, however, has increased significantly using the 1mm nozzle, being 65.2°.

The final rough hydrophobic coating variations do meet the initial design requirements of full and complete coverage of the glass surface with no exposure of the glass. They do not, however, meet the requirements of hierarchical roughness as the roughness is relatively low and only on a single scale. This lack of hierarchical roughness, much less of the proper scale, indicates that it will perform very poorly in ice shedding events as the roughness will not reduce the adhesion but increase it as it will create mechanical interlocking as the water will penetrate the roughness morphology before freezing. This coating does not meet the requirements of an icephobic coating and will be incapable for use as an ice resistant coating.

Effect of hydrophobic copolymer coating on ice adhesion

It is necessary to test the ice adhesion of hydrophobic coatings because of the potential they show for reducing ice adhesion and preventing ice accumulation. Because active methods of ice removal (thermal, mechanical, chemical fluids) are energy hungry and expensive passive methods represent a cheaper option (17). Although, currently there is no known material that can completely prevent ice or snow from accumulating on its surface, hydrophobic coatings can provide reduced adhesion, and as the hydrophobicity of the surface increases, the ice adhesion decreases (18) (121).

The ice adhesion using the dip coated copolymer coating on glass sample averaged over five trials was 1248.2 kPa, ranging from 970.3 kPa to 1507.1 kPa with a standard deviation of 198 kPa or 15.9%. From figure 141. it can be seen that the addition of the dip-coated copolymer coating to the glass did not make a significant reduction in the ice adhesion (1561.5 to 1248.2 kPa), and resulted in an increase of the standard deviation (112.8 to 198 kPa). The surface profilometry scans and environmental electron microscopy images of the surface of the dip coated copolymer coating sample that has undergone an ice shedding event showed extensive damage to the coating surface. The scans show damage in the forms of linear gouges (Figures 144 & 145) creating troughs of exposed glass surface, they also show the jagged edges of the coating where large areas of the coating have been delaminated (Figure 146 - 149) with the ice exposing large areas of glass throughout the sample. Some have the appearance of brittle fracture. Despite showing positive characteristics and meeting the design requirements for a smooth, ice-resistant, hydrophobic coating, the copolymer coating failed under ice shedding events. The ice adhesion measurements, the surface profilometry, and the environmental scanning electron microscopy images reveal that the coating delaminated under the stress of ice removal and performed poorly in reducing the ice adhesion. A coating with more mechanical robustness should be used in the next trial.

Effect of ultrasonic vibration on ice adhesion

The IAC can measure the ice adhesion of any sample substrate under ultrasonic vibration by using the same method as previously explained method with one additional step. When the linear actuator is started and applying in turn apply the shearing force to the ice/substrate interface, the ultrasonic transducer which can be installed in one of two positions, will be activated and will send vibrations through the ice/substrate interface at 20,000 cycles per second to break or weaken the bonds. Due to the current inability of the hydrophobic coatings to consistently prevent any adherence of ice it is necessary to couple the hydrophobic coatings with an ultrasonic transducer to mechanically break what weak bonds may have been able to form between the coating/substrate and the ice. This then dictates the necessity to measure the ice adhesion of candidate hydrophobic coatings in order to determine which can most prevent the adhesion of ice while maintaining the other necessary factors for a coating to be used in photovoltaic device applications (transparency, durability, etc). This characterization of the coating will also allow for the selection of a transducer which will use as little energy as is needed to remove the ice because it has been intelligently coupled with the hydrophobic coating. Without proper understanding of how the hydrophobic coating will affect the ice adhesion an ultrasonic transducer may be used that is not optimized and over the lifetime of the system it will use many time more energy than would be needed.

The ice adhesion on glass using ultrasonic vibration at 20 kHz at 700W in the transverse direction to the ice/sample interface averaged over ten trials was 58.5 kPa, ranging from 0 kPa to 182.4 kPa with a standard deviation of 75.2 kPa or 128.5%. From figure 242. It can be seen that the introduction of the ultrasonic vibration (700W, 20 kHz, transverse direction) during ice adhesion testing on glass has drastically decreased the adhesion with which ice can adhere, from 1561.5 to 58.5 kPa on average, a decrease of 96.3%. With the success of the 700W ultrasonic transducer at 20 kHz, smaller power sizes (250W or 500W) can be tested and combined with hydrophobic coatings to optimize the efficiency of the system.

6. Summary & Conclusions

In conclusion, the objective of this investigation has been completed. A method of measuring the ice adhesion of various materials with differing surface conditions with the option of adding ultrasonic vibrational input has been designed and fabricated. The design features of the ice adhesion tester include the ability to be able to hold interchangeable samples, in order to change the material being tested and/or the surface conditions of the sample. It includes a feature that allows known surface areas of ice to be frozen to the samples and has the ability to apply strictly shearing forces to only the ice in sufficient quantities capable of breaking the bonds of ice to the sample. There is a convenient means of calculating or measuring the shearing force that was required to debond the ice from the sample. The ice adhesion tester has a computer interface for operation, and an electronic data acquisition system for the accumulation and interpretation of the data obtained. It possesses the ability to mount ultrasonic transducers of varying power in both the normal and transverse direction to the ice/substrate interface and to remotely operate it. Finally, it is able to control the climate conditions that the tests are exposed to and be capable of measuring and monitoring these conditions.

Additionally, a custom-designed apparatus was built to investigate the surface wettability of samples of varying materials with differing surface conditions, called a goniometer. This goniometer is specially adapted to measure the angle that a droplet of liquid makes contact with the surface. The design features of the goniometer include the ability to be able to capture and save images of the droplet profile while resting on the sample surface. The goniometer is capable of recording videos of the addition and withdrawal of liquid to and from the droplets resting on the sample surface. It is capable of sharing information through a computer interface to work with electronic data. The device can deposit and withdrawal very precise volumes of water, down to the microliter. Lastly, the device has a method of determining the angle with which the droplet of water meets the sample surface which will indicate the water contact angle, and allow the calculation of the water contact angle hysteresis.

There is a large difference in the accuracy and repeatability of the ice adhesion measurements when the initial starting temperatures of the water and sample are varied to create varying degrees of thermal gradients between the water and the sample, and the sample and the stage of the ice adhesion tester creating different conditions for ice nucleation and ice adhesion. The tests run using the frozen sample and ice water, and the frozen sample and water at standard temperature and pressure showed the highest standard deviations at 22.2% and 24.9%, both of these freezing conditions allow for a very rapid transfer of heat from the water/sample interface which will result in rapid ice nucleation and freezing. The test run using a sample and water at standard temperature and pressure exhibited markedly decreased standard deviation of only 10.5% and represents the condition in which heat will be transferred away from the water/sample interface the slowest and slows the rate of ice nucleation and freezing. The lowest thermal gradient between the water and the sample has exhibited the smallest standard deviation and represents the combination of initial starting temperatures for the water and sample that will give the most accurate results

Despite a small difference in average surface roughness between the polished metal samples of aluminum and stainless steel (22.2 nm and 2.74 nm) there is very little difference in average ice adhesion (1039.2 kPa and 1022 kPa). This is in stark contrast, however, to the large difference in average ice adhesion of the polished metal samples with the smooth glass sample of similar roughness. The average adhesion varies from 1022/1039.2 kPa to 1561.5 kPa when the surface roughness of the glass lies between that of the aluminum and stainless steel samples, 11.27 nm. This demonstrates that the average ice adhesion does not vary significantly between metallic samples of aluminum and stainless steel provided their surface roughness is similar. The average ice adhesion between ceramic materials and metallic materials varies considerably, however, despite the same similarity in surface roughness. This outcome could be predicted as the glass displayed an average water contact angle of just 22.2° classifying it as very hydrophilic. The glass samples also displayed a very high water contact angle hysteresis for such a low water contact angle at 15.5°, or 69.8%. This demonstrates that the glass surface is attracting and transiently bonding with the water droplet and exhibits high adhesion in the liquid state which will in turn become high adhesion in the solid/ice state. The polished aluminum and stainless steel samples, in contrast, showed water contact angles of 103.5° and 97.2° respectively, and water contact angle hysteresis of 43.83° and 58.17° respectively. It can be seen that the polished metallic samples exhibited much higher water contact angles and only marginally higher water contact angle hysteresis, relative. Although there is clearly attractive forces interacting between the water and metallic samples, the wettability results demonstrate there is less adhesive force in the liquid state, resulting in less adhesive force in the solid/ice state.

The ice adhesion on aluminum of different surface conditions shows a clear trend with the ice adhesion increasing as the surface condition includes a higher roughness. It can be seen from Table 61 and Figure 193. that when the average surface roughness of the samples are measured and plotted against the ice adhesion they behave in a linearly proportional manner. As the average surface roughness of the aluminum sample increased, so did the ice adhesion.

The ice adhesion on stainless steel of different surface conditions shows a clear trend with the ice adhesion increasing as the surface condition includes a higher roughness. It can be seen from

Table 65 and Figure 228. that when the average surface roughness of the samples are measured and plotted against the ice adhesion they behave in a linearly proportional manner. As the average surface roughness of the stainless steel sample increased, so did the ice adhesion.

The ice adhesion on glass using ultrasonic vibration at 20 kHz at 700W in the transverse direction to the ice/sample interface averaged over ten trials was 58.5 kPa, ranging from 0 kPa to 182.4 kPa with a standard deviation of 75.2 kPa or 128.5%. From figure 242. It can be seen that the introduction of the ultrasonic vibration (700W, 20 kHz, transverse direction) during ice adhesion testing on glass has drastically decreased the adhesion with which ice can adhere, from 1561.5 to 58.5 kPa on average, a decrease of 96.3%. With the success of the 700W ultrasonic transducer at 20 kHz, smaller power sizes (250W or 500W) can be tested and combined with hydrophobic coatings to optimize the efficiency of the system.

The speed of dipping does not have a significant effect on the wettability properties on the dip-coated copolymer coatings of one or two layers. Likewise, the comparison of the average water contact angle and average water contact angle hysteresis of the one and two layer dip-coated copolymer coatings are very similar. The single layer coatings showed an average water contact angle of 109°, while the two layer coating showed an average water contact angle of 107.1°, a difference of only 1.9°. The single layer coating also showed an average contact angle hysteresis of 34°, while the two layer coating showed an average water contact angle hysteresis of 33.4°, a difference of only 0.6°.

The ice adhesion using the dip coated copolymer coating on glass sample averaged over five trials was 1248.2 kPa, ranging from 970.3 kPa to 1507.1 kPa with a standard deviation of 198 kPa or 15.9%. From figure 235. it can be seen that the addition of the dip-coated copolymer coating to the glass did not make a significant reduction in the ice adhesion (1561.5 to 1248.2 kPa), and resulted in an increase of the standard deviation (112.8 to 198 kPa). The surface profilometry scans and environmental electron microscopy images of the surface of the dip coated copolymer coating sample that has undergone an ice shedding event showed extensive damage to the coating surface. The scans show damage in the forms of linear gouges (Figures 243, 244, & 254) creating troughs of exposed glass surface, they also show the jagged edges of the coating where large areas of the coating have been delaminated (Figure 245 – 248, & 249 - 253) with the ice exposing large areas of glass throughout the sample. Some have the appearance of brittle fracture. Despite showing positive characteristics and meeting the design requirements for a smooth, ice-resistant, hydrophobic coating, the copolymer coating failed under ice shedding events. The ice adhesion measurements, the surface profilometry, and the environmental scanning electron microscopy images reveal that the coating delaminated under the stress of ice removal and performed poorly in reducing the ice adhesion. A coating with more mechanical robustness should be used in the next trial.

When using the 2mm nozzle, using 2, 4, or 6 passes will not significantly affect the static water contact angle, with a deviation of less 1°, or the contact angle hysteresis, with a deviation of only 2.74°. The lightly sprayed coating of 2 passes with a 1mm nozzle showed an increase in static water contact angle over the 2mm nozzle, being 118.3°. The water contact angle hysteresis, however, has increased significantly using the 1mm nozzle, being 65.2°.

The final rough hydrophobic coating variations do meet the initial design requirements of full and complete coverage of the glass surface with no exposure of the glass. They do not, however, meet the requirements of hierarchical roughness as the roughness is relatively low and only on a single scale. This lack of hierarchical roughness, much less of the proper scale, indicates that it will perform very poorly in ice shedding events as the roughness will not reduce the adhesion but increase it as it will create mechanical interlocking as the water will penetrate the roughness morphology before freezing. This coating does not meet the requirements of an icephobic coating and will be incapable for use as an ice resistant coating.

Suggestions for future research

The current study concentrated on building the foundational framework for the research of ice adhesion and surface engineering in renewable energy fields at the University of Windsor. Considerable time and expense were dedicated to the custom design and in-house fabrication of the goniometer and ice adhesion tester used in this study. Furthermore, preliminary testing of the machines, samples, and coatings were necessary to establish precise working conditions for the future generations of this project. Future study of prevention of ice accumulation and adhesion on various materials for the renewable energy sector can be achieved by research in the following areas:

1. A future candidate for the smooth hydrophobic coating should show considerable mechanical robustness if it is to withhold its adhesion as the ice is being removed. A possible control coating to use for further study or comparison could be a diamond like carbon (DLC) coating due to the intrinsic low surface roughness, good hydrophobicity, transparency, and mechanical robustness.
2. A future candidate for the rough hydrophobic coating should possess a facile method of hierarchical roughness fabrication included in the method of its deposition. This will ensure the proper roughness which is critically important when considering rough hydrophobic coatings. A possible candidate for future study can be a polymeric based coating that uses a nano- porous silica powder to create an intrinsic roughness.

3. Lower powers of ultrasonic transducers can be tested. An ultrasonic transducer at 700W, 20 kHz, in the transverse direction was used with great success, it is likely that a lower powered transducer will provide similar benefits at less power expended. Furthermore, if possible a transducer could be used at the same power with varying frequencies to maximize the delaminating benefits of the vibration when it hits the natural or resonant frequency of the device.
4. Lastly, combinations of suitable hydrophobic coatings and the optimized ultrasonic vibration can be used together and tested against the ice adhesion of various materials with various surface conditions to achieve a truly optimized, remotely operated de-icing apparatus that can be used in many renewable energy sector applications.

References

1. *Ice adhesion issues in renewable energy infrastructure.* **R. Carriveau, A. Edrisy, P. Cadieux, and R. Mailloux.** 2012, J. Adhes. Sci. Technol., pp. 26(4-5): 447-461.

2. *Estimation of the energetic and environmental impacts of a roof-mounted building-integrated photovoltaic system.* **F. Cucchiella, and I. Dadamo.** 7, 2012, Renew. Sust. Energ. Rev., Vol. 16, pp. 5245-5259.

3. *State-scale evaluation of renewable electricity policy: The role of renewable electricity credits and carbon taxes.* **T. Levin, V. M. Thomas, and A. J. Lee.** 2, 2010, Energ. Policy, Vol. 39, pp. 950-960.

4. *Potential of renewable energy systems in China.* **W. Liu, H. Lund, B. V. Mathiesen, and X. Zhang.** 2, 2011, Appl. Energ., Vol. 88, pp. 518-525.

5. *Canada's energy perspective and policies for sustainable development.* **K. Hofman, and X. Li.** 4, 2009, Appl. Energ., Vol. 86, pp. 407-415.

6. **Administration, U.S. Energy Information.** *International Energy Outlook.* Washington, DC : U.S. Department of Energy, 2010.

7. *The transition to renewables: Can PV provide an answer to the peak oil and climate change challenges?* **B. Lloyd, and A. S. Forest.** 11, s.l. : Energ. Policy, 2010, Energ. Policy, Vol. 38, pp. 7378-7394.

8. *A global perspective on the renewable energy consumption-growth nexus.* **N. Apergis, and J. E. Payne.** 3, 2012, Energ. Source. Part B, Vol. 7, pp. 314-322.

9. *Energy for sustainable development: Key issues and challenges.* **Kaygusuz, K.** 1, 2007, Energ. Source. Part B, Vol. 2, pp. 73-83.

10. **Program, United Nations Development.** *World Energy Assessment: Energy and the challenge of sustainability.* New York : Goldemberg, J. ed, 2000.

11. *A review of modern wind turbine technology.* **Balat, M.** 17, s.l. : Energ. Source. Part A, 2009, Energ. Source. Part A, Vol. 31, pp. 1561-1572.

12. *Potential contribution of geothermal energy to climate change adaption: A case study of the arid and semi-arid eastern baringo lowlands, Kenya.* **P. F. A. Ogola, B. Davidsdottir, and I. B. Fridleifsson.** 6, 2012, Renew. Sust. Energ. Rev., Vol. 16, pp. 4222-4246.

13. *Solar energy conversion by dye-sensitized photovoltaic cells.* **Gratzel, M.** 20, 2005, Inorganic Chemistry, Vol. 44, pp. 6841-6851.

14. *A review of surface engineering issues critical to wind turbine performance.* **N. Dalili, A. Edrisy, and R. Carriveau.** 2, 2009, Renew. Sust. Energ. Rev. , Vol. 13, pp. 428-438.

15. *Modeling and prevention of ice accretion on wind turbines.* **L. Makkonen, T. Laakso, M. Marjaniemi, and K. J. Finstad.** 1, 2001, Wind Eng., Vol. 25, pp. 3-21.

16. *Effects of hostile terrains on wind turbine performance and loads: The acqua spruzza experience.* **G. Botta, M. Cavaliere, S. Viani, and S. Pospisil.** 1998, J. Wind Eng. Ind. Aerod., Vols. 74-76, pp. 419-431.

17. *Elaboration of Al2O3/PTFE icephobic coatings for protecting aluminum surfaces.* **R. Menini, and M. Farzaneh.** 14, 2009, Surf. Coat. Tech., Vol. 203, pp. 1941-1946.

18. *Ice adhesion on super-hydrophobic surfaces.* **S. A. Kulinich, and M. Farzaneh.** 18, 2009, Appl. Surf. Sci., Vol. 255, pp. 8153-8157.

19. *Frost formation and ice adhesion on superhydrophobic surfaces.* **K. K. Varanasi, T. Deng, J. D. Smith, M. Hsu, and N. Bhate.** 23, 2010, Appl. Phys. Lett., Vol. 97.

20. *How wetting hysteresis influences ice adhesion strength on superhydrophobic surfaces.* **S. A. Kulinich, and M. Farzaneh.** 16, 2009, Langmuir, Vol. 25, pp. 8854-8856.

21. *On ice-releasing properties of rough hydrophobic coatings.* **S. A. Kulinich, and M. Farzaneh.** 1, 2011, Cold Reg. Sci. Technol., Vol. 65, pp. 60-64.

22. *Mechanically durable superhydrophobic surfaces.* **T. Verho, C. Bower, P. Andrew, S. Franssila, O. Ikkala, and R. H. A. Ras.** 5, 2011, Adv. Mater., Vol. 23, pp. 673-678.

23. *Anti-icing superhydrophobic coatings.* **L. Cao, A. K. Jones, V. K. Sikka, J. Wu, and D. Gao.** 21, 2009, Langmuir, Vol. 25, pp. 12444-12448.

24. *Superhydrophobic surfaces: Are they really ice-repellent?* **S. A. Kulinich, S. Farhadi, K. Nose, and X. W. Du.** 1, 2011, Langmuir, Vol. 27, pp. 25-29.

25. *Instantaneous de-icing of freezer ice via ultrasonic actuation.* **J. Palacios, E. Smith, J. Rose, R. Royer.** 6, 2011, AIAA Journal, Vol. 49.

26. *Design of a transparent hydrophobic coating.* **Nakajima, A.** 1310, 2004, J. Ceram. Soc. Jpn., Vol. 112, pp. 533-540.

27. *Model for contact angles and hysteresis on rough and ultraphobic surfaces.* **Extrand, C. W.** 21, 2002, Langmuir, Vol. 18, pp. 7991-7999.

28. *Hierarchical roughness optimization for biomimetic superhydrophobic surfaces.* **M. Nosonovsky, and B. Bhushan.** 10-11, 2007, Ultramicroscopy, Vol. 107, pp. 969-979.

29. *Studies at phase interfaces. I. the sliding of liquid drops on solid surfaces and a theory for spray retention.* **Furmidge, C. G. L.** 4, 1962, J. Colloid Sci., Vol. 17, pp. 309-324.

30. *Purity of the sacred lotus, or escape from contamination in biological surfaces.* **W. Barthlott, and C. Neinhuis.** 1, 1997, Planta, Vol. 202, pp. 1-8.

31. *Characterization and distribution of water-repellant, self-cleaning plant surfaces.* **C. Neinhuis, and W. Barthlott.** 6, 1997, Ann. Botany, Vol. 79, pp. 667-677.

32. *Mimicking natural superhydrophobic surfaces and grasping the wetting process: A review on recent progress in preparing superhydrophobic surfaces.* **Y. Y. Yan, N. Gao, and W. Barthlott.** 2, 2011, Adv. Colloid Interfac., Vol. 169, pp. 80-105.

33. *Nanowire dye-sensitized solar cells.* **M. Law, L. E. Greene, J. C. Johnson, R. Saykally, and P. Yang.** 6, 2005, Nature Mater., Vol. 4, pp. 455-459.

34. *Hierarchical ZnO nanowire-nanosheet architectures for high power conversion efficiency in dye-sensitized solar cells.* **F. Xu, M. Dai, Y. Lu, and L. Sun.** 6, 2010, J. Phys. Chem. C, Vol. 114, pp. 2776-2782.

35. *Microfabricated adhesive mimicking gecko foot-hair.* **A. K. Geim, S. V. Dubonos, I. V. Grigorieva, K. S. Novoselov, A. A. Zhukov, and S. Y. Shapoval.** 7, 2003, Nature Mater., Vol. 2, pp. 461-463.

36. *A reversible wet/dry adhesive inspired by mussels and geckos.* **H. Lee, B. P. Lee, and P. B. Messersmith.** 7151, 2007, Nature, Vol. 448, pp. 338-341.

37. *Fabrication of high aspect ratio microfiber arrays that mimic gecko foot hairs.* **S. Y. Liu, P. Zhang, H. Lu, C. W. Zhang, and Q. Xia.** 4, 2012, Chin. Sci. Bull., Vol. 57, pp. 404-408.

38. *Adhesion design maps for bio-inspired attachment systems.* **R. Spolenak, S. Gorb, and E. Arzt.** 1, 2005, ActaBiomater., Vol. 1, pp. 5-13.

39. *Mussel adhesive protein mimetic polymers for the preparation of nonfouling surfaces.* **J. L. Dalsin, B. Hu, B. P. Lee, and P. B. Messersmith.** 14, 2003, J. Am. Chem. Soc., Vol. 125, pp. 4253-4258.

40. *Morpho butterfly wing scales demonstrate highly selective vapour response.* **R. A. Potyrailo, H. Ghiradella, A. Vertiatchikh, K. Dovidenko, J. R. Cournover, and E. Olson.** 2, 2007, Nature Photon, Vol. 1, pp. 123-128.

41. *Controlled replication of butterfly wings for achieving tunable photonic properties.* **J. Huang, X. Wang, and Z. L. Wang.** 10, 2006, Nano Lett., Vol. 6, pp. 2325-2331.

42. *Biomimetics of photonic nanostructures.* **A. R. Parker, and H. E. Townley.** 6, 2007, Nat. Nanotechnol., Vol. 2, pp. 347-353.

43. *Nano-optics in the biological world: Beetles, butterflies, birds, and moths.* **Srinivasarao, M.** 7, 1999, Chem. Rev., Vol. 99, pp. 1935-1961.

44. *Photonic structures in biology.* **P. Vukusic, and J. R. Sambles.** 6950, 2003, Nature, Vol. 424, pp. 852-855.

45. *Bioinspired self-cleaning antireflection coatings.* **W. Min, B. Jiang, and P. Jiang.** 20, 2008, Adv. Mater., Vol. 20, pp. 3914-3918.

46. *A facile approach for artificial biomimetics surfaces with both superhydrophobicity and iridescence.* **D. Wu, Q. Chen, H. Xia, J. Jiao, B. Xu, X. Lin, and H. Sun.** 2, 2010, Soft Matter., Vol. 6, pp. 263-267.

47. *Biomimetic surfaces for high-performance optics.* **Y. Li, J. Zhang, S. Zhu, H. Dong, F. Jia, Z. Wang, and B. Yang.** 46, 2009, Adv. Mater., Vol. 21, pp. 4731-4734.

48. *Stable polytetrafluoroethylene superhydrophobic surfaces with lotus-leaf structure.* **W. Hou, and Q. Wang.** 1, 2009, J. Colloid Interfac., Vol. 333, pp. 400-403.

49. *Biomimetic hierarchical structure for self-cleaning.* **B. Bhushan, K. Koch, and Y. C. Jung.** 9, 2008, App. Phys. Lett., Vol. 93.

50. *Superhydrophobic and superhydrophilic plant surfaces: An inspiration for biomimetic materials.* **K. Koch, and W. Barthlott.** 1893, 2009, Phil. Trans. R. Soc. A., Vol. 367, pp. 1487-1509.

51. *Bioinspired surfaces with special wettability.* **T. Sun, L. Feng, X. Gao, and L. Jiang.** 8, 2005, Acc. Chem. Res., Vol. 38, pp. 644-652.

52. *Water-repellent legs of water striders.* **X. Gao, and L. Jiang.** 7013, 2004, Nature, Vol. 432, p. 36.

53. *Nanostructuring of a polymeric substrate with well-defined nanometer-scale topography and tailored surface wettability.* **W. Lee, M. Jin, W. Yoo, and J. Lee.** 18, 2004, Langmuir, Vol. 20, pp. 7665-7669.

54. *Superhydrophobic surfaces: From natural to biomimetic to functional.* **Z. Guo, W. Liu, and B. Su.** 2, 2011, J. Colloid Interfac., Vol. 353, pp. 335-355.

55. *Super-hydrophobic surfaces: From natural to artificial.* **L. Feng, S. Li, Y. Li, H. Li, L. Zhang, J. Zhai, and D. Zhu.** 24, 2002, Adv. Mater., Vol. 14, pp. 1857-1860.

56. *Mimicking biological structured surfaces by phase-separation micromolding.* **J. Gao, Y. Liu, H. Xu, Z. Wang, and X. Zhang.** 8, 2009, Langmuir, Vol. 25, pp. 4365-4369.

57. *Biostructure-like surfaces with thermally responsive wettability prepared by temperature-induced phase separation micromolding.* **J. Gao, Y. Liu, H. Xu, Z. Wang, and X. Zhang.** 12, 2010, Langmuir, Vol. 26, pp. 9673-9676.

58. *Fabrication of biomimetic superhydrophobic surfaces inspired by lotus leaves and silver ragwort leaf.* **J. Lin, Y. Cai, X. Wang, B. Ding, J. Yu, and M. Wang.** 3, 2011, Nanoscale, Vol. 3, pp. 1258-1262.

59. *The dream of staying clean: Lotus and biomimetic surfaces.* **A. Solga, Z. Cerman, B. F. Striffler, M. Spaeth, and W. Barthlott.** 4, 2007, Bioinspir. Biomim., Vol. 2, pp. S126-S134.

60. *An essay on the cohesion of fluids.* **Young, T.** 1805, Phil. Trans. R. Soc. London, Vol. 95, pp. 65-87.

61. *Resistance of solid surfaces to wetting by water.* **Wenzel, R. N.** 8, 1936, Ind. Eng. Chem. Res., Vol. 28, pp. 988-994.

62. *Surface roughness and contact angle.* **Wenzel, R. N.** 9, 1949, J. Phys. Colloid. Chem., Vol. 53, pp. 1466-1467.

63. *Wettability of porous surfaces.* **A. B. D. Cassie, and S. Baxter.** 1944, Trans. Farad. Soc., Vol. 40, pp. 546-551.

64. *Contact angles.* **Cassie, A. B. D.** 1948, Discuss. Farad. Soc., Vol. 3, pp. 11-16.

65. *Optically transparent, superhydrophobic methyltrimethoxysilane based silica coatings without silylating reagent.* **M. S. Kavale, D. B. Mahadik, V. G. Parale, P. B. Wagh, S. C. Gupta, A. V. Rao, and H. C. Barshilia.** 1, 2011, Appl. Surf. Sci., Vol. 258, pp. 158-162.

66. *Properties of films of adsorbed fluorinated acids.* **E. F. Hare, E. G. Shafrin, and W. A. Zisman.** 3, 1954, J. Phys. Chem., Vol. 58, pp. 236-239.

67. *The lowest surface free energy based on -CF3 alignment.* **T. Nishino, M. Meguro, K. Nakamae, M. Matsushita, and Y. Ueda.** 13, 1999, Langmuir, Vol. 15, pp. 4321-4323.

68. *Hydrophobic and self-cleaning coatings.* **H. Dodiuk. P. F. Rios, A. Dotan, and S. Kenig.** 9, 2007, Polymer Adv. Tech., Vol. 18, pp. 746-750.

69. *Superhydrophobic surfaces with hierarchical structure.* **N. Gao, Y. Y. Yan, X. Y. Chen, and D. J. Mee.** 19-20, 2011, Mater. Lett., Vol. 65, pp. 2902-2905.

70. *Multiscale roughness and stability of superhydrophobic biomimetic interfaces.* **Nosonovsky, M.** 6, 2007, Langmuir, Vol. 23, pp. 3157-3161.

71. *Fabrication of biomimetic superhydrophobic coating with a micro-nano-binary structure.* **N. Zhao, J. Xu, Q. Xie, L. Weng, X. Guo, X. Zhang, and L. Shi.** 13, 2005, Macrocol. Rapid Commun., Vol. 26, pp. 1075-1080.

72. *The effects of nanostructure and composition on the hydrophobic properties of solid surfaces.* **P. F. Rios, H. Dodiuk, S. Kenig, S. McCarthy, and A. Dotan.** 6, 2006, J. Adhes. Sci. Technol. , Vol. 20, pp. 563-587.

73. *Transparent ultra-hydrophobic surfaces.* **P. F. Rios, H. Dodiuk, S. Kenig, S. McCarthy and A. Dotan.** 5-6, 2007, J. Adhes. Sci. Technol., Vol. 21, pp. 399-408.

74. *Characteristics of ultra-water-repellent thin films prepared by combined process of microwave plasma-enhanced CVD and oxygen-plasma treatment.* **Y. Wu, Y. Inoue, H. Sugimura, O. Takai, H. Kato, S. Murai, and H. Oda.** 1-2, 2002, Thin Solid Films, Vol. 407, pp. 45-49.

75. *Fabrication of microtemplates for the control of bacterial immobilization.* **Y. Miyahara, K. Mitamura, N. Saito, and O. Takai.** 5, 2009, J. Vac. Sci. Technol. A, Vol. 27, pp. 1183-1187.

76. *PECVD of fluorocarbon coatings from hexafluoropropylene oxide: Glow vs. afterglow.* **F. Intravuovo, E. Sardella, P. Rossini, R. D'Agostino, and P. Favia.** 4-6, 2009, Chem. Vap. Deposition, Vol. 15, pp. 95-100.

77. *Plasma nanostructuring of polymers: Different routes to superhydrophobicity.* **A. Milella, R. Di Mundo, F. Palumbo, P. Favia, F. Fracassi, and R. D'Agostino.** 6-7, 2009, Plasma Processes Polym., Vol. 6, pp. 460-466.

78. *Superhydrophobic coatings with reduced ice adhesion.* **D. K. Sarkar, and M. Farzaneh.** 9, 2009, J. Adhes. Sci. Tech., Vol. 23, pp. 1215-1237.

79. *Formation of superhydrophobic boehmite film on glass substrate by sol-gel method.* **X. Fang, Z. Yu, X. Sun, X. Liu, and F. Qin.** 1, 2009, Front. Chem. Eng. Chin., Vol. 3, pp. 97-101.

80. *Transparent superhydrophobic silica coatings on glass by sol-gel method.* **S. A. Mahadik, M. S. Kavale, S. K. Mukherjee, and A. V. Rao.** 2, 2010, Appl. Surf. Sci., Vol. 257, pp. 333-339.

81. *Superhydrophobic silica films by sol-gel co-precursor method.* **S. S. Latthe, H. Imai, V. Ganesan, and A. V. Rao.** 1, 2009, Appl. Surf. Sci., Vol. 256, pp. 217-222.

82. *Porous superhydrophobic silica films by sol-gel process.* **S. S. Latthe, H. Imai, V. Ganesan, and A. V. Rao.** 1-3, 2010, Microporous Mesoporous Mater., Vol. 130, pp. 115-121.

83. *Self-cleaning silica coatings on glass by single step sol-gel route.* **V. V. Ganbavle, U. K. H. Bangi, S. S. Latthe. S. A. Mahadik, and A. V. Rao.** 23-24, 2011, Surf. Coat. Technol. , Vol. 205, pp. 5338-5344.

84. *Durable superhydrophobic and antireflective surfaces by trimethylsilanized silica nanoparticles based sol-gel processing.* **M. Manca, A. Cannavale, L. De Marco, A. S. Arico, R. Cingolani, and G. Gigli.** 11, 2009, Langmuir, Vol. 25, pp. 6357-6362.

85. *Optically transparent superhydrophobic silica-based films.* **H. M. Shang, Y. Wang, S. J. Limmer, T. P. Chou, K. Takahashi, and G. Z. Cao.** 1-2, 2005, Thin Solid Films, Vol. 472, pp. 37-43.

86. *Simple nanofabrication of a superhydrophobic and transparent biomimetic surface.* **H. Lim, D. Jung, J. Noh, G. Choi, and W. Kim.** 19, 2009, Chin. Sci. Bull., Vol. 54, pp. 3613-3616.

87. *Effective slip and friction reduction in nanograted superhydrophobic microchannels.* **C. Choi, U. Ulmanella, J. Kim, C. Ho, and C. Kim.** 8, 2006, Phys. Fluids, Vol. 18.

88. *Design of surface hierarchy for extreme hydrophobicity.* **Y. Kwon, N. Patankar, J. Choi, and J. Lee.** 11, 2009, Langmuir, Vol. 25, pp. 6129-6136.

89. *Bioinspired degradable substrates with extreme wettability properties.* **W. Song, D. D. Veiga, C. A. Custodio, and J. F. Mano.** 18, 2009, Adv. Mater. , Vol. 21, pp. 1830-1834.

90. *Stable biomimetic superhydrophobic surfaces fabricated by polymer replication method from hierarchically structured surfaces of al templates.* **Y. Lee, K. Ju, and J. Lee.** 17, 2010, Langmuir, Vol. 26, pp. 14103-14110.

91. *A novel preparation of polystyrene film with a superhydrophobic surface using a template method.* **Z. Yuan, H. Chen, J. Tang, H. Gong, Y. Liu, Z. Wang, and X. Chen.** 11, 2007, J. Phys. D: Appl. Phys., Vol. 40, pp. 3485-3489.

92. *Facile fabrication of transparent superhydrophobic surfaces by spray deposition.* **H. S. Hwang, N. H. Kim, S. G. Lee, D. Y. Lee, K. Cho, and I. Park.** 7, 2011, ACS Appl. Mater. Interfaces, Vol. 3, pp. 2179-2183.

93. *Superhydrophobic and transparent ZnO thin films synthesized by spray pyrolysis technique.* **N. L. Tarwil, and P. S. Patil.** 24, 2010, Appl. Surf. Sci., Vol. 256, pp. 7451-7456.

94. *Versatility of chemical spray pyrolysis technique.* **Patil, P. S.** 3, 1999, Mater. Chem. Phys., Vol. 59, pp. 185-198.

95. *Self-cleaning antireflective coatings assembled from peculiar mesoporous silica nanoparticles.* **X. Li, X. Du, and J. He.** 16, 2010, Langmuir, Vol. 26, pp. 13528-13534.

96. *Superhydrophobic surfaces formed using layer-by-layer self-assembly with aminated multiwall carbon nanotubes.* **K. Liao, A. Wan, J. D. Batteas, and D. E. Bergbreiter.** 8, 2008, Langmuir, Vol. 24, pp. 4245-4253.

97. *A facile layer-by-layer deposition process for the fabrication of highly transparent superhydrophobic coatings.* **Y. Li, F. Liu, and J. Sun.** 2009, Chem. Commun., Vol. 19, pp. 2730-2732.

98. *Optical lithography with printed metal mask and a simple superhydrophobic surface.* **T. Kim, C. H. Baek, K. Y. Suh, S. Seo, and H. H. Lee.** 2, 2008, Small, Vol. 4, pp. 182-185.

99. *Contact angle hysteresis on rough hydrophobic surfaces.* **B. He, J. Lee, and N. A. Patankar.** 1-3, 2004, Colloids Surf. A, Vol. 248, pp. 101-104.

100. *Dewetting of conducting polymer inkjet droplets on patterned surfaces.* **J. Z. Wang, Z. H. Zheng, H. W. Li, W. T. S. Huck, and H. Sirringhaus.** 3, 2004, Nat. Mater., Vol. 3, pp. 171-176.

101. *Wetting and self-cleaning properties of artificial superhydrophobic surfaces.* **R. Furstner, W. Barthlott, C. Neinhuis, and P. Walzel.** 3, 2005, Langmuir, Vol. 21, pp. 956-961.

102. **Fletcher, N. H.** *The Chemical Physics of Ice.* Cambridge, Great Britain : Cambridge University Press, 1970.

103. *Ice nucleation in nature: Supercooling point (SCP) measurements and the role of heterogeneous nucleation.* **P. W. Wilson, A. F. Heneghan, and A. D. J. Haymet.** 1, 2003, Cryobiology, Vol. 46, pp. 88-89.

104. *Models for the growth of rime, glaze, icicles and wet snow on structures.* **Makkonen, L.** 1776, 2000, Phil. Trans. R. Soc. A, Vol. 358, pp. 2913-2939.

105. *Strategies for combating ice adhesion. Evaluation application-specific methods that help ensure smooth funtion of the world's infrastructure.* **Petrie, E. M.** 2, 2009, Met. Finish, Vol. 107, pp. 56-59.

106. *Preparation and characterization of silica/fluorinated acrylate copolymers hybrid films and the investigation of their icephobicity.* **Y. Huang, M. Hu, S. Yi, X. Liu, H. Li, C. Huang, and Y. Li.** 17, 2012, Thin Solid Films, Vol. 520, pp. 5644-5651.

107. *Dynamics of ice nucleation on water repellent surfaces.* **A. Alizadeh, M. Yamada, R. Li, W. Shang, S. Otta, S. Zhong, and M. L. Blohm.** 6, 2012, Langmuir, Vol. 28, pp. 3180-3186.

108. *Delayed freezing on water repellent materials.* **P. Tourkine, M. L. Merrer, and D. Quere.** 13, 2009, Langmuir, Vol. 25, pp. 7214-7216.

109. *Effects of contact angle hysteresis on ice adhesion and growth on superhydrophobic surfaces under dynamic flow conditions.* **M. A. Sarshar, C. Swarctz, S. Hunter, J. Simpson, and C. H. Choi.** 2013, ColloidPolym. Sci., Vol. 291, pp. 427-435.

110. *Understanding the effects of superhydrophobic coatings on energy reduction in anti-icing systems.* **C. Antonini, M. Innocenti, T. Horn, M. Marengo, and A. Amirfazli.** 1-2, 2011, Cold Reg. Sci. Technol., Vol. 67, pp. 58-67.

111. *Effects of nano-fluorocarbon coatings on icing.* **H. Wang, G. He, and Q. Tian.** 18, 2012, Appl. Surf. Sci., Vol. 258, pp. 7219-7224.

112. *Relationship between water wettability and ice adhesion.* **A. J. Meuler, J. D. Smith, K. K. Varanasi, J. M. Mabry, G. H. McKinley and R. E. Cohen.** 11, 2010, ACS Appl. Mater. Interfaces, Vol. 2, pp. 3100-3110.

113. *Ice adhesion on super-hydrophobic surfaces.* **S. A. Kulinich, and M. Farzaneh.** 18, 2009, Appl. Surf. Sci. , Vol. 255, pp. 8153-8157.

114. *Why superhydrophobic surfaces are not always icephobic.* **M. Nosonovsky, and V. Hejazi.** 10, 2012, ACS Nano, Vol. 6, pp. 8488-8491.

115. *Physical mechanisms responsible for ice adhesion.* **I. A. Ryzhkin, and V. F. Petrenko.** 32, 1997, J. Phys. Chem. B, Vol. 101, pp. 6267-6270.

116. *Prevention of ice accretion on aluminum surfaces by enhancing their hydrophobic properties.* **N. Saleema, M. Farzaneh, R. W. Paynter, and D. K. Sarkar.** 1-3, 2011, J. Adhes. Sci. Technol., Vol. 25, pp. 27-40.

117. *Highly resistant icephobic coatings on aluminum alloys.* **R. Menini, Z. Ghalmi, and M. Farzaneh.** 1, 2010, Cold Reg. Sci. Technol., Vol. 65, pp. 65-69.

118. *Effect of dew condensation on the wettability of rough hydrophobic surfaces coated with two different silanes.* **T. Furuta, M. Sakai, T. Isobe, and A. Nakajima.** 16, 2010, Langmuir, Vol. 26, pp. 13305-13309.

119. *Exploiting topographical texture to impart icephobicity.* **A. J. Meuler, G. H. McKinley, and R. E. Cohen.** 12, 2010, ACS Nano, Vol. 4, pp. 7048-7052.

120. *Ice accreation on superhydrophobic aluminum surfaces under low-temperature conditions.* **F. Wang, C. Li, Y. Lu, F. Lu, and Y. Du.** 1, 2010, Cold Reg. Sci. Technol., Vol. 62, pp. 29-33.

121. *Frost formation and ice adhesion on superhydrophobic surfaces.* **K. K. Varanasi, T. Deng, J. D. Smith, M. Hsu, and N. Bhate.** 23, 2010, Appl. Phys. Lett. , Vol. 97.

122. *Frost formation on a superhydrophobic surface under natural convection conditions.* **Z. Liu, Y. Gou, J. Wang, and S. Cheng.** 25-26, 2008, Int. J. Heat Mass Transfer, Vol. 51, pp. 5975-5982.

123. *Study on restraining frost growth at initial stage by hydrophobic coating and hygroscopic coating.* **L. Cai, R. Wang, P. Hou, and X. Zhang.** 5, 2011, Energy Build., Vol. 43, pp. 1159-1163.

124. *Adhesion and sliding of snow on hydrophobic solid surface.* **T. Kako, A. Nakajima, Z. Kato, K. Uematsu, T. Watanabe, and K. Hashimoto.** 1279, 2002, J. Ceram. Soc. Jpn., Vol. 110, pp. 186-192.

125. *Superhydrophobic surfaces cannot reduce ice adhesion* . **J. Chen, J. Liu, M. He, K. Li, D. Cui, Q. Zhang, and Y. Song.** 11, 2012, Appl. Phys. Lett., Vol. 101.

126. *Superhydrophobic and icephobic surfaces prepared by RF-sputtered polytetrafluoroethylene coatings.* **R. Jafari, R. Menini, and M. Farzaneh.** 5, 2010, Appl. Surf. Sci., Vol. 257, pp. 1540-1543.

127. *Anti-icing performance of superhydrophobic surfaces.* **S. Farhadi, M. Farzaneh, and S. A. Kulinich.** 14, 2011, Appl. Surf. Sci., Vol. 257, pp. 6264-6269.

128. *Verification of icephobic/anti-icing properties of a superhydrophobic surface.* **Y. Wang, J. Xue, Q. Chen, and J. Ding.** 2013, ACS Appl. Mater. Interface, Vol. 5, pp. 3370-3381.

129. *Do self-cleaning surfaces repel ice?* **H. Dodiuk, S. Kenig, and A. Dotan.** 4-5, 2012, J. Adhes. Sci. Technol., Vol. 26, pp. 701-714.

130. *Influence of roughness on a transparent superhydrophobic coating.* **K. L. Cho, I. I. Liaw, A. H. Wu, and R. N. Lamb.** 25, 2010, J. Phys. Chem. C, Vol. 114, pp. 11228-11233.

131. *Transparent, thermally stable and mechanically robust superhydrophobic surfaces made from porous silica capsules.* **X. Deng, L. Mammen, Y. Zhao. P. Lellig, K. Mullen, C. Li, and D. Vollmer.** 26, 2011, Adv. Mater., Vol. 23, pp. 2962-2965.

132. *Transparent superhydrophobic films based on silica nanoparticles.* **J. Bravo, L. Zhai, Z. Wu, R. E. Cohen, and M. F. Rubner.** 13, 2007, Langmuir, Vol. 23, pp. 7293-7298.

133. *Self-cleaning and antireflective packaging glass for solar modules.* **L. K. Verma, M. Sakhuja, J. Son, A. J. Danner, H. Yang, H. C. Zeng, and C. S. Bhatia.** 9, 2011, Renewable Energy, Vol. 36, pp. 2489-2493.

134. *One-step fabrication of fluoropolymer transparent films with superhydrophobicity by dry method.* **J. Wang, L. Wang, and L. Feng.** 1, 2011, J. Appl. Polym. Sci., Vol. 120, pp. 524-529.

135. *Single-step fabrication of transparent superhydrophobic porous polymer films.* **H. Yabu, and M. Shimomura.** 21, 2005, Chem. Mater., Vol. 17, pp. 5231-5234.

136. *Preparation of transparent super-hydrophobic polymer film with brightness enhancement property.* **K. Takeda, M. Sasaki, N. Kieda, K. Katayama, T. Kako, K. Hashimoto, and A. Nakajima.** 23, 2001, J. Mater. Sci. Lett., Vol. 20, pp. 2131-2133.

137. *A facile dip-coating approach based on three silica sols to fabrication of broadband antireflective superhydrophobic coatings.* **L. Gao, and J. He.** 2013, J. Colloid Interfac. Sci., Vol. 400, pp. 24-30.

138. *Broadband anti-reflective and water-repellent coatings on glass substrates for self-cleaning photovoltaic cells.* **X. Li, J. He, and W. Liu.** 2013, Mater. Res. Bull., Vol. 48, pp. 2522-2528.

139. *Surface hydrophobic co-modification of hollow silica nanoparticles toward large-area transparent superhydrophobic coatings.* **L. Gao, and J. He.** 2013, J. Colloid Interface Sci., Vol. 396, pp. 152-59.

140. *Nanodome solar cells with efficient light management and self-cleaning.* **J. Zhu, C. Hsu, Z. Yu, S. Fan, and Y. Cui.** 6, 2010, Nano Lett., Vol. 10, pp. 1979-1984.

141. *Direct structuring of a biomimetic antireflective, self-cleaning surface for light harvesting in organic solar cells.* **S. Choi, and S. Huh.** 6, 2010, Macromol. Rapid Commun., Vol. 31, pp. 539-544.

142. *Self-cleaning surfaces-virtual realities.* **Blossey, R.** 5, 2003, Nat. Mater., Vol. 2, pp. 301-306.

143. *Superhydrophobic and low light reflectivity silicon surfaces fabricated by hierarchical etching.* **Y. Xiu, S. Zhang, V. Yelundur, A. Rohathi, D. W. Hess, and C. P. Wong.** 18, 2008, Langmuir, Vol. 24, pp. 10421-10426.

144. *All-nanoparticle thin-film coatings.* **D. Lee, M. F. Rubner, and R. E. Cohen.** 10, 2006, Nano Lett., Vol. 6, pp. 2305-2312.

145. *Stable and transparent superhydrophobic nanoparticle films.* **X. Y. Ling, I. Y. Phang, G. J. Vansco, J. Huskens, and D. N. Reinhoudt.** 5, 2009, Langmuir, Vol. 25, pp. 3260-3263.

146. *Development of multifunctional sol-gel coatings: Anti-reflection coatings with enhanced self-cleaning capacity.* **R. Prado, G. Beobide, A. Marcaide, J. Goikeotxea, and A. Aranzabe.** 6, 2010, Sol. Energy Mater. Sol. Cells, Vol. 94, pp. 1081-1088.

147. *A practical superhydrophilic self cleaning and antireflective surface for outdoor photovoltaic applications.* **J. Son, S. Kundu, L. K. Verma, M. Sakhuja, A. J. Danner, C. S. Bhatia, and H. Yang.** 2012, Sol. Energy Mater. Sol. Cells, Vol. 98, pp. 46-51.

148. *Fabrication of highly antireflective silicon surfaces with superhydrophobicity.* **M. Cao, X. Song, J. Zhai, J. Wang, and Y. Wang.** 26, 2006, J. Phys. Chem. B, Vol. 110, pp. 13072-13075.

149. *Double-layered TiO2-SiO2 nanostructured films with self-cleaning and antireflective properties.* **X. Zhang, A. Fujishima, M. Jin, A. V. Emeline, and T. Murakami.** 50, 2006, J. Phys. Chem. B, Vol. 110, pp. 25142-25148.

150. *Self-cleaning particle coating with antireflection properties.* **X. Zhang, O. Sato, M. Taguchi, Y. Einaga, T. Murakami, and A. Fujishima.** 3, 2005, Chem. Mater., Vol. 17, pp. 696-700.

151. *Enhanced super-hydrophobic and switching behavior of ZnO nanostructured surfaces prepared by simple solution - immersion successive ionic layer adsorption and reaction process.* **P. Suresh Kumar, J. Sundaramurthy, D. Mangalaraj, D. Nataraj, D. Rajarathnam, and M. P. Srinivasan.** 1, 2011, J. Colloid Interface Sci. , Vol. 363, pp. 51-58.

152. *One-step preparation of antireflection film by spin-coating of polymer/solvent/nonsolvent ternary system.* **M. S. Park, Y. Lee, and J. K. Kim.** 15, 2005, Chem. Mater., Vol. 17, pp. 3944-3950.

153. *Antireflective coating fabricated by chemical deposition of ZnO for spherical Si solar cells.* **T. Minemoto, T. Mizuta, H. Takaura, and Y. Hamakawa.** 2-3, 2007, Sol. Energy Mater. Sol. Cells, Vol. 91, pp. 191-194.

154. *Chemically etched porous silicon as an anti-reflection coating for high efficiency solar cells.* **L. Schirone, G. Sotgui, and E. P. Califano.** 1-2, 1997, Thin Solid Films, Vol. 297, pp. 296-298.

155. *Biomimetic hierarchical ZnO structure with superhydrophobic and antireflective properties.* **J. Xiong, S. N. Das, B. Shin, J. P. Kar, J. H. Choi, and J. Myoung.** 1, 2010, J. Colloid Interface Sci., Vol. 350, pp. 344-347.

156. *The role of antireflective coatings in silicon solar cells - the influence on their electrical parameters.* **B. Swatowska, T. Stapinski, K. Drabczyk, and P. Panek.** 2, 2011, Optica Applicata, Vol. 41, pp. 487-492.

157. *Efficiency enhancement of InGaN-based multiple quantum well solar cells employing antireflective ZnO nanorod arrays.* **G. J. Lin, K. Y. Lai, C. A. Lin, Y. Lai, and J. H. He.** 8, 2011, IEEE Electron Device Lett., Vol. 32, pp. 1104-1106.

158. *Assembly and characterization of colloid-based antireflective coatings on multicrystalline silicon solar cells.* **B. G. Prevo, E. W. Hon, and O. D. Veley.** 8, 2007, J. Mater. Chem., Vol. 17, pp. 791-799.

159. *Mechanically durable superhydrophobic surfaces.* **T. Verho, C. Bower, P. Andrews, S. Franssila, O. Ikkala, and R. H. A. Ras.** 5, 2011, Adv. Mater., Vol. 23, pp. 673-678.

160. *Stable superhydrophobic surfaces induced by dual-scale topography on SU-8.* **J. Marquez-Velasco, M. Vlachopoulou, A. Tserepi, and E. Gogolides.** 5-8, 2010, Microelectron Eng., Vol. 87, pp. 782-785.

161. *Stable superhydrophobic surfaces over a wide pH range.* **L. Guo, W. Yuan, J. Li, Z. Zhang, and Z. Xie.** 7, 2008, Appl. Surf. Sci., Vol. 254, pp. 2158-2161.

162. *Mechanically stable and corrosion resistant superhydrophobic sol-gel coatings on copper substrate.* **A. V. Rao, S. S. Latthe, S. A. Mahadik, and C. Kappenstein.** 13, 2011, Appl. Surf. Sci., Vol. 257, pp. 5772-5776.

163. *Long-lived superhydrophobic surfaces.* **C. H. Xue, and J. Z. Ma.** 2013, J. Mater. Chem. A, Vol. 1, pp. 4146-4161.

164. *Processing and properties of transparent super-hydrophobic polymer film with low surface electric resistance.* **M. Sasaki, N. Kieda, K. Katayama, K. Takeda, and A. Nakajima.** 11, 2004, J. Mater. Sci., Vol. 39, pp. 3717-3722.

165. *Transparent superhydrophobic thin films with self-cleaning properties.* **A. Nakajima, K. Hashimoto, T. Watanabe, K. Takai, G. Yamauchi, and A. Fujishima.** 17, 2000, Langmuir, Vol. 16, pp. 7044-7047.

166. *Durable icephobic coating for stainless steel.* **L. B. Boinovich, A. M. Emelyanenko, V. K. Ivanov, and A. S. Pashinin.** 2013, ACS Appl. Mater. Interfaces, Vol. 5, pp. 2549-2554.

167. *Transparent nanostructured coatings with UV-shielding and superhydrophobicity properties.* **T. Wang, T. T. Isimjan, J. Chen, and S. Rohani.** 26, 2011, Nanotechnology, Vol. 22.

168. *Nanostructures for superhydrophobicity and low adhesion.* **B. Bhushan, K. Koch, Yong Chae Jung.** 4, 2008, Soft Matter, pp. 1799-1804.

169. *Multi-scale structured, superhydrophobic and wide-angle, antireflective coating in the near-infrared region.* **K. C. Camargo, A. F. Michels, F. S. Rodembusch, F. Horowitz.** 2012, Chemical Communications, Vol. 48, pp. 4992-4994.

170. *Fabrication of highly transparent and superhydrophobic silica-based surface by TEOS/PPG hybrid with adjustment of the pH value.* **K. C. Chang, Y.K. Chen, H. Chen.** 2008, Surface & Coating Technology, Vol. 202, pp. 3822-3831.

171. *Ultrahydrophobic and Ultralyophobic Surfaces: Some Comments and Examples.* **W. Chen, A.Y. Fadeev, M.C. Hsieh, D. Oner, J. Youngblood, T.J. McCarthy.** 10, 1999, Langmuir, Vol. 15, pp. 3395-3399.

172. *Superhydrophobic films on glass surface derived from trimethylsilanized silica gel nanoparticles.* **D. Goswami, S.K. Medda, G. De.** 2011, Applied Materials & Interfaces, Vol. 3, pp. 3440-3447.

173. *Super-hydrophobic PDMS surface with ultra-low adhesive force.* **M. Jin, X. Feng, J. Xi, J. Zhai, K. Cho, L. Feng, L. Jiang.** 2005, Macromolecular Rapid Communications, Vol. 26, pp. 1805-1809.

174. *Ultrasonic Shear Wave Anti-Icing System for Helicopter Rotor Blades.* **J. L. Palacios, Edward C. Smith, Huidong Gao, Joseph L. Rose.** 2006, American Helicopter Society International, Vol. 62, pp. 1-11.

Appendix A

Operating the Goniometer

Measuring Water Contact Angle

1. Load the sample onto the center of the stage of the goniometer, directly beneath the automatic syringe.
2. Use the dial wheel on the right side of the syringe to adjust the height and lower the syringe to 5mm from the sample surface.
3. Set the automatic controller to deposit 10 µL of distilled water, and click run.
4. Open the computer interface Toup View to capture a snapshot of the droplet profile. Save this image to the computer.
5. Open software program imagej and open the droplet profile image.
6. Click image on the upper toolbar in imagej, then click type, then change the picture to 32-bit (contact angle measuring software will only open black and white images).
7. Click on Plugins on the upper toolbar in imagej, then click drop_analysis, and finally, Drop Analysis LB_ADSA to open droplet contact angle measurement tool.
8. Set d [pixels] to 4.
9. Use y0 [pixels] to lower the top of the green outline to match the top of the droplet.
10. Use x0 [pixels] to center the green outline with the droplet.
11. Use h [pixels] to lower bottom of green outline to match bottom of droplet.
12. Use c[m-2] to adjust the shape of the green outline to an approximate of the droplet.
13. Adjust b [pixels] to match the shape of the green outline to the droplet as best as possible, if necessary, use c[m-2] to fine tune.
14. Read the contact angle under DROP PROPERTIES, Contact angle (Canvas): XX

Measuring Water Contact Angle Hysteresis

1. Load the sample onto the center of the stage of the goniometer, directly beneath the automatic syringe.
2. Use the dial wheel on the right side of the syringe to adjust the height and lower the syringe to 5mm from the sample surface.
3. Set the automatic controller to deposit 10 µL of distilled water, and click run.
4. Open the computer interface Toup View to capture a video of the droplet profile.
5. While capturing a video, deposit another 5 µL of distilled water, then also using the automatic syringe withdraw 10 µL of distilled water. Save this video to the computer.
6. Take snapshots of the video the moment before the contact line between the water and the sample surface advances when water is added, and the moment before the contact line recedes when water is removed.
7. Open software program imagej and open the advancing droplet profile image.
8. Click image on the upper toolbar in imagej, then click type, then change the picture to 32-bit (contact angle measuring software will only open black and white images).
9. Click on Plugins on the upper toolbar in imagej, then click drop_analysis, and finally, Drop Analysis LB_ADSA to open droplet contact angle measurement tool.
10. Set d [pixels] to 4.
11. Use y0 [pixels] to lower the top of the green outline to match the top of the droplet.
12. Use x0 [pixels] to center the green outline with the droplet.
13. Use h [pixels] to lower bottom of green outline to match bottom of droplet.
14. Use c[m-2] to adjust the shape of the green outline to an approximate of the droplet.
15. Adjust b [pixels] to match the shape of the green outline to the droplet as best as possible, if necessary, use c[m-2] to fine tune.
16. Read the contact angle under DROP PROPERTIES, Contact angle (Canvas): XX
17. Repeat steps 7-16 to measure the receding water contact angle.
18. Subtract the receding contact angle from the advancing contact angle

Operating the Ice Adhesion Tester

1. Connect the communications port from the data acquisition module and the ice adhesion tester to the computer.
2. Open the program CRK Motion Creator.
3. Set the running velocity to 100 pulse/sec.
4. Ensure that there is some slack in the cable connecting the sliding mechanism to the linear actuator.
5. Unscrew brace from horizontal sliders to have access to the sample holder.
6. Place room temperature sample into sample holder.
7. Secure brace to the horizontal sliders and insert the polycarbonate cylinder, pressing it firmly into place for a flush fit.
8. Working quickly, pour 25 mL of room temperature distilled water into the mold and allow that to freeze for 30 minutes at -20°C.
9. After 30 minutes, open the program instruNet World. Click File → Open → Network Setup and choose the location of Final Setup.
10. Click start, then choose the file to save the data recorded.
11. Set the direction of the linear actuator to positive and start the motion at 100 pulse/sec.
12. Let the experiment run until ice has been debonded form surface, then click stop on the instrunet program and the CRK Motion Creator program to stop the data recording and motion of the linear actuator.
13. Repeat steps 1-12 for as many trials as necessary.

Vita Auctoris

Name: Ryan Fillion

Place of Birth: Windsor, Canada

Year of Birth: 1988

Education: Ontario Secondary School Diploma
Essex District High School
Essex, ON
2002 – 2006

Bachelor of Applied Science
Mechanical Engineering – Material Option
University of Windsor
Windsor, ON
2007 – 2012

Masters of Applied Science
Engineering Materials
University of Windsor
Windsor, ON
2012 - 2015

Publications: R. M. Fillion, R. Riahi, A. Edrisy. A review of icing prevention in photovoltaic devices by surface engineering. *Renew. Sust. Energ. Rev.* 2014; 32: 797-809